Simulation of the thermoforming process of UD fiber-reinforced thermoplastic tape laminates

Zur Erlangung des akademischen Grades
Doktor der Ingenieurwissenschaften
von der KIT-Fakultät für Maschinenbau
des Karlsruher Instituts für Technologie (KIT)

genehmigte
Dissertation
von

M.Sc. Dominik Dörr
geboren am 22.03.1989 in Hardheim

Abstract

Forming of two-dimensional pre-products into complex geometries is one of the most determining process steps in manufacturing of continuously fiber-reinforced plastics. Thereby, thermoforming of unidirectional (UD) fiber-reinforced thermoplastic tape laminates plays an increasingly import role, especially in the automotive industry, due to low cycle times, material efficiency and recycleability. By means of thermoforming simulation, manufacturability of a specific geometry can be assured virtually and therefor required process parameters can be determined, preventing a time- and cost-expensive "trial and error" process design.

In this work, the requirements on thermoforming simulation of semi-crystralline thermoplastic UD-tapes are initially derived based on experimental results of a thermoforming study and material characterizations, showing that a thermomechanical approach considering rate- and temperature-dependent material modeling as well as crystallization kinetics is desirable for thermoforming simulation. Based on this, a thermoforming simulation approach using the commercial Finite Element (FE) software Abaqus in combination with several so-called user-subroutines is developed.

First, hypo- and hyperelastic material modeling is investigated and rate-dependent intra-ply modeling approaches are proposed. Thereby, an emphasis is laid on rate-dependent bending behavior, since this is a material characteristic usually neglected in thermoforming simulation. For this purpose, hypoviscoelastic modeling approaches following either a nonlinear Voigt-Kelvin or a nonlinear generalized Maxwell approach are presented. In comparison with experimental forming tests, a good agreement is observed. Besides this, an influence of rate-dependent bending modeling on the prediction of wrinkling behavior is observed.

In a next step, the aforementioned framework is enhanced by a "Discrete Kirchhoff Triangle" shell formulation, implemented as user-element in Abaqus. This enables in contrast to the approach presented in the previous chapter hyperviscoelastic material modeling for both, membrane and bending behavior. Based on this, a nonlinear Voigt-Kelvin as well as a nonlinear generalized Maxwell approach, which is based on a multiplicative decomposition of the deformation gradient, are presented. The presented approaches are applied to thermoforming simulation with a good agreement to experimental tests. The results reveal that a nonlinear Voigt-Kelvin approach is sufficient for membrane modeling.

Besides intra-ply modeling approaches, also inter-ply modeling approaches are presented. An advanced approach accounting for the relative orientation between the slipping plies, additionally to the usually considered dependency on the state variables transversal pressure and slip-rate, is proposed. In application of this approach to thermoforming simulation, however, negligible differences are observed compared to a conventional approach.

The presented approach for thermoforming simulation is finally enhanced to a coupled thermomechanical approach. The related thermal modeling takes into account radiation, convection and heat conduction as well as crystallization kinetics, where mechanical behavior is coupled to thermal behavior w.r.t. temperature and relative crystallinity. Based on this, the transition from the molten to the solid material state is predicted and considered in modeling of forming behavior. An improved agreement to experimental thermoforming results is observed for the thermomechanical approach, where also the local temperature evolution is accurately predicted. Severe crystallization during forming is observed for a disadvantageous choice of process parameters. Moreover, only the thermomechanical approach captures the influence of all relevant process parameters. Hence, it is concluded that the consideration of thermal effects as well as crystallization kinetics is favorable for the virtual process design of thermoforming processes with semi-crystalline thermoplastic UD-tapes.

Kurzfassung

Einer der entscheidendsten Prozessschritte bei der Herstellung von kontinuierlich faserverstärkten Kunstoffen ist die Umformung von zweidimensionalen Halbzeugen in komplexe Geometrien. Hierbei spielt das nicht-isotherme Stempelumformverfahren von unidirektional (UD) faserverstärkten thermoplastischen Tape-Laminaten aufgrund geringer Zykluszeiten, Materialeffizienz und Recyclingfähigkeit insbesondere in der Automobilindustrie eine immer größer werdende Rolle. Durch die Umformsimulation kann die Herstellbarkeit einer bestimmten Geometrie virtuell abgesichert und hierfür notwendige Prozessparameter bestimmt werden, wodurch eine zeit- und kostenintensive "Trial and Error" Prozessauslegung vermieden werden kann.

In dieser Arbeit werden initial anhand einer experimentellen Umformstudie und Materialcharakterisierungen die Anforderungen an die Umformsimulation von teilkristallinen thermoplastischen UD-Tapes abgeleitet. Hierbei zeigt sich, dass ein thermomechanischer Ansatz, unter Berücksichtigung der raten- und temperaturabhängigen Materialeigenschaften, als auch der Kristallisationskinetik, erstrebenswert ist. Darauf aufbauend wird mit der kommerziellen Finite Elemente (FE) Software Abaqus, in Kombination mit mehreren sogenannten User-Subroutinen, ein entsprechender Simulationsansatz entwickelt.

Zunächst werden hypo- und hyperelastischen Materialmodellierungsansätze untersucht, sowie ratenabhängige intra-ply Materialodellierungsansätze vorgestellt. Dabei liegt ein Schwerpunkt auf dem ratenabhängigen Biegeverhalten, da diese Materialeigenschaft üblicherweise nicht berücksichtigt wird, weshalb hierfür hypoviskoelastische Modellierungsansätze auf Basis eines nichtlinearen Voigt-Kelvinsowie eines nichtlinearen generalisierten Maxwell-Ansatzes vorgestellt werden. Unter Anwendung dieser Ansätze zeigt sich im Vergleich mit experimentellen Umformergebnissen eine gute Übereinstimmung. Darüber hinaus wird ein Einfluss der ratenabhängigen Biegeeigenschaften auf die Vorhersage der Faltenbildung beobachtet.

Im nächsten Schritt wird der Ansatz um eine "Discrete Kirchhoff Triangle" (DKT) Schalenformulierung erweitert, welche in Abaqus als User-Element implementiert ist. Dies ermöglicht im Gegensatz zu dem im vorherigen Kapitel vorgestellten Ansatz die hyperviskoelastische Modellierung des Membran- und des Biegeverhaltens. Darauf aufbauend werden ein nichtlinearer Voigt-Kelvin-, sowie ein nichtlinearer generalisierter Maxwell-Ansatz, welcher auf einer multiplikativen Zerlegung des Deformationsgradienten basiert, vorgestellt. In der Umformsimulation zeigt sich eine gute Übereinstimmung mit experimentellen Umformergebnissen. Darüber hinaus wird beobachtet, dass ein nichtlinearer Voigt-Kelvin-Ansatz für die Modellierung des Membranverhaltens ausreichend ist.

Neben intra-ply werden auch inter-ply Modellierungsansätze untersucht. Hierfür wird ein erweiterter Ansatz vorgestellt, der neben den üblicherweise berücksichtigten Zustandsgrößen Abgleitgeschwindigkeit und Transversaldruck auch die Relativorientierung zwischen den abgleitenden Schichten berücksichtigt. Bei der Anwendung dieses Ansatzes in der Umformsimulation werden jedoch nur geringe Unterschiede gegenüber einem herkömmlichen Ansatz beobachtet.

Der präsentierte Ansatz für die Umformsimulation von thermoplastischen UD-Tapes wird final zu einem gekoppelten thermomechanischen Ansatz erweitert. Die entsprechende thermische Modellierung berücksichtigt Strahlung, Konvektion und Wärmeleitung, sowie die Kristallisationskinetik, wobei das mechanische Verhalten über die Temperatur und die relative Kristallinität an das thermische Verhalten gekoppelt ist. Hiermit wird der Übergang vom schmelzflüssigen zum Festkörperzustand vorhergesagt und in der Modellierung des Umformverhaltens berücksichtigt. Hierdurch wird eine verbesserte Übereinstimmung mit den experimentellen Umformergebnissen erzielt und auch die lokale Temperaturentwicklung akkurat vorhergesagt. Darüber hinaus zeigt sich, dass bei einer ungünstigen Wahl der Prozessparameter eine starke Kristallisation schon während der Umformung auftritt. Da außerdem nur der thermomechanische Ansatz den Einfluss aller relevanten Prozessparameter berücksichtigen kann, wird geschlussfolgert, dass die Berücksichtigung thermischer Effekte sowie der Kristallisationskinetik vorteilhaft für die virtuelle Prozessauslegung nicht-isothermer Stempelumformverfahren mit teilkristallinen Thermoplasten ist.

Contents

1 Introduction

1.1 Motivation

Lightweight design is a development strategy, which aims to realize functions under specified technical, economical, environmental and social constraints by a system of minimum mass, while its reliability is ensured. Therefore, lightweight design can be regarded as a holistic development strategy and the enhancement of a system's efficiency rather than just reducing the mass [1, 2]. Composite materials reveal a particularly high lightweight potential, due to their excellent weight-specific material properties and their capability to be tailored to specific applications. While the automotive industry still mostly uses commodity materials such as steel and short glass fiber-reinforced composites [3], which are well-established since many years [4], the aerospace industry is using high-performance composite materials such as carbon fiber-reinforced materials since decades. This is attributable to automotive mass production, where the material dominates the overall costs, due to the high throughput. Hence, automotive industry requires highly automated and robust production technologies, which may induce a high investment, but are affordable as long as material costs are sufficiently low. In contrast, low cost tooling and processes are in focus for aerospace industry due to the limited quantities produced. Hence, semi-automatic processes including also manual labor are applied.

For automotive applications, it is necessary that system-efficient composite solutions are developed, which consider besides technical and technological targets also economical boundary conditions. Therefore, the increasing demand for the reduction of CO_2 emissions can be an enabler for composites in automotive industry. However, too high production costs and a limited understanding of automotive-specific processes still hinder high-performance composites to enter the automotive mass-production market.

Continuous fiber-reinforced plastics (CoFRP), however, reveal an exceptional lightweight potential and are particularly suited for structural components, due to their excellent weight-specific mechanical properties [5]. Nonetheless, automotive CoFRP manufacturing involves different challenges. First, raw materials are mostly expensive, which requires an optimal usage of the material. Thus, material consumption and waste needs to be optimized. Second, complexly shaped parts and their forming substantially influences the fiber structure. Besides this, manufacturing defects such as wrinkling or fiber undulations might occur. Henceforth, also injection, solidification and structural behavior of the final part is influenced by the forming process. For these reasons, a reliable virtual prediction of forming behavior by means of forming simulation is of utmost importance to enable a time- and cost-effective process and product design. Beyond that, prediction accuracy of subsequent simulation steps is in conjunction with a continuous CAE chain significantly increased, as presented by Kärger et al. [6] (cf. Figure 1.1). Within the CAE chain, relevant information is virtually predicted, retained and passed on successively to subsequent simulation steps.
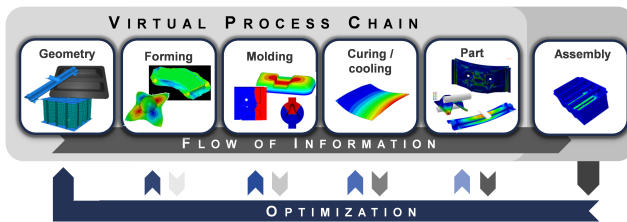
Figure 1.1: Schematic illustration of a continuous CAE chain for the reliable virtual analysis of manufacturing and structural behavior of continuously fiber-reinforced plastics (CoFRP) [6].

Finally, the need for low cycle times is also a challenge for automotive manufacturing of CoFRP. Low cycle times are achievable for theromset-based CoFRP with Resin Transfer Molding (RTM) or Wet Compression Molding (WCM) in combination with fast-curing resins. Another and for the automotive industry increasingly important process route is thermoforming of continuously fiber-reinforced thermo-

plastics (CoFRTP), due to low cycle times, material efficiency and recycleability [7, 8]. Thermoforming can be divided in three process steps, which namely are automated tape laying, pre-consolidation and thermostamping. Modern tape laying technologies are capable to produce highly automatized near net-shaped layups, with cuts in angles to minimize waste, to meet one of the key requirement large scale production outlined above. In combination with low cycle times, thermoforming reveals a great potential for automotive CoFRP applications, which implies a major importance for a robust thermoforming simulation approach for process design and process optimization, to assert CoFRTP in automotive industry.

1.2 State of the art

Composite forming processes can in general be divided according to the formed material system, which can be dry textiles or pre-impregnated textiles, usually denoted as prepregs. For prepregs, the according resin can be either thermoset or thermoplastic. Depending on the type of material, pre-product preparation as well as forming processes differ. Nonetheless, many similarities and synergies between the different processes exist. This is attributable to the fact, that forming behavior is governed by a very high tensile stiffness in fiber direction and a comparable low rigidity of all other deformation modes. For this reason, the state of the art is outlined in the following for forming processes (Section 1.2.1), material characterization for forming processes (Section 1.2.2) and forming simulation (Section 1.2.3) for the aforementioned material systems. Thereby, an emphasis is laid on thermoforming, according to the scope of this study.

1.2.1 Forming processes

1.2.1.1 Engineering textiles

Engineering textiles are dry, fibrous pre-products, which are available in different reinforcement types. The most applications include either woven fabrics or non-crimp fabrics (NCF) (cf. Figure 1.2). Such textiles are mostly manufactured in Resin-Transfer-Molding (RTM) processes, where conventional RTM processes are established in industry for many years [9]. To qualify this process for large volume production, however, further developments and modifications in terms of automatized handling and highly reactive resins for rapid filling and curing are necessary, in order to achieve low cycle times. For this purpose, special equipment compared to conventional RTM is required, which allows an exact and rapid dosing under high pressure. Based on this, resins which cure in less than 3 minutes can be used [10].

RTM processes can be divided into two main process steps: preforming of an initially flat pre-product into a three-dimensional preform and resin infiltration of the preform plus curing. The preforming step is often denoted as draping process and consists of the sequentially concurrent operations of tailored cutting of the fabrics, application of a binder and finally the draping of the fabric and consolidation of

Figure 1.2: Exemplary segment of engineering textiles: Unidirectional (UD) non-crimp fabric (a) and woven fabric (b) [11].

the binder. The application of a binder guarantees the dimensional stability of the pre-form after draping. For draping of engineering textiles, different process types exist, where the reader is referred to comprehensive reviews available in literature [12, 13].

Draping behavior can be influenced by inducing tensile membrane forces [14, 15, 16]. Therefore, tensile membrane forces are applied in draping processes, in order to reduce or avoid draping defects, such as wrinkling. Wrinkling during draping is studied to the most extent compared to other forming defects in both, experimental and virtual investigations. The mechanisms and remedies for wrinkling during draping are well understood, as shown in a comprehensive review by Boisse et al. [17]. To influence forming behavior by tensile membrane forces, often blank-holders are applied. The application of blank-holders, however, requires excessive material, which implies material waste. Beyond that, blank holders may reduce wrinkling, but at the same time may also induce other draping defects such as gapping, yarn distortion or even yarn damage, as shown by several authors [18, 19, 20]. The investigation and remedies for those defects, as well as further highly local defects such as yarn buckling, is part of ongoing experimental investigations [18, 21, 22, 23].

Besides blank-holders, also other strategies to prevent manufacturing defects are presented in literature. An active manipulation of the pre-form by piezo-activated metal interlayers is presented by Nezami et al. [20], which aims to reduce manufacturing defects by reducing inter-ply friction in multi-layer draping processes. An alternative draping

concept for the reduction of draping defects is the so-called sequential draping process, which is based on the segmentation of the draping tool into several stamps, to resemble the strike-out of wrinkles in hand-layup processes in a fully automatized process [24]. Another approach is the segmentation of the preform in so-called sub-preforms, which are assembled in a sequential draping process. Based on this, drapeability can be improved, while the loss in mechanical performance is reduced by an appropriate assembly of the according sub-preforms [25]. Besides preventing draping defects, also automatized handling, which is necessary for enabling large volume production [26], is part of current research. This includes the development of tailored textiles [27] or tailored stitching [28, 29], to optimize the balance between handleability and local drapeability.

Besides RTM processes, another currently investigated process including forming of engineering textiles is Wet Compression Molding (WCM) [30, 31, 32, 33]. In this process, preforming and injection is parallelized by means of resin application prior to forming. This enables short flow paths for the resin as well as low cycle times. Beyond that, a beneficial forming behavior of the infiltrated engineering textiles against dry engineering textiles is observed by Poppe et al. [30] and Hüttl et al. [34].

1.2.1.2 Thermoplastic prepregs

Continuously fiber-reinforced thermoplastic prepregs are available as so-called organosheets and unidirectional (UD) tapes (cf. Figure 1.3). Organosheets are supplied as rectangular and fully impregnated plates with a woven reinforcement. On the contrary, UD tapes are supplied as impregnated stripes on a role with a unidirectional fiber-reinforcement. UD tapes are the basis for manufacturing of so-called tailored laminates, which reduce material waste by means of near net-shape forming. Beyond that, a highly optimized material effort is possible, since the stripes can be placed in arbitrary directions at arbitrary positions. UD tapes can be manufactured based on two different process routes: in-situ tape placement or thermoforming, where the latter can also be applied to organosheets.

(a)   (b)
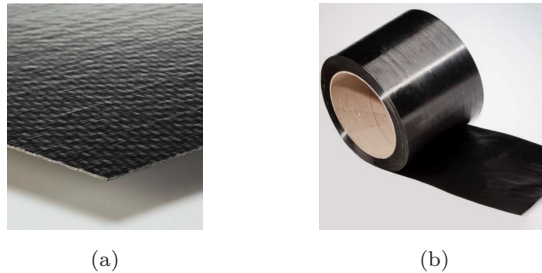
Figure 1.3: Exemplary pre-products of thermoplastic prepregs for thermoform-
ing: Organosheet (a) and UD tape (b) [35].

In-situ tape placement   The so-called in-situ thermoplastic tape
placement is one possible process route for manufacturing of UD
tapes, where single tape layers are locally heated above the melt-
ing temperature of the thermoplastic and consolidated layer-by-layer
by applying local pressure. This process is most suitable for large
structures, where long process cycle times are tolerable, such as in
aerospace applications [36].

Thermoforming   The second process route for manufacturing of ther-
moplastic prepregs is thermoforming, which is applicable for both,
organosheets and UD tapes. Thermoforming plays an increasingly
important role in the automotive industry, due to low cycle times and
the possible degree of automation [7, 37]. This process route can be
divided in three different process steps: automated tape laying, pre-
consolidation and thermostamping. The according material states of
these steps are exemplified in Figure 1.4.

Tape laying   For automated tape laying, several stripes of UD
tapes are laid layer-by-layer adjacent to each other and based on this
a laminate is stacked (cf. Figure 1.4(a)). Modern tape laying tech-
nologies are capable to produce highly automatized near net-shaped
layups with cuts in angles, to minimize material waste. The laid lam-
inates are usually ultrasonic spot-welded for handling and subsequent
pre-consolidation.

7

| (a) | (b) | (c) |
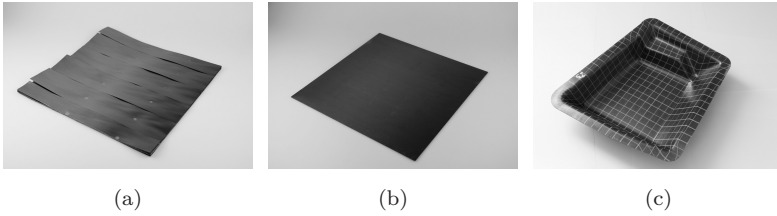
Figure 1.4: Resulting material states for the thermoforming process steps: layup after automatized tape-laying and spot-welding (a), laminate after pre-consolidation (b) and final part after thermostamping (c) [38].

Pre-consolidation   For pre-consolidation, the whole layup is heated well above the melting temperature of the thermoplastic and cooled, whilst transversal pressure is applied. In this manner, a monolithic laminate (cf. Figure 1.4(b)) mostly without voids is prepared, which improves the final part quality after thermostamping [39, 40]. Pre-consolidation is usually conducted by press consolidation with a plate tool in a hydraulic press. Another variant is the so-called vacuum-assisted pre-consolidation, which was proposed by Baumgärtner et al. [38, 41] and industrialized by Dieffenbacher GmbH (Germany) through the so-called FiberCon. Based on this strategy, high quality pre-consolidated laminates can be produced in a highly time- and energy-efficient manner.

Thermostamping   The pre-consolidated laminates serve as pre-product for thermostamping, for which different process variants exist. One possible process variant is double diaphragm forming. However, fast processing capabilities of thermoplastic composites are not fully exploited in double diaphragm forming, since the whole setup needs to be heated and cooled during each cycle [42, 43]. Therefore, matched-die forming, the second variant for thermostamping, is usually preferred for large volume production. The according process stages are schematically illustrated in Figure 1.5. In matched-die thermostamping, the pre-consolidated laminate is initially heated well-above the melting temperature of the thermoplastic. Usually, the laminates are dried prior to thermostamping, to prevent deconsolidation during heating [44]. Subsequently, the heated laminate is
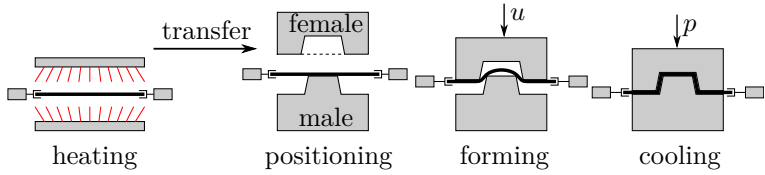
Figure 1.5: Schematic illustration of the different stages in matched-die thermostamping.

transferred and positioned in the mold. In the next stage, the mold closes and the part is formed, where the closing of the mold is usually displacement-controlled. Finally, the formed part is cooled, whilst a controlled transversal pressure is applied, to achieve an appropriate surface quality and a low porosity. A tool temperature lower than the laminate temperature induces a rapid cooling of the laminate and thus enables low cycle times.

For thermostamping, either a combination of metal and rubber dies, to improve a homogeneous pressure application [45, 46, 47], or solely metal dies can be applied. A combination of rubber and metal dies, however, is dedicated to unbalanced residual stresses due to inhomogeneous cooling of the laminate [48]. Furthermore, rubber molds are prone to degradation. Therefore, the industry usually tends to purely metallic dies.
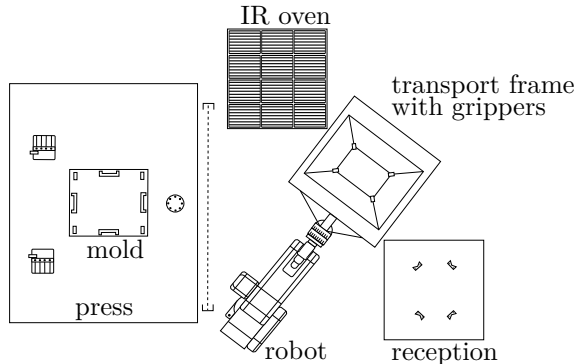
Figure 1.6: Schematic illustration of a possible layout for a fully automatized production cell for thermostamping [49].

A possible layout for a fully automatized manufacturing cell for large volume production, as it is applied at Fraunhofer ICT in Pfinztal (Germany), is exemplified in Figure 1.6. This includes an industrial robot, on which a transport frame is mounted for automatized laminate handling, an infrared (IR) field for heating of the laminate as well as a hydraulic press for thermostamping. Based on this, large volume production as well as highly reproducible forming cycles are enabled.

Forming defects During thermostamping, defects like wrinkling, gapping or fiber undulations can occur, in analogy to draping processes of engineering textiles. These forming defects occur depending on the applied material system, layup sequence and process parameters, as shown by several authors in experimental investigations [50, 51, 52, 53, 54, 55]. It is observed by Sachs [52] that unidirectional reinforcements tend to more pronounced wrinkling in critical areas compared to organosheets for the same matrix material and layup sequence. Beyond that, Vanclooster [50] has shown for organosheets that an increasing relative orientation between the layers increases the tendency to wrinkling behavior. The same tendency is observed for UD tapes by Schug et al. [54], since more pronounced wrinkling is observed for a quasi-isotropic compared to an orthotropic layup. Lastly, the process parameters forming velocity, tool and initial laminate temperature influence forming behavior, where a tendency to improved formability for a higher laminate temperature throughout forming is observed. This is achievable by a higher tool or laminate temperature, as well as by a higher forming velocity [51, 53, 54, 55]. The complex influence of process parameters on cooling and formability of the laminate, as well as the interaction of both, rate- and temperature-dependent material behavior on forming behavior, however, is not sufficiently investigated so far.

1.2.2 Characterization of forming behavior

The assessment of the complex deformation behavior of thermoplastic tape laminates during thermoforming is facilitated by a categorization into separate deformation mechanisms. Such a categorization has been assessed by several authors, e.g. by Cogswell [56]. Defor-

mation mechanisms can be defined on different length scales, where microscopic deformation mechanisms are related to the redistribution of fibers and matrix. On ply- and laminate-level, which is usually also denoted as meso- and macroscopic level, Figure 1.7 summarizes the major deformation mechanisms, in line with the categorization proposed by Haanappel [57].
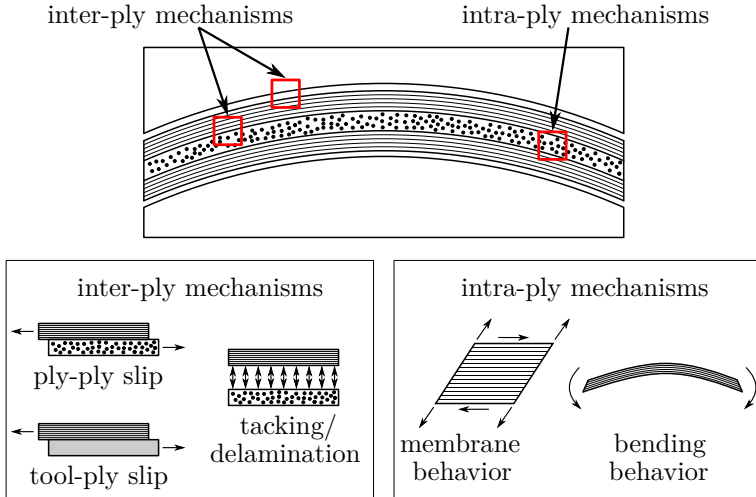
Figure 1.7: Deformation mechanisms during forming of continuously fiber-reinforced composites categorized according to inter- and intra-ply mechanisms.

Intra-ply mechanisms represent the forming behavior of the single ply of a multilayer laminate. On the contrary, inter-ply mechanisms represent the deformation mechanisms at the interfaces between the single plies of the stacked laminate as well as between the tool and the laminate. Due to the high tensile stiffness in both fiber directions and the comparably low stiffness of all other deformation modes, forming behavior of woven reinforcements is governed by in-plane (longitudinal) shear, bending as well as by inter-ply slip, which can be further subdivided into ply-ply and tool-ply slip. For unidirectional reinforcements, additionally the deformation behavior in transversal direction will also influence forming behavior. To characterize these

11

deformation mechanisms, several material characterization setups are presented in literature, depending on the material and deformation mechanism to be characterized.

1.2.2.1 Intra-ply shear behavior

Intra-ply shear testing is a common procedure for strength and stiffness characterization in structural analyses. Different test setups were developed to test composite laminates in their solid material state and reviews on this topic can be found in literature [58, 59]. Thereby, three rail shear tests, off-axis tests and picture frame tests are standardized testing procedures. These, however, are not necessarily standardized for composite material testing [60]. Nonetheless, the most relevant test setups for CoFRP pre-products are the picture frame test and the so-called bias extension test, which can be regarded as an off-axis tension test under 45° relative orientation of a woven or biaxial reinforcement to tension direction. Comparative studies on the picture frame test and the bias extension test reveal that redundant results are obtained for balanced woven engineering textiles [61, 62, 63]. Nonetheless, both test setups have different advantages and drawbacks. The most relevant difficulty in bias extension tests is its sensitivity to mesoscopic effects, such as yarn sliding, which is observed for woven reinforcements [62, 64] as well as for biaxial NCF [65]. Such mesoscopic effects prevent the application of analytical approaches for the extraction of mechanical properties. On the contrary, mesoscopic effects are not observed for picture frame tests, since "pure shear" deformation is intrinsically prescribed. Picture frame tests, however, are highly sensitive to undesired fiber pretensioning, due to a misalignment of the specimen [66]. Nonetheless, controlled fiber tensioning is a topic recently investigated in literature for picture frame testing, to identify the influence of shear-tension-coupling [14, 15, 67, 68].

Bias extension tests and picture frame tests are to the most extent applied to biaxial reinforcements for different material systems, which includes engineering textiles [62, 63], thermoset prepregs [61, 69, 70] as well as organosheets [71, 72]. An extended procedure based on off-axis tension tests is proposed by Schirmaier et al. [11, 73] for unidirectional NCF. For thermoplastic UD tapes, however, picture frame tests and bias extension tests are not applicable, since the small thickness of

the tapes yields ply splitting, strain localization and fiber buckling (cf. Figure 1.8(a)). Therefore, the well-established torsion bar test proposed by Haanappel et al. [60] is usually preferred for longitudinal shear characterization of thermoplastic UD tapes (cf. Figure 1.8(b)). Further attempts for intra-ply shear characterization are presented in literature, as comprehensively reviewed by Haanappel et al. [60]. These tests, however, are not presented here for brevity.

The torsion bar test deals with a prismatic bar, which is subjected to torsion by a rigid-body fixture within a standard rheometer. Since standard rheometers usually include a thermal chamber, testing at elevated and controlled temperatures is straightforward. The fibers in the specimens are aligned in direction of the torsional axis. Due to the high tensile stiffness in fiber direction, longitudinal shear deformation is introduced into the specimen, while the resulting torsional moment is captured as characterization result. Haanappel et al. [60] evaluated the shear response based on linear viscoelasticity theory in the small strain regime, in order to extract dynamic shear moduli.

(a)   (b)
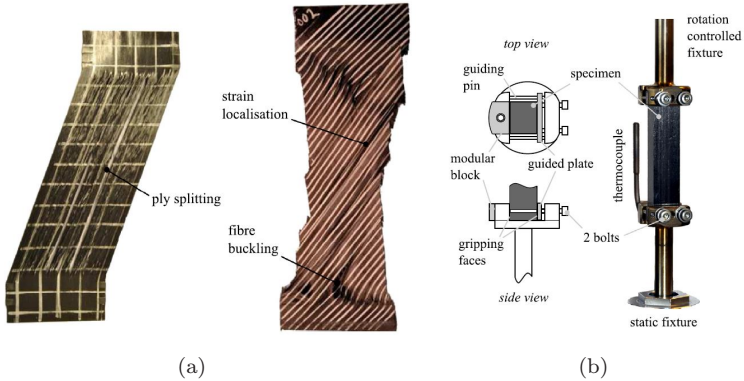
Figure 1.8: Characterization results for UD/PEEK in a picture frame test (left) and bias extension test (right) (a) and torsion bar characterization setup (b) [60].

1.2.2.2 Intra-ply bending behavior

For characterization of bending behavior of composites in the solid material state, three- or four-point bending tests are well-established. These tests, however, require a sufficiently large bending stiffness. For textile pre-products, this is given only by thick enough reinforcements, such as three-dimensional reinforcements [74], or for small specimens. The latter is utilized in dynamic mechanical analyses by Margossian et al. [75] and Ropers et al. [76] for UD tapes and organosheets, respectively. To the most extent, however, the so-called Peirce cantilever test [77], an extended Peirce cantilever test [78, 79, 80] or the Kawabata bending test (KES-FB2) [81] are applied for bending characterization of CoFRP pre-products.

The Peirce cantilever test [77] is based on cantilever bending of a specimen under its own weight over a skew plane, where the overhanging length is successively increased until the specimen makes contact with this skew plane (cf. Figure 1.9(a)). The bending modulus is determined by solving the differential equation expressing the equilibrium of a small part of a beam under large bending deformation by neglecting higher order effects. As presented by Lammens et al. [82], ignoring higher order effects in solving this differential equation can lead to large errors. Therefore, they propose a numerical solving strategy, which leads to a perfect agreement with FE solutions.

An extension of the Peirce cantilever test is realized by Bilbao et al. [78] as well as by Liang et al. [79, 80], based on digital image

<div align="center">(a)   (b)</div>
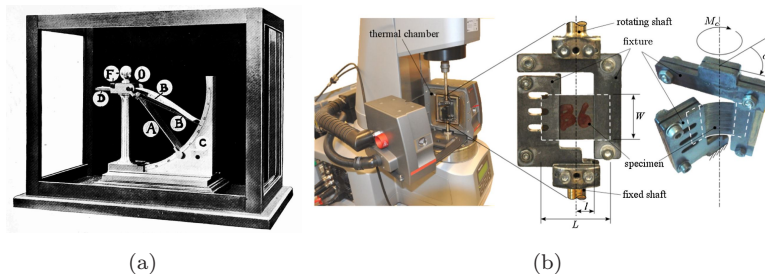
Figure 1.9: Peirce cantilever test (a) [77] and bending characterization based on the Kawabata principle in a standard rheometer (b) [83].

correlation (DIC) for the determination of the bending line, which enables to determine a moment deflection curve for arbitrary overhanging lengths. Based on this, bending behavior can be determined for a large variety of curvatures. Moreover, also dissipative effects can be determined, as shown by Bilbao et al. [78]. Besides these extensions, also variants with a vertical alignment of the cantilever test, in combination with a suitable load application exist in literature [84, 85, 86, 87]. These setups prevent a twist of the specimen and thus exclude an erroneous determination of the bending line.

Another test setup for bending characterization of CoFRP pre-products is the Kawabata bending test (KES-FB2) [81]. In this test, the specimen is clamped between a moving and a fixed clamp, where a movement within the moving clamp is allowed. This allows pure bending and prevents fiber tensioning. The moving clamp follows a circular path and thus a changing curvature is enforced. Based on this, the usually nonlinear and hysteretic behavior of CoFRP pre-products is directly measured [17]. Moreover, rate-dependent effects can be directly captured. Such loading cycles are far less easy to achieve and extract from cantilever tests.

A variant of the Kawabata bending test based on a rheometer setup is presented by Sachs and Akkerman [83] (cf. Figure 1.9(b)). This setup is highly suited for bending characterization of UD tapes and organosheets, since bending behavior is rate- and temperature-dependent [52, 75, 76, 83] and standard rheometers are usually capable to test at prescribed deformation rates and temperatures, by means of a thermal chamber. Moreover, higher curvatures than in DMA testing can be achieved.

1.2.2.3 Intra-ply tensile behavior

Intra-ply tensile behavior is characterized for the uniaxial as well as for the biaxial case using standard testing procedures. For woven reinforcements, nonlinear and biaxial tensile behavior in both fiber directions is observed [88, 89, 90, 91]. This results from the rovings, which are undulated in the initial configuration and straightened by means of increasing tensile forces during testing.

For biaxial NCF materials, no biaxial and less pronounced nonlinear tensile behavior resulting from fiber straightening is observed [66].

The same observation applies for unidirectional reinforcements in fiber direction. Therefore, tensile behavior in fiber direction is usually not characterized, since it is mostly linear as well as several orders of magnitudes stiffer compared to the other deformation modes.

On the contrary, a very compliant tensile behavior in transversal direction is in general observed for unidirectional reinforcements. For unidirectional NCF, a high sensitivity to the clamping situation with respect to the stitching is observed by Schirmaier et al. [11]. For UD tapes in the molten material state, a very low and also rate-dependent transversal stiffness is observed by Margossian et al. [92], which is characterized by means of DMA testing.

1.2.2.4 Inter-ply slip behavior

Several characterization setups are presented in literature for characterization of inter-ply slip, where a comprehensive review and benchmark study is presented by Sachs et al. [93]. In general, inter-ply slip characterization is based on pressure application on friction surfaces and the controlled pulling of a specimen out of these surfaces (pull-out tests) or through these surfaces (pull-through tests). These kind of tests are conducted for characterization of both, ply-ply and tool-ply slip, by providing the according friction surfaces. The inter-ply slip testing procedure is exemplified by the approach presented by Sachs [52] in Figure 1.10.
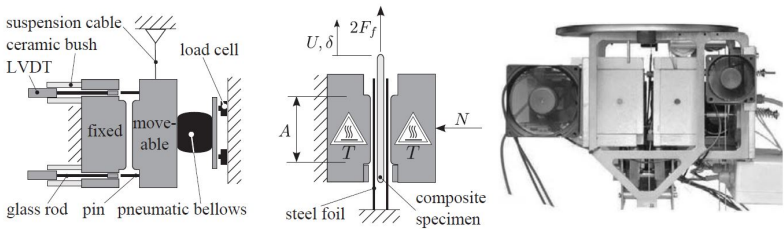
Figure 1.10: Schematic representation of the applied friction test set-up presented by Sachs [52].

The results of the benchmark study by Sachs et al. [93] reveal that fairly consistent results are obtained for the different investigated se-

tups. However, it is also outlined that inter-ply slip is prone to systematic errors, which can be reduced by means of larger friction surfaces and chamfered edges of the friction surfaces. Beyond that, pull-through tests are preferable rather than pull-out tests, to support a homogeneous pressure application.

Characterization results for engineering textiles [94, 95], UD tapes [52, 96, 97] and organosheets [52, 98, 99, 100, 101], as well as for thermoset prepregs [102, 103, 104, 105] are presented in literature. In general, slip-rate-, temperature- and pressure-dependent frictional behavior is observed. Beyond that, a dependency of ply-ply slip on the relative orientation between the slipping plies is observed for woven reinforcements due to the mesoscopic structure [34, 94] as well as for UD fiber reinforced thermoplastics [96, 97].

1.2.3 Forming simulation

For forming simulation of CoFRP, mainly two different modeling approaches can be distinguished: kinematic and mechanics-based approaches [12, 106]. While kinematic approaches are exclusively based on geometric mapping algorithms, mechanics-based algorithms take into account material behavior and process conditions by means of constitutive equations and boundary conditions, respectively. For this purpose, Finite Element Method (FEM) is highly suitable, since the final shape as well as the stress and strain distribution can be predicted by means of constitutive modeling of the relevant deformation mechanisms (cf. Figure 1.7). In the following, state of the art of forming simulation of CoFRP is outlined. Since in analogy to forming processes and material characterization similarities and synergies between different CoFRP material systems exist, state of the art is initially outlined independent of the material system for kinematic forming simulation (Section 1.2.3.1) and Finite Element forming simulation (Section 1.2.3.2). Subsequently, state of the art specifically for thermoforming simulation is reviewed (Section 1.2.3.3).

1.2.3.1 Kinematic forming simulation

Kinematic approaches transform the initially flat pre-product into a three-dimensional part based on geometric mapping algorithms. For

this purpose, assumptions about the kinematics are made, which are summarized for different reinforcement types by Lim and Ramakrishna [106]. Foremost, it is assumed that the material deforms incompressible and inextensible in fiber direction for all reinforcement types. For unidirectional reinforcements, it is additionally assumed that the normal distance between the fibers remains constant under in-plane shearing. This deformation mode is usually denoted as "simple shear" (cf. Figure 1.11(a)). By virtue of the assumption of material incompressibility, a constant thickness is predicted, since the in-plane area remains unchanged. In contrast, so-called "pure shear" or "Trellis shear" is assumed for woven reinforcements, which prescribes that the roving crossover points act as ideal pivots, whereas the lengths in both fiber directions remain unchanged (cf. Figure 1.11(b)). Based on material incompressibility, material thickens under shear deformation.
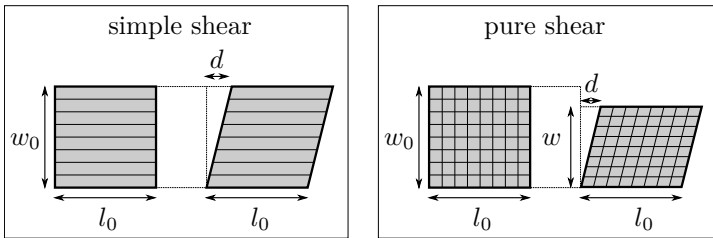
Figure 1.11: Schematic illustration of shear deformation mechanisms: "simple shear" for unidirectional reinforcements and "pure shear" for woven reinforcements.

Kinematic draping simulations are conducted since the mid '50s [107]. Since then, research in the context of kinematic draping simulation has focused on different mapping approaches [108, 109, 110, 111]. In general, kinematic approaches require the definition of a starting point or path as initial situation and the subsequent prediction of fiber orientation and resulting shear angle is comparable to an evolving flow front. Based on this, beneficial results can be obtained for manual processes, such as hand-draping [112, 113] or for automated processes, for which a reasonable guess of the initial situation is feasible. Nonetheless, the solution highly depends on the definition of an initial situation, which

can severely fail for unsymmetrical molds under the definition of a starting point [114]. A further restriction of kinematic approaches is the limitation to single layer forming processes, since no interaction between the different layers of multi-layer laminates can be taken into account. Beyond that, also process boundary conditions such as local grippers or blank holders cannot be taken into account. Moreover, forming defects such as wrinkling are not predictable, due to the neglected material behavior. Only a guess about wrinkling in highly sheared areas, where wrinkling is to be expected, is possible.

1.2.3.2 Finite Element forming simulation

Mechanics-based forming simulation takes into account material behavior and process conditions by means of constitutive equations and boundary conditions, respectively. Usually, the Finite Element Method (FEM) is applied for mechanics-based forming simulation. For constitutive modeling in composite forming simulation, the specificities of the composite reinforcements have to be taken into account. These specificities result from the internal structure of the composites, which are made up of thousands of fibers, between which a relative motion is possible. This makes the composite reinforcements to a multi-scale material, yielding a very specific material behavior. Thereby, it is usually distinguished between the micro-, meso- and macro-scale (cf. Figure 1.12).

For virtual process design, the macro-scale is to be preferred, since very efficient models capable to describe the relevant effects during forming can be established. Despite a great amount of work on FE composite forming simulation, however, there is no widely accepted macro-scale model. Besides this, more detailed models on lower scales are available, which are either applied to virtual material characterization or to a limited extent to forming simulation. Based on this, three different types in mechanical modeling approaches are distinguished: continuous, discrete or mesoscopic and semi-discrete approaches, where comprehensive reviews on this topic can be found in literature [17, 115, 116, 117].
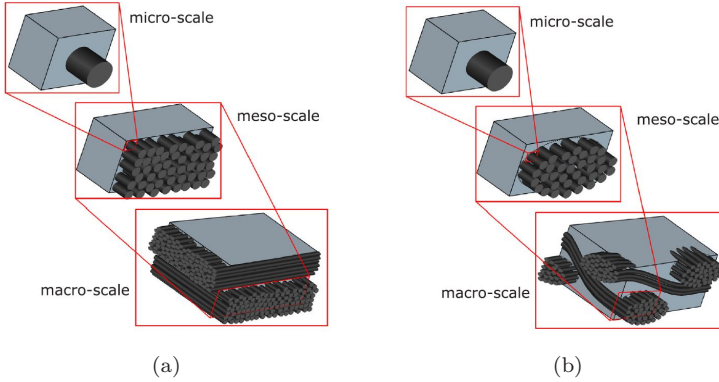
Figure 1.12: Schematic illustration of the different scales of composites for unidirectional (a) and woven reinforcements (b) [115].

Continuous approaches   The formed material is assumed for continuous approaches as a continuous medium in a homogenized manner on the macro-scale and the related deformation mechanisms are modeled by constitutive equations. While inter-ply mechanisms are modeled by contact models, intra-ply behavior is modeled by suitable material models.

A major aspect to be considered for intra-ply behavior is that conventional plate and shell theories are not applicable for CoFRP pre-products [17]. This is caused by the governing relative movement between the fibers under bending deformation, which is induced on micro-scale by the extremely low transverse shear stiffness (pre-impregnated textiles) or friction (engineering textiles) between the fibers compared to the quasi-inextensible fibers. Based on this, standard shell theories fail to predict the resulting very low bending stiffness by means of conventional thickness-based approaches. Following conventional shell theory, membrane and bending behavior is therefore usually considered in a decoupled fashion [118, 119, 120, 121]. On the contrary, enhanced approaches such as generalized continua are necessary to accurately predict bending behavior for three-dimensional shell approaches, which is part of ongoing research [17].

Another main requirement on intra-ply modeling is to accurately account for fiber rotation, which is induced by the extremely low rigidity of in-plane shear. This geometric nonlinearity is usually accounted for by applying either hypo- or hyperelastic material modeling approaches. Besides this, the so-called intra-ply shear locking or tension locking, which is a numerical locking effect, has to be prevented in composite forming simulation.

Material modeling approaches itself as well as the considered physical mechanisms differ for the continuous approaches presented in literature. These differences are outlined in the following. Thereby, it is distinguished between hypoelastic, hyperelastic and higher order approaches. Beyond that, the numerical tension locking and suitable remedies presented in literature are outlined.

Tension locking Locking phenomena are of high importance in Finite Element Analyses (FEA) and are based on the fact that in some cases the approximation made by the discretization is not compatible with a specific deformation state. Several locking effects exist and are well understood [122]. A locking effect observed in continuous composite forming simulation, which induces too stiff shear behavior, was first addressed by Yu et al. [123], who denoted this phenomena as intra-ply shear locking. The alignment of the mesh to the fiber direction is proposed as a possible remedy against this locking effect. A thorough investigation of the origin of this locking phenomena based on virtual bias extension tests is presented by Hamila et al. [124], who have shown that the locking is reducible to artificial fiber strains. It is shown for a quadrilateral element that the artificial fiber strains result from the inextensibility constraint in fiber direction in combination with the interpolation in a fully integrated quadrilateral element. Therefore, they called the locking phenomena tension locking, in order to be consistent with the naming of other locking phenomena [122]. In analogy to Thije et al. [125], they propose reduced integration for the inextensibility constraint as a possible remedy against tension locking. However, even for selective reduced integration, where solely the inextensibility constraint is under-integrated, severe zero energy modes in terms of hourglassing are observed for higher shear angles in bias extension tests [124]. Beyond that, a large impact on

shear behavior of standard hourglass stabilization procedures is observed. Therefore, a suitable stabilization procedure acting on the non-constant part of shear deformation is presented by Hamila et al. [124] for under-integrated quadrilateral elements, which enables non-aligned meshes for CoFRP forming simulation. So far, no triangular element for non-aligned meshes based on solely displacement degrees of freedom is available for CoFRP forming simulation.

Another remedy against tension locking is the application of multifield elements, which have displacement and strain degrees of freedom, as proposed by Thije et al. [125]. Unfortunately, this leads to a high numerical cost, which is hardly compatible with an explicit time integration usually applied in continuous forming simulation. Consequently, on the one hand quadrilateral elements with selective reduced integration and a suitable stabilization procedure to prevent hourglass modes can be applied in non-aligned meshes. On the other hand, standard triangular or quadrilateral elements in combination with full integration and fiber-aligned meshes can be adopted.

Hypoelastic approaches Material modeling based on a hypoelastic approach in combination with a suitable material frame is a possible approach for continuous forming simulation. Hypoelasticity can be assigned to large strain elasticity theory and is defined for the physically linear case by [122]

$$\boldsymbol{\sigma}^{\triangledown} = \mathbb{C} : \boldsymbol{D}, \tag{1.1}$$

where $\boldsymbol{\sigma}^{\triangledown}$ represents an objective rate of the Cauchy stress $\boldsymbol{\sigma}$, $\boldsymbol{D}$ the rate-of-deformation tensor and $\mathbb{C}$ the fourth-oder elasticity tensor. By means of the definition of an objective stress-rate, a material-fixed frame is introduced, in order to identify the rigid-body rotation, where rigid body translation is eliminated directly by gradient operations applied for the determination of the kinematic magnitudes. This enables the incremental integration of the hypoelastic constitutive equation in Equation 1.1 w.r.t. time within the material-fixed frame $\{\boldsymbol{e}_1, \boldsymbol{e}_2\}$ by means of the integration scheme presented by Hughes and Winget [126]:

$$\boldsymbol{\sigma}^{n+1} = \boldsymbol{\sigma}^n + \Delta\boldsymbol{\sigma}^{n+1} \quad \text{with} \quad \Delta\boldsymbol{\sigma}^{n+1} = \mathbb{C} : \Delta\boldsymbol{\varepsilon}^{n+1}, \tag{1.2}$$

where $\Delta \boldsymbol{\varepsilon}$ is the logarithmic strain increment within an according time step. Based on this, the constitutive equations are described solely in the current configuration by means of the Cauchy stress.

Commonly applied objective stress-rates are the Jaumann or the Green-Naghdi stress-rate. However, these stress-rates are based on an orthogonal material-fixed frame $\{\boldsymbol{e}_1, \boldsymbol{e}_2\}$, which makes them not directly applicable to continuous forming simulation, since the principal material orientations $\{\boldsymbol{f}_1, \boldsymbol{f}_2\}$ become non-orthogonal during forming due to shear deformation. Beyond that, the rotation of the material frame does in general not conform to the fiber rotation. These relations are exemplified for "pure shear" deformation in Figure 1.13.
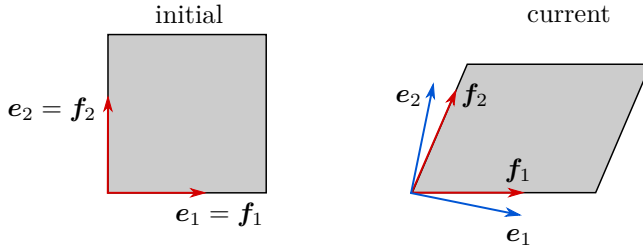
Figure 1.13: Schematic illustration of the rotation of an orthogonal, material-fixed frame (Green-Naghdi's frame) $\{\boldsymbol{e}_1, \boldsymbol{e}_2\}$ and principal material orientations $\{\boldsymbol{f}_1, \boldsymbol{f}_2\}$ under "pure shear" deformation from the initial to the current (deformed) configuration.

Therefore, several authors presented different non-orthogonal hypoelastic material modeling approaches, to account for the relative orientation between an orthogonal material-fixed frame and the fiber orientation in the current configuration. An incremental non-orthogonal formulation in agreement with the general definition of hypoelasticity (cf. Equation 1.1) was initially presented by Peng et al. [127, 128, 129]. This approach is based on the transformation of the elasticity tensor, to account for the relative orientation between the material-fixed frame and the principal material orientations. Badel et al. [130], however, have shown that the incremental formulation initially proposed by Peng et al. [127] leads to spurious tensile strains under shear deformation, which is reducible to the stress summation (cf. Equation

23

1.2) within the orthogonal material-fixed frame $\{\boldsymbol{e}_1, \boldsymbol{e}_2\}$. To overcome this issue, stress integration needs to be performed within a fiber parallel (auxiliary) frame $\{\boldsymbol{f}_1, \boldsymbol{f}_2\}$ and the resulting total stress is to be transformed to the orthogonal material-fixed frame. This approach is successfully applied to forming simulation by Badel et al. [131] and Khan et al. [132, 133]. Also Machado et al. [134, 135] applied this approach in the context of thermostamping of organosheets to model temperature- and rate-dependent shear behavior.

Independent from that, non-orthogonal material modeling based on absolute stress-strain-relations instead of incremental formulations were presented. Although these approaches do not follow the conventional integration scheme of hypoelastic approaches (cf. Equation 1.2), these are assigned to hypoelasticity, since they relate stress and strain in a material-fixed frame in the current configuration based on a non-orthogonal formulation. Yu et al. [136, 137] and later also Lin et al. [138] determined the stress-strain-relation based on geometric relations within a unit cell. On the contrary, Xue et al. [139], Cao et al. [140] and Lee et al. [141, 142] transformed the elasticity tensor to determine the total Cauchy stress based on the total logarithmic strain tensor.

Hyperelastic approaches Material modeling based on hyperelastic (or Green elastic) constitutive equations is another possible approach for continuous forming simulation. Hyperelastic materials are defined by a stored strain energy function ψ that is a potential for the stress [122]:

$$\boldsymbol{S} = 2\frac{\partial \psi(\boldsymbol{C})}{\partial \boldsymbol{C}}, \tag{1.3}$$

where $\boldsymbol{S}$ is the second Piola-Kirchhoff stress tensor and $\boldsymbol{C}$ the right Cauchy-Green deformation tensor. Besides this strain-based definition, the stored energy function may also be expressed by a set of invariants I_a of the symmetric right or left Cauchy-Green deformation tensors [143]. Since chain-rule applies by

$$\boldsymbol{S} = 2\sum_{a=1}^{N} \left(\frac{\partial \psi}{\partial I_a} \frac{\partial I_a}{\partial \boldsymbol{C}} \right), \tag{1.4}$$

the invariant-based definition of the stored energy function is complementary to the strain-based definition. In the context of composite forming, first approaches based on hyperelasticity are presented by Thije et al. [144] and Haanappel et al. [119] in the context of thermo-forming simulation. These approaches follow the so-called "Ideal Fiber Reinforced Material" (IFRM) theory presented by Spencer [145, 146], which assumes material incompressibility and inextensibility in fiber direction by

$$\boldsymbol{\sigma} = -p\mathbf{1} + T_1^{\mathrm{f}}\boldsymbol{a}_1 \otimes \boldsymbol{a}_1 + T_2^{\mathrm{f}}\boldsymbol{a}_2 \otimes \boldsymbol{a}_2 + \boldsymbol{\sigma}^{\mathrm{add}}, \tag{1.5}$$

where p is a hydrostatic pressure, $\mathbf{1}$ the second order identity tensor, T_1^{f} and T_2^{f} stresses in direction of the fiber orientations $\boldsymbol{a}_1$ and $\boldsymbol{a}_2$, respectively, and $\boldsymbol{\sigma}^{\mathrm{add}}$ an extra stress term to account for the material characteristic. Thije et al. [144] and Haanappel et al. [119] apply this theory based on a uniaxial hyperelastic constitutive equation to describe the fiber stresses T_1^{f} and T_2^{f}. The related constitutive equation can be regarded as the uniaxial case of a so-called St. Venant-Kirchhoff material [122]. Based on this, the inextensibility constraint is relaxed to a quasi-inextensibility constraint. Moreover, an isotropic Voigt-Kelvin approach is implemented for the extra stress term $\boldsymbol{\sigma}^{\mathrm{add}}$, by means of a St. Venant Kirchhoff model [122] for the elastic part and a Cross model [147] for the viscous part. Based on this, rate-dependent membrane behavior is modeled in thermoforming simulation.

Besides the above outlined strain-based hyperelastic approaches, hyperelastic approaches based on invariants are presented by Aimène et al. [148] and Peng et al. [149] for woven engineering textiles. The presented approaches are similar and include the tensile invariants I_1 and I_2 as well as a shear invariant I_{12}:

$$I_1 = \mathrm{tr}\left(\boldsymbol{C} \cdot \boldsymbol{L}_{11}\right), \tag{1.6}$$

$$I_2 = \mathrm{tr}\left(\boldsymbol{C} \cdot \boldsymbol{L}_{22}\right), \tag{1.7}$$

$$I_{12} = \frac{1}{I_1 I_2}\mathrm{tr}\left(\boldsymbol{C} \cdot \boldsymbol{L}_{11} \cdot \boldsymbol{C} \cdot \boldsymbol{L}_{22}\right), \tag{1.8}$$

where $\boldsymbol{L}_{ij}$ is the structure tensor $\left(\boldsymbol{L}_{ij} = \boldsymbol{A}_i \otimes \boldsymbol{A}_j\right)$. Subsequent investigations are presented for woven engineering textiles by Peng et

al. [150, 151] and further developments by Gong et al. for hyperelastic thermoforming simulation of organosheets [152] and shear-tension-coupling in draping simulation of woven engineering textiles [153].

The aforementioned two-dimensional invariant-based hyperelastic approaches are extended to a three-dimensional approach for 3D interlock composites by Charmetant et al. [154], based on the introduction of further invariants for compaction and out-of-plane shear. It is shown, however, that an additional bending stiffness modeled by beam elements, additionally to the stiffnesses modeled by the invariants, is necessary to correctly describe bending behavior. Rather than using discrete beam elements, this can also be achieved based on continuous approaches by generalized continuum mechanics, as shown among others by Mathieu et al. [155]. Such approaches are described briefly in the following paragraph.

The three-dimensional approach presented by Charmetant et al. [154] is extended by Guzman-Maldonado et al. [156] to a thermomechanical approach, based on alternating thermal and mechanical analyses. This includes a hyperviscoelastic approach based on Prony-series, to account for rate- and temperature-dependent shear behavior in thermoforming simulation of organosheets. Additionally, also dissipative effects in non-monotonous shear loading of woven fabrics are investigated in a recent study by the same research group by Denis et al. [157] based on a hyperelastic approach in combination with the multiplicative decomposition of the deformation gradient of Kröner-Lee [158].

Generalized continua approaches Recently, some researchers focus in the context of composite forming simulation on the application of so-called second gradient approaches, which can be defined in a general form by [159]

$$\psi(\boldsymbol{C}, \nabla\boldsymbol{\varphi}) = \psi_{\mathrm{I}}(\boldsymbol{C}) + \psi_{\mathrm{II}}(\nabla\boldsymbol{\varphi}), \tag{1.9}$$

where ψ_{I} corresponds to the first order hyperelastic strain energy potential outlined above and ψ_{II} to a second order strain energy potential based on a micro-descriptor $\boldsymbol{\varphi}$. A general form is introduced by choosing this micro-descriptor as the right Cauchy-Green deformation tensor $\boldsymbol{C}$. Based on this, it is enabled to account for gradients of shear

deformation such as in shear transition zones observed in bias extension test [160, 161, 162]. Besides this, also local in- and out-of-plane bending can be accounted for based on kinematic measures for the curvature:

$$
\begin{aligned}
\psi_{\mathrm{II}}(\nabla \boldsymbol{C}) =& \psi_{\mathrm{II}}(\nabla I_{\mathrm{ct1}}, \nabla I_{\mathrm{ct2}}, \nabla I_{\mathrm{cp}}) \\
=& \frac{1}{2} k_{\mathrm{cp}} ||\nabla I_{\mathrm{cp}}||^2 + \frac{1}{2} k_{\mathrm{ct1}} ||\nabla I_{\mathrm{ct1}}||^2 + \frac{1}{2} k_{\mathrm{ct2}} ||\nabla I_{\mathrm{ct2}}||^2
\end{aligned}
\tag{1.10}
$$

where ∇I_{ct1} and ∇I_{ct2} are kinematic measures for the out-of-plane curvature and ∇I_{cp} for the in-plane curvature. Based on this, bending behavior of thick interlock fabrics with a considerable amount of transverse shear can be correctly described [74, 155, 163]. Moreover, also in-plane roving bending in shear transition zones can be accounted for. It is shown by several authors [160, 161, 164] that neglecting of the according in-plane roving bending, which cannot be captured by first order approaches, leads to discontinuities in the rotation of the fibers in such shear transition zones. It is shown for panthographic structures that similar results are obtained by second order approaches and discrete modeling approaches, which are directly capable to account for in-plane bending [165, 166].

It should be noted that for thin reinforcements, which are usually described by conventional shells and a two-dimensional approach rather than by three-dimensional approaches, decoupling of membrane and bending behavior is comparable to the introduction of a second order strain energy potential (cf. Equation 1.9) for out-of-plane bending, since also in this case a separate strain energy potential based on a kinematic measure for the curvature is introduced to describe bending behavior.

Second order gradient approaches are so far mostly restricted to virtual analyses and investigations on coupon level. The only application to draping simulation is presented by Barbagallo et al. [167] for a thick reinforcement. Nonetheless, second order approaches reveal a promising strategy to further improve composite forming simulation, especially in order to further develop the consideration of mesoscopic effects, such as in-plane roving bending, on macroscopic level.

Discrete and mesoscopic approaches In discrete and mesoscopic modeling approaches, each constituent of the material is modeled individually. Based on this, the heterogeneity of the formed materials is directly captured. Nonetheless, the more details modeled lead to a large number of degrees of freedom, which makes such approaches CPU time intensive. Discrete approaches model each constituent in an abstract manner by 1D or a combination of 1D and 2D elements. In contrast, mesoscopic approaches model each constituent by 2D or 3D elements, where more detailed approaches are solely applied to virtual material characterization and less detailed approaches also to forming simulation. The differences between these modeling approaches are outlined in the following.

Discrete approaches - 1D elements. A network of spring, truss or beam elements is a possible approach for discrete forming simulation based on 1D elements (cf. Figure 1.14). This can also include pivot elements as well as torsional springs at the crossing points. A truss network for draping simulation of woven fabrics with a nonlinear shear modulus modeled by a truss under 45° is presented by Sharma and Sutcliffe [169]. This approach is extended for woven prepregs accounting for strain-rate-dependency and applied to stochastic analyses by Skordos et al. [170, 171].
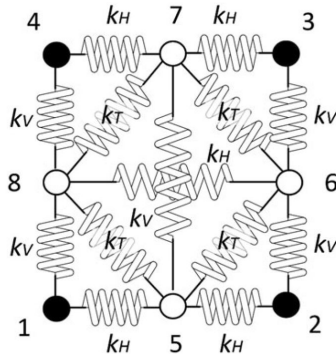
Figure 1.14: Lumped spring network for draping simulation of knitted meshes [168].

Similar approaches based on a network of lumped springs, which is comparable to a network of truss elements, is presented by Valantini et al. [168] for draping simulation of knitted meshes (cf. Figure 1.14). Besides applying solely linear springs, a network of linear and rotational springs is presented by Sze and Liu [172] as well as by Ben Boubaker et al. [173, 174], which enables to also account for in- and out-of-plane bending. Beyond that, also bar elements in combination with internal pivots [160, 175] or torsional spring [176, 177, 178] are also applied for panthographic lattice structures as well as for engineering textiles.

Discrete approaches based on 1D elements reveal a straightforward strategy to account for mesoscopic effects by conventional elements. Nonetheless, such approaches are restricted to single layer analyses, since no interaction between the layers can be modeled.

Discrete approaches - 1D and 2D elements Besides the application of solely 1D elements, also discrete forming simulation approaches based on a combination of 1D and 2D elements, such as membrane and shell elements (cf. Figure 1.15), are presented in literature by different research groups.
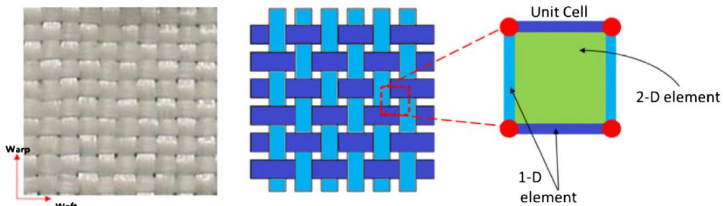
Figure 1.15: A representative fabric unit cell for the finite element discretization of a woven textile reinforcement based on a discrete approach with one- and two-dimensional elements [85].

The first approaches go back to Cherouat et al. [179, 180], who applied this approach to woven prepregs, under combination of membrane and truss elements to model the shear characteristic and the reinforcement, respectively. Bending behavior was not accounted for. Nonetheless, a remeshing technique [181, 182, 183, 184] to refine the mesh in order to conform to the geometry in highly curved areas is presented for

this approach. A similar approach, but under combination of truss and shell elements, is presented by Li et al. [185] and Gorczyca et al. [99, 186] for thermostamping of commingled fiberglass-polypropylene plain-weave fabric, where out-of-plane bending was not in focus so far. This approach is enhanced by using bar elements instead of truss elements by Dangora et al. [84, 85, 187], to also account for out-of-plane bending behavior and related forming defects. Also by Harrison et al. [51, 188, 189, 190], truss elements are applied initially, which are later replaced by bar elements [191], to account for the out-of-plane as well as for the in-plane bending stiffness. The approaches are applied to both, woven engineering textiles and organosheets. In the latter research, also a special emphasis is laid on the in-plane flexural rigidity representing the in-plane roving bending stiffness, which has proven to have a large impact on the modeling of shear transition zones in bias extension tests. The similar behavior is also observed in the context of second order gradient approaches by several authors [160, 161, 162], as outlined above.

Detailed mesoscopic approaches The constituents are modeled in their geometric dimensions by means of three-dimensional constitutive modeling approaches for detailed mesoscopic approaches, as exemplified for a unit cell of a woven engineering textile in Figure 1.16(a). Such approaches are characterized by the highly detailed modeling of small samples and are usually applied to virtual material characterization only. One exception is presented by Tavana et al. [192], who applied a mesoscopic approach for a single layer forming simulation of a woven fabric. Another promising approach is recently presented by Iwata et al. [193, 194], who propose to use mesoscopic approaches for subspaces, for which the according boundary conditions are determined by continuous approaches. This enabled to predict yarn buckling, which is a very local defect not predictable by continuous approaches.

Regarding virtual material characterization, Wang et al. [195] presented a detailed mesoscopic analysis of a three-dimensional textile reinforcement regarding transverse and longitudinal compaction. Beyond that, other researchers focused on mesoscopic analyses for virtual material characterization of woven engineering textiles for tensile and

shear behavior [90, 196, 197, 198, 199]. For such virtual analyses, suitable constitutive equations are necessary, which is also part of current research [130, 197, 200].

(a)   (b)
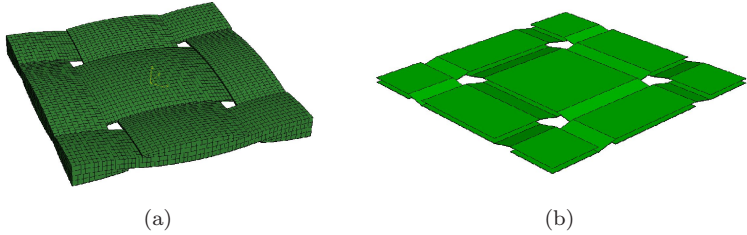
Figure 1.16: Comparison of mesoscopic unit cells: (a) detailed mesoscopic unit cell modeled by volume elements and (b) simplified mesoscopic unit cell modeled by shell elements [201].

Simplified mesoscopic approaches   Compared to detailed mesoscopic approaches, less details are modeled in simplified mesoscopic approaches, in order to reduce the degrees of freedom. Such a simplification is exemplified for a unit cell of a woven engineering textile in Figure 1.16(b). Based on this simplification, mesoscopic approaches are besides virtual material characterization also applicable to forming simulation of small geometries, as shown by Boisse et al. [201] for a woven engineering textile. Beyond that, simplified mesoscopic approaches are also presented in the context of non-crimp fabrics, for which the stitching is modeled by bar elements and the rovings are modeled either by solid elements [202, 203, 204] or shell elements [205, 206] in a discrete manner. Moreover, some approaches exist, which model the rovings in a continuous manner and the intra-ply stitching of non-crimp fabrics or an inter-ply stitching in multi-layer draping analyses by bar elements [29, 207]. Based on the simplification of continuous rovings, a great amount of computational effort can be saved, since possible contact areas are significantly reduced. An intermediate between discrete and continuous modeling of the rovings is the approach presented by Kärger et al. [6], who model the gaps between the rovings by a dummy shell with a negligible stiffness.

Semi-discrete approaches   To overcome the difficulties to describe the textile material as a continuum and the difficulties to model the rovings and their contact by discrete approaches, an intermediate approach can be applied, which is denoted as semi-discrete forming simulation. In general, semi-discrete approaches are based on the decomposition of an element into the according unit cells and the determination of the nodal forces of the element based on the evaluation of the constitutive equations for each unit cell. Based on this, the virtual work for a woven engineering textile is given for yarn tension and shearing by [208]

$$
\boldsymbol{\eta}^{\mathrm{T}} \boldsymbol{F}_{\mathrm{int}} = \sum_{p=1}^{nwa} \int_{p_l} {}^{p}T^{11p}\varepsilon_{11}(\underline{\eta}) \, \mathrm{d}l + \sum_{p=1}^{nwa} \int_{p_l} {}^{p}T^{22p}\varepsilon_{22}(\underline{\eta}) \, \mathrm{d}l + \sum_{p=1}^{nwa} {}^{q}C_s{}^{q}\gamma(\underline{\eta}),
$$

(1.11)

where $\boldsymbol{F}_{\mathrm{int}}$ are the nodal forces and $\boldsymbol{\eta}$ the virtual displacements. This approach is initially presented by Boisse et al. [209] and took only the biaxial tensile behavior into account. Later, also the in-plane shear stiffness is added [210, 211]. Beyond that, mesh dependency is eliminated and out-of-plane bending stiffness is added by Hamila et al. [208, 212]. This approach is applied to woven engineering textiles by Allaoui et al. [118] and Wang et al. [213], to thermoplastic prepregs by Liang et al. [79] and Wang et al. [214] and to biaxial NCF by Bel et al. [215].

1.2.3.3 Thermoforming simulation

In analysis of the state of the art of thermoforming simulation, a focus on either continuous, semi-discrete or discrete approaches with 1D and 2D elements is recognizable. Regarding semi-discrete and discrete approaches, a reasonable unit cell for the mesoscopic structure can be defined for woven reinforcements, as shown in the context of thermoforming simulation by several authors [51, 85, 98, 182, 214]. This is not possible for thermoplastic UD tapes, since there is no mesoscopic structure amenable on macroscopic level, since the fibers are homogeneously distributed within the plies. Therefore, an emphasis is laid in the following on continuous thermoforming approaches.

In general, material modeling approaches for continuous thermoforming simulation differ. Important material characteristics to be consid-

ered in thermoforming simulation of CoFRTP are the distinct rate-
and temperature-dependency at process conditions. In thermoforming
simulation, rate-dependent material behavior is considered for mem-
brane behavior in recent studies for organosheets. In this context,
Haanappel et al. [119] presented a hyperviscoelastic Voigt-Kelvin
(VK) approach with a nonlinear viscous behaviour. Furthermore,
Machado et al. [134] presented a hypoelastic approach with a nonlin-
ear shear modulus depending on shear angle and shear rate. Both
approaches are paremeterized according to characterization results
from bias extension tests at several deformation rates. Beyond that,
Guzman-Maldonado et al. [156] presented a linear hyperviscoelastic
approach based on a Prony series, which is parametrized according
to stress relaxation determined from the bias extension test. Re-
garding thermoplastic UD tapes, Haanappel et al. [119] presented
a purely hyperelastic approach for PEEK-CF, based on parametriza-
tion results from the well established torsion bar test [60] in the small
strain regime. From this test, dynamic shear moduli and a shear
relaxation modulus were extracted and transferred to the transient
regime by means of linear viscoelasticity theory (LVE). Since no dis-
tinct rate-dependency was observed, the material was modeled purely
hyperelastic. However, it is not guaranteed that rate-dependency can
be neglected outside the small strain regime and for other material
systems.

Regarding bending behavior, it is well known that bending has a dis-
tinct influence on wrinkling behavior [17, 57, 120]. Bending behavior
needs to be modeled in a decoupled fashion, which is a common proce-
dure in continuous composite forming simulation, as outlined in detail
in Section 1.2.3.2. In recently presented thermoforming simulation ap-
proaches [119, 152, 156], bending behavior is modeled purely elastic.
The distinct rate-dependent bending behavior observed in material
characterization by several authors [52, 75, 76] is usually neglected.
Rate-dependent bending behavior is first investigated by Dörr et al.
[216] and later also considered by Alshahrani et al. [87] using the
AniForm code.

Besides intra-ply deformation mechanisms, also inter-ply deformation
mechanisms need to be accounted for in continuous thermoforming
simulation. Usually, the pressure- and rate-dependency of inter-ply
slip is accounted for [119, 217, 218, 219]. However, it is assumed so far

that inter-ply slip is isotropic and independent of the fiber orientation of the slipping plies, although a dependency of inter-ply slip on the relative orientation of the slipping plies is observed for several material systems [34, 94, 96, 97].

Another mechanism considered only sparsely so far is thermal behavior in combination with the consideration of temperature-dependent material behavior within a thermomechanical analysis. A thermomechanical approach enables besides improved material modeling also to consider the influence of additional process parameters, namely tool and laminate temperature, which were identified to have a relevant influence on forming behavior (cf. Section 1.2.1.2). Machado et al. [135] presented a coupled thermomechanical approach, in which shear behavior of the considered semi-crystalline organosheet (PP-GF) is modeled temperature-dependent. An influence of the transient temperature on the resulting shear angle distribution is observed in this purely numerical study. Beyond that, Guzman-Maldonado et al. [156] presented a thermomechanical approach based on alternating thermal and mechanical analyses for a semi-crystalline organosheet (PA66-GF). The temperature field is predicted throughout forming and mechanical properties are defined as a function of temperature. It is shown, that the temperature field is significantly modified during forming. Both studies [135, 156] are restricted to temperatures well above the onset of recrystallization of the semi-crystalline thermoplastics. The onset of crystallization, however, induces a significant increase of mechanical properties [220]. It is not known so far, if crystallization during forming can be excluded in general.

1.3 Objective

This study focuses on the development of simulation methods for the stamp forming stage in thermoforming processes of UD fiber-reinforced thermoplastic tape laminates (cf. Figure 1.17) for the efficient application to virtual process design.
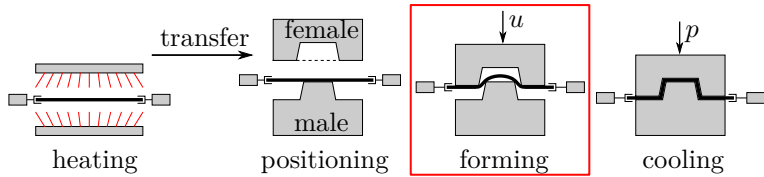
Figure 1.17: Schematic illustration of the different stamp forming stages in thermoforming processes.

In comparison of the state of the art for thermoforming simulation to draping simulation of engineering textiles, a clear focus on engineering textiles with an emphasis on wovens is observed. On the contrary, far less investigations are found with regard to thermoforming simulation, particularly for thermoplastic UD tape laminates. Based on the mechanisms not considered so far in thermoforming simulation (cf. Section 1.2.3.3), the following objectives for this study are derived:

- Experimental verification of the process parameters with a relevant influence on formability

- Experimental verification of the material characteristics to be considered in thermoforming simulation with an emphasis on temperature- and rate-dependency

- Development of a continuous forming simulation approach accounting for the influence of the experimentally identified relevant process parameters and material characteristics

- Validation of the developed forming simulation approach on part level for a complexly shaped geometry

- Identification of the most relevant mechanisms to be considered in thermoforming simulation for the accurate prediction of forming and wrinkling behavior

35

Delimitation   This study focuses on the development of a continuous thermoforming simulation approach based on conventional shell theory, which is expected to be a reasonable assumption for thermoforming simulation of thermoplastic UD tapes, due to the high slenderness ratio of the single plies. Therefore, compaction is not captured and transversal shear deformation is captured indirectly via decoupled bending behavior.

1.4 Outline

Following the objectives defined in the previous section, the influence of varying process parameters on the formability and the local temperature evolution are investigated in Chapter 2, based on results from an experimental forming study. Moreover, material characterization results are analyzed. Based on this, the requirements on thermoforming simulation are derived.

In the subsequent chapters, a thermoforming simulation approach using the commercial FE solver Abaqus in combination with several user-subroutines is developed. Within each chapter, the developed modeling approaches are parametrized and applied for validation to thermoforming simulation for a complexly shaped geometry. Moreover, the influence of the developed modeling approaches on formability prediction is analyzed. Thereby, the development of the according thermoforming simulation approach is structured as follows.

Chapter 3 investigates the restrictions of Abaqus to be applied to continuous composite forming simulation and presents an isothermal approach for thermoforming simulation based on superimposed elements in combination with user-defined material modeling and shell section integration. Hypo- and hyperelastic material modeling approaches are investigated for the application to composite forming simulation, since the superimposed bending enables only hypo(visco)elastic material modeling. An emphasis is laid on rate-dependent bending behavior. For this purpose, hypoviscoelastic modeling approaches following either a nonlinear Voigt-Kelvin or a nonlinear generalized Maxwell approach are presented.

Chapter 4 presents a further approach for isothermal thermoforming simulation based on the implementation of a user-element following

a geometric nonlinear "Discrete Kirchhoff Theory" (DKT) shell formulation, in combination with hyperviscoelastic constitutive equations. The constitutive equations follow either a nonlinear Voigt-Kelvin approach or a nonlinear generalized Maxwell approach based on a multiplicative decomposition of the deformation gradient. Based on the user-element, the same constitutive equations with different parametrizations are applied to model membrane and bending behavior, which is not possible with the approach presented in the previous chapter.

Chapter 5 presents inter-ply slip modeling approaches, which includes an approach to predict and consider the relative orientation between the slipping plies in inter-ply slip modeling. The approaches presented and investigated in this chapter are applied also to thermoforming simulation in the other chapters.

Chapter 6 presents a coupled thermomechanical approach. Thermal behavior is predicted by enhancing the user-element developed in Chapter 4 by a temperature degree of freedom. Crystallization kinetics is predicted and coupled to thermal and mechanical modeling. Finally, Chapter 7 provides a summary of the conclusions and recommendations for future activities.

1.5 Investigated material

The material investigated in the scope of this study is a continuously fiber-reinforced thermoplastic tape with a polyamide 6 matrix called Ultratape B3EC12 UD02 and supplied by the BASF SE. The reinforcement type is unidirectional and fibers are made from carbon. The basic material properties according to the material data sheet are listed in Table 1.1.

Trade name	Ultratape B3EC12 UD02 0160
Supplier	BASF SE
Matrix	Polyamide 6
Fibers	Carbon
Reinforcement type	Unidirectional
Fiber volume content (%)	49.0
Density (g/cm^3)	1.46
Thickness (mm)	0.16
Young's modulus (longit.) (GPa)	102.0

Table 1.1: Main material properties of the unidirectional PA6-CF tape investigated in the scope of this study at room temperature [221].

2 Experimental analysis of thermoforming behavior

Abstract

In order to derive the requirements on thermoforming simulation, the experimental results of a thermoforming study and material characterizations are investigated in the scope of this chapter. The experimental thermoforming study is based on variation of layup sequence, forming velocity, tool temperature and gripper force for a complexly-shaped and generic geometry. The results include besides surface measurements of the formed parts also local temperature measurements. In material characterization, crystallization kinetics as well as shear, bending and frictional behavior at the tool-ply and ply-ply interfaces are investigated at process conditions. In summary, a dependency of formability on all of the varied process parameters as well as temperature- and rate-dependent material behavior is observed. Based on the experimental results, the requirements on thermoforming simulation are derived, showing that a thermomechanical approach considering rate- and temperature-dependent material modeling as well as crystallization kinetics is desirable for thermoforming simulation.

The assessment of the complex forming behavior of thermoplastic UD tape laminates during thermoforming is facilitated by a categorization into separate deformation mechanisms (cf. Section 1.2.2). Such deformation mechanisms can be defined on different length scales. On ply- and laminate-level, usually also denoted as meso- and macroscopic level, Figure 1.7 summarizes the major deformation mechanisms.

The global deformation of the laminate during thermoforming is determined by a complex interaction between these deformation mechanisms, which in turn are influenced by process parameters as boundary or initial conditions as well as by material behavior. In the scope of this chapter, the complex forming behavior as well as the deformation mechanisms are analyzed experimentally for the material investigated in the scope of this study (cf. Section 1.5). This study pursues the identification of the relevant process parameters and material characteristics to be considered in thermoforming simulation. Based on this, the requirements on thermoforming simulation of thermoplastic UD tapes are derived. For this purpose, initially experimental methods based on surface measurements are introduced in Section 2.1. These methods will be applied throughout this study for experimental investigations as well as for validation of thermoforming simulation. Subsequently, experimental forming tests as well as material characterization results are investigated in Section 2.2 and 2.3, respectively.

2.1 Experimental surface analyses

Surface measurements are adopted in the scope of this study for both, experimental investigations and forming simulation validation. Different commercial surface measurement systems exist on the market [222]. In general, the result of surface measurements are point clouds describing the surface of the measured specimen. Point clouds can be triangularized, in order to provide a discretized surface mesh, which enhances the possibilities for geometric postprocessing [223]. Such a triangular surface mesh is exemplified in Figure 2.1 for a thermoformed part at a remaining tool travel of 5 mm.
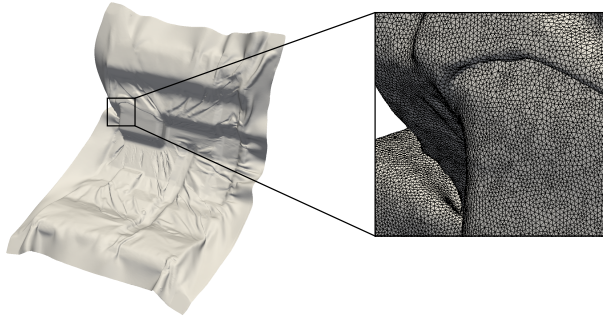
Figure 2.1: Triangularized 3D measurement of a thermoformed part with a quasi-isotropic layup and 5 mm remaining tool travel with shielded and visible element edges (detail).

2.1.1 Outer contour quantification

The determination of optimal tailorings of pre-products for near-net shaped forming is one of the major tasks and benefits of forming simulation. Therefore, the outer contour represents an important validation magnitude for thermoforming simulation. For outer contour quantification, the point cloud obtained from surface measurements or the nodes from a forming simulation result can be adopted to determine a so-called α-shape [224], which defines the outer contour of the according result. In this study, the outer contour projection in z-direction (forming direction) is determined by a 2D α-shape, based on the alignment of the investigated specimen in the x-y-plane. By means of an appropriate choice of the α-value, the outer contour is intrinsically smoothened. This can be useful when applying the outer contour determination to a surface measurement result with image noise or insufficiently scanned areas along the outer contour.

Figure 2.2 shows an exemplary result for a thermoformed part with a quasi-isotropic layup at a remaining tool travel of 5 mm. The result reveals that the outer contour (black) is tracked accurately.
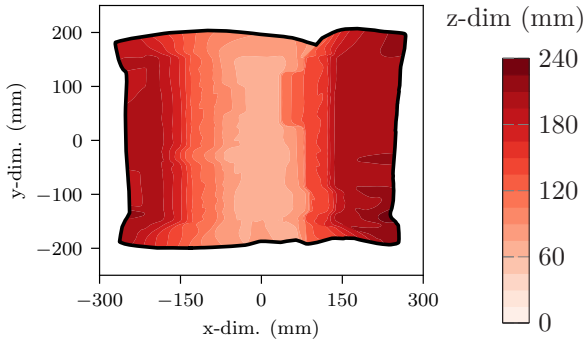
Figure 2.2: Exemplary contour plot of the coordinate in forming direction (z-dim.) and outer contour tracked by a 2D α-shape (black) for a thermoformed part with a quasi-isotropic layup and 5 mm remaining tool travel.

2.1.2 Wrinkling quantification

Wrinkling is a major issue in thermoforming processes of complexly shaped geometries [13, 119]. Therefore, a method for wrinkling quantification is desirable for the systematic experimental assessment of thermoforming processes as well as for validation of thermoforming simulation. Different methods for wrinkling quantification are presented in literature, which originate from the textile industry for the quantification of fabric wrinkling. Often, imaging techniques based on gray value analyses of infrared lighted specimens are applied in combination with wavelet transforms, to quantify features like wrinkle density or wrinkle orientation [225, 226, 227]. This approach, however, is usually applied only to wrinkling quantification of two-dimensional specimens. A promising approach for wrinkling quantification was initially proposed for thermoformed parts by Haanappel [57], which is based on surface curvature estimation by means of a triangularized surface. The underlying triangular surface mesh enables the application to both, surface measurements and forming simulation results. Therefore, this approach is adopted in the scope of this study and the algorithm for curvature estimation presented by Dong and Wang [223] is implemented in an in-house Python postprocessing script. A 2-ring neighborhood is chosen for normal curvature estimation, since other-

wise poor results are obtained for structured finite element meshes, as adopted in forming simulation.

The algorithm by Dong and Wang [223] provides an estimation of the principal curvatures κ_i^{I} and κ_i^{II} at each node i of the triangularized surface. Based on the principal curvatures, the modified mean curvature proposed by Haanappel [57] is evaluated as equivalent scalar value by

$$\bar{\kappa}_i = \frac{1}{2} \left(\left| \kappa_i^{\mathrm{I}} \right| + \left| \kappa_i^{\mathrm{II}} \right| \right).\tag{2.1}$$

This value is also applied in the scope of this study, since the arithmetic mean would yield zero curvature for a saddle point with equal absolute but opposite principal curvatures. An exemplary result for the modified mean curvature $\bar{\kappa}$ is shown in Figure 2.3. The distinct wrinkling behavior observed for the quasi-isotropic layup at a remaining tool travel of 5 mm is clearly captured by the modified mean curvature.
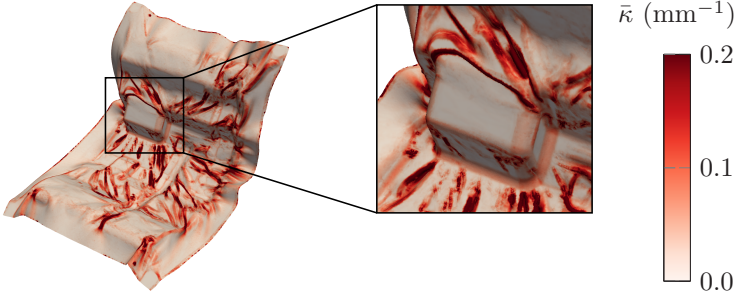
Figure 2.3: Modified mean curvature $\bar{\kappa}$ exemplarily determined for a thermoformed part with a quasi-isotropic layup and a remaining tool travel of 5 mm.

In order to provide a scalar response variable for the whole specimen, the nodal modified mean curvature is transformed to an elemental magnitude based on the interpolation to the centroid by

$$\bar{\kappa}_i^{\mathrm{el}} = N_j \left(\xi = \tfrac{1}{3}, \eta = \tfrac{1}{3} \right) \bar{\kappa}_{ij} = \frac{1}{3} \sum_{j=1}^{3} \bar{\kappa}_{ij},\tag{2.2}$$

where N_j is the triangular and linear shape function [228], ξ and η the covariant coordinates and j the nodes of the triangle i. Based on the elemental modified mean curvature $\bar{\kappa}_i^{\text{el}}$, the arithmetic mean of the modified mean curvature weighted by the triangle area A_i is determined by

$$\langle \bar{\kappa}^{\text{el}} \rangle = \frac{\sum_{i=1}^{N^{\text{el}}} \left(\bar{\kappa}_i^{\text{el}} A_i \right)}{\sum_{i=1}^{N} A_i}, \tag{2.3}$$

where N^{el} is the number of elements of the whole specimen. This yields a scalar response variable describing wrinkling intensity of the whole specimen, which can be applied to response surface methodology (RSM) [229] for the quantitative assessment of the interaction between e.g. process parameters and wrinkling behavior.

2.2 Experimental process analysis

Formability as well as the influence of process parameters on formability is experimentally analyzed in the following. For this purpose, the results of a thermoforming study conducted by Tobias Joppich [230] at the Fraunhofer ICT in Pfinztal, Germany for a generic geometry and with the material investigated in the scope of this study (cf. Section 1.5) are adopted. In this study, tool temperature T^{tool}, forming velocity $\bar{v}^{\text{tool}}$ and gripper force F^{grip} is varied according to a face-centered central composite design (CCD) [229] for two different layups. This results in 15 design points for each layup, where each design point is replicated three times. The according levels of the varied design factors are listed in Table 2.1.

Design factors	Unit	Levels
Tool temperature (T^{tool})	(°C)	$\{70 ; 110 ; 150\}$
Mean forming vel. ($\bar{v}^{\text{tool}}$)	(mm/s)	$\{5 ; 15 ; 45\}$
Gripper force (F^{grip})	(N)	$\{0 ; 24.73 ; 66.0\}$
Layup	(deg)	$\{[0;90]_{2\text{s}} ; [0;-45;45;90]_{\text{s}}\}$

Table 2.1: Design factors and levels varied according to a face-centered central composite design (CCD) for the two considered layups.

The adopted results of this study include besides surface measurements of the formed parts also local temperature measurements during heating, transfer and forming. Both is adopted for the investigation of the interaction between the varied parameters and formability, which is outlined in the following. Initially, the employed experimental setup for thermoforming experiments is presented in Section 2.2.1. Subsequently, the influence of the varied process parameters on forming behavior is analyzed in Section 2.2.2, based on surface measurements of the formed parts. Finally, the influence of the varied parameters on the local temperature evolution is investigated in Section 2.2.3.

2.2.1 Experimental setup

Industrial-scaled equipment, which is schematically illustrated in Figure 2.4, is adopted at Fraunhofer ICT in Pfinztal, Germany for the experimental thermoforming study [230]. This comprises an infrared(IR)-field, a transfer system and a hydraulic press.
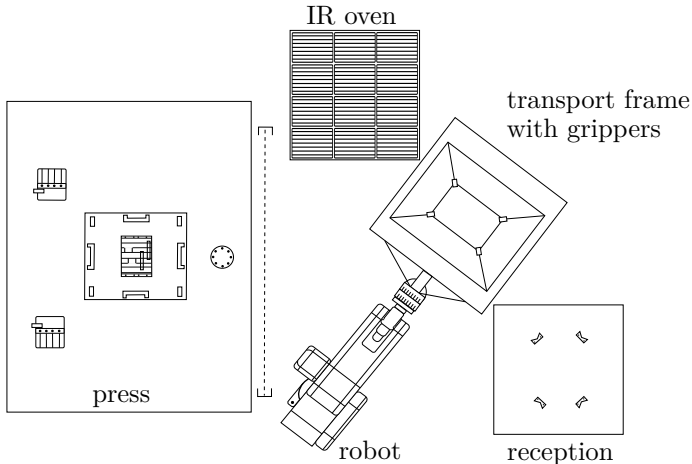
Figure 2.4: Schematic illustration of the industrial-scaled process equipment applied for the experimental thermoforming study.

The IR-field is used for the controlled heating of the laminate. The transfer system consists of an industrial robot and a transport frame

with pneumatic cylinders and needle grippers, which is mounted on the industrial robot. This transfer system is used for the fully automatized transfer of the laminate from the material reception through the IR-field to the mold. Moreover, the pneumatic cylinders are used to apply membrane forces during forming. During forming, the tool stroke is conducted displacement-controlled by the upper male mold. As soon as the mold is fully closed, the press switches from a displacement- to a force-control, to apply a controlled part pressure for consolidation of the laminate.

The part investigated in the scope of this study is shown in Figure 2.5 and measures a basal area of $300\,\text{mm} \times 416\,\text{mm}$ and a depth of $150\,\text{mm}$. This part and according tools were designed to investigate forming behavior by means of a complexly shaped geometry, including corner bendings and beads with high local curvatures, since such kind of geometries can be found in automotive applications of thermoplastic UD tape laminates.
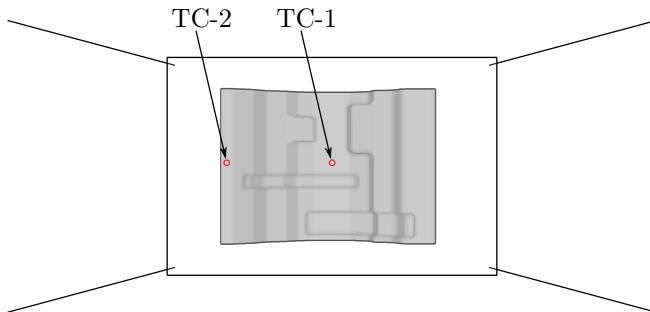
Figure 2.5: CAD model of the investigated generic geometry as well as schematic illustration of the initial blank and thermocouple (TC) position and gripper arrangement.

The pre-consolidated laminates, which are dried prior to forming, are initially flat and rectangular, measure $420\,\text{mm} \times 636\,\text{mm}$ and consist of 8 single plies. The laminate is centered over the mold by the transfer system with a slight local contact between the laminate and the lower female mold prior to forming. The grippers have a relative orientation of 15° w.r.t. the longitudinal axis of the part. The initial temperature

of the laminates after the heating stage is approximately 285 °C for all of the 30 design points.

2.2.2 Analysis of formability

To enable the analysis of forming behavior, the press profile is adapted to stop at a defined remaining tool travel Δz. Since the laminate cools and therefore the thermoplastic solidifies, the incompletely formed parts can be ejected. Based on this, the analysis of formability and evolving wrinkles is enabled, as exemplarily shown in Figure 2.6.

$\Delta z = 30.0\,\mathrm{mm}$ $\qquad$ $\Delta z = 17.5\,\mathrm{mm}$ $\qquad$ $\Delta z = 5.0\,\mathrm{mm}$
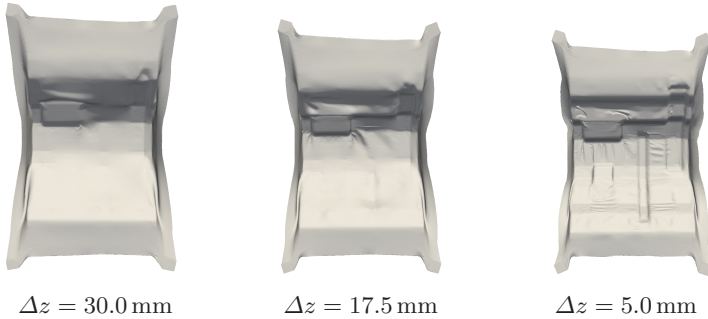
Figure 2.6: Exemplary experimental forming results digitalized by 3D scans for the orthotropic layup and several remaining tool travels Δz.

It becomes evident from these surface measurements that material draw-in and the evolution of wrinkles is straightforward to be investigated with this kind of analysis. Since the laminate cools rapidly and the grippers support the laminate, the results are expected to accurately reflect the deformation stage for the analyzed remaining tool travels. The influence of part distortion during cooling is expected to be small, due to the symmetric layups, the geometric stiffness of the formed part as well as the order of magnitude of deformations investigated in forming studies.

To investigate the influence of the varied factors and layups on formability in terms of wrinkling behavior, the modified mean surface curvature $\bar{\kappa}$ (cf. Section 2.1.2) is determined for each specimen. Since the main focus of this study is the investigation of wrinkling behavior in the order of magnitude predictable by forming simulation, highly local

47

surface defects need to be eliminated from the surface measurement results. This is achieved by remeshing the surface with the commercially available software Geomagic prior to curvature determination with an approximate element edge length of 1.9 mm. Based on this, the surface is smoothened (cf. Figure 2.7).

(a) without remesing
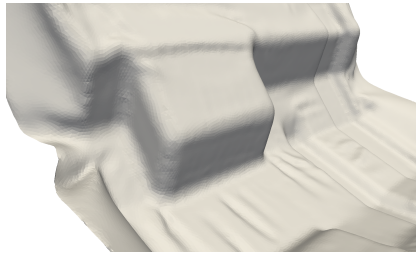
(b) with remeshing

Figure 2.7: Exemplary 3D scan results of a thermoformed part: Without remeshing (a) and with remeshing with an approximate element length of 1.9 mm for surface smoothening (b).

In the following, the experimental thermoforming results are investigated for a remaining tool travel Δz of 5 mm. This setting is chosen, since it is close to a fully closed mold and the full shaping of wrinkling is expected for this forming stage. Initially, the results are compared qualitatively in Section 2.2.2.1. Subsequently, the response surface methodology (RSM) [229] is adopted in Section 2.2.2.2, to quantitatively analyze the influence of the varied factors on formability.

2.2.2.1 Qualitative analysis

The modified mean curvature $\bar{\kappa}$ (cf. Section 2.1.2) is determined for each replicate. Moreover, the weighted arithmetic mean and standard variation of the elemental modified mean curvature $\langle \bar{\kappa}^{\text{el}} \rangle$ over the whole specimen is determined for each design point and the related three replicates. The according results including a representative replicate are shown in the Figures 2.8 - 2.13 for the high, intermediate and low gripping force, respectively.

An overall low standard variation compared to the mean value is observed for each of the design points, which reveals the highly reproducible wrinkle intensity for each design point. Thus, the qualitative comparison between the different design points based on a single representative replicate for each design point is expected to be reasonable.

Orthotropic layup For the orthotropic layup in Figure 2.8, 2.9 and 2.10, wrinkles are observed for all of the considered variants. Wrinkles are mostly induced by the corner bendings, where especially a large fold above the bigger corner bending reveals the most distinct forming defect. This fold is visible for all variants, but is reduced towards a higher tool temperature T^{tool} and higher forming velocity $\bar{v}^{\text{tool}}$. Besides this, an influence of gripper force F^{grip} is observed. The outer contour is most distinctively influenced by the gripping force, since higher gripper forces lengthen the final shape w.r.t. the longitudinal axis of the formed part. Additionally, a higher wrinkling intensity is observed for the high gripper force. Nonetheless, the large fold above the bigger corner bending mostly vanishes for the high tool temperature, high forming velocity and high gripper force.

Quasi-isotropic layup For the quasi-isotropic in Figure 2.11, 2.12 and 2.13, distinctively increased wrinkling behavior compared to the orthotropic layup is observed. Nonetheless, the same dependencies as outlined for the orthotropic layup are maintained, since a higher tool temperature T^{tool}, higher forming velocity $\bar{v}^{\text{tool}}$ and a lower gripping force induces an improved formability, where these influences seem more sensitive for the quasi-isotropic layup compared to the orthotropic layup.

49

$(T^{\mathrm{tool}} \nearrow \mid \bar{v}^{\mathrm{tool}} \searrow)$

$\langle \bar{\kappa}^{\mathrm{el}} \rangle = 0.0291 \pm 0.0006$

$(T^{\mathrm{tool}} \nearrow \mid \bar{v}^{\mathrm{tool}} \nearrow)$

$\langle \bar{\kappa}^{\mathrm{el}} \rangle = 0.0282 \pm 0.0011$

$(T^{\mathrm{tool}} \rightarrow \mid \bar{v}^{\mathrm{tool}} \rightarrow)$

$\langle \bar{\kappa}^{\mathrm{el}} \rangle = 0.0297 \pm 0.0005$

$(T^{\mathrm{tool}} \searrow \mid \bar{v}^{\mathrm{tool}} \searrow)$

$\langle \bar{\kappa}^{\mathrm{el}} \rangle = 0.0303 \pm 0.0003$

$(T^{\mathrm{tool}} \searrow \mid \bar{v}^{\mathrm{tool}} \nearrow)$

$\langle \bar{\kappa}^{\mathrm{el}} \rangle = 0.0314 \pm 0.0006$

$\bar{\kappa}^{\mathrm{el}} \ (\mathrm{mm}^{-1})$

0.000   0.075   0.150

Figure 2.8: Results for the elemental modified mean curvature $\bar{\kappa}^{\mathrm{el}}$ under variation of tool temperature T^{tool} and forming velocity $\bar{v}^{\mathrm{tool}}$ for the high gripping force F^{grip} for the orthotropic layup and a remaining tool travel of 5 mm.

$(\bar{v}^{\text{tool}} \rightarrow | \ T^{\text{tool}} \nearrow)$
$\langle\bar{\kappa}^{\text{el}}\rangle{=}0.0265 \pm 0.0004$

$(\bar{v}^{\text{tool}} \searrow | \ T^{\text{tool}} \rightarrow)$
$\langle\bar{\kappa}^{\text{el}}\rangle{=}0.0293 \pm 0.0010$

$(\bar{v}^{\text{tool}} \rightarrow | \ T^{\text{tool}} \rightarrow)$
$\langle\bar{\kappa}^{\text{el}}\rangle{=}0.0287 \pm 0.0005$

$(\bar{v}^{\text{tool}} \nearrow | \ T^{\text{tool}} \rightarrow)$
$\langle\bar{\kappa}^{\text{el}}\rangle{=}0.0280 \pm 0.0005$

$(\bar{v}^{\text{tool}} \rightarrow | \ T^{\text{tool}} \searrow)$
$\langle\bar{\kappa}^{\text{el}}\rangle{=}0.0296 \pm 0.0003$

$\bar{\kappa}^{\text{el}} \ (\text{mm}^{-1})$

| 0.000 | 0.075 | 0.150 |

Figure 2.9: Results for the elemental modified mean curvature $\bar{\kappa}^{\text{el}}$ under variation of tool temperature T^{tool} and forming velocity $\bar{v}^{\text{tool}}$ for the intermediate gripping force F^{grip} for the orthotropic layup and a remaining tool travel of 5 mm.

51

$(T^{\mathrm{tool}} \nearrow \mid \bar{v}^{\mathrm{tool}} \searrow)$

$\langle \bar{\kappa}^{\mathrm{el}} \rangle = 0.0251 \pm 0.0008$

$(T^{\mathrm{tool}} \nearrow \mid \bar{v}^{\mathrm{tool}} \nearrow)$

$\langle \bar{\kappa}^{\mathrm{el}} \rangle = 0.0240 \pm 0.0007$

$(T^{\mathrm{tool}} \rightarrow \mid \bar{v}^{\mathrm{tool}} \rightarrow)$

$\langle \bar{\kappa}^{\mathrm{el}} \rangle = 0.0243 \pm 0.0002$

$(T^{\mathrm{tool}} \searrow \mid \bar{v}^{\mathrm{tool}} \searrow)$

$\langle \bar{\kappa}^{\mathrm{el}} \rangle = 0.0263 \pm 0.0007$

$(T^{\mathrm{tool}} \searrow \mid \bar{v}^{\mathrm{tool}} \nearrow)$

$\langle \bar{\kappa}^{\mathrm{el}} \rangle = 0.0239 \pm 0.0001$

$\bar{\kappa}^{\mathrm{el}} \; (\mathrm{mm}^{-1})$

0.000   0.075   0.150

Figure 2.10: Results for the elemental modified mean curvature $\bar{\kappa}^{\mathrm{el}}$ under variation of tool temperature T^{tool} and forming velocity $\bar{v}^{\mathrm{tool}}$ for the low gripping force F^{grip} for the orthotropic layup and a remaining tool travel of $5\,\mathrm{mm}$.

$(T^{\text{tool}} \nearrow \mid \bar{v}^{\text{tool}} \searrow)$

$\langle \bar{\kappa}^{\text{el}} \rangle = 0.0416 \pm 0.0010$

$(T^{\text{tool}} \nearrow \mid \bar{v}^{\text{tool}} \nearrow)$

$\langle \bar{\kappa}^{\text{el}} \rangle = 0.0369 \pm 0.0018$

$(T^{\text{tool}} \rightarrow \mid \bar{v}^{\text{tool}} \rightarrow)$

$\langle \bar{\kappa}^{\text{el}} \rangle = 0.0416 \pm 0.0013$

$(T^{\text{tool}} \searrow \mid \bar{v}^{\text{tool}} \searrow)$

$\langle \bar{\kappa}^{\text{el}} \rangle = 0.0459 \pm 0.0020$

$(T^{\text{tool}} \searrow \mid \bar{v}^{\text{tool}} \nearrow)$

$\langle \bar{\kappa}^{\text{el}} \rangle = 0.0400 \pm 0.0006$

$\bar{\kappa}^{\text{el}} \ (\text{mm}^{-1})$

0.000   0.075   0.150

Figure 2.11: Results for the elemental modified mean curvature $\bar{\kappa}^{\text{el}}$ under variation of tool temperature T^{tool} and forming velocity $\bar{v}^{\text{tool}}$ for the high gripping force F^{grip} for the quasi-isotropic layup and a remaining tool travel of 5 mm.

$(\bar{v}^{\mathrm{tool}} \rightarrow | \; T^{\mathrm{tool}} \nearrow)$

$\langle \bar{\kappa}^{\mathrm{el}} \rangle = 0.0357 \pm 0.0015$

$(\bar{v}^{\mathrm{tool}} \searrow | \; T^{\mathrm{tool}} \rightarrow)$

$\langle \bar{\kappa}^{\mathrm{el}} \rangle = 0.0430 \pm 0.0010$

$(\bar{v}^{\mathrm{tool}} \rightarrow | \; T^{\mathrm{tool}} \rightarrow)$

$\langle \bar{\kappa}^{\mathrm{el}} \rangle = 0.0380 \pm 0.0006$

$(\bar{v}^{\mathrm{tool}} \nearrow | \; T^{\mathrm{tool}} \rightarrow)$

$\langle \bar{\kappa}^{\mathrm{el}} \rangle = 0.0378 \pm 0.0009$

$(\bar{v}^{\mathrm{tool}} \rightarrow | \; T^{\mathrm{tool}} \searrow)$

$\langle \bar{\kappa}^{\mathrm{el}} \rangle = 0.0387 \pm 0.0006$

$\bar{\kappa}^{\mathrm{el}} \; (\mathrm{mm}^{-1})$

0.000   0.075   0.150

Figure 2.12: Results for the elemental modified mean curvature $\bar{\kappa}^{\mathrm{el}}$ under variation of tool temperature T^{tool} and forming velocity $\bar{v}^{\mathrm{tool}}$ for the intermediate gripping force F^{grip} for the quasi-isotropic layup and a remaining tool travel of 5 mm.

$(T^{\text{tool}} \nearrow \mid \bar{v}^{\text{tool}} \searrow)$
$\langle \bar{\kappa}^{\text{el}} \rangle = 0.0348 \pm 0.0007$

$(T^{\text{tool}} \nearrow \mid \bar{v}^{\text{tool}} \nearrow)$
$\langle \bar{\kappa}^{\text{el}} \rangle = 0.0330 \pm 0.0009$

$(T^{\text{tool}} \rightarrow \mid \bar{v}^{\text{tool}} \rightarrow)$
$\langle \bar{\kappa}^{\text{el}} \rangle = 0.0338 \pm 0.0007$

$(T^{\text{tool}} \searrow \mid \bar{v}^{\text{tool}} \searrow)$
$\langle \bar{\kappa}^{\text{el}} \rangle = 0.0369 \pm 0.0005$

$(T^{\text{tool}} \searrow \mid \bar{v}^{\text{tool}} \nearrow)$
$\langle \bar{\kappa}^{\text{el}} \rangle = 0.0333 \pm 0.0008$

$\bar{\kappa}^{\text{el}} \; (\text{mm}^{-1})$
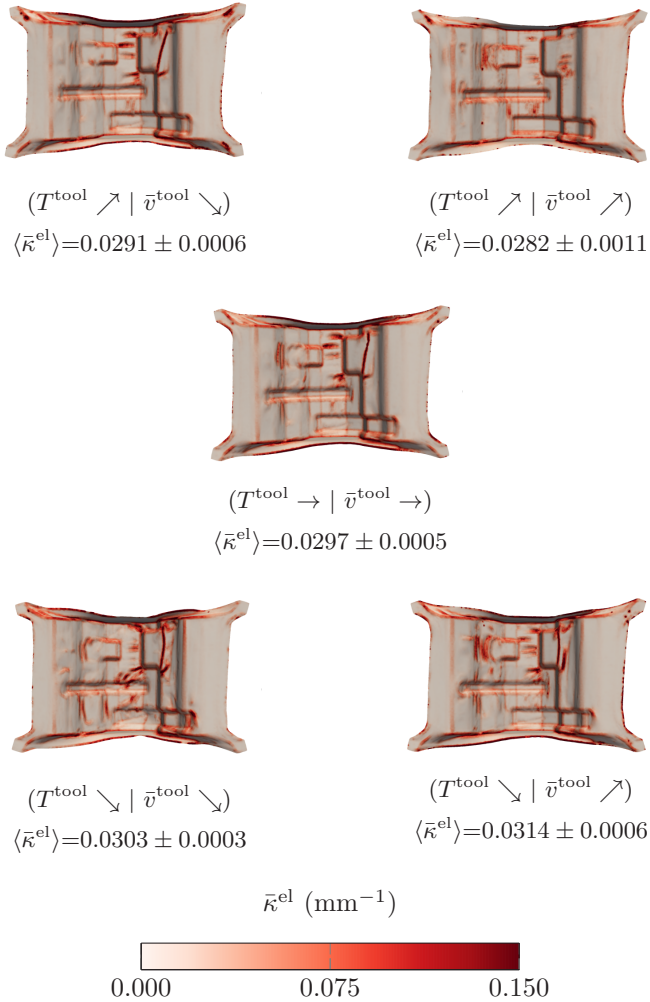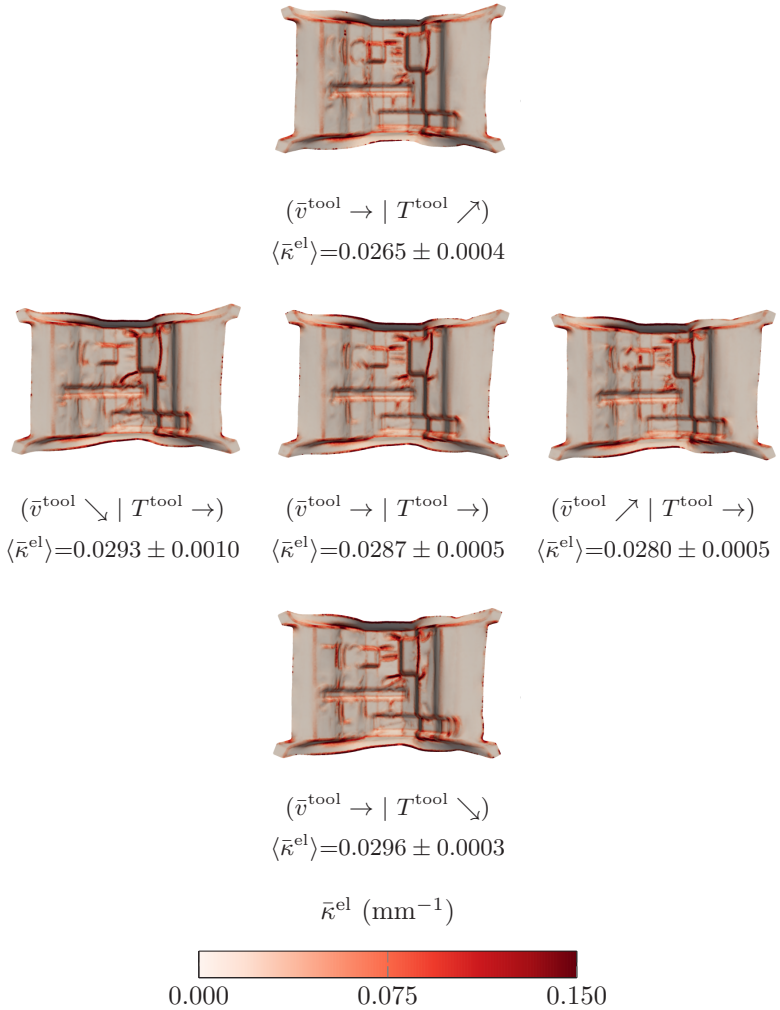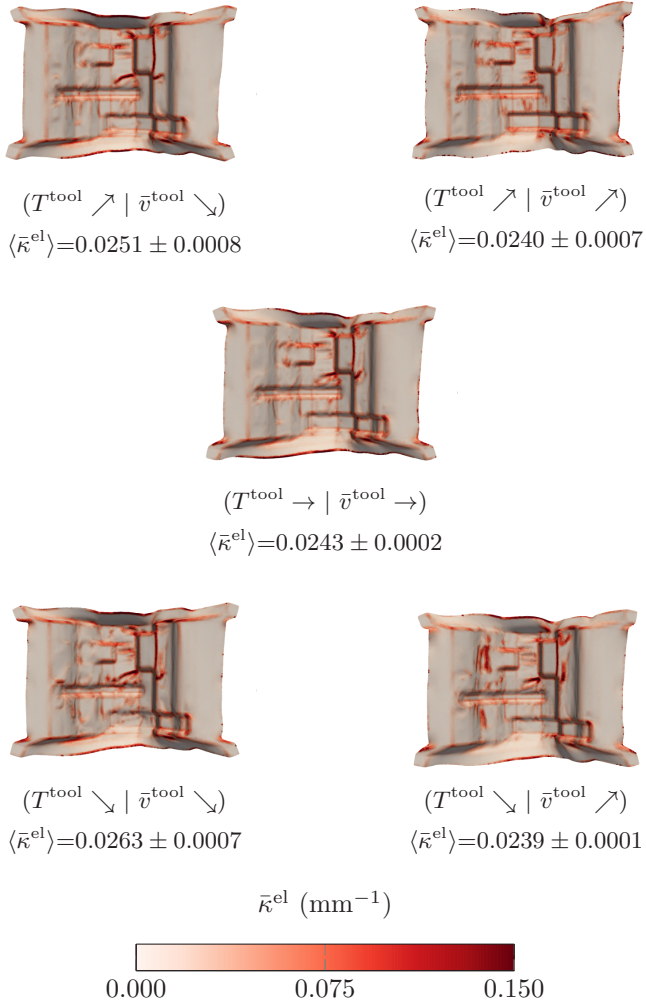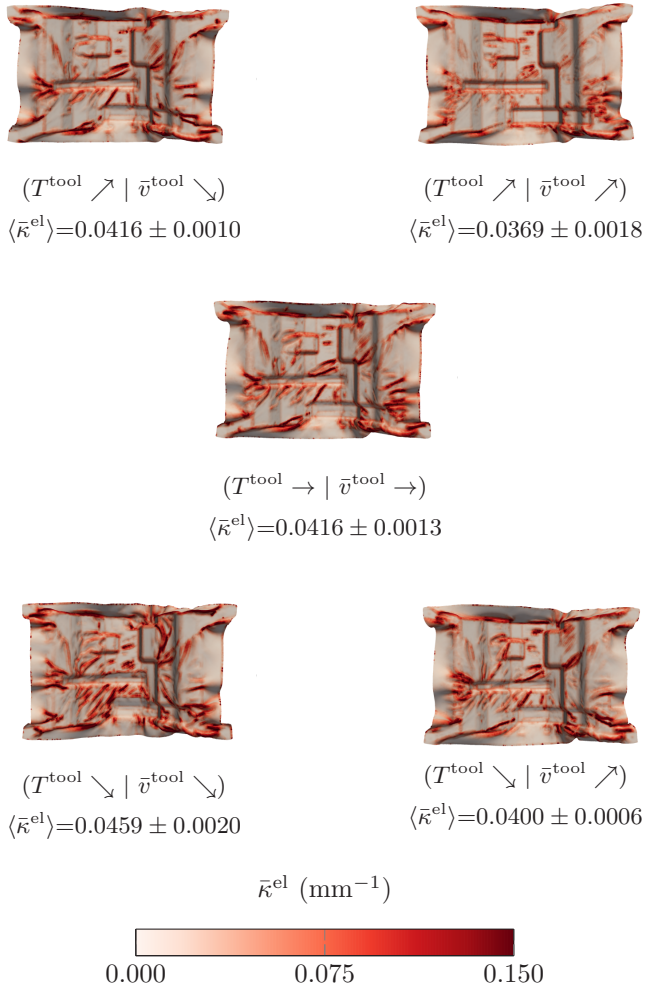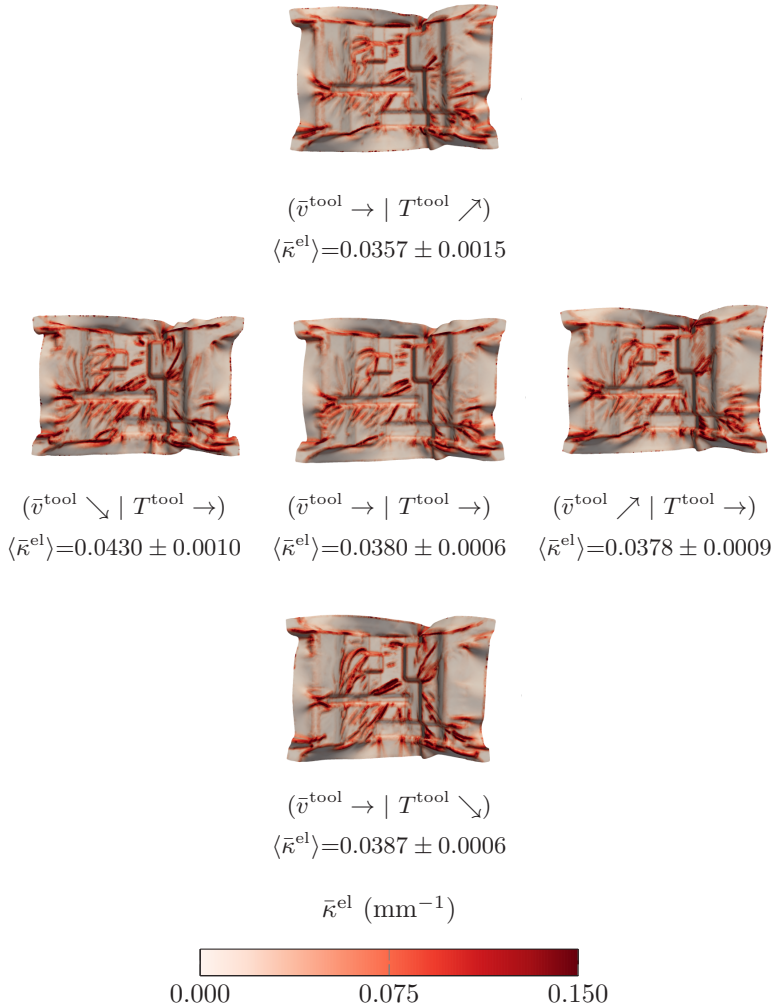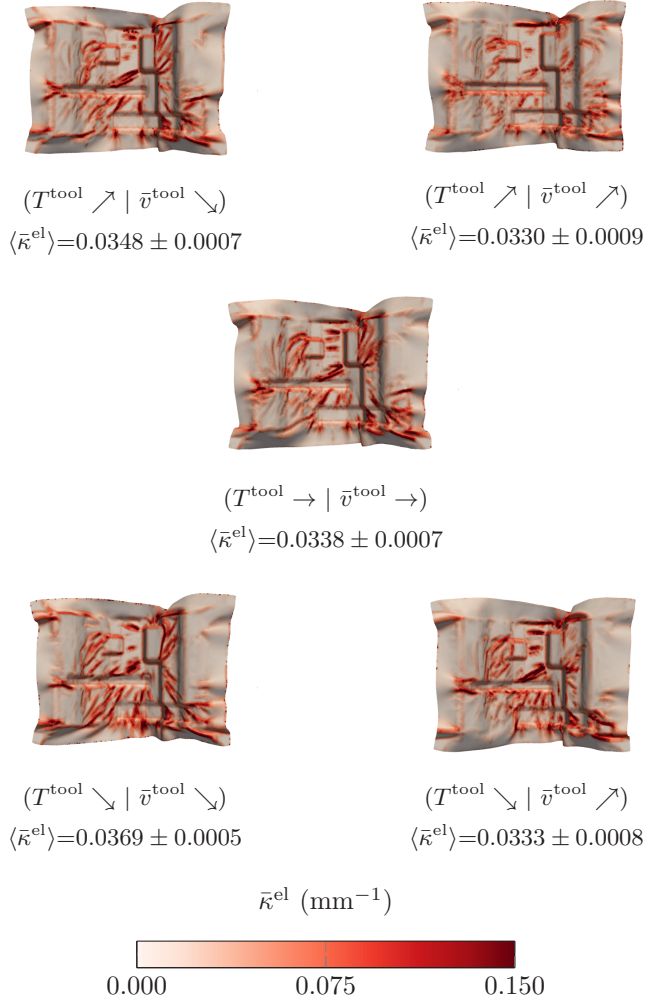
0.000   0.075   0.150

Figure 2.13: Results for the elemental modified mean curvature $\bar{\kappa}^{\text{el}}$ under variation of tool temperature T^{tool} and forming velocity $\bar{v}^{\text{tool}}$ for the low gripping force F^{grip} for the quasi-isotropic layup and a remaining tool travel of 5 mm.

2.2.2.2 Quantitative analysis

For a quantitative assessment of the experimental forming study, the arithmetic mean of the elemental modified mean curvature weighted by the element area $\langle \bar{\kappa}^{\mathrm{el}} \rangle$ (cf. Section 2.1.2) is adopted as scalar measure for wrinkling intensity and applied to response surface methodology (RSM) [229]. Based on this, the varied factors and the target value are correlated by means of a model function. To guarantee an unambiguous relation between the regression coefficients α_i of the model function and the influence of the according normalized design factors x_i^*, a first-order model with interaction terms is chosen:

$$
\begin{aligned}
\langle \bar{\kappa}^{\mathrm{el}} \rangle \approx & \alpha_0 + \alpha_{\mathrm{T}} x_{\mathrm{T}}^* + \alpha_{\mathrm{v}} x_{\mathrm{v}}^* + \alpha_{\mathrm{F}} x_{\mathrm{F}}^* \\
& + \alpha_{\mathrm{Tv}} x_{\mathrm{T}}^* x_{\mathrm{v}}^* + \alpha_{\mathrm{TF}} x_{\mathrm{T}}^* x_{\mathrm{F}}^* + \alpha_{v F} x_{\mathrm{v}}^* x_{\mathrm{F}}^* + \epsilon,
\end{aligned}
\tag{2.4}
$$

where α_0 is a constant offset, α_{T}, α_{v} and α_{F} are the regression coefficients for forming velocity, tool temperature and gripper force, respectively, and α_{Tv}, α_{TF} and $\alpha_{v F}$ are the according interaction coefficients. Additionally, ϵ is a constant error, which is allowed but minimized by the method of least squares [229]. All replicates are considered for regression. The regression yields high coefficients of determination R^2 for both layups (cf. Figure 2.14), which makes the assessment of the obtained response surface models reasonable.

Figure 2.14 shows contour plots of the obtained response surface models for the two layups and constant gripper force, respectively. The more pronounced wrinkling behavior of the quasi-isotropic layup is reflected clearly by a higher curvature level. Besides this, a decrease of wrinkling tendency for higher tool temperatures, forming velocity and lower gripping force is clearly captured. For the orthotropic layup, the overall sensitivity remains mostly constant under a changing gripper force, since mostly no change in the contour interval width is observed. Nonetheless, the influence of forming velocity vanishes towards the high gripper force. In contrast, a distinct increase of the overall sensitivity towards higher gripping forces is observed for the quasi-isotropic layup. Thereby, the balance between the sensitivity of forming velocity and tool temperature, however, remains mostly unchanged.
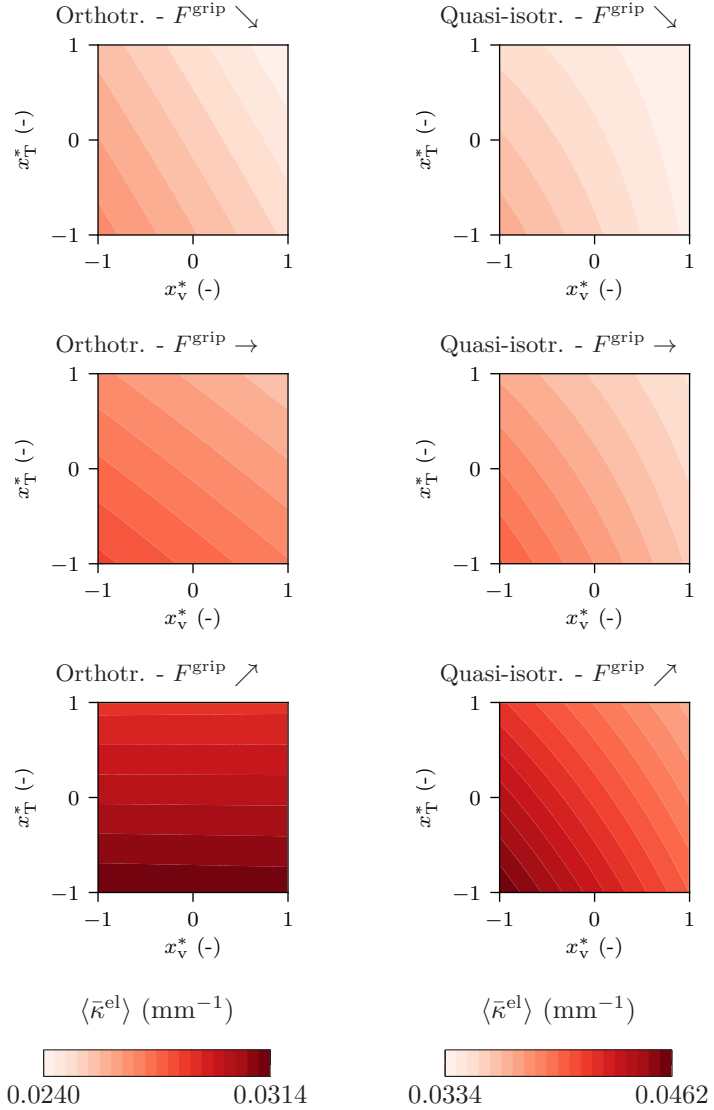
Figure 2.14: Contour plots for the first-order response surfaces for the orthotropic ($R^2 = 0.9197$) (left) and the quasi-isotropic ($R^2 = 0.9193$) (right) layup for constant gripper forces, respectively.

2.2.3 Analysis of local temperature evolution

Thermocouples of type K are incorporated into the formed laminates at different positions prior to pre-consolidation, in order to analyze the local temperature evolution during thermoforming. The initial positions of the investigated thermocouples over the lower female mold and prior to forming are shown in Figure 2.5. Based on this, core temperature is measured throughout the thermoforming process at two different positions. Only the orthotropic layup is considered for temperature measurement, since severe wrinkling is observed for the quasi-isotropic layup. Moreover, temperature measurements are available for all factor levels. However, only the results for the low gripper force are presented for brevity.

The results of the local temperature measurements in Figure 2.15 show a full thermoforming cycle, which consists of the stages heating, transfer, forming and cooling. The stages heating and transfer last approximately equally long for all of the considered design points. In contrast, the duration of the forming stage varies, according to the mean forming velocity $\bar{v}^{\text{tool}}$. During heating, a hesitation in temperature increase is observed for all variants, when the thermoplastic is molten at approximately 220 °C. The heating stage is finished, as soon as almost a homogeneous temperature of 285 °C is reached. This is followed by the transfer of the laminate into the press. The laminate is positioned in the press with a slight local contact between the tool and the laminate in the area of TC-2. This is evident from a more pronounced cooling at the beginning of the forming stage compared to TC-1. This cooling behavior changes during forming, which is clearly visible for the design points with low forming velocity, indicating that the tool-ply contact situation at TC-2 changes during forming. In this stage, cooling rates at TC-1 and TC-2 become comparable.

Regarding the temperature at the end of the forming stage, a clear influence of the varied factors is observed. This becomes evident especially in comparison of the design point with high tool temperature and high forming velocity, inducing the lowest cooling, to the design point with low tool temperature and forming velocity, which induces the highest cooling. The temperatures at the end of the forming stage are well above the recrystallization temperature T^{recryst} (measured at a cooling rate of 10 °C/min) for almost all of the considered process

$(T^{\text{tool}} \searrow \mid \bar{v}^{\text{tool}} \nearrow \mid F^{\text{grip}} \searrow)$ $(T^{\text{tool}} \nearrow \mid \bar{v}^{\text{tool}} \nearrow \mid F^{\text{grip}} \searrow)$

$(T^{\text{tool}} \rightarrow \mid \bar{v}^{\text{tool}} \rightarrow \mid F^{\text{grip}} \searrow)$

$(T^{\text{tool}} \searrow \mid \bar{v}^{\text{tool}} \searrow \mid F^{\text{grip}} \searrow)$ $(T^{\text{tool}} \nearrow \mid \bar{v}^{\text{tool}} \searrow \mid F^{\text{grip}} \searrow)$
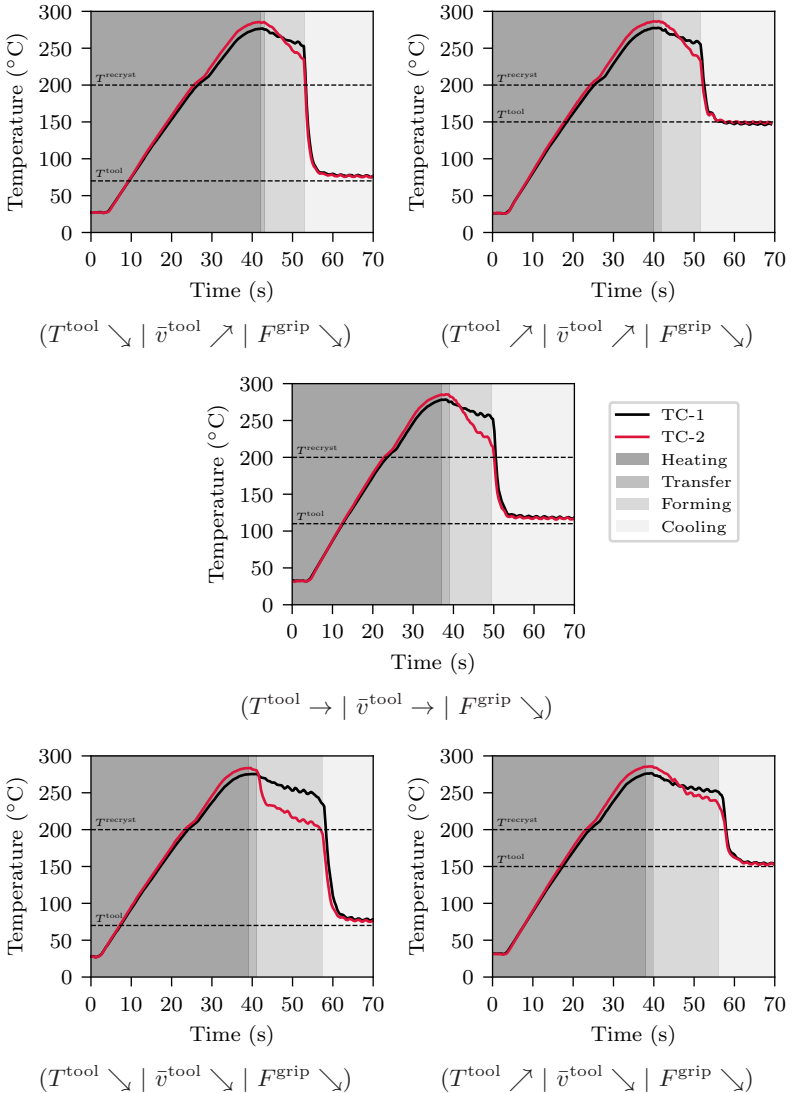
Figure 2.15: Local temperature measurement results for the orthotropic layup under variation of tool temperature T^{tool} and mean forming velocity $\bar{v}^{\text{tool}}$ for the low gripper force F^{grip}; recrystallization temperature T^{cryst} characterized at a constant cooling rate of $10\,^{\circ}\text{C/min}$.

variants, except for the design point with the low tool temperature and low forming velocity. Indeed, higher cooling rates are expected during forming, which lowers recrystallization temperature. Nonetheless, recrystallization already during forming cannot be excluded in general and especially not for the outer plies, since convection at free surfaces and especially conduction at tool-laminate-interfaces is expected to render a high temperature gradient over the thickness of the laminate and thus distinctively lower temperatures are expected in the outer plies. In the further course of the process cycle, as soon as the tools are fully closed, a significant increase in cooling rate is observed, until the laminate temperature conforms to the tool temperature.

2.3 Material characterization

Material characterization results of the material investigated in the scope of this study (cf. Section 1.5) at process conditions are presented and investigated in the following, in order to derive the requirements on material modeling for thermoforming simulation. Material characterizations include DSC measurements, for characterization of crystallization kinetics of the semi-crystalline thermoplastic (Section 2.3.1), as well as mechanical characterization of the major deformation mechanisms (cf. Figure 1.7). These namely are in-plane shear (Section 2.3.2), bending (Section 2.3.3) and inter-ply slip (Section 2.3.4). It is to be noted that the results presented in the following originate from collaborations with colleagues and partners, which is indicated individually in each subsection.

2.3.1 Crystallization kinetics

Thermoforming often comprise semi-crystalline thermoplastics due to their improved mechanical performance against amorphous thermoplastics. This is also valid for the material investigated in the scope of this study (cf. Section 1.5). During cooling of a semi-crystalline thermoplastic from a temperature well above the melting temperature, the thermoplastic undergoes a partial alignment of the molecular chains during solidification, which is called crystallization. Thus, crystallization defines the transition from the molten to the solid ma-

terial state, which is usually characterized by means of differential scanning calorimetry (DSC) [231].

The DSC measurement results presented in the following were commissioned by Dipl.-Ing. Daniel Kugele and the according evaluations originate from a joint study on crystallization kinetics modeling [232].

Characterization setup and testing procedure   Crystallization kinetics is characterized by differential scanning calorimetry (DSC) by means of measuring the exothermic heat flow during recrystallization. For this purpose, on the one hand, standard differential calorimetry (S-DSC) measurements were conducted with a Perkin-Elmer DSC 8000 for moderate cooling rates ($0.167\,°C/s$ to $1\,°C/s$). The according specimens have an approximate weight of $10\,mg$ and are heated with a rate of $0.167\,°C/s$, starting at $30\,°C$ and held at $240\,°C$ for $2\,min$ prior to cooling. On the other hand, fast differential scanning calorimetry (F-DSC) measurements with a Mettler-Toledo Flash DSC 1 device were performed at the Institute of Physics at the University of Rostock for high cooling rates ($15\,°C/s$ to $100\,°C/s$). The according specimens are heated with a rate of $100\,°C/s$ and held at a temperature of $280\,°C$ for $3\,s$ prior to cooling. Due to the small size of the specimens, unfortunately, the mass of the specimens cannot be determined.

Characterization results   The result of the S- and F-DSC measurements investigated in the scope of this study is the absolute heat flow as a function of temperature or time during cooling of the specimen with a constant cooling rate. The investigation of the absolute heat flow is necessary, since the exact mass of the F-DSC specimens is unknown. This prevents the determination of a specific heat flow, which is usually adopted for crystallization kinetics investigations. Therefore, the relative crystallinity $\alpha(t)$ at the time t is derived by means of the absolute heat flow $Q^{\mathrm{cryst}}(t)$ by

$$\alpha(t) = \frac{1}{\Delta H^{\mathrm{cryst}}} H^{\mathrm{cryst}}(t) \quad \text{with} \quad H^{\mathrm{cryst}}(t) = \int_{t_0}^{t} Q^{\mathrm{cryst}}(\hat{t}) \mathrm{d}\hat{t}, \quad (2.5)$$

where t_0 is the time of the onset of crystallization and $\Delta H^{\mathrm{cryst}}$ the absolute crystallization enthalpy, which is defined by the area enclosed by the absolute heat flow and a baseline defined by the straight connection between the onset and end of recrystallization, as exemplarily shown in Figure 2.16.
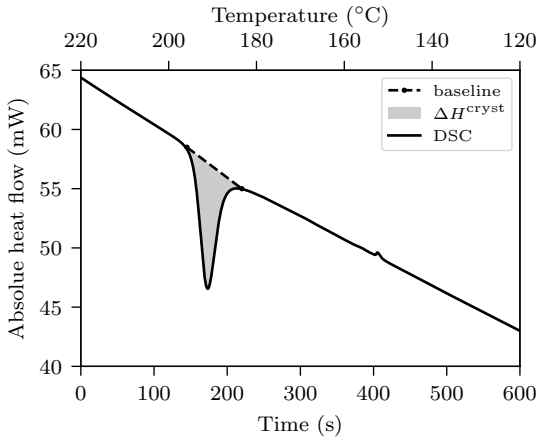
Figure 2.16: Extraction of the crystallization peak from DSC data based on the definition of a baseline, exemplified for a S-DSC measurement at 10 K/min cooling rate.

It is to be noted that only the relative crystallinity α is investigated in the scope of this study, since the specimen mass is unknown for the F-DSC measurements. Hence, the measured absolute crystallization enthalpy cannot be related to the specific crystallization enthalpy, which in turn would be necessary to determine the absolute crystallinity. This, however, is sufficient for this study, since the main objective is to identify the transition from the molten to the solid material state rather than the analysis of the absolute degree of crystallinity. The latter would become more interesting e.g. in the context of structural analyses and fracture mechanics, if the degree of crystallinity defines the type of fracture.

The results for the relative crystallinity α are shown in Figure 2.17 for all of the considered cooling rates. Based on the relation between relative crystallinity and temperature, characteristic temperatures for

the onset, peak and end of recrystallization are determined, which are shown in Figure 2.18.
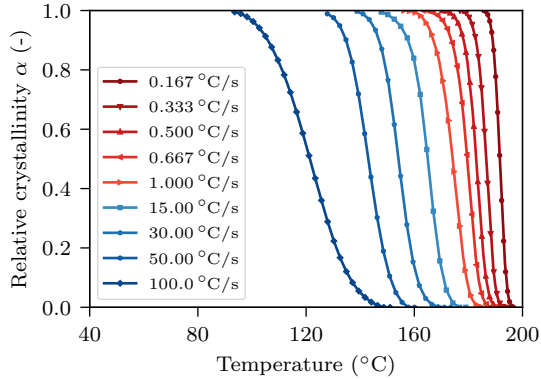
Figure 2.17: Relative crystallinity α determined from Standard-DSC (red) and Flash-DSC (blue) measurements for several cooling rates.
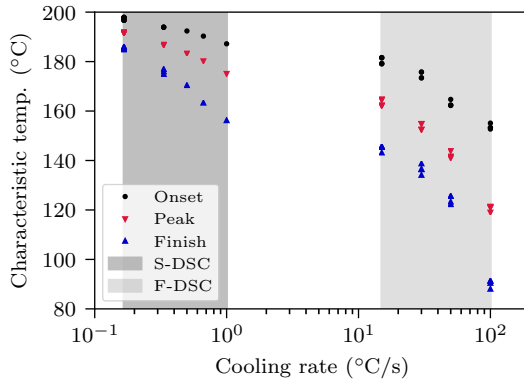
Figure 2.18: Characteristic temperatures for recrystallization behavior determined from Standard and Flash-DSC measurements for several cooling rates.

The onset of recrystallization is observed for the lowest cooling rate approximately at 200 °C. For increasing cooling rates, the typical shift of recrystallization towards lower temperatures [231] is observed. This

shift yields in comparison of the lowest to the highest cooling rate up to 50 °C regarding the onset of recrystallization. Beyond that, the temperature range, over which the recrystallization proceeds, broadens for higher cooling rates.

In comparison of S- and F-DSC results, there is no intersection w.r.t. cooling rate, which is prevented by the maximum and minimum achievable cooling rate of the S- and F-DSC devices, respectively. Nonetheless, a monotonous decrease of the characteristic temperatures w.r.t. increasing cooling rates is observed (cf. Figure 2.18). In summary, a distinct influence of cooling rate on crystallization is observed.

2.3.2 Shear behavior

The torsion bar test presented by Haanappel et al. [60] is applied for shear characterization. This custom setup deals with a prismatic bar, which is subjected to torsion in a standard rheometer. Usually, the test is conducted with a unidirectional laminate, where the fibers are aligned in direction of the torsional axis. Thus, longitudinal shear deformation is introduced into the specimen, while the resulting torsional moment is captured as characterization result. A detailed description of this testing setup is provided in Section 1.2.2.1.

In the following, isothermal shear characterization tests are presented in Section 2.3.2.1. The according tests were conducted at TPRC ("ThermoPlastic Composite Reasearch Center") in Enschede, the Netherlands under the commissioning of Wojciech Brymerski (Audi AG) within the public funded project SMiLE. The according tests are conducted for characterization in the molten material state, with a focus on temperature- and rate-dependency.

Below the temperatures considered in isothermal shear characterization, isothermal recrystallization cannot be excluded. Thus, stationary material properties w.r.t. time cannot be guaranteed, even at constant temperatures. Therefore, non-isothermal shear characterization under a stationary, oscillating load and different cooling rates is presented in Section 2.3.2.2, to investigate material properties over a wide range of temperatures and beyond recrystallization, in dependence on cooling rate. The according tests were conducted by the author at the Fraunhofer ICT in Pfinztal, Germany.

2.3.2.1 Isothermal large strain shear characterization

Characterization setup and testing procedure   The characterization tests are conducted on an Anton Paar MCR 501 rheometer equipped with a CTD 450 thermal chamber, which is nitrogen-purged to avoid thermo-oxidative degradation of the polymer. Unidirectional specimens with the dimensions $60\,\text{mm} \times 13\,\text{mm} \times 10.7\,\text{mm}$ are tested. The specimens are dried at $80\,°\text{C}$ for at least $24\,\text{h}$ prior to testing, to avoid any influence of moisture in the specimens on the characterization results. A transient load under a single deflection with a controlled deformation rate outside the small strain regime is applied. This is in contrast to the work presented by Haanappel et al. [60], in which an oscillating load within the small strain regime is applied. Three different deflection rates n ($10.0\,\text{rpm}$, $1.0\,\text{rpm}$ and $0.1\,\text{rpm}$) of the rheometer shaft are investigated, where the rheometer shaft is rotated once to a deflection angle of $30\,\text{deg}$. Moreover, three different temperatures T ($270\,°\text{C}$, $250\,°\text{C}$ and $226\,°\text{C}$) above the recrystallization temperature of the thermoplastic are considered. For the lowest temperature, the specimens are initially overheated and subsequently cooled to $226\,°\text{C}$, to guarantee the thermoplastic to be fully molten.

Characterization results   The isothermal shear characterization results are shown in Figure 2.19. The initial overshoot of the measured torsion moment for the highest deformation rate and all temperatures at low deflection angles is attributable to inertia effects and the control system of the rheometer. In comparison of the moment-deflection-curves at constant temperature, a distinct rate-dependency is observed for each of the investigated temperatures, since distinctively higher torsional moments are obtained for higher deformation rates. Furthermore, an increase of shear rigidity is observed for decreasing temperatures, as exemplified for the intermediate deformation rate ($n = 1.0\,\text{rpm}$) in Figure 2.19(d). For the lowest temperature, however, an increase in standard deviation is observed, which might be attributable to the overheating and subsequent cooling steps, possibly yielding slightly varying temperature distributions in the specimen. Moreover, the onset of isothermal recrystallization is a possible cause. Both, however, are only possible causes and cannot be quantified based on the available data. The obtained moment-deflection
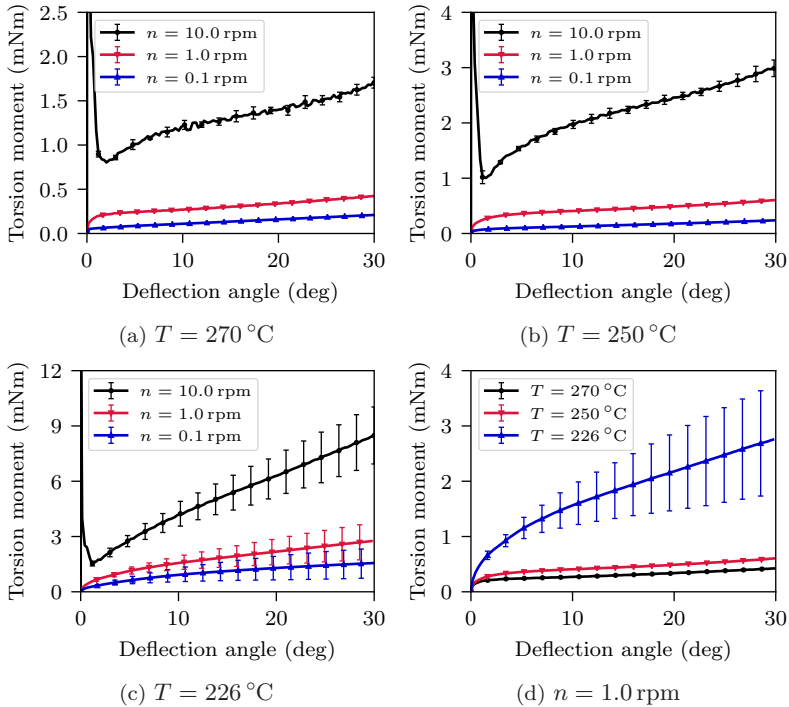
Figure 2.19: Isothermal shear characterization based on the torsion bar test at several temperatures T and deflection rates n.

curves show nonetheless the same characteristic as observed for the remaining temperatures, for which a low standard deviation is observed. In summary, a distinct temperature- and rate-dependency is observed for shear behavior for the investigated molten material state.

2.3.2.2 Non-isothermal small strain shear characterization

Characterization setup and testing procedure   The non-isothermal torsion bar tests are in analogy to the isothermal tests presented in Section 2.3.2.1 conducted on an Anton Paar MCR 501 rheometer equipped with a thermal chamber CTD 450, which is nitrogen-purged to avoid thermo-oxidative degradation of the polymer. An oscillating

load is applied in a temperature-transient testing procedure at several cooling rates, in order to analyze shear behavior during cooling and across the phase transition due to recrystallization. The investigated specimens have an orthotropic lauyp ($[0; 90]_{2s}$), in analogy to the layup investigated in Section 2.2 in the experimental process analysis, and measure $60.0\,\text{mm} \times 13.0\,\text{mm} \times 1.35\,\text{mm}$. The according test setup is shown in Figure 2.20.
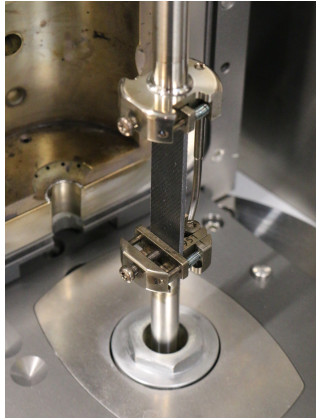
Figure 2.20: Characterization setup for the non-isothermal torsion bar tests with the orthotropic layup ($[0; 90]_{2s}$).

Prior to testing, the specimens are dried at $80\,°\text{C}$ for at least $24\,\text{h}$, to avoid any influence of moisture in the specimens. For testing, the thermal chamber is initially heated to $280\,°\text{C}$ and after holding temperature for $10\,\text{min}$, to guarantee a homogeneous temperature distribution in the specimen, the thermal chamber is cooled with a constant cooling rate, where different cooling rates ($5\,°\text{C/min}$, $10\,°\text{C/min}$ and $15\,°\text{C/min}$) are investigated. Even higher cooling rates are not achievable with the available equipment. Anyhow, higher cooling rates are accompanied with the higher tendency to temperature gradients within the specimens. Therefore, the achievable cooling rates are expected to be in a reasonable range for this testing setup, since a homogeneous temperature distribution is expected for the thin specimens and the comparably low cooling rates. While cooling, a stationary

oscillating mechanical load with a frequency of 1.0 Hz and an amplitude of 0.5° is applied. This results according to Haanappel et al. [60] in a maximum strain amplitude of 0.025 % for the applied specimen dimensions.

Characterization results   The characterization results of the non-isothermal torsion bar test are shown in Figure 2.21(a). During cooling, a negligible increase in shear response is observed until approximately 200 °C. Below this temperature, a distinct increase of approximately two orders of magnitude is observed. Moreover, a shift of this increase towards lower temperatures is observed for higher cooling rates.

(a)   (b)
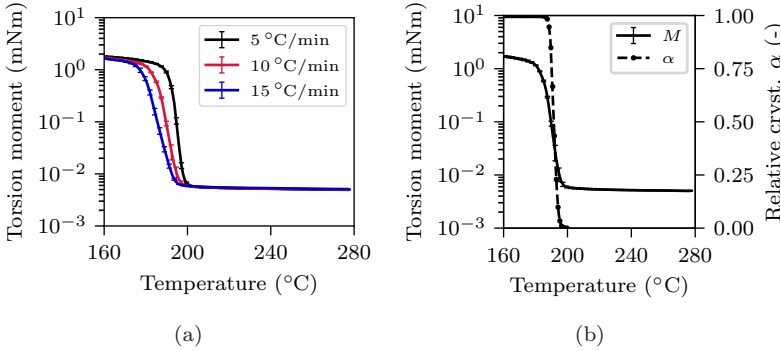
Figure 2.21: Non-isothermal shear characterization results: torsion moment at several cooling rates (a) and comparison of torsion moment M to the relative crystallinity α from a S-DSC measurement at 10 °C/min cooling rate (b).

In comparison of the shear response to results of the relative crystallinity determined from DSC measurements for the intermediate cooling rate of 10 °C/min in Figure 2.21(b), a high agreement between the shear response and recrystallization is observed. This reveals that phase transition and also the shift of phase transition distinctively affects mechanical behavior, which makes the mechanical behavior not only temperature-, but also cooling-rate-dependent.

2.3.3 Bending behavior

Characterization setup and testing procedure The custom bending characterization setup proposed by Sachs et al. [52] is applied at Fraunhofer ICT in Pfinztal, Germany for bending characterization. The according characterization setup is shown in Figure 2.22.
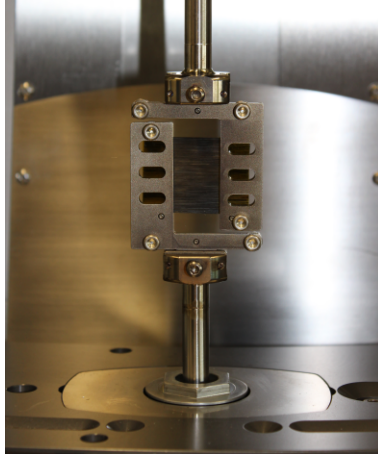
Figure 2.22: Characterization setup for the isothermal bending tests in longitudinal direction with a single ply of UD tape within a standard rheometer.

Bending behavior of a single UD tape ply in longitudinal direction is characterized. Unfortunately, characterization of bending behavior in transversal direction is not possible for unidirectional reinforcements using this characterization setup, since the specimens are too compliant in the molten material state to be loaded under bending in transversal direction. The bending setup is mounted on an Anton Paar MCR 501 rheometer equipped with a thermal chamber CTD 450, which is nitrogen-purged to avoid thermo-oxidative degradation of the polymer.

The tested specimens measure $35\,\text{mm} \times 25\,\text{mm}$. The ends of the specimen are covered with heat resistant polyimide tape, to avoid sticking of the molten thermoplastic within the clamps. The clamps have a constant distance between each other, such that the specimen can

freely move within the fixture. The resulting bending length of the specimen amounts 15 mm and bending deformation is induced by the rotating upper shaft while the lower shaft is fixed. The bending moment over deflection angle is captured as characterization result. Prior to testing, the specimens are dried for at least 8 h to avoid any influence of moisture within the specimens on the characterization results. Three different temperatures T (270 °C, 250 °C and 226 °C) above the recrystallization temperature of the thermoplastic are considered for isothermal testing. For the lowest temperature, the specimens are initially overheated and subsequently cooled to 226 °C, to guarantee the polymer to be fully molten. For each temperature, three different rotation speeds n (10.0 rpm, 1.0 rpm and 0.1 rpm) of the rheometer shaft are adopted in a transient testing procedure, for which the rheometer shaft is rotated once to a deflection angle of 30 deg.

Characterization results The characterization results of the isothermal bending test are shown in Figure 2.23. The initial overshoot of the measured bending moment for the highest deformation rate at low deflection angles for all of the considered temperatures is attributable to inertia effects and to the control system of the rheometer. This effect is slightly more pronounced compared to shear characterization in Section 2.3.2.1, since the measured moments are very low due to the low nominal thickness of 0.16 mm of the single UD tape ply. The moment-deflection curves reveal a distinct rate-dependency for each of the investigated temperatures, since distinctively higher bending moments are observed for higher deformation rates. Besides this, higher bending moments are observed for lower temperatures, as exemplified in Figure 2.23(d) for the intermediate rotation speed of 1.0 rpm. In summary, a distinct rate- and temperature dependency is observed for the isothermal bending characterization in the molten material state.

(a) $T = 270\,°C$

(b) $T = 250\,°C$

(c) $T = 226\,°C$

(d) $n = 1.0\,\text{rpm}$
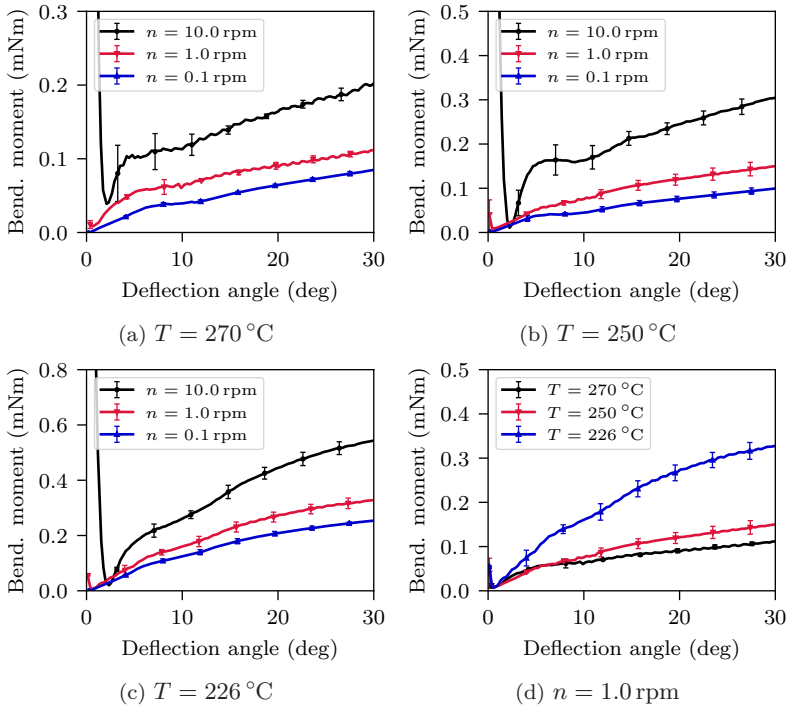
Figure 2.23: Isothermal longitudinal bending characterization based on the custom rheometer test at several temperatures T and deflection rates n.

2.3.4 Frictional behavior

Several characterization setups for frictional behavior are presented in literature (cf. Section 1.2.2.3), while no standard procedure exists. A custom friction characterization setup tailored for thermoplastic tapes is implemented at Fraunhofer ICT in Pfinztal, Germany and frictional behavior is characterized for the investigated material within several student's theses [233, 234, 235]. The characterization results include ply-ply characterization under variation of transversal pressure, slip rate and temperature [233, 235], as well as under variation of the relative orientation between the slipping plies [234]. Moreover, tool-ply

friction characterization is conducted under variation of transversal pressure, slip rate and temperature [233]. In the following, initially the characterization setup and testing procedure are presented (Section 2.3.4.1). Subsequently, characterization results are evaluated exemplarily, in order to investigate the influence of the above outlined parameters on frictional behavior for the ply-ply interface (Section 2.3.4.2) and the tool-ply interface (Section 2.3.4.3).

2.3.4.1 Characterization setup and evaluation procedure

The custom friction characterization setup shown in Figure 2.24 is mounted on a standard tensile testing machine and is designed to conduct pull-through and pull-out tests for the characterization of tool-ply and ply-ply friction.
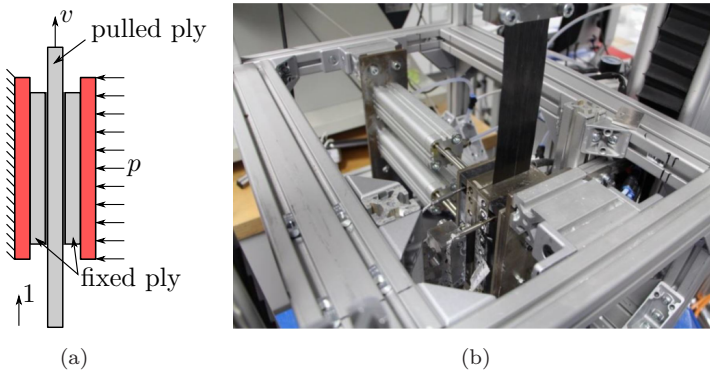
Figure 2.24: Schematic illustration of the friction test setup for a pull-through testing procedure [236] (a) and custom friction test setup mounted on a standard tensile testing machine [234] (b).

The custom setup enables to characterize frictional behavior under prescribed temperature T, slip rate v^{slip}, transversal pressure $p^{\perp}$ and relative orientation φ^{rel} between the slipping plies. Transversal pressure is applied by a pneumatic cylinder onto which a heating plate is mounted, whilst the opposite and parallel heating plate is fixed. The heating plates are temperature-controlled and heated by three heating units. By pulling the tested specimen through or out of the two heating plates by a standard tensile testing machine, frictional behavior is

characterized following pull-through or pull-out testing, respectively. For pull-through testing, two additional heating plates are used for pre-heating of the free specimen area.

For evaluation of frictional behavior, the coefficient of friction (CoF) μ is determined from the measured force F by

$$\mu = \frac{\tau}{p^\perp} \quad \text{with} \quad \tau = \frac{F}{2A^\text{fric}} \quad \text{and} \quad p^\perp = \frac{F^\perp}{A^\text{fric}}. \tag{2.6}$$

Here, τ is the friction stress, A^fric the friction area and $F^\perp$ the transversal force applied by the pneumatic cylinders. For pull-through tests, the friction area remains constant. Thus, also transversal pressure remains constant. In contrast, the transversal pressure increases for increasing slip distances u^slip for pull-out tests, since the friction area decreases. Based on the constant transversal force $F^\perp$, the current transversal pressure $p_1^\perp$ is determined by

$$p_1^\perp(u^\text{slip}) = \frac{F^\perp}{A_0^\text{fric}} \left(\frac{l_0^\text{fric}}{l_0^\text{fric} - u^\text{slip}} \right), \tag{2.7}$$

Here, A_0^fric is the initial friction area and l_0^fric the initial length of the friction surface in slip direction. Additionally to the CoF, the relation between the so-called Hersey number He and the CoF μ, which is denoted as Stribeck curve [237], can be used to distinguish between different regimes of lubricated friction. The Hersey number is given by [237]

$$He = \frac{\eta v^\text{slip}}{p^\perp}, \tag{2.8}$$

where η is the viscosity. Based on a decrease of the CoF for an increasing Hersey number, mixed lubrication is identified. On the contrary, hydrodynamic lubrication is identified for an increasing CoF and increasing Hersey number [237]. This concept originates from the investigation of the lubrication in bearings and is adopted for the investigation of frictional behavior of CoFRP pre-products by several authors [50, 52, 186].

2.3.4.2 Ply-ply friction

Characterization procedure   Pull-through tests are conducted within student's theses [234, 235] under variation of the transversal pressure $p^\perp$, slip velocity v^{slip} and relative orientation φ^{rel} at a constant but different temperature T. The friction areas measure $150\,\mathrm{mm} \times 50\,\mathrm{mm}$ for the tests with $0\,\mathrm{deg}$ relative orientation and $50\,\mathrm{mm} \times 50\,\mathrm{mm}$ for the tests with $90\,\mathrm{deg}$ relative orientation. The two fixed and the pulled tape plies are ultra-sonic spot-welded in a preparation step, to enable an accurate initial positioning in the custom friction characterization setup. The specimens are dried at least for $8\,\mathrm{h}$ at $80\,^\circ\mathrm{C}$, to exclude any influence of moisture within the tested specimens.

On the one hand, characterization results under variation of transversal pressure, slip velocity and relative orientation at $240\,^\circ\mathrm{C}$ according to a full factorial test plan are outlined [234], in order to investigate the influence of the varied factors in the molten material state. The according levels are listed in Table 2.2. On the other hand, characterization results for the intermediate transversal pressure, intermediate slip velocity, $90\,\mathrm{deg}$ relative orientation and under variation of temperature in steps of $10\,^\circ\mathrm{C}$ from $280\,^\circ\mathrm{C}$ to $200\,^\circ\mathrm{C}$ are outlined [235], in order to investigate the influence of temperature in the molten material state, as well as at the transition from the molten to the solid material state. For the related tests below or equal $210\,^\circ\mathrm{C}$, the specimens are initially heated to $240\,^\circ\mathrm{C}$ and subsequently cooled to the testing temperature, to ensure the thermoplastic to be fully molten.

Factors	Unit	Levels
Temperature T	(°C)	{240}
Relative orientation φ^{rel}	(deg)	{0 ; 90}
Slip velocity v^{slip}	(mm/s)	{0.83 ; 2.5 ; 8.33}
Transversal pressure $p^\perp$	(MPa)	{0.01 ; 0.02 ; 0.04}

Table 2.2: Factors and according levels of the isothermal ply-ply friction characterization following a full-factorial test plan.

Characterization results   An excerpt of the characterization results at $240\,^\circ\mathrm{C}$ is shown for both relative orientations in Figure 2.25. The

according results vary around the center point of the full-factorial test plan.
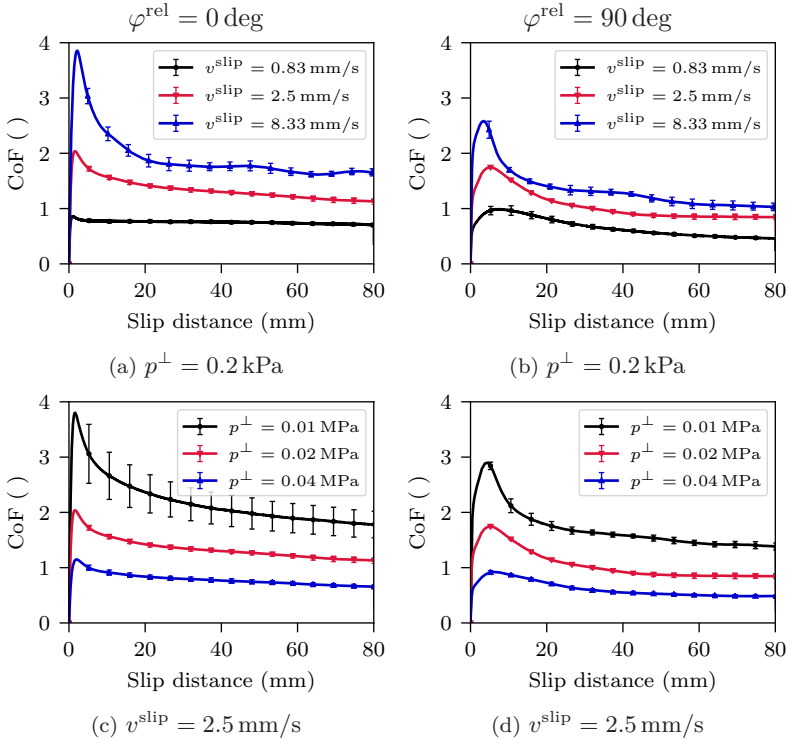
Figure 2.25: Pull-through results for the ply-ply interface at 240 °C under variation of relative orientation φ^{rel}, slip velocity v^{slip} and transversal pressure $p^{\perp}$.

The typical evolution of the CoF over the slip distance as also observed by Sachs et al. [93] is obtained for all levels. This includes a peak at the onset of slipping, which is usually referred to as static friction. This peak is sharper for the tests with 0 deg relative orientation, which might be attributable to the high stiffness in fiber direction of the fixed plies under 0 deg relative orientation compared to the limited rigidity of the fixed transverse and pre-tensioned tapes under 90 deg relative orientation. The initial peak is followed by a stationary regime, which

is usually referred to as dynamic friction. A slight decrease of the CoF is observed for some specimens in the stationary regime. In general, high CoF close to and markedly higher than 1.0 are observed. Thus, classical Coulomb friction, which defines the friction stress by a fraction of transversal pressure ($\tau = \mu p^\perp$), is exceeded.

A distinct influence of transversal pressure and slip velocity on frictional behavior is observed for both relative orientations. An increasing slip velocity and a decreasing transversal pressure leads to an increase of the CoF. By relating this qualitative observation to the evolution of a Hersey number (cf. Equation 2.8) in terms of a Stribeck curve, the ply-ply friction characteristic can be assigned to hydrodynamic lubrication. Therefore, the molten thermoplastic is expected to be the main driver for frictional behavior rather than the dry interaction between the fibers. Moreover, an increasing relative orientation between the slipping plies leads to lower CoF, whilst the aforementioned characteristic of hydrodynamic friction is maintained.

The results for the intermediate slip rate, intermediate transversal pressure and a relative orientation of 90 deg under variation of temperature are shown in Figure 2.26.

(a)   (b)
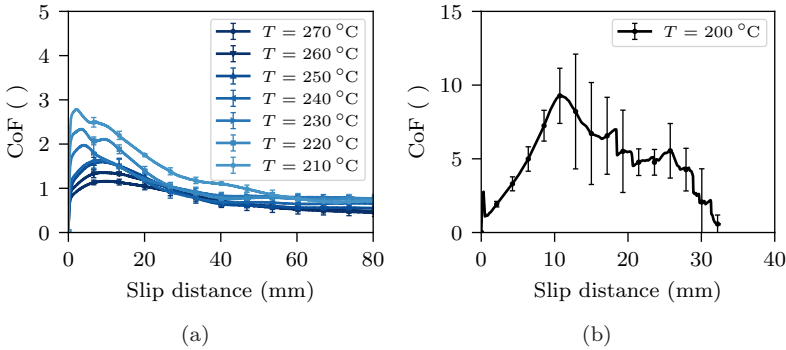
Figure 2.26: Pull-through results for the ply-ply interface under variation of temperature T with a relative orientation of 90 deg, a slip velocity of 2.5 mm/s and transversal pressure of 0.02 MPa.

From 270 °C to 230 °C, it is observed that the initial peak increases and sharpens for lower temperatures, whilst the stationary regime is mostly unaffected (cf. Figure 2.26(a)). It is to be noted that for

temperatures below the melting temperature of the thermoplastic at 226 °C, isothermal recrystallization cannot be excluded. Thus, stationary material properties are not guaranteed. This might explain the changed evolution of the CoF at 220 °C and 210 °C, where a double peak is observed. The stationary regimes, however, are less affected. Below 210 °C, no friction but tacking is observed for 200 °C, which leads to enormous CoF (cf. Figure 2.26(b)) and a damaged specimen. Thus, the application of the isothermal friction characterization setup is not reasonable for temperatures below 230 °C for this material system.

In summary, a distinct dependency of ply-ply friction on slip velocity v^{slip}, transversal pressure $p^{\perp}$ and relative orientation φ^{rel} is observed. Besides this, a comparably smaller influence of temperature T on frictional behavior in the stationary regime is observed. This, however, changes rapidly when recrystallization cannot be excluded.

2.3.4.3 Tool-ply friction

Characterization procedure Pull-out tests are conducted within a student's thesis [233] for the characterization of tool-ply friction under variation of the transversal pressure $p^{\perp}$, slip velocity v^{slip} and temperature T following a full-factorial test plan. Only the center point is replicated 5 times. Therefore, a standard deviation is available only for the center point. The characterization results are part of another study than the ply-ply characterization in Section 2.3.4.2. Therefore, slightly different factor levels are investigated, which are listed in Table 2.3. The initial friction area measures $150\,\mathrm{mm} \times 50\,\mathrm{mm}$, based on the tape width of 50 mm and the length of the heating plates of 150 mm. The specimens are dried at least for 8 h at 80 °C, to exclude any influence of moisture in the tested specimens.

Factors	Unit	Levels
Temperature T	(°C)	{210; 240 ; 270}
Slip velocity v^{slip}	(mm/s)	{0.83 ; 2.5 ; 8.33}
Transversal pressure $p^{\perp}$	(MPa)	{0.02 ; 0.04 ; 0.06}

Table 2.3: Factors and according levels of the isothermal tool-ply friction characterization following a full-factorial test plan.

Characterization results An excerpt of the characterization results at 240 °C is shown in Figure 2.27. The according results vary around the center point of the full-factorial test plan.


(a) $v^{\mathrm{slip}} = 2.5\,\mathrm{mm/s}$; $T = 240\,°\mathrm{C}$ (b) $p^\perp = 0.04\,\mathrm{MPa}$; $T = 240\,°\mathrm{C}$

(c) $v^{\mathrm{slip}} = 2.5\,\mathrm{mm/s}$; $p^\perp = 0.04\,\mathrm{MPa}$
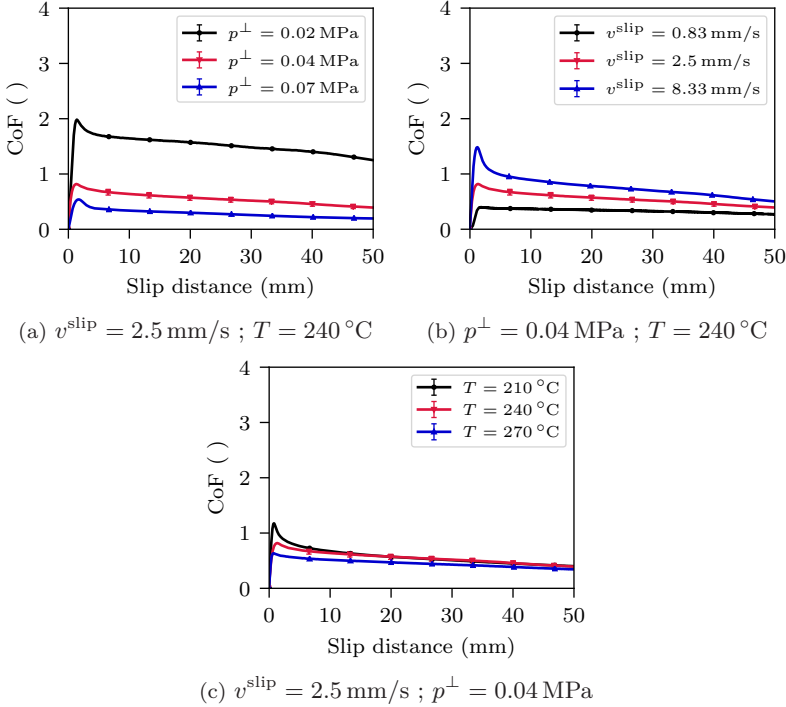
Figure 2.27: Pull-out results for the tool-ply interface under variation of slip velocity v^{slip}, transversal pressure $p^\perp$ and temperature T.

A low standard deviation is observed for the center point, which makes multiple replicates only for the center point reasonable. Regarding the evolution of the CoF over the slip distance, the characteristic evolution of the CoF over the slip distance is obtained, in analogy to ply-ply characterization. Compared to the ply-ply characterization, a systematically lower CoF is observed for the tool-ply interface. Thereby, it is to be noted that not all of the investigated factor levels can be directly compared. Regarding the influence of the varied factors, a higher slip

velocity, a lower transversal pressure and a lower temperature induce a higher CoF, where transversal pressure reveals the most significant influence. In contrast, the influence of temperature is almost negligible. Nonetheless, relating the evolution of the CoF and the Hersey number (cf. Equation 2.8) according to the Stribeck approach, also tool-ply friction can be assigned to hydrodynamic friction, based on the aforementioned qualitative dependencies and the usual increase of the viscosity of thermoplastics with decreasing temperatures.

In summary, a distinct dependency of tool-ply friction on slip velocity and transversal pressure is observed. Besides this, a comparably small influence of temperature is observed.

2.4 Discussion and conclusion

The results of an experimental forming study as well as from material characterization at process conditions are presented and investigated in the scope of this chapter. These, as well as the resulting requirements on thermoforming simulation are discussed in the following.

Process analysis   The experimental forming study in Section 2.2 is based on the variation of layup sequence, forming velocity, tool temperature and gripper force for a complexly-shaped and generic geometry, following a face-centered central composite design (CCD). Each factor level is repeated three times. Formability is investigated w.r.t. wrinkling behavior, which is quantified by means of surface curvature approximated from triangularized surface measurement results. The experimental forming study is quantitatively assessed by means of the response surface methodology (RSM).

The experimental investigations reveal that layup sequence has the largest impact on wrinkling behavior, where the quasi-isotropic layup induces distinctively pronounced wrinkling behavior compared to the orthotropic layup. This observation is in agreement with the investigations by Haanappel et al. [119], who state that more than two fiber directions hinder intra-ply shear deformation, which induces local wrinkling if a certain double-curvature is exceeded and bending rigidity is not high enough to prevent wrinkling. Regarding the factors varied for both layups, which namely are tool temperature, form-

ing velocity and gripper force, qualitatively the same dependencies are observed for both layups: a higher forming velocity, a higher tool temperature and a lower gripper force yield a decrease in wrinkling behavior. It is to be noted that such kind of observations depend on the investigated geometry. This is expected to be in particular valid for the varied gripper force, since laminate gripping and tensioning is usually and also successfully applied in composite forming for minimizing and preventing wrinkling [50, 55, 238, 239]. Anyhow, a suitable gripper modeling approach accurately accounting for the according boundary conditions is desirable for thermoforming simulation, since grippers obviously influence forming behavior. A more general insight is expected for the influence of tool temperature and forming velocity, where similar dependencies are found by several authors [54, 55, 240]. On the contrary, De Luca et al. [238] have found that lower forming velocities can improve part quality, which, however, has to be compensated by higher initial laminate and tool temperatures [240].

In comparison of the influence of tool temperature and forming velocity, forming velocity shows the more significant influence. This sensitivity may result from rate-dependent forming behavior as well as from the changing cooling behavior determined by the time of tool-ply contact (gap conductance) and exposure to the cooler environment (convection and radiation). Rate-dependent forming behavior is clearly observed in material characterization. Besides this, also an influence of the varied process parameters on the local cooling is found in the experimental forming study. These effects, unfortunately, cannot be investigated isolated in experimental forming tests, which impedes further investigations of the influence of forming velocity on wrinkling behavior. As shown in the experimental study, however, a higher forming velocity induces a decrease in local cooling, but an increase in material stiffness. Therefore, the changing cooling behavior is expected to mostly determine wrinkling behavior rather than the rate-dependent material stiffness, since otherwise the dependencies are expected to behave vice versa. Unfortunately, this cannot be verified experimentally. In contrast, a thermoforming simulation approach including the prediction of thermal behavior as well as rate- and temperature-dependent material modeling would enable the isolated analysis of the aforementioned interactions.

Material characterization To investigate material behavior of the thermoplastic UD tape investigated in the scope of this study at process conditions, crystallization kinetics as well as shear, bending and frictional behavior is characterized. Standard and flash differential scanning calorimetry (DSC) tests are conducted for characterization of crystallization kinetics, which in combination cover a wide range of cooling rates (0.167 °C/s to 100 °C/s). The typical shift of recrystallization towards lower temperatures for higher cooling rates [231] is observed, which yields up to 50 °C for the considered range of cooling rates. Since recrystallization defines the transition from the molten to the solid material state, crystallization as well as the influence of cooling rate is expected to distinctively influence the formability prediction, if crystallization already during forming cannot be excluded. The measurements of the local temperature evolution during thermoforming in Section 2.2.3 reveal core temperatures close to the recrystallization temperature for a low cooling rate. The same is observed by Machado et al. [135] for another geometry and material, even if crystallization is not directly addressed in their study. Recrystallization might have onset in the outer plies, since tool-ply gap conductance is expected to render a high temperature gradient in thickness direction onto the laminate. Therefore, thermal behavior and crystallization kinetics is expected to be worthwhile to be considered in thermoforming simulation for further investigations.

Regarding intra-ply material characterization for shear and bending behavior, a distinct rate- and temperature-dependency is observed for isothermal testing outside the small strain regime in the molten material state. The same observation is made for another UD tape material system by Haanappel et al. [60] for shear behavior and by Sachs [52] for bending behavior. Therefore, these characteristics are to be considered in a thermoforming simulation approach.

Besides isothermal testing, also non-isothermal shear characterization based on the torsion bar test under a stationary oscillating load in the small strain regime is conducted. The results show a distinct increase of shear rigidity with the onset of recrystallization, which is in agreement with the observations by Donderwinkel et al. [220]. Additionally, a shift of the onset of the sharp increase of shear rigidity due to recrystallization towards lower temperatures is observed for higher cooling rates. Therefore, a thermomechanical coupling in

thermoforming simulation require not only the coupling of mechanical behavior to the temperature, but also to the degree of crystallinity. Besides this, the observed temperature-dependency in the molten material state is nearly negligible in the related small strain regime. In contrast, a distinct temperature-dependency is observed in the related isothermal tests in the large strain regime. Similarly, predominantly elastic behavior was observed in the small strain regime and distinctive rate-dependency in the large strain regime by Haanappel et al. [60], under application of the torsion bar test for another UD tape material system. Henceforth, it is questionable if the torsion bar test is capable to exploit the full material characteristic in the small strain regime. However, the increase of shear stiffness w.r.t. recrystallization is expected to be unaffected from this observation.

Regarding inter-ply characterization, frictional behavior for the ply-ply as well as for the tool-ply interfaces is investigated. The results for characterization in the molten material state reveal a dependency of frictional behavior on transversal pressure, slip velocity and temperature, where temperature shows a minor influence. Similar insights were made in the experimental benchmark study by Sachs et al. [93]. Besides this, also a dependency of ply-ply frictional behavior on the relative orientation between the slipping plies is observed, where a decrease in frictional resistance is observed for increasing relative orientation. Also this mechanism was experimentally addressed by several authors for different material systems [96, 97, 218], but not considered in thermoforming simulation so far and is therefore worth to be investigated. At temperatures close to recrystallization, the single plies are tacking, sliding is prevented and the tested specimens are damaged in the friction characterization setup. Nonetheless, friction characterization reveals, in agreement with previous studies presented in literature, that frictional behavior needs to be taken into account for the molten material state, which makes a layer-by-layer approach, including the consideration of the above outlined dependencies of frictional behavior, desirable.

Requirements on thermoforming simulation   Based on the above outlined discussion and conclusion on the experimental process analyses and material characterization results, the following requirements on thermoforming simulation can be summarized:

- Rate- and temperature-dependent intra-ply material modeling at finite strains

- Layer-by-layer analysis of thermoforming processes to take into account inter-ply slipping

- Consideration of the influence of transversal pressure, slip velocity, temperature and relative orientation between the slipping plies in inter-ply slip modeling

- Thermal and crystallization kinetics modeling for the prediction of the phase transition from the molten to the solid material state as a function of cooling rate

- Thermomechanical coupling w.r.t. temperature and the degree of crystallinity

- Modeling of gripper forces and kinematics

- (Decoupling of membrane and bending behavior)

The last item is not experimentally investigated, but included for completeness. The necessity for decoupling of membrane and bending behavior for intra-ply material modeling is a well known requirement on composite forming simulation, as outlined in detail in Section 1.2.3.2.

83

3 Hyper- and hypoviscoelastic intra-ply modeling with superimposed elements

Abstract

A framework for isothermal forming simulation using the commercial FE solver Abaqus is presented. This includes decoupled membrane and bending behavior based on superimposed built-in membrane and shell elements in combination with a user-defined material modeling and shell section integration, respectively. Hypo- and hyperelastic material modeling is investigated and rate-dependent intra-ply modeling approaches are proposed. An emphasis is laid on rate-dependent bending behavior, since this is a material characteristic usually neglected in thermoforming simulation. The proposed viscoelastic constitutive equations are based on a Voigt-Kelvin and a generalized Maxwell approach. Parametrization results reveal that only the generalized Maxwell approach is capable to describe the whole material characteristic for the investigated material. Finally, the presented approaches are applied to thermoforming simulation with a good agreement to experimental tests. Besides this, an influence of rate-dependent bending modeling on the prediction of wrinkling behavior is observed, which emphasizes the necessity to consider this material characteristic in thermoforming simulation.

In the scope of this chapter, isothermal intra-ply modeling for thermoforming simulation based on superimposed elements for decoupling of membrane and bending behavior is presented. An emphasis is laid on rate-dependent bending behavior, since recently presented thermoforming simulation approaches [119, 152, 156] model bending behavior purely elastic, although distinct rate-dependent bending behavior observed in material characterization by several authors [52, 75, 76, 83, 221, 241] as well as in material in characterization in the previous chapter.

The first approach accounting for rate-dependent bending behavior was presented by Dörr et al. [216]. This approach is represented and the related studies are extended in the scope of this chapter. For the implementation of the thermoforming simulation approaches presented in the following, the commercial FE solver Abaqus is applied in combination with several user-subroutines. The according framework, which is based on conventional shell theory, is schematically illustrated in Figure 3.1.
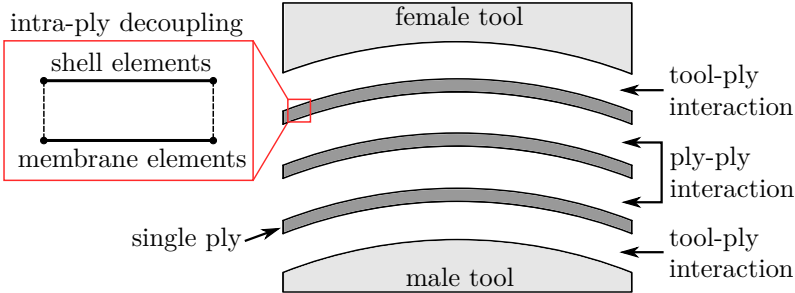
Figure 3.1: Schematic illustration of the framework for continuous FE forming simulation with superimposed elements based on conventional shell theory.

Following a continuous modeling approach, each ply of the stacked laminate is modeled by separate element layers. The resulting surfaces split into tool-ply and ply-ply interfaces. At the tool-ply interfaces, normal pressures and traction forces are expected to be low while the laminate is being formed and prior to the application of the consolidation pressure. Since solely steel tools are considered within this study, minimal deformations in the tools are to be expected. There-

fore, the tools are modeled as rigid and discrete surfaces. Regarding intra-ply material modeling, thermoforming simulation requires to decouple membrane and bending behavior as well as to account for rate-dependent material behavior, as outlined in Section 1.2.3.2 and Chapter 2, respectively. Moreover, material modeling at finite strains has to be considered, which requires to take into account the rotation of the principal material orientations under large shear deformations, due to the distinctively anisotropic material behavior. For this purpose, either hypoelastic or hyperelastic modeling approaches are usually applied in composite forming simulation (cf. Section 1.2.3.2). In the following, an approach for decoupling of membrane and bending behavior by superimposed membrane and shell elements using the commercial FE solver Abaqus is outlined (Section 3.1). Subsequently, a comparison of hypo- and hyperelastic modeling approaches is presented (Section 3.2), identifying their benefits and drawbacks for FE composite forming simulation. Finally, rate-dependent modeling approaches for membrane and bending behavior are presented (Section 3.3), parameterized for the investigated material (Section 3.4) and applied for validation and comparison to thermoforming simulation (Section 3.5).

3.1 Membrane and bending decoupling

Conventional shell theory is applied in the scope of this study for modeling intra-ply deformation behavior, due to the high slenderness ratio of the single plies. Conventional shell theory is usually based on translational and rotational degrees of freedom (DOF) at each node, which describe the curved mid-face of the shell element. In the scope of this chapter, the Abaqus built-in conventional shell elements (S4(R), S3) and membrane elements (M3D4(R), M3D3) are employed for modeling membrane and bending behavior, respectively. The virtual internal energy $\delta\Pi$ of the related conventional shell element splits into [242]

$$\delta\Pi = \int_V \sigma_{\alpha\beta} \left(\delta\varepsilon^0_{\alpha\beta} + F^0_{33}\xi_3\delta\kappa_{\alpha\beta} \right) \, \mathrm{d}V, \tag{3.1}$$

where $\sigma_{\alpha\beta}$ is the Cauchy stress, $\varepsilon^0_{\alpha\beta}$ and $\kappa_{\alpha\beta}$ the generalized section strains in terms of membrane strains and curvature changes, respec-

tively, F_{33}^0 the deformation in thickness direction, ξ_3 the distance to the mid-face and V the element volume. Section forces $N_{\alpha\beta}$ and section moments $M_{\alpha\beta}$ can be introduced by

$$N_{\alpha\beta} = \int_{t_0} \sigma_{\alpha\beta}(\xi_3) F_{33}^0 \, \mathrm{d}\xi_3 \quad \text{and} \quad M_{\alpha\beta} = \int_{t_0} \sigma_{\alpha\beta}(\xi_3) \xi_3 (F_{33}^0)^2 \, \mathrm{d}\xi_3,$$
(3.2)

based on the integration of the Cauchy stress over the initial thickness t_0 of the shell element. This allows to reformulate the virtual internal energy into

$$\delta \Pi = \int_A \left(N_{\alpha\beta} \delta \varepsilon_{\alpha\beta}^0 + M_{\alpha\beta} \delta \kappa_{\alpha\beta} \right) \, \mathrm{d}A,$$
(3.3)

where A is the area of the shell element mid-face. Hence, the virtual internal energy $\delta \Pi$ splits additively into a membrane and a bending part, which is additively separable by the introduction of section forces $N_{\alpha\beta}$ and section moments $M_{\alpha\beta}$. In conventional applications, such as structural analyses, section forces and section moments are obtained based on the evaluation of a single constitutive equation for determination of the according stress $\sigma_{\alpha\beta}$. For continuous composite forming simulation following convention shell theory, however, the decoupling of membrane and bending behavior is a basic requirement on intra-ply modeling (cf. Section 1.2.3.2).

To achieve a decoupling of membrane and bending behavior, separate membrane and plate (bending) elements can be superimposed by shared nodes, as schematically illustrated in Figure 3.2. Using Abaqus built-in elements, a decoupling of membrane and bending behavior can only be achieved by superimposed membrane (M3D4(R), M3D3) and shell elements (S4(R), S3), since no plate elements are directly available. A plate element is obtained based on built-in techniques by means of a section integration prior to the analysis and the section idealization "bending only". This, however, restricts modeling of bending behavior to physically linear material behavior. Moreover, the geometric nonlinear effect of fiber rotation under large shear deformation is not captured accurately, which is discussed in more detail in Section 3.2. Hence, membrane and bending can be decoupled based
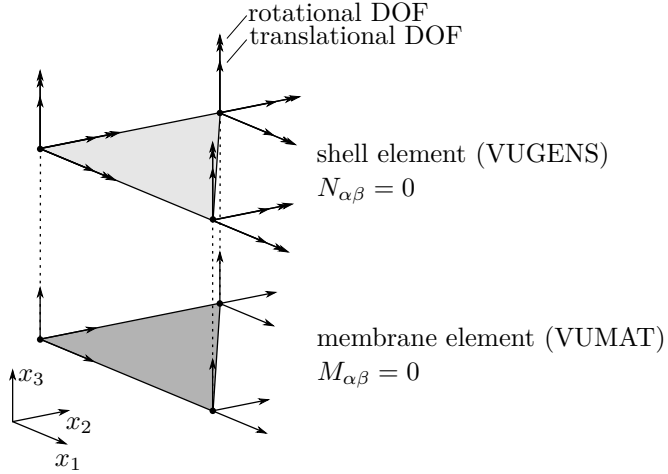
Figure 3.2: Schematic illustration of the decoupling of membrane and bending behavior with superimposed membrane and shell elements and the according user-interfaces in Abaqus.

on Abaqus built-in modeling techniques only in a simplified and approximate manner.

As remedy, a user-defined shell section integration is implemented in a so-called VUGENS subroutine [243]. This user-interface provides the incremental membrane strain $\Delta\varepsilon^0_{\alpha\beta}$, the incremental curvature $\Delta\kappa_{\alpha\beta}$ as well as the membrane deformation gradient $f_{\alpha\beta}$ as input. Based on these kinematic magnitudes, the constitutive equations and shell section integration are defined by the user, in order to determine the section forces $N_{\alpha\beta}$ and section moments $M_{\alpha\beta}$, which are passed back to the solver. Based on this, the user-interface VUGENS is applied in the scope of this chapter, to consider only the bending part of shell element by

$$N_{\alpha\beta} = 0 \quad \text{and} \quad M_{\alpha\beta} = \int_{t_0} \sigma_{\alpha\beta}(\xi_3)\xi_3(F^0_{33})^2 \, \mathrm{d}\xi_3, \qquad (3.4)$$

where a Gaussian integration scheme [228] is chosen for the numerical thickness integration. On the contrary, the membrane part is modeled by the superimposed membrane element (cf. Figure 3.2).

For evaluation of the bending constitutive equations, only the physical incremental curvature change $\Delta \kappa_{\alpha\beta}$ is available as kinematic measure for the bending part. The incremental curvature change is determined by [242]

$$\Delta \kappa_{\alpha\beta} = \text{sym} \left[b_{\alpha\beta}^{t+\Delta t} - b_{\alpha\gamma}^{t} \Delta R_{\delta\gamma} \Delta V_{\delta\beta} \right], \qquad (3.5)$$

where $b_{\alpha\beta}^{t+\Delta t}$ and $b_{\alpha\beta}^{t}$ is the surface gradient at the beginning and at the end of the increment, respectively, $\Delta R_{\delta\gamma}$ the incremental rigid-body rotation and $\Delta V_{\delta\beta}$ the incremental left stretch tensor. This enables to evaluate hypoelastic constitutive equations based on the incremental total strain (membrane and bending), which is given by

$$\Delta \varepsilon_{\alpha\beta} = \Delta \varepsilon_{\alpha\beta}^{0} + \xi_3 F_{33}^{0} \Delta \kappa_{\alpha\beta}. \qquad (3.6)$$

For the evaluation of hyperelastic constitutive equations, in general the deformation gradient $F_{\alpha\beta}$ or other kinematic measures derived from the deformation gradient are adopted. For the adopted conventional shell elements, the total deformation gradient (membrane and bending) is determined by [242]

$$F_{\alpha\beta} = F_{\alpha\beta}^{0} + \xi_3 F_{33}^{0} b_{\alpha\gamma} F_{\gamma\beta}^{0}, \qquad (3.7)$$

Thus, the surface gradient $b_{\alpha\gamma}$ is necessary to determine the total deformation gradient $F_{\alpha\beta}$. Unfortunately, only the incremental physical curvature change $\Delta \kappa_{\alpha\beta}$ is available in the VUGENS subroutine, which prevents the implementation of hyperelastic constitutive equations, since the surface gradient cannot be derived from the physical incremental curvature due to the symmetrization (cf. Equation 3.5). For membrane modeling, the user-interface for material modeling VU-MAT is used. This user-interface is called at each integration point of the membrane elements and supplies the incremental strains as well as the deformation gradient as kinematic magnitudes, and passes the Cauchy stress back to the solver. Based on this, material modeling following either hypo- or hyperelastic modeling approaches is enabled

for the membrane elements. Details on hyper- and hypoelastic material modeling approaches as well as the benefits and drawbacks for composite forming simulation are presented and investigated in the following section.

3.2 Hyper- vs. hypoelastic material modeling

A basic requirement for intra-ply modeling in composite forming simulation is to accurately account for fiber rotation, respectively the rotation of the principal material orientations. This effect is induced by a comparably low shear stiffness accompanied with a high fiber stiffness, which is a material characteristic generally observed for CoFRP pre-products at process conditions. Figure 3.3 exemplifies the changing principal material orientation under "simple shear" deformation, resulting in non-orthogonal principal material orientations $\boldsymbol{a}_i$ in the current configuration.

initial configuration   current configuration
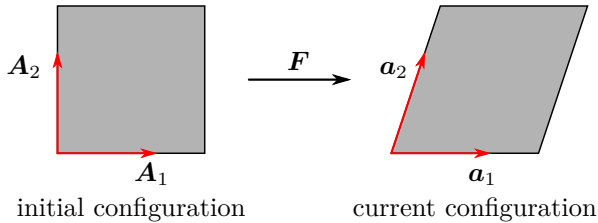
Figure 3.3: Schematic illustration of the rotation and stretch of the principal material orientation under "simple shear" deformation.

The initial and the current configuration are related by the deformation gradient $\boldsymbol{F}$. The deformation gradient is employed to "push" a vector from the initial configuration $\boldsymbol{A}_i$ to the current configuration $\boldsymbol{a}_i$ by

$$\boldsymbol{a}_i = \boldsymbol{F} \cdot \boldsymbol{A}_i. \tag{3.8}$$

The linearly transformed principal material orientation $\boldsymbol{a}_i$ comprise in general a rotation and a stretch. The uniaxial stretch can be quantified

91

for example by the uniaxial logarithmic strain in direction of the i-th principal material orientation based on basic vector operations by

$$\varepsilon_i^{\ln} = \ln\left(\frac{l_i}{L_i}\right) \quad \text{with} \quad L_i = ||\boldsymbol{A}_i|| \quad \text{and} \quad l_i = ||\boldsymbol{a}_i||. \tag{3.9}$$

The same applies for fiber rotation, which can be quantified by

$$\angle\left(\boldsymbol{a}_i, \boldsymbol{A}_i\right) = \cos\left(\frac{\boldsymbol{a}_i \cdot \boldsymbol{A}_i}{||\boldsymbol{a}_i||\,||\boldsymbol{A}_i||}\right). \tag{3.10}$$

To account for fiber rotation and principal material orientations becoming non-orthogonal in material modeling, either hyper- or hypoelastic approaches can be applied (cf. Section 1.2.3.2). To identify the benefits and drawbacks of these approaches, both approaches are compared in the following. For this purpose, initially the applied material modeling approaches are introduced (Section 3.2.1 and 3.2.2) and subsequently compared in unit cell tests (Section 3.2.3) and virtual bias extension tests (Section 3.2.4).

3.2.1 Hyperelastic material modeling

In the scope of this study, a strain-based hyperelastic material formulation [143] is applied. For this purpose, the standard covariant metric tensor $\boldsymbol{g}$ in the current configuration is introduced to evaluate the covariant convected current metric by

$$\boldsymbol{C} = \boldsymbol{F}^\top \cdot \boldsymbol{g} \cdot \boldsymbol{F}, \tag{3.11}$$

which is usually denoted as the right Cauchy-Green tensor, representing a Lagrangian deformation measure. The according mapping from the current to the initial configuration is usually referred to as "pull-back" operation. Since Cartesian coordinates are chosen, the standard covariant metric in the current configuration $\boldsymbol{g}$ and in the initial configuration $\boldsymbol{G}$ are represented by the second-order identity

tensor ($g_{ij} = G_{ij} = \delta_{ij}$). Based on this, Green-Lagrange strain is determined through

$$\boldsymbol{E} = \frac{1}{2}\left(\boldsymbol{C} - \boldsymbol{1}\right) = \frac{1}{2}\left(\boldsymbol{F}^{\top} \cdot \boldsymbol{F} - \boldsymbol{1}\right), \qquad (3.12)$$

where $\boldsymbol{1}$ is the second-order identity tensor. Accordingly, Green-Lagrange strain is a Lagrangian strain measure and thus defined in the initial configuration. For composite pre-products, the principal material orientations are usually orthogonal and thus aligned to the Cartesian base vectors in the initial configuration. Therefore, the evaluation of strain invariants, such as fiber strain in 1- and 2-direction, is straightforward:

$$\varepsilon_1^{\mathrm{GL}} = \boldsymbol{E} : (\boldsymbol{A}_1 \otimes \boldsymbol{A}_1) = E_{11}, \qquad (3.13)$$

$$\varepsilon_2^{\mathrm{GL}} = \boldsymbol{E} : (\boldsymbol{A}_2 \otimes \boldsymbol{A}_2) = E_{22}. \qquad (3.14)$$

By means of material modeling based on a Lagrangian kinematic measure, the constitutive equations can be defined within an orthonormal material frame, and fiber rotation due to large shear deformation is intrinsically captured.

The second Piola-Kirchhoff stress $\boldsymbol{S}$ is the work conjugate to the Green-Lagrange strain $\boldsymbol{E}$. In the scope of this study, the so-called St. Venant-Kirchhoff material is applied for hyperelastic material modeling, which defines a physically linear relation between the Green-Lagrange strain and the second Piola-Kirchhoff stress:

$$\boldsymbol{S} = \mathbb{C} : \boldsymbol{E}, \qquad (3.15)$$

where $\mathbb{C}$ is a fourth-order elasticity tensor. The second Piola-Kirchhoff stress can be mapped to the current configuration by a so-called "push-forward" operation by

$$\boldsymbol{\tau} = \boldsymbol{F} \cdot \boldsymbol{S} \cdot \boldsymbol{F}^{\top} \quad \text{and} \quad \boldsymbol{\sigma} = \frac{1}{J}\boldsymbol{\tau} \quad \text{with} \quad J = \det(\boldsymbol{F}), \qquad (3.16)$$

where $\boldsymbol{\tau}$ and $\boldsymbol{\sigma}$ are the Kirchhoff and the Cauchy stress, respectively, both representing a Eulerian stress measure. Figure 3.4 gives a geometric illustration of the mappings of the kinematic and stress mea-

sures between the covariant current configuration $\mathscr{B}_1$ and initial configuration $\mathscr{B}_0$ as well as the according contravariant current configuration $\mathscr{B}_1^*$ and contravariant initial configuration $\mathscr{B}_0^*$. It is to be noted that for hyperelastic approaches, the stored internal energy depends on the final state only ($\psi = \psi(\boldsymbol{F})$). Therefore, hyperelastic approaches are path independent [122] and also exact for arbitrary time (deformation) steps in incremental solving procedures.
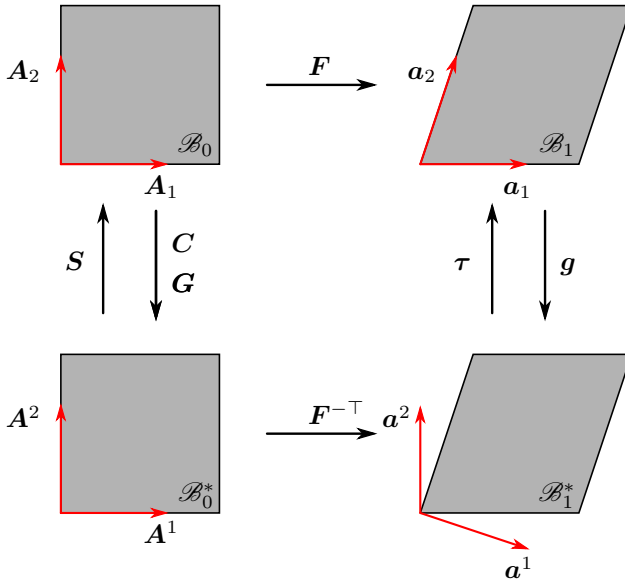
Figure 3.4: Schematic illustration of the definition of the metric and stress tensors as mappings between the covariant initial $\mathscr{B}_0$ and covariant current configuration $\mathscr{B}_1$ and the according contravariant configurations $\mathscr{B}_0^*$ and $\mathscr{B}_1^*$.

3.2.2 Hypoelastic material modeling

Hypoelastic constitutive equations relate the rate of deformation to the rate of stress. This stress rate should be objective and thus related to an objective deformation rate measure, in order to satisfy material

frame indifference [122]. A hypoelastic constitutive equation in the physical linear form is given by

$$\boldsymbol{\sigma}^{\triangledown} = \mathbb{C} : \boldsymbol{D}, \tag{3.17}$$

where $\boldsymbol{\sigma}^{\triangledown}$ represents an objective rate of the Cauchy stress, $\boldsymbol{D}$ the rate-of-deformation tensor and $\mathbb{C}$ a fourth-order elasticity tensor. Both are Eulerian variables and thus, the constitutive equation is defined in the current configuration. An objective rate of Cauchy stress is defined in general by [122]

$$\boldsymbol{\sigma}^{\triangledown} = \boldsymbol{Q} \cdot \left(\frac{\mathrm{d}}{\mathrm{d}t} \left(\boldsymbol{Q}^{\top} \cdot \boldsymbol{\sigma} \cdot \boldsymbol{Q} \right) \right) \cdot \boldsymbol{Q}^{\top}, \tag{3.18}$$

where $\boldsymbol{Q}$ is the rigid-body rotation. Denoting $\boldsymbol{\Omega} = \dot{\boldsymbol{Q}} \cdot \boldsymbol{Q}^{\top}$ as the corresponding spin, the generalized objective stress rate can be rewritten:

$$\boldsymbol{\sigma}^{\triangledown} = \dot{\boldsymbol{\sigma}} + \boldsymbol{\sigma} \cdot \boldsymbol{\Omega} - \boldsymbol{\Omega} \cdot \boldsymbol{\sigma}. \tag{3.19}$$

Different objective stress rates exist in literature, which differ regarding the approach for identification of rigid-body rotation. In the scope of this chapter, the Abaqus built-in conventional shell and membrane elements are applied. Therefore, following Abaqus conventions [242], Green-Naghdi's objective rate is applied, which is discussed in the following for the application to composite forming simulation.

Green-Naghdi's frame Rigid body rotation is identified for Green-Naghdi's frame by means of the so-called polar decomposition of the deformation gradient, which is given by [122]

$$\boldsymbol{F} = \boldsymbol{R} \cdot \boldsymbol{U} = \boldsymbol{V} \cdot \boldsymbol{R}. \tag{3.20}$$

This defines the right stretch tensor $\boldsymbol{U}$ and the left stretch tensor $\boldsymbol{V}$, which by definition are symmetric, as well as rigid body rotation of Green-Naghdi's frame by means of the orthogonal (rotation) tensor $\boldsymbol{R} = \boldsymbol{Q}$. For the application of Green-Naghdi's frame to anisotropic materials, it has to be considered that the average rigid-body rotation identified by polar decomposition is not unambiguously related to the rotation of the principal material directions. This is straightforward

to be shown by the linear transformation of a line segment describing the principal material orientations in the initial configuration $\boldsymbol{A}_i$ into the current configuration by

$$\boldsymbol{a}_i = \boldsymbol{V} \cdot \boldsymbol{R} \cdot \boldsymbol{A}_i. \tag{3.21}$$

Based on this, the line segment is initially rotated to Green-Naghdi's frame by the orthogonal tensor $\boldsymbol{R}$ and subsequently stretched and rotated by the left stretch tensor $\boldsymbol{V}$. The latter induces under shear deformation a misalignment between Green-Naghdi's frame and the principal material orientations. To exemplify the misalignment of Green-Naghdi's frame and the principal material orientation, the rotation of Green-Naghdi's frame φ_i^{GN} and the rotation of the principal material orientation φ_i^{F} are evaluated for "simple shear" deformation (cf. Figure 3.3) by means of Equation 3.10. The results are shown in Figure 3.5.
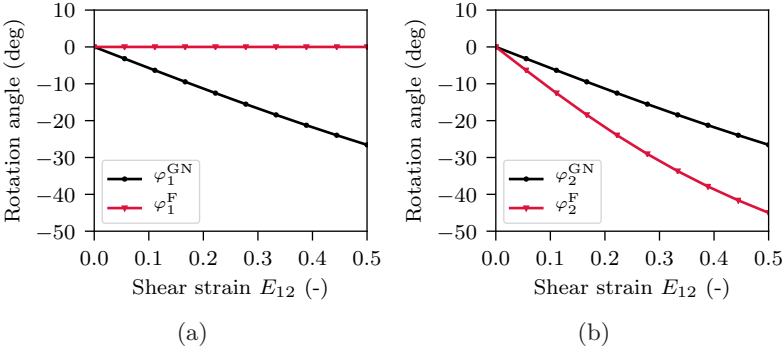
Figure 3.5: Rotation of Green-Naghdi's frame φ_i^{GN} and the principal material orientations φ_i^{F} under "simple shear" deformation in 1-direction (a) and 2-direction (b).

The results reveal that no rotation of the principal material orientation is observed in 1-direction (φ_1^{F}), whereas the principal material orientation in 2-direction (φ_2^{F}) rotates. Hence, the principal material orientations become non-orthogonal. In contrast, Green-Naghdi's frame remains orthogonal ($\varphi_1^{\mathrm{GN}} = \varphi_2^{\mathrm{GN}}$) by definition and therefore identifies an average rigid-body rotation. This yields a severe misalign-

ment between the principal material orientations and Green-Naghdi's frame, which reveals unambiguously that Green-Naghdi's frame is not suitable to be applied for the evaluation of anisotropic constitutive equations under large shear deformation.

Fiber parallel frame   As remedy for the above outlined misalignment between Green-Naghdi's frame and the principal material orientations under shear deformation, an additional fiber-parallel frame, which is schematically illustrated in Figure 3.6, is introduced. This fiber-parallel frame follows fiber rotation for arbitrary deformations and thus enables to model non-orthogonal material behavior within Green-Naghdi's frame $\{\boldsymbol{e}_i\}$. The according covariant base $\{\boldsymbol{g}_i\}$ and contravariant base $\{\boldsymbol{g}^i\}$ are determined by

$$\boldsymbol{g}_i = U_{ij}\boldsymbol{e}_i \quad \text{and} \quad \boldsymbol{g}^i = U_{ij}^{-\top}\boldsymbol{e}_j \quad \text{with} \quad \boldsymbol{U} = U_{ij}\boldsymbol{i}_i \otimes \boldsymbol{i}_j, \quad (3.22)$$

where U_{ij} are the tensor components of the right stretch tensor within a spatially fixed base $\{\boldsymbol{i}_i\}$. This magnitude is supplied by the solver and it can be shown that

$$[U]_{\{\boldsymbol{i}_i \otimes \boldsymbol{i}_j\}} \equiv [V]_{\{\boldsymbol{e}_i \otimes \boldsymbol{e}_j\}}. \quad (3.23)$$

Hence, the components of the right stretch tensor in a spatially fixed frame define fiber rotation within Green-Naghdi's frame and therefore are denoted in the following as fiber-parallel metric coefficients. The co- and contravariant bases satisfy the orthogonality condition ($\boldsymbol{g}^i \cdot \boldsymbol{g}_j = \delta^i_j$) and the according metric coefficients are defined by

$$G_{ij} = \boldsymbol{g}_i \cdot \boldsymbol{g}_j \quad \text{and} \quad G^{ij} = \boldsymbol{g}^i \cdot \boldsymbol{g}^j. \quad (3.24)$$

These metric coefficients relate the co- and contravariant bases by

$$\boldsymbol{g}^i = G^{ij}\boldsymbol{g}_j \quad \text{and} \quad \boldsymbol{g}_i = G_{ij}\boldsymbol{g}^j \quad (3.25)$$

and can also be obtained by the tensor components of the right stretch tensor U_{ij} in a spatially fixed system by

$$G_{ij} = U_{ik}^{\top}U_{ki} \quad \text{and} \quad G^{ij} = U_{ik}^{-1}U_{kj}^{-\top}. \quad (3.26)$$

97

The according mappings between the metric coefficients as well as between Green-Naghdi's frame and the co- and contravariant fiber-parallel frames are illustrated in Figure 3.6.
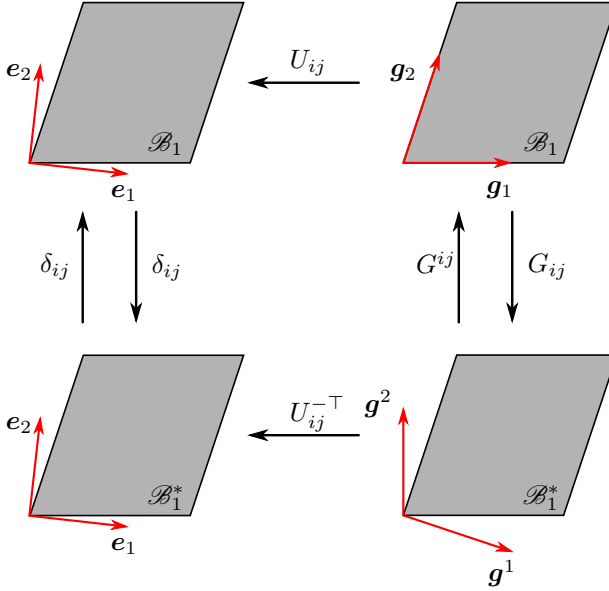
Figure 3.6: Schematic illustration of the transformations in the current configuration between Green-Naghdi's frame $\{e_i\}$ and the covariant $\{g_i\}$ and contravariant $\{g^i\}$ fiber parallel frame.

It is to be noted that the above introduced co- and contravariant bases are not normalized, which implies that a physical magnitude would not only be reflected by the tensor components, but also by the tensor base. To overcome this issue, the fiber-parallel metric coefficients are normalized by

$$U_{ij}^* = \frac{1}{\sqrt{G_{\underline{jj}}}} U_{ij} \quad \text{with} \quad \sqrt{G_{\underline{ii}}} = ||g_i||, \tag{3.27}$$

Here, the underlined indices indicate that the summation convention does not apply. It is to be noted that the symmetry condition of the

fiber-parallel metric coefficients (right stretch tensor) is lost by this normalization. The normalized fiber-parallel metric coefficients are applied for the transformation of the base vectors by

$$\boldsymbol{e}_i = U_{ij}^{*\top}\boldsymbol{g}^{*j} \quad \text{and} \quad \boldsymbol{g}_i^* = U_{ij}^*\boldsymbol{e}_j, \tag{3.28}$$

which are required for the evaluation of the hypoelastic constitutive equations within the fiber-parallel frame. A physically linear hypoelastic constitutive equation within the fiber-parallel frame is defined by

$$\left[\boldsymbol{\sigma}^{\triangledown}\right]_{\{\boldsymbol{g}_i^*\otimes\boldsymbol{g}_j^*\}} = [\mathbb{C}]_{\{\boldsymbol{g}_i^*\otimes\boldsymbol{g}_j^*\otimes\boldsymbol{g}_k^*\otimes\boldsymbol{g}_l^*\}} : [\boldsymbol{D}]_{\{\boldsymbol{g}^{*k}\otimes\boldsymbol{g}^{*l}\}}, \tag{3.29}$$

which is evaluated by means of the incremental integration scheme proposed by Hughes and Winget [126]. This yields the incremental stress summation given by

$$\left[^{t+\Delta t}\boldsymbol{\sigma}\right]_{\{\boldsymbol{g}_i^*\otimes\boldsymbol{g}_j^*\}} = \left[^t\boldsymbol{\sigma}\right]_{\{\boldsymbol{g}_i^*\otimes\boldsymbol{g}_j^*\}} + [\Delta\boldsymbol{\sigma}]_{\{\boldsymbol{g}_i^*\otimes\boldsymbol{g}_j^*\}}. \tag{3.30}$$

In order to evaluate the contravariant stress increment based on the linear-elastic constitutive equation, the covariant strain increment is determined by

$$\Delta\tilde{\varepsilon}_{ij} = U_{ik}^*\Delta\varepsilon_{kl}U_{lj}^{*\top} \quad \text{with} \quad \Delta\varepsilon_{ij}\boldsymbol{e}_i\otimes\boldsymbol{e}_j = \Delta\tilde{\varepsilon}_{ij}\boldsymbol{g}^{*i}\otimes\boldsymbol{g}^{*j}, \tag{3.31}$$

where the transformation defined in Equation 3.28 is applied. Based on this, the elastic constitutive equation can be evaluated, in order to determine the contravariant stress increment by

$$\Delta\tilde{\sigma}^{ij}\boldsymbol{g}_i^*\otimes\boldsymbol{g}_j^* = \left(\tilde{C}^{ijkl}\boldsymbol{g}_i^*\otimes\boldsymbol{g}_j^*\otimes\boldsymbol{g}_k^*\otimes\boldsymbol{g}_l^*\right) : \left(\Delta\tilde{\varepsilon}_{mo}\boldsymbol{g}^{*m}\otimes\boldsymbol{g}^{*o}\right) \tag{3.32}$$
$$= \tilde{C}^{ijkl}\Delta\tilde{\varepsilon}_{kl}\boldsymbol{g}_i^*\otimes\boldsymbol{g}_j^*,$$

by making use of the orthogonality condition of the co- and contravariant bases. Following Equation 3.30, the total contravariant stress $\tilde{\sigma}^{ij}$ is obtained, which is transformed back to Green-Naghdi's frame by

$$\sigma_{ij} = U_{ik}^{*\top}\tilde{\sigma}^{kl}U_{lj}^* \quad \text{with} \quad \sigma_{ij}\boldsymbol{e}_i\otimes\boldsymbol{e}_j = \tilde{\sigma}^{ij}\boldsymbol{g}_i^*\otimes\boldsymbol{g}_j^*, \tag{3.33}$$

based on the transformation defined in Equation 3.28. Thereby, it is to be noted that all of the above outlined transformations of the Eulerian kinematic and stress measures are solely base changes. This is in contrast to the hyperelastic mappings in Figure 3.4, for which the kinematic and stress measures are convected between the initial and current configuration, by keeping the base unchanged.

3.2.3 Unit cell tests

Hypoelastic constitutive equations are path-dependent, due to the incremental integration scheme [244]. This means that for a nonlinear relation between the rate of deformation and the rate of stress, the final stress state depends on the deformation path. For the hypoelastic approach and according fiber-parallel frame presented in Section 3.2.2, the effective material stiffness depends on the deformation state, due to the rotation of the principal material orientations. In combination with the incremental integration scheme, a sufficiently small integration step width is necessary for accurate results. To investigate the accuracy of the fiber-parallel frame depending on the time integration step width, "simple shear" (cf. Figure 3.3) is investigated on unit cell level. The incremental solution for the logarithmic stretch in principal material directions is compared to the corresponding exact solution obtained from Equation 3.9 for different numbers of increments. The hyperelastic approach is not investigated on unit cell level, since the exact solution is obtained independent of the number of increments.

Figure 3.7 shows the results of the unit cell investigation under "simple shear" deformation. The expected error for the incremental solution is observed for all of the considered numbers of increments. This error is quiet severe for the lowest number of increments. The error is reduced for a larger number of increments and thus for a lower time step width with a first-order rate of convergence.

Time steps are intrinsically small in FEA with explicit time integration and the outlined error will therefore not significantly affect the solution. On the contrary, implicit time integration can go along with large time steps, where the above outlined error might have an impact on the obtained results. To investigate this influence, virtual bias extension tests are presented in the following.
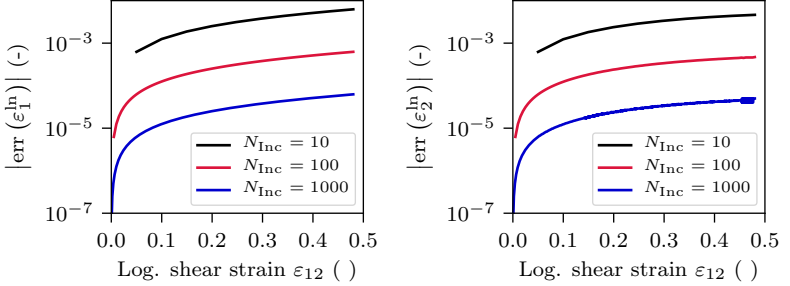
Figure 3.7: Absolute error of the principal logarithmic stretch for the hypoelastic approach in the fiber-parallel frame compared for different number of time integration increments N_{Inc} under "simple shear" deformation.

3.2.4 Virtual bias extension tests

Bias extension tests are usually conducted to characterize shear behavior for woven engineering textiles and prepregs with a woven fiber architecture (cf. Section 1.2.2.1). Therefore, this characterization goes along with large fiber rotation due to shear deformation. Hence, virtual bias extension tests reveal a good opportunity to analyze the capability of material modeling approaches to capture fiber rotation under large shear deformation. In order to compare hyper- and hypoelastic material modeling approaches, virtual bias extension tests for specimens with the size $100\,\mathrm{mm} \times 50\,\mathrm{mm}$ and a coarse discretization of 32 triangular elements are conducted. Implicit time integration is applied, to analyze the influence of the time integration step width on the obtained results. A fiber modulus of $1000\,\mathrm{MPa}$ in 1- and 2-direction and a shear modulus of $0.1\,\mathrm{MPa}$ is chosen as generic material parameters, resulting in a high degree of anisotropy. The principal material orientations are aligned $45\,\mathrm{deg}$ to the direction of deflection. In the scope of this study, the algorithmic stiffness tangent is determined numerically by the approach presented by Sun et al. [245] with a perturbation parameter of 1.0×10^{-5} for both material modeling approaches. This prevents the analytic determination of the material and geometric stiffness, which is available in literature for the hyperelastic approach [122], but which is not straightforward to be obtained for the fiber-parallel hypoelastic approach.

Maximum deflection   In a first study, the maximum deflection $u^{\max}$ converging within one increment is determined for the investigated material modeling approaches. The according results in Figure 3.8 show the typical shape and the three different shear zones observed in theoretical solutions of the bias extension tests. Only a small maximum deflection is achievable in one increment by the hypoelastic approach, whereas a large maximum deflection close to the point where the area of the elements in the inner shear zone would become zero is achieved within one increment by the hyperelastic approach.
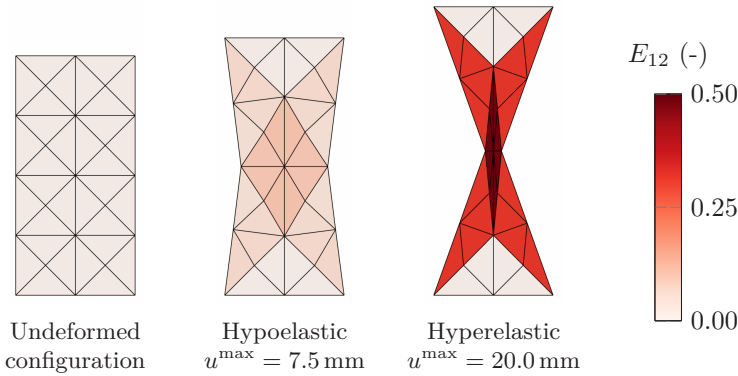
Figure 3.8: FEA results for the virtual bias extension tests for the maximum achievable deflection $u^{\max}$ within one increment in an implicit analysis with the fiber-parallel hypoelastic and the hyperelastic approach.

Time step width   Besides the maximum deflection achievable in one increment, also the influence of the time step width Δt on the obtained deflection force history is analyzed. The according results are shown in Figure 3.9. For the hyperelastic approach, identical results independent of the chosen time step width are obtained. Compared to the hypoelastic approach, a higher material stiffness is observed for the hyperelastic approach, although the same material parameters are applied to both approaches. This is attributable to the different material frames adopted for the evaluation of the linear-elastic relation between stress and strain, where an orthonormal frame is applied by the hyperelastic approach and a fiber-parallel frame by the

(a) Hyperleastic
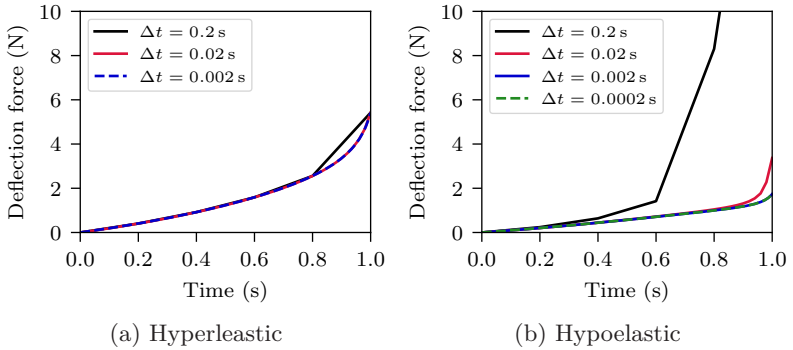
(b) Hypoelastic

Figure 3.9: Results for the deflection forces for different time step widths Δt for the hyperelastic (a) and the fiber-parallel hypoelastic (b) approach.

hypoelastic approach. Consequently, parameterization according to experimental tests would yield different parameters. Besides this, a distinct impact of the time step width is observed for the hypoelastic approach. Different locking behavior is observed, especially for the lowest time step width, where no convergent solution is obtained for the final displacement. Only for a comparably small time step width of $0.002\,\mathrm{s}$, a convergent result is observed.

E_{12} (-)

$u^{\mathrm{final}} = 17.48\,\mathrm{mm}$ $u^{\mathrm{final}} = 20.0\,\mathrm{mm}$ $u^{\mathrm{final}} = 20.0\,\mathrm{mm}$
$\Delta t = 0.2\,\mathrm{s}$ $\Delta t = 0.02\,\mathrm{s}$ $\Delta t = 0.002\,\mathrm{s}$
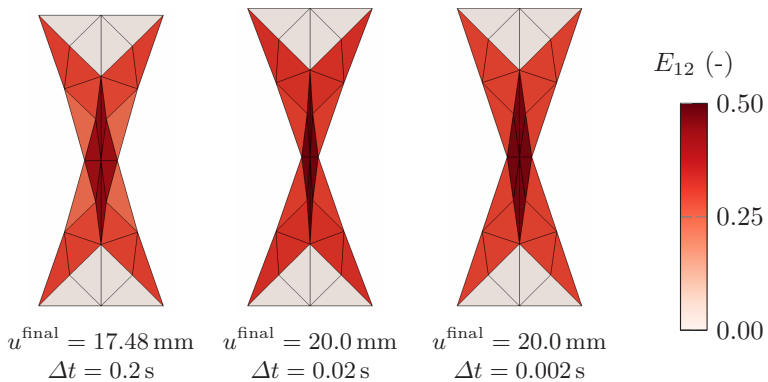
Figure 3.10: FEA results for the virtual bias extension test with the fiber-parallel hypoelastic approach for different time step widths Δt at the final deflection u^{final} achievable in an implicit analysis.

Figure 3.10 shows the shear strain for the final deflection u^{final} for the different time step widths Δt considered for the comparison of the force history. It is to be noted that for the lowest time step width, no convergent result for the final displacement is obtained, which includes a large number of cut backs of the time increment. Moreover, it is observed that only for the two lowest time step widths of 0.002 s and 0.0002 s, the prescribed time step width can be held over the whole analysis. Besides this, a non-homogeneous shear strain distribution is observed within the different shear zones for the time step widths of 0.2 s and 0.02 s. This is another indicator for the numerical error made by the fiber-parallel hypoelastic approach for insufficiently small time increments, besides the artificial locking behavior, if the time step width is not sufficiently small.

3.2.5 Concluding remarks

Hyperelastic and hypoelastic material modeling approaches for application to composite forming simulation are presented and compared. Both approaches reveal to be suitable, since both fulfill the general requirement to account for fiber rotation under shear deformation. This is intrinsically valid for hyperelastic approaches, whereas for hypoelastic approaches a suitable fiber-parallel material frame has to be used instead of the usually adopted orthonormal frames, such as Green-Naghdi's frame. For the latter, it is to be noted that sufficiently small time step widths are necessary to accurately capture fiber rotation, as shown in numerical tests. This, however, reflects the main difference between hypoelastic and hyperelastic approaches, which depend on the final state only and thus are accurate for arbitrary time integration step widths. Composite forming simulation is usually based on explicit time integration. Therefore, the aforementioned numerical error will not affect the accuracy of the obtained results. In contrast, since material characterization tests might last up to several seconds or minutes, implicit time integration becomes preferable, which might go along with large time (deformation) step widths. Since the material modeling approaches need to be applied to both, inverse parameter identification by FEA and composite forming simulation, hyperelastic approaches are in the author's opinion preferable, to guarantee numerical efficiency.

3.3 Rate-dependent intra-ply modeling

Intra-ply material modeling is based on decoupling of membrane and bending behavior, as outlined in detail in Section 3.1. In the following, rate-dependent modeling approaches are presented for both, membrane and bending behavior.

3.3.1 Hyperviscoelastic membrane modeling

A rate-dependent hyperviscoelastic approach is applied for membrane behavior, which is implemented using the Abaqus material user-interface (V)UMAT. The approach applied for material modeling is based on the so-called "Ideal Fibre Reinforced Material" according to Spencer [145, 146] and rate-dependency is modeled following a nonlinear Voigt-Kelvin approach.

Ideal fibre reinforced material The so-called "Ideal Fibre Reinforced Material" is based on the assumption of inextensibility in fiber direction and material incompressibility. To incorporate these assumptions into a constitutive equation, the total Cauchy stress $\boldsymbol{\sigma}$ is subdivided into a reaction stress term $\boldsymbol{\sigma}^{\text{react}}$ and an additional stress term $\boldsymbol{\sigma}^{\text{add}}$:

$$\boldsymbol{\sigma} = \boldsymbol{\sigma}^{\text{react}} + \boldsymbol{\sigma}^{\text{add}} \quad \text{with} \quad \boldsymbol{\sigma}^{\text{react}} = -p\mathbf{1} + \underbrace{T_i^{\text{f}}\boldsymbol{a}_i \otimes \boldsymbol{a}_i}_{\boldsymbol{\sigma}^{\text{f}}}, \qquad (3.34)$$

where p is a hydrostatic pressure invoking material incompressibility, $\mathbf{1}$ the second order identity tensor and T_i^{f} a fiber stress invoking the inextensibility condition in the fiber directions $\boldsymbol{a}_i$. Thereby, it is to be noted that this theory enables the introduction of an arbitrary number of fiber directions $\boldsymbol{a}_i$. Incompressibility is enforced by the kinematic prescription of the deformation in thickness direction of the membrane element by

$$F_{33}^0 = \frac{1}{F_{11}^0 F_{22}^0 - F_{12}^0 F_{21}^0}, \qquad (3.35)$$

where F_{33}^0 is the deformation in thickness direction and $F_{\alpha\beta}^0$ the membrane deformation gradient. This results in a pseudo three-dimensional deformation gradient, which is applied to evaluate the

105

three-dimensional constitutive equations for the pseudo three-dimensional additional stress term σ^{add}. This stress term is condensated to a plane stress state by choosing a hydrostatic pressure p that would enforce incompressibility under a free deformation in thickness direction by

$$\sigma_{33} \overset{!}{=} 0 \quad \rightarrow \quad p = \sigma_{33}^{\mathrm{add}}. \tag{3.36}$$

Fiber inextensibility is regularized by the introduction of a uniaxial, linear-elastic stiffness E^{f}. The according constitutive equation for the i-th fiber orientation is evaluated in the initial configuration by

$$\boldsymbol{S}_i^{\mathrm{f}} = E_i^{\mathrm{f}} \varepsilon_i^{\mathrm{GL}} \boldsymbol{A}_i \otimes \boldsymbol{A}_i \quad \text{with} \quad \varepsilon_i^{\mathrm{GL}} = \boldsymbol{E} : (\boldsymbol{A}_i \otimes \boldsymbol{A}_i) \tag{3.37}$$

The resulting second Piola-Kirchhoff (PK2) fiber stress $\boldsymbol{S}_i^{\mathrm{f}}$ is "pushed" to the current configuration by

$$\boldsymbol{\sigma}_i^{\mathrm{f}} = \frac{1}{J} \left(\boldsymbol{F} \cdot \boldsymbol{S}_i^{\mathrm{f}} \cdot \boldsymbol{F}^{\top} \right). \tag{3.38}$$

Voigt-Kelvin approach The constitutive equations of the Voigt-Kelvin approach are based on the parallel connection of an elastic with a viscous element, which yields

$$\boldsymbol{\sigma}^{\mathrm{add}} = \boldsymbol{\sigma}^{\mathrm{elast}} + \boldsymbol{\sigma}^{\mathrm{visc}}. \tag{3.39}$$

For the elastic part, an isotropic hyperelastic St. Venant-Kirchhoff material [122] is adopted, which is given in terms of the second Piola-Kirchhoff stress by

$$\boldsymbol{S}^{\mathrm{elast}} = \mathbb{C}^{\mathrm{iso}} : \boldsymbol{E}, \tag{3.40}$$

where $\mathbb{C}^{\mathrm{iso}}$ is an isotropic fourth-order elasticity tensor. In contrast, the viscous part is modeled by means of a Cross model, which defines an isotropic and shear-rate dependent viscosity by [147]

$$\boldsymbol{\sigma}^{\mathrm{visc}} = \frac{2\eta}{J} \boldsymbol{D} \quad \text{with} \quad \eta = \frac{\eta_0 - \eta_\infty}{1 + m\dot{\gamma}^{(1-n)}} + \eta_\infty, \tag{3.41}$$

where η_0, η_∞, m and n are material parameters and $\dot{\gamma}$ is the shear-rate defined by

$$\dot{\gamma} = \sqrt{2\boldsymbol{D} : \boldsymbol{D}}. \tag{3.42}$$

3.3.2 Hypoviscoelastic bending modeling

Bending behavior is implemented using the Abaqus (V)UGENS user-interface, which is necessary for decoupling of membrane and bending behavior. Unfortunately, the implementation of hyperelastic constitutive equations is not possible with this user-interface, as outlined in detail in Section 3.1. Therefore, purely elastic as well as rate-dependent bending modeling approaches based on hypoelastic material modeling and a fiber-parallel material frame are developed. The drawbacks of hypoelastic material modeling approches are outlined in Section 3.2. For bending modeling in material parameter extraction by means of FEA, however, hypoelastic approaches have no drawback, since no fiber rotation due to shear deformation occurs. This enables large time step widths in according implicit analyses, although a hypoelastic approach is adopted.

In the following, initially a purely elastic approach is outlined. This is followed by a generalized Maxwell approach, which is subsequently reduced to a Voigt-Kelvin approach.

Elastic approach   The purely elastic approach follows basically the constitutive equations for hypoelastic material modeling within the fiber-parallel frame outlined in Section 3.2.2. Since the fiber-parallel frame is determined based on the membrane deformation gradient $F^0_{\alpha\beta}$, the covariant strain increment in the fiber parallel frame is obtained through

$$[\Delta\boldsymbol{\varepsilon}(z)]_{\{\boldsymbol{g}^{*i}\otimes\boldsymbol{g}^{*j}\}} = [\Delta\bar{\boldsymbol{\varepsilon}}]_{\{\boldsymbol{g}^{*i}\otimes\boldsymbol{g}^{*j}\}} + \xi_3 F^0_{33}\,[\Delta\boldsymbol{\kappa}]_{\{\boldsymbol{g}^{*i}\otimes\boldsymbol{g}^{*j}\}}\,. \tag{3.43}$$

Moreover, the incremental stress $\Delta\boldsymbol{\sigma}$ can be integrated over the thickness to determine the total contravariant section moments in the fiber parallel frame by

$$\left[{}^{t+\Delta t}\boldsymbol{M}\right]_{\{\boldsymbol{g}_i^*\otimes\boldsymbol{g}_j^*\}} = \left[{}^t\boldsymbol{M}\right]_{\{\boldsymbol{g}_i^*\otimes\boldsymbol{g}_j^*\}} + \int_{t_0}\left[\Delta\boldsymbol{\sigma}(\xi_3)\right]_{\{\boldsymbol{g}_i^*\otimes\boldsymbol{g}_j^*\}}(F_{33}^0)^2\xi_3\,\mathrm{d}\xi_3.$$

$$(3.44)$$

For the integration over the thickness of the shell element, Gaussian quadrature [228] is applied. It should be noted that membrane strains can be omitted for the evaluation of the constitutive equations for the linear-elastic case, due to the symmetry condition of the integrand in Equation 3.44 and a closed form solution for the incremental section moments is given by

$$\left[{}^{t+\Delta t}\Delta\boldsymbol{M}\right]_{\{\boldsymbol{g}_i^*\otimes\boldsymbol{g}_j^*\}} = \left[\mathbb{C}\right]_{\{\boldsymbol{g}_i^*\otimes\boldsymbol{g}_j^*\otimes\boldsymbol{g}_k^*\otimes\boldsymbol{g}_l^*\}} : \left(\left[\Delta\boldsymbol{\kappa}\right]_{\{\boldsymbol{g}^{*k}\otimes\boldsymbol{g}^{*l}\}}\frac{t_0^3(F_{33}^0)^3}{12}\right).$$

$$(3.45)$$

Regarding the transformation of the incremental curvature $\Delta\boldsymbol{\kappa}$ and the total section moments $\boldsymbol{M}$ between Green-Naghdi's frame and the fiber parallel frame, the same relations and transformation as for the incremental strain $\Delta\boldsymbol{\varepsilon}$ and total stress $\boldsymbol{\sigma}$ presented in Section 3.2.2 apply.

Generalized Maxwell approach In material modeling, generalized Maxwell approaches have proven to be useful to describe time- and rate-dependent material behavior [246]. A generalized Maxwell model consists of a single spring element connected in parallel with an arbitrary number of Maxwell elements, which consist of a spring element connected in series with a dashpot element (cf. Figure 3.11(a)). The constitutive equations outlined in the previous paragraph are applied for the purely elastic element of the generalized Maxwell approach. For the Maxwell elements, in contrast, the rate-of-deformation tensor $\boldsymbol{D}$ additively splits into an elastic part $\boldsymbol{D}^{\mathrm{e}}$ and a viscous part $\boldsymbol{D}^{\mathrm{v}}$:

$$\boldsymbol{D} = \boldsymbol{D}^{\mathrm{e}} + \boldsymbol{D}^{\mathrm{v}}. \tag{3.46}$$
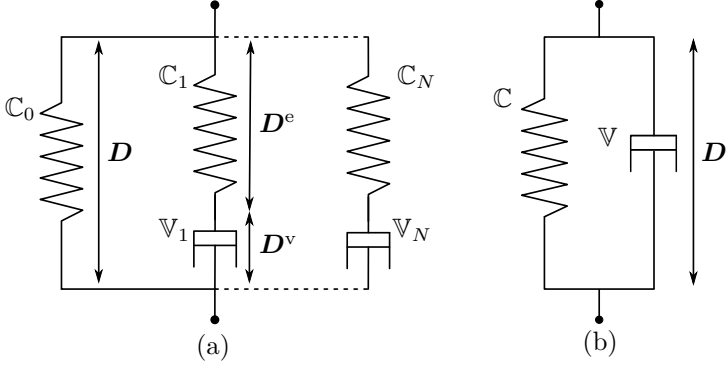
Figure 3.11: Schematic illustration of a generalized Maxwell approach (a) and a Voigt-Kelvin approach (b) for the implementation based on hypo-elastic material modeling.

By introducing constitutive equations for the elastic and the viscous part, an ordinary differential equation is obtained:

$$\boldsymbol{D} = \underbrace{\mathbb{S} : \boldsymbol{\sigma}^{\triangledown}}_{\boldsymbol{D}^{\mathrm{e}}} + \underbrace{\mathbb{V}^{-1} : \boldsymbol{\sigma}}_{\boldsymbol{D}^{\mathrm{v}}}, \tag{3.47}$$

where $\mathbb{S}$ and $\mathbb{V}$ are the fourth-order compliance and viscosity tensor, respectively. This equation can be rearranged to be expressed w.r.t. the objective stress rate by

$$\boldsymbol{\sigma}^{\triangledown} = \mathbb{C} : \underbrace{\left(\boldsymbol{D} - \mathbb{V}^{-1} : \boldsymbol{\sigma}\right)}_{\boldsymbol{D}^{\mathrm{e}}}, \tag{3.48}$$

which reveals that the stress within the Maxwell element can be determined by the elastic stiffness $\mathbb{C}$ and the elastic part of the rate-of-deformation tensor $\boldsymbol{D}^{\mathrm{e}}$. For the implementation of this constitutive equation, an explicit solution procedure based on the central difference method [122] is chosen, to integrate the ordinary differential equation in Equation 3.48 in time. The fiber-parallel frame introduced in Section 3.2.2 is adopted for evaluation of the according constitutive equations. For simplicity, the specification of the according co- and contravariant bases is omitted in the following.

The stress and strain rates in the fiber-parallel frame are approximated for time integration by

$$\boldsymbol{\sigma}^{\triangledown} \approx \frac{\Delta\boldsymbol{\sigma}}{\Delta t} \quad \text{and} \quad \boldsymbol{D} \approx \frac{\Delta\boldsymbol{\varepsilon}}{\Delta t}. \tag{3.49}$$

Based on Equation 3.48, Equation 3.49 and the approximation of the stress for the Maxwell element i in the mid of the increment by

$$^{t+\frac{1}{2}\Delta t}\boldsymbol{\sigma}_i = {}^{t}\boldsymbol{\sigma}_i + \frac{1}{2}{}^{t+\Delta t}\Delta\boldsymbol{\sigma}_i, \tag{3.50}$$

the stress increment over the whole time increment for the Maxwell element i is obtained by central difference method by

$$^{t+\Delta t}\Delta\boldsymbol{\sigma}_i = \left({}^{t+\frac{1}{2}\Delta t}\mathbb{S}_i + {}^{t+\frac{1}{2}\Delta t}\mathbb{V}_i^{-1}\frac{\Delta t}{2} \right)^{-1} : \left({}^{t+\Delta t}\Delta\boldsymbol{\varepsilon} - {}^{t+\frac{1}{2}\Delta t}\mathbb{V}_i^{-1} : {}^{t}\boldsymbol{\sigma}_i\Delta t \right). \tag{3.51}$$

In the scope of this chapter, a nonlinear dashpot element following a hyperbolic sine law is applied, which is defined by

$$\eta_i = A_i \sinh\left(m_i\sigma_{\text{eq}}\right)^{n_i} \quad \text{with} \quad \sigma_{\text{eq}} = \sqrt{{}^{t+\frac{1}{2}\Delta t}\boldsymbol{\sigma}_i : {}^{t+\frac{1}{2}\Delta t}\boldsymbol{\sigma}_i}, \tag{3.52}$$

where η_i is a scalar viscosity and A_i, m_i and n_i are material parameters. The viscosity is assumed to be isotropic without a directional coupling ($\mathbb{V} = \eta\mathbb{I}$).

For evaluation of Equation 3.52, the stress ${}^{t+\frac{1}{2}\Delta t}\boldsymbol{\sigma}_i$ within the i-th Maxwell element in the mid of the increment has to be determined. For this purpose, forward difference method is applied to Equation 3.48 and the stress in the mid of the increment is approximated by Equation 3.50, which yields

$$^{t+\frac{1}{2}\Delta t}\boldsymbol{\sigma}_i = {}^{t}\boldsymbol{\sigma}_i + \frac{1}{2}\left[{}^{t}\mathbb{C}_i : \left(\Delta\boldsymbol{\varepsilon} - {}^{t}\mathbb{V}_i^{-1} : {}^{t}\boldsymbol{\sigma}_i\Delta t \right) \right]. \tag{3.53}$$

Voigt-Kelvin approach A Voigt-Kelvin model consists of a spring-element connected in parallel with a single dashpot element (cf. Figure 3.11(b)). Therefore, the generalized Maxwell approach presented above is reduced to a Voigt-Kelvin approach by replacing the spring

element within a Maxwell element by a rigid element. Thus, the according viscous stress is evaluated by omitting the compliance $\mathbb{S}$ in Equation 3.51, which yields

$$^{t+\Delta t}\Delta\boldsymbol{\sigma}^{\mathrm{v}} = \frac{2}{\Delta t}{}^{t+\frac{1}{2}\Delta t}\mathbb{V} : \left({}^{t+\Delta t}\Delta\boldsymbol{\varepsilon} - {}^{t+\frac{1}{2}\Delta t}\mathbb{V}^{-1} : {}^{t}\boldsymbol{\sigma}^{\mathrm{v}}\Delta t\right). \quad (3.54)$$

In analogy to the generalized Maxwell approach, the fiber-parallel frame introduced in Section 3.2.2 is applied for evaluation of the constitutive equations. The specification of the according co- and contravariant bases in Equation 3.54 is omitted for simplicity.

3.4 Parametrization of intra-ply modeling

The isothermal characterization results from the torsion bar test (cf. Section 2.3.2) and the rheometer bending test (cf. Section 2.3.3) are adopted for parametrization of the intra-ply modeling approaches presented in the previous section. In the scope of this chapter, the characterization results at $270\,^\circ\mathrm{C}$ and three different deformation rates ($0.1\,\mathrm{rpm}$, $1.0\,\mathrm{rpm}$ and $10.0\,\mathrm{rpm}$) are considered for both tests. The according characterization setups are modeled in an FEA for the inverse identification of the material parameters based on an optimization procedure. The normalized summed squared error given by

$$SSEN = \frac{1}{N}\sum_{i=1}^{N}\left(\frac{\left(\hat{M}_i - M_i\right)^2}{M_i^2}\right), \quad (3.55)$$

is applied as target function, where $\hat{M}_i$ and M_i are the torsion or bending moments determined by the FEA and by the characterization test, respectively. In the scope of this chapter, the bending modeling approaches are varied, following a purely elastic, a Voigt-Kelvin and a generalized Maxwell approach (cf. Section 3.3.2). On the contrary, solely a Voigt-Kelvin approach is applied for membrane behavior (cf. Section 3.3.1). In the following, the parametrization approaches and results are presented. The obtained material parameters are listed in the Appendix A.1.

111

3.4.1 Membrane behavior

The torsion bar test is modeled in an FEA to inversely identify the material parameters for membrane behavior. An exemplary result is shown in Figure 3.12.

<center>(a) E_{12} (b) E_{13}</center>
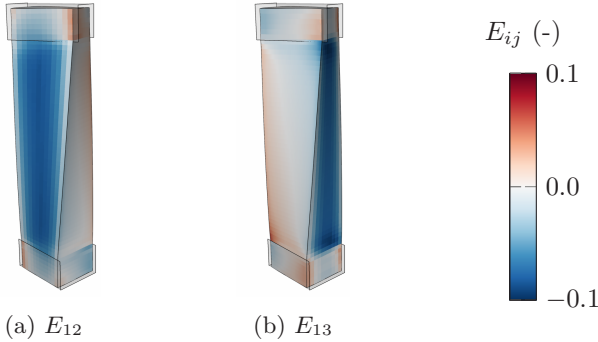
Figure 3.12: Exemplary FEA result of the torsion bar test for the longitudinal Green-Lagrange shear strains E_{1j} with transparent fixtures at 30 deg deflection.

The fixtures of the characterization setup are modeled in the FEA by rigid, discrete surfaces and the tested specimen by hybrid, linear and three-dimensional brick elements (C3D8H). This element type has three translational degrees of freedom at each node and one additional pressure degree of freedom, which is adopted to invoke material incompressibility. Full integration is applied, in order to prevent the necessity to use an hourglass stabilization, since the distinctively shear compliant material behavior is prone to zero energy modes and hourglass stabilization is likely to influence shear behavior. Material modeling is based on the hyperviscoelastic constitutive equations following the nonlinear Voigt-Kelvin approach presented in Section 3.3.1, which are implemented three-dimensionally in a user-interface for material modeling (UMAT). Implicit time integration is chosen for numerical efficiency, since the characterization tests last up to 50 s. Moreover, fully incompressible material modeling is enabled based on the implicit analysis in combination with the above outlined hybrid element, which would not be possible in an explicit analysis. The parameters

to be identified for the Voigt-Kelvin approach are the isotropic elastic stiffness E and the isotropic viscosity η, according to Equation 3.40 and 3.41.

Linear Voigt-Kelvin approach   Following a linear Voigt-Kelvin approach with constant material properties, each of the considered deformation rates n is fitted separately. This enables to investigate the variation of the material parameters for the different deformation rates. The according parameters are determined by the optimization procedure presented by Nelder and Mead [247]. This gradient-based optimization procedure is sufficient for the present case, since only a single minimum exists for the linear Voigt-Kelvin approach.

(a)

(b)
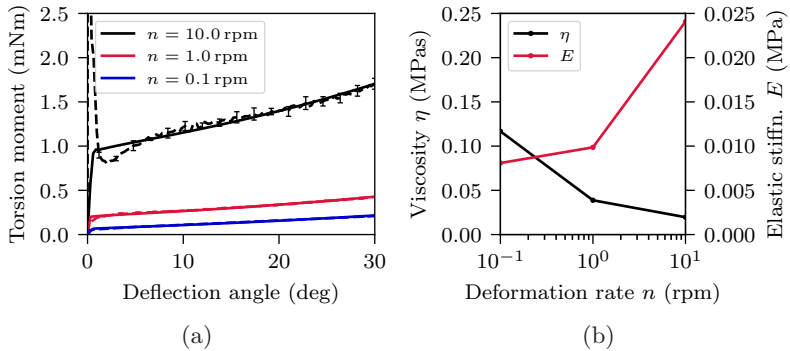
Figure 3.13: Membrane parametrization results for the linear Voigt-Kelvin approach fitted separately to each deformation rate n at 270 °C (a) and variation of the according material parameters w.r.t. the deformation rate n (b).

The parametrization results in Figure 3.13 reveal that both, the elastic stiffness E and the viscosity η, vary w.r.t. deformation rate n. The elastic stiffness increases, whereas the viscosity decreases for higher deformation rates. The latter is denoted as shear thinning behavior, which is a well-known phenomena for polymer liquids [248]. The relative change of the elastic stiffness and the viscosity is comparable, whereas the absolute change is one order of magnitude higher for the viscosity. In summary, a linear Voigt-Kelvin approach is not suffi-

cient for modeling rate-dependent shear behavior, since the material parameters depend on the deformation rate n.

Nonlinear Voigt-Kelvin approach   To consider the dependency of shear behavior on the deformation rate, the Cross model (cf. Equation 3.41) is applied. The elastic stiffness, on the contrary, is kept constant, since a comparably lower variation w.r.t. the deformation rate n is observed.

It is to be noted that no unambiguous solution (minimum) exists for the Cross model, since a multitude of parameters describe the same shear response in the characterized range of deformation rates. Special attention needs to paid for extrapolation outside the characterized range. As remedy, the gradient-based optimization scheme presented by Nelder-Mead [247] is applied in combination with starting values determined by a manual correlation of the Cross model to the viscosities η determined by means of the linear Voigt-Kelvin for each deformation rate n.
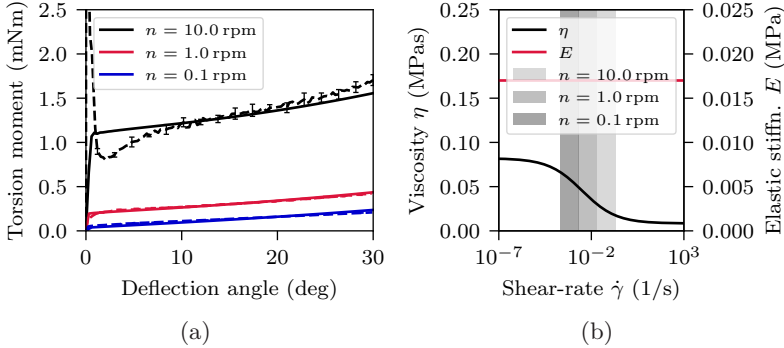
Figure 3.14: Membrane parameterization results for the nonlinear Voigt-Kelvin approach at $270\,^{\circ}$C with constant elastic stiffness E and nonlinear viscosity η (Cross model) (a) and variation of the according material parameters w.r.t. shear-rate $\dot{\gamma}$ (b).

The parametrization results in Figure 3.14 reveal that the nonlinear Voigt-Kelvin approach leads to a constant slope for each deformation rate, which is determined by the constant elastic stiffness E. Moreover, a constant offset between the curves is predicted, which is

induced by the viscosity η and the related Cross model. The according evolution of the material parameters over the shear-rate $\dot{\gamma}$ as well as the characterized shear-rate regions for the different deformation rates n are shown in Figure 3.14(b), which reveal that an unreasonable extrapolation of the viscosity is circumvented by the determined parameter set. In summary, the proposed nonlinear Voigt-Kelvin approach is capable to approximately describe the shear characteristic, where small deviations are observed solely for the high deformation rate ($n = 10\,\text{rpm}$).

3.4.2 Bending behavior

The rheometer bending test is modeled in an FEA to inversely identify the material parameters for bending behavior. An exemplary FEA result is shown in Figure 3.15.

(a) Undeformed   (b) Deformed
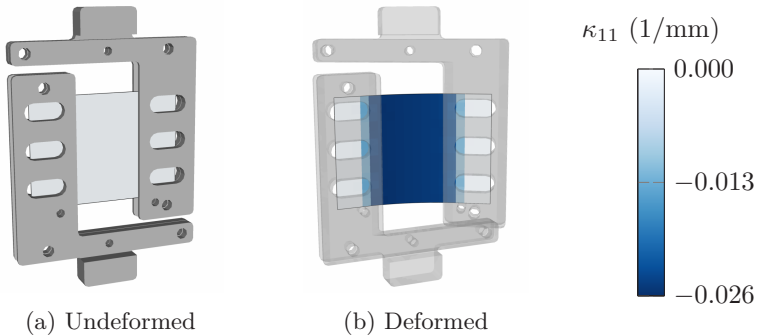
Figure 3.15: Exemplary FEA result of the rheometer bending test for the curvature κ_{11} in bending direction: Undeformed configuration (a) and deformed configuration at $30\,\text{deg}$ deflection (b).

The fixtures are modeled in the FEA as rigid and discrete surfaces and the specimen by superimposed quadrilateral membrane (M3D4R) and shell elements (S4R) for decoupling of membrane and bending behavior by the approach presented in Section 3.1. Reduced integration is applied for numerical efficiency. Membrane behavior is modeled for simplicity by an equivalent elastic approach, since only the fiber stiffness in bending direction influences the analysis. In contrast, material

115

modeling for bending behavior is varied, following either a purely elastic, a Voigt-Kelvin or a generalized Maxwell approach. The according constitutive equations are implemented in a user-defined shell section integration (UGENS). Implicit time integration is chosen for numerical efficiency, since the characterization tests last up to 50 s.

It is to be noted that only longitudinal bending behavior is parameterized, since characterization in transversal direction is unfortunately not possible with this characterization setup (cf. Section 2.3.3). Therefore, a knockdown factor of 100 is assumed for bending behavior in transversal direction.

Elastic approach Two different scenarios are considered for the purely elastic approach. First, the optimization procedure presented by Nelder and Mead [247] is applied to determine a "best-fit" for all of the considered deformation rates. Second, the elastic stiffness is fitted to the average "initial stiffness" at low deflection angles.
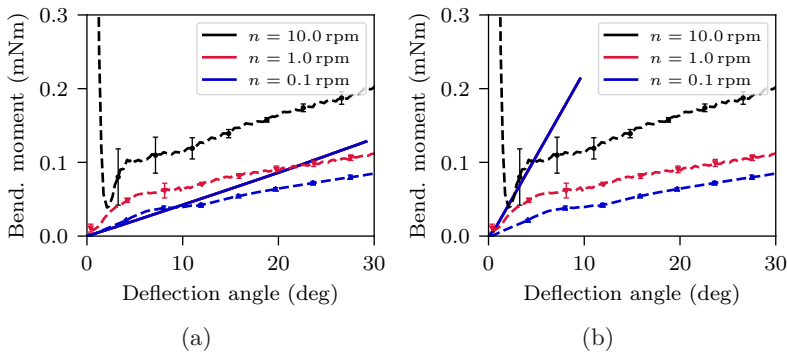
Figure 3.16: Parameterization results for the purely elastic approach at 270 °C fitted to all deformation rates n: "best-fit" result from the optimization procedure (a) and fitting to the average "initial stiffness" (b).

The parametrization results in Figure 3.16 show a linear relation between bending moment and deflection angle for the purely elastic approach. Hence, the bending characteristic observed in the rheometer bending test is not describable by a purely elastic approach, since the rate-dependency as well as the nonlinear evolution of the bending moment over the deflection angle cannot be captured.

116

Linear Voigt-Kelvin approach Following a linear Voigt-Kelvin approach with constant elastic stiffness E and constant viscosity η, each of the considered deformation rates n is fitted separately. This enables to investigate the variation of the material parameters w.r.t. the deformation rate. The according parameters are determined by the optimization procedure presented by Nelder and Mead [247].
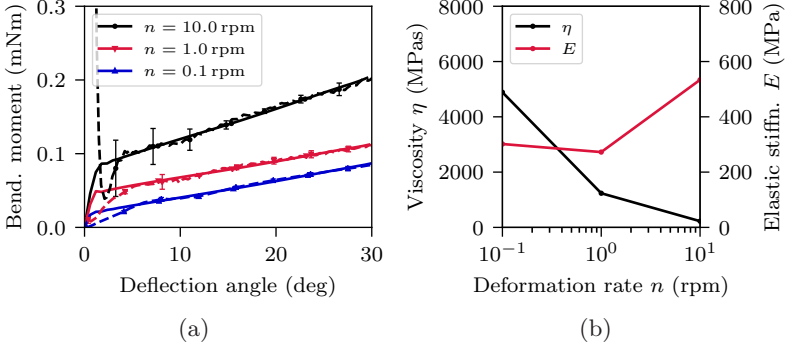
Figure 3.17: Bending parametrization results for the linear Voigt-Kelvin approach fitted separately to each deformation rate n at $270\,°\text{C}$ (a) and variation of the according material parameters w.r.t. the deformation rate n (b).

The parametrization results shown in Figure 3.17 reveal that both, the elastic stiffness E and the viscosity η vary with the considered deformation rates. The elastic stiffness mostly increases, whereas the viscosity decreases with increasing deformation rate. The latter is denoted as shear thinning behavior, which is a well-known phenomena for polymer liquids [248].

Nonlinear Voigt-Kelvin approach To consider the dependency of bending behavior on the deformation rate, the Cross model (cf. Equation 3.41) is applied to describe the viscosity η depending on the shear-rate ($\dot{\gamma}_{\text{bend}} = \sqrt{2\boldsymbol{D} : \boldsymbol{D}}$), which is denoted in the following as bending-rate, to circumvent confusions. On the contrary, the elastic stiffness E is kept constant, since a comparably lower variation w.r.t. the deformation rate n is observed. In analogy to the membrane parameterization, the gradient-based optimization scheme presented

117

by Nelder-Mead [247] is applied in combination with manually determined starting values, to prevent an unreasonable extrapolation of the viscosity.
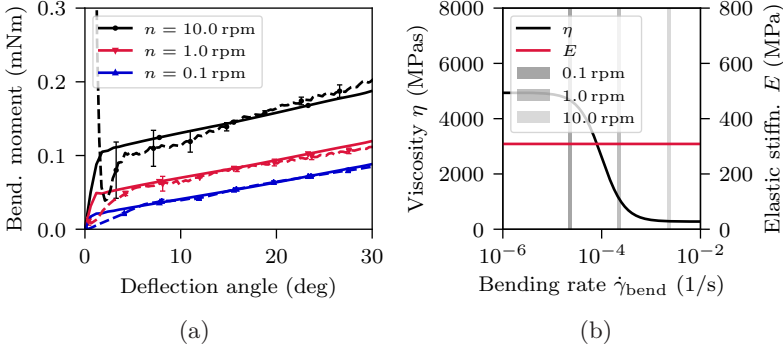
Figure 3.18: Bending parameterization results for the nonlinear Voigt-Kelvin approach at $270\,°\text{C}$ with constant elastic stiffness E and nonlinear viscosity η (Cross model) (a) and variation of the according material parameters w.r.t. bending-rate $\dot{\gamma}_{\text{bend}}$ (b).

The parametrization results in Figure 3.18(a) reveal that the elastic stiffness E determines the slope of the curves and the viscosity η the constant offset between the curves. Figure 3.18(b) shows the evolution of the material parameters over the shear-rate as well as the characterized regions for the different deformation rates, which reveals that an unreasonable extrapolation for the viscosity is prevented. Moreover, approximately constant bending-rates $\dot{\gamma}_{\text{bend}}$ are observed for each deformation rate n. In summary, the nonlinear Voigt-Kelvin approach is capable to approximately describe the bending characteristic at $270\,°\text{C}$. A good agreement is observed for the lower deformation rates, whereas deviations are observed for the highest deformation rate ($n = 10\,\text{rpm}$).

Nonlinear generalized Maxwell approach   A single spring-element in parallel with two nonlinear Maxwell elements are applied for the generalized Maxwell approach, since this number of Maxwell elements has proven to be sufficient for bending modeling. The nonlinear Maxwell elements consist of a linear spring and a nonlinear dashpot

element with a hyperbolic sine law to describe the nonlinear viscous behavior (cf. Equation 3.52). A two-step procedure is applied for parameter identification. Initially, the covariance matrix adaption evolution strategy (CMA-ES) introduced by Hansen and Ostermeier [249] is applied. This approach is chosen, since in contrast to the nonlinear Voigt-Kelvin approach, an educated guess for the initial parameter values necessary for a gradient-based optimization procedure is not possible for nonlinear generalized Maxwell approach. Therefore, a global optimization procedure, such as the CMA-ES algorithm, is necessary. Since a large number of evaluations is necessary for this optimization procedure, a substitute model is applied for evaluation of the target function (cf. Equation 3.55) rather than an FEA. This substitute model is based on the homogeneous curvature distribution in the specimen (cf. Figure 3.15), which enables to approximate the bending moment by means of a single material point by

$$\hat{M}(\boldsymbol{\kappa}) \approx H \int_t \boldsymbol{\sigma}(z\,\kappa_{11}\boldsymbol{e}_1 \otimes \boldsymbol{e}_1)\,\mathrm{d}z, \qquad (3.56)$$

where H is the height and t the thickness of the specimen, κ_{11} the curvature at the considered material point in bending direction $\boldsymbol{e}_1$ and $\boldsymbol{\sigma}$ the Cauchy stress tensor resulting from the evaluation of the according constitutive equation. Based on this, the bending moment can be approximated efficiently by a single material point by means of the curvature history $\kappa_{11}(t)$ determined by an FEA.

Subsequently, the parameters determined by the CMA-ES are used as initial values for the gradient-based optimization procedure presented by Nelder and Mead [247] in combination with an FEA. Based on this two-step procedure, an efficient global optimization is enabled.

The parametrization results obtained from the final FEA are shown in Figure 3.19. A good agreement between FEA and experimental characterization results is obtained by the generalized Maxwell approach. The slope of the moment deflection curves varying with the deformation is captured. Moreover, also the starting behavior is modeled accurately by the generalized Maxwell approach. Therefore, an improved agreement is observed for the generalized Maxwell approach compared to the results obtained from the nonlinear Voigt-Kelvin approach.
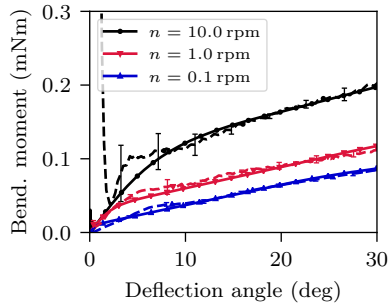
Figure 3.19: Bending parameterization results for the nonlinear generalized Maxwell approach ($N = 2$) at 270 °C with constant elastic stiffness E and a hyperbolic sine law to describe viscous behavior.

Extrapolation behavior of the rate-dependent approaches Thermoforming might be accompanied with bending deformation rates higher than the deformation rates considered in bending characterization. Therefore, extrapolation behavior of the rate-dependent bending modeling approach, namely the nonlinear Voigt-Kelvin and the generalized Maxwell approach, is investigated in a virtual study. For this purpose, two deformation higher than the maximum possible deformation rate of the rheometer bending test ($n = 10$ rpm) are investigated. The results are shown in Figure 3.20.
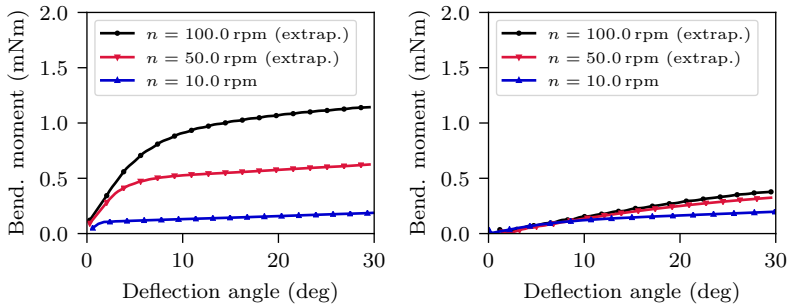
Figure 3.20: Extrapolation of bending behavior for higher deformation rates n for the nonlinear Voigt-Kelvin approach (a) and the generalized Maxwell approach ($N = 2$) at 270 °C.

The results reveal that the two bending modeling approach extrapolate rate-dependency completely different. Distinctively higher bending moments are observed for the nonlinear Voigt-Kelvin approach compared to the generalized Maxwell approach. The different extrapolation behavior results from the different arrangement of elastic and viscous elements of the according modeling approaches. For the Voigt-Kelvin approach, the higher deformation rate directly acts on the viscous element (cf. Figure 3.11(b)), which therefore induces a constant offset between the curves determined by the deformation rate. On the contrary, bending stiffness is running into a maximum for the generalized Maxwell approach. Higher deformation rates stiffen the viscous elements. Therefore, the resulting bending stiffness is determined by the elastic elements (cf. Figure 3.11(a)), which are not influenced by deformation rate.

3.5 Isothermal forming simulation

The intra-ply modeling approaches presented above are applied in combination with the inter-ply modeling approaches presented in Chapter 5 to isothermal thermoforming simulation in the scope of this section. Two perspectives are pursued. First, the forming simulation approach presented in this chapter is validated, based on the comparison of the forming simulation results to experimental tests. Second, the necessity to account for rate-dependent bending behavior in forming simulation is investigated. For this purpose, the bending modeling approaches are varied, while the membrane and inter-ply modeling approaches remain unchanged.

For forming simulation, explicit time integration is applied in real time, to accurately account for rate-dependency. The parameterization at $270\,°C$ is applied, which is close to the initial laminate temperature usually adopted for the investigated material in thermoforming processes. Initially, the hemisphere test proposed by Haanappel [57] is investigated in Section 3.5.1 as directly amenable and virtual study. Subsequently, the complexly shaped geometry also adopted for the experimental forming tests presented in Chapter 2 is investigated in Section 3.5.2, including the comparison of forming simulation results to experimental tests for validation.

3.5.1 Virtual hemisphere test

The hemisphere with a radius of 125 mm and a height of approximately 40 mm is formed with a constant velocity of 50 mm/s, which is in the order of magnitude usually applied in thermoforming processes. Forming simulation is conducted without gravity and gripper loading, to exclude any influence of additional boundary conditions. Three different layups are considered for this virtual study: A biaxial $[0; 90; 90; 0]$, a triaxial $[0; -45; +45; 0]$ and a quasi-isotropic $[0; -45; +45; 90]$ layup. These layups are chosen, since an increase of wrinkling tendency is expected for the increasing number of fiber families [119]. Each of the single plies is modeled by separate element layers with 50,643 triangular elements per layer.

Layup variation Figure 3.21 shows a comparison of the forming simulation results obtained for the different layups with the nonlinear Voigt-Kelvin for modeling both, membrane and bending behavior, at several remaining tool travels Δz. The forming simulation results reveal the expected forming behavior regarding the increasing wrinkling tendency for an increasing number of fiber families. Smooth in-plane shear deformation and no wrinkles are observed for the biaxial layup, which is ascribable to "pure shear" deformation of the laminate without pronounced inter-ply slip. In contrast, the onset (Stage 1), evolution (Stage 2 and 3) and flattening (Stage 4) of wrinkling is observed for the triaxial and the quasi-isotropic layup, where even more pronounced wrinkling is observed for the quasi-isotropic layup. Thereby, wrinkling is double-symmetric for the quasi-isotropic layup, whereas pronounced wrinkling in 90 deg direction is observed for the triaxial layup, which is the bending compliant direction for this layup. To the end of forming, wrinkles are either folded or flattened. The latter enforces in-plane shear deformation, which is expressed in forming simulation results by localized excessive shearing.

Stage 1: $\Delta z \approx 30\,\mathrm{mm}$

Stage 2: $\Delta z \approx 20\,\mathrm{mm}$

Stage 3: $\Delta z \approx 10\,\mathrm{mm}$

Stage 4: $\Delta z \approx 0\,\mathrm{mm}$

Orthotr.	**Triaxial**	**QI**
$[0; 90; 90; 0]$	$[0; -45; +45; 0]$	$[0; -45; +45; 90]$

$E_{12}\ (-)$

$-0.15 \qquad 0.00 \qquad 0.15$
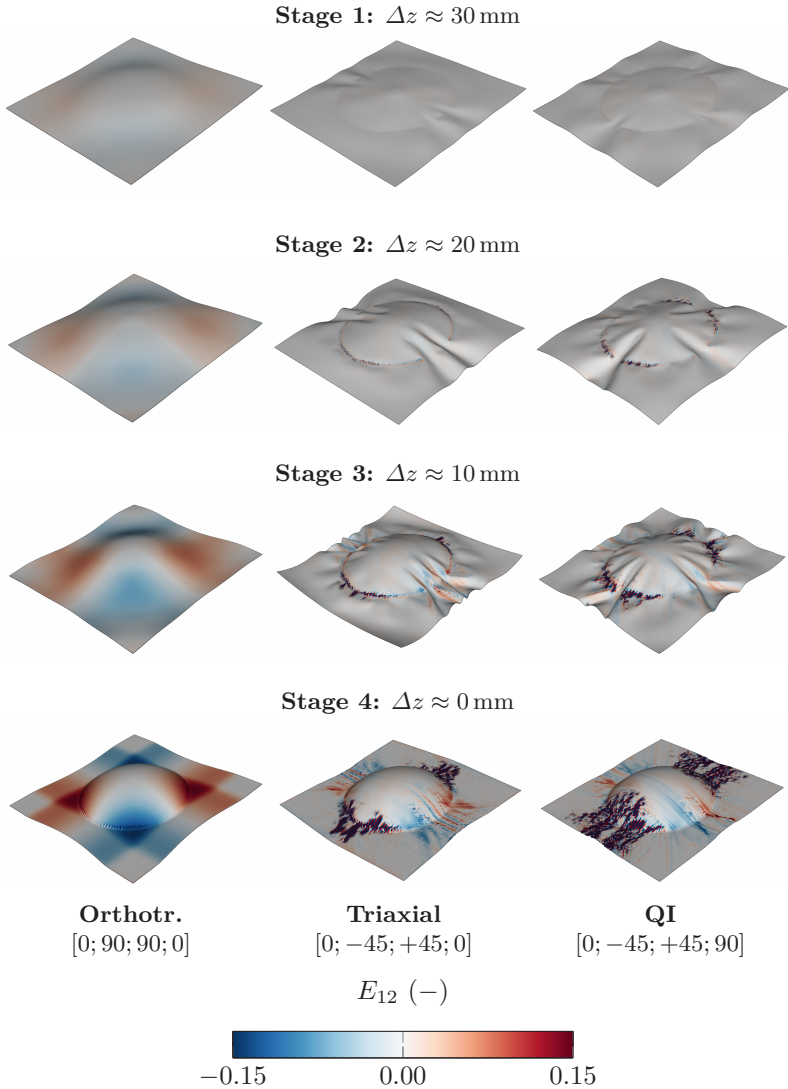
Figure 3.21: Hemisphere forming simulation results for different layups at several remaining tool travels Δz for the Green-Lagrange shear strain E_{12} under application of the nonlinear Voigt-Kelvin approach for intra-ply modeling.

Figure 3.22 shows the evolution of the observed modified mean curvature $\bar{\kappa}^{\mathrm{el}}$ and bending-rate $\dot{\gamma}_{\mathrm{bend}}$ by means of the median, lower $(25\,\%)$ and upper $(75\,\%)$ quantile for the different layups. Moreover, also the corresponding maximum values considered in bending characterization are shown. Regarding the evolution of the curvature, a smooth increase until a maximum, followed by a steep decrease due to the flattening of the laminate to the end of forming is observed for the orthotropic layup. In contrast, a distinct increase of curvature is observed for the triaxial and the quasi-isotropic due to the onset of wrinkling at a remaining tool travel of approximately $30\,\mathrm{mm}$ (cf. Figure 3.21 - Stage 1). This induces also a peak in the bending rate $\dot{\gamma}_{\mathrm{bend}}$, which increases monotonously in the further course of forming. In summary, curvatures mostly within the characterized range are observed, whereas bending rates within the characterized range are only observed at the beginning of forming. To the end of forming, bending rates one order of magnitude higher than the maximum characterized value are observed.

(a) (b)
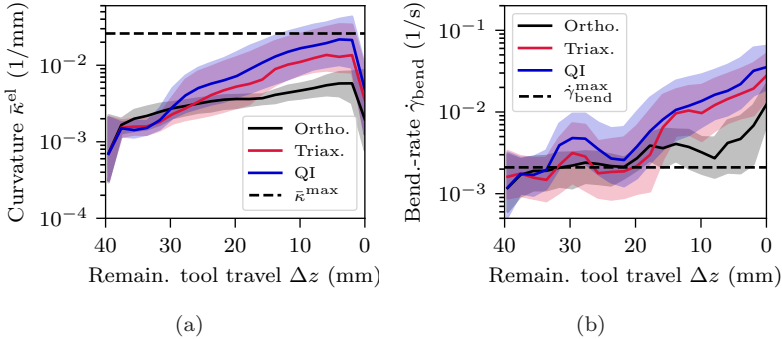
Figure 3.22: Evolution of the median, lower $(25\,\%)$ and upper $(75\,\%)$ quantile for the elemental modified mean curvature $\bar{\kappa}^{\mathrm{el}}$ (a) and the bending-rate $\dot{\gamma}_{\mathrm{bend}}$ (b) observed during forming simulation, as well as the related maximum values, κ_{max} and $\dot{\gamma}_{\mathrm{bend}}^{\mathrm{max}}$, considered in bending characterization.

Variation of bending modeling approaches   The different bending modeling approaches (cf. Section 3.3.2) and according parameterizations (cf. Section 3.4.2) are varied for the hemisphere test, while membrane and inter-ply modeling remain unchanged. Based on this, the influence of the different bending modeling approaches on formability prediction is investigated for the different layups. For this purpose, the elemental modified curvature $\bar{\kappa}^{\text{el}}$ (cf. Section 2.1.2) is determined for a remaining tool travel of approximately 4 mm and 2 mm, which reveals forming stages in which the wrinkles are fully shaped. The according results are shown in Figure 3.23 and 3.24.

The results reveal that the increase in wrinkling behavior with increasing number of fiber orientations is predicted by all of the bending modeling approaches. In comparison, mostly no influence of the bending modeling approach on formability prediction is observed for the orthotropic layup, except for the elastic "best-fit", which predicts some localized curvatures towards the edges in 45 deg direction, which is the bending compliant direction for the orthotropic layup. These local curvatures, however, are influenced by bending oscillations when the laminate touches the lower tool, due to the purely elastic behavior with a low bending modulus, rather than exceeding the forming limit. For the triaxial and quasi-isotropic layup, in contrast, a clear influence of the bending modeling approaches on wrinkling prediction is observed. The least wrinkling is observed for the nonlinear Voigt-Kelvin approach, which is followed with similar but slightly increased wrinkling behavior by the elastic approach fitted to the "initial stiffness" and the "generalized Maxwell approach". On the contrary, distinctively pronounced wrinkling behavior is observed for the elastic "best-fit" approach.

Nonlinear Voigt-Kelvin

Nonlinear generalized Maxwell

Elastic "initial stiffness"

Elastic "best-fit"

Orthotr.	**Triaxial**	**QI**
$[0; 90; 90; 0]$	$[0; -45; +45; 0]$	$[0; -45; +45; 90]$

$\bar{\kappa}^{\mathrm{el}}\ (\mathrm{mm}^{-1})$
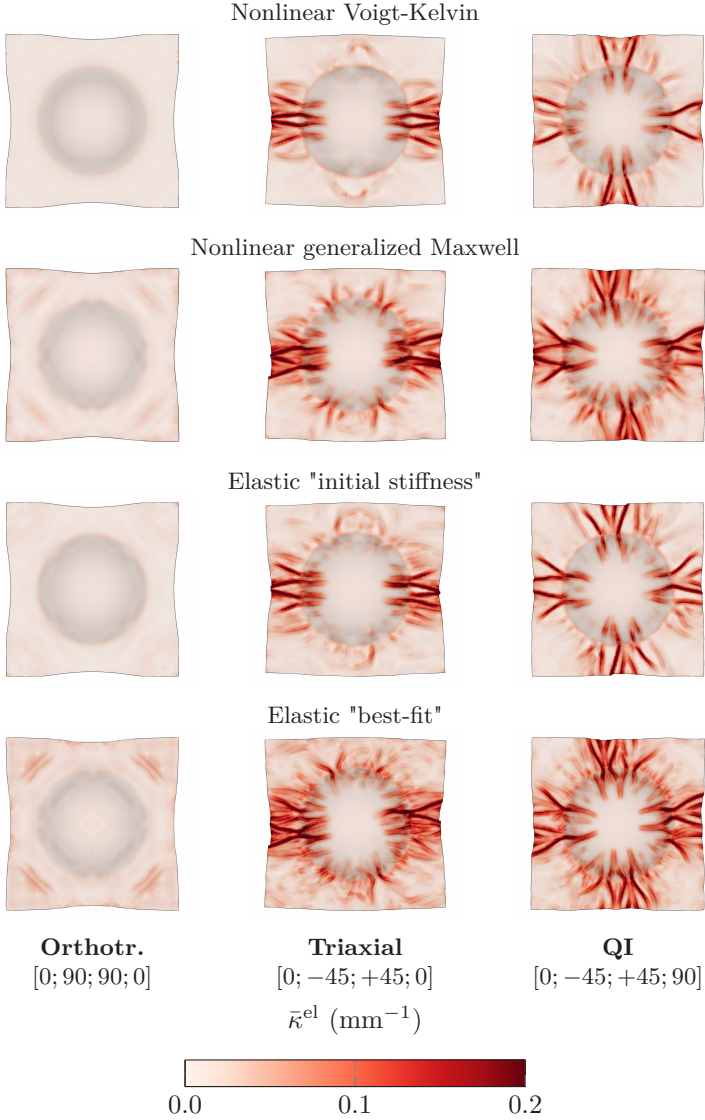
Figure 3.23: Hemisphere forming simulation result for different layups and a remaining tool travel of approximately $4\,\mathrm{mm}$ under variation of the bending modeling approaches.
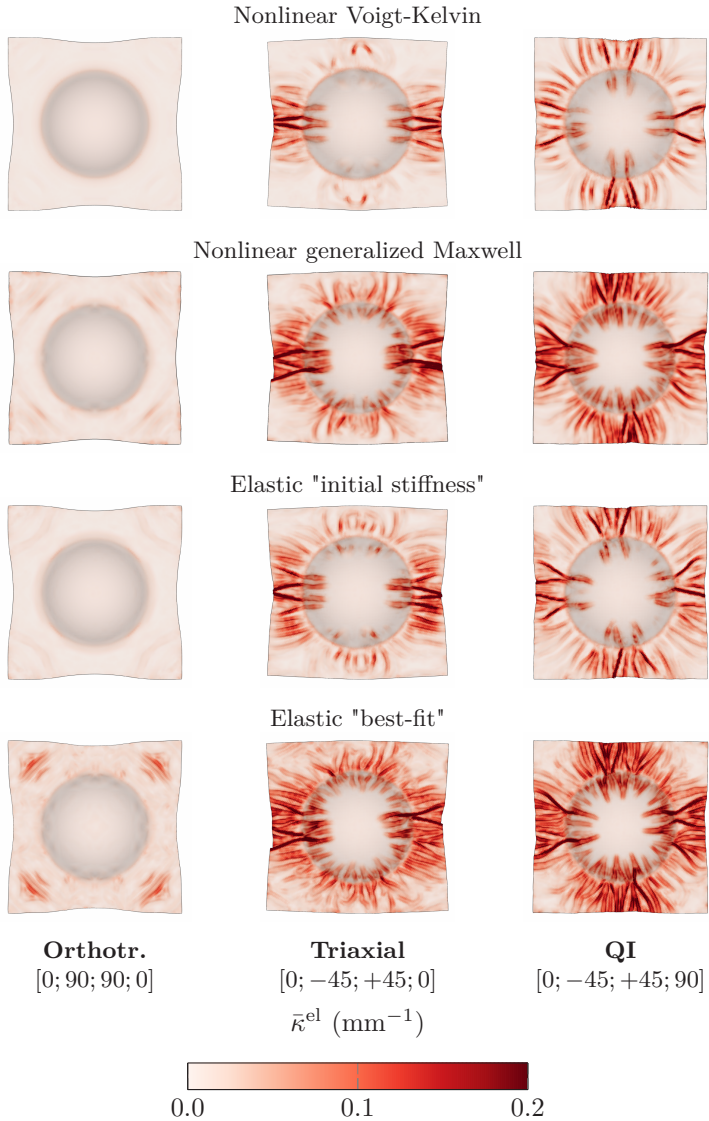
Figure 3.24: Hemisphere forming simulation result for different layups and a remaining tool travel of approximately 2 mm under variation of the bending modeling approaches.

3.5.2 Validation for complexly shaped geometry

The generic geometry and related process setup presented in Section 2.2.1 is applied as complexly shaped geometry and for validation to forming simulation. Two different layups are considered, which namely are an orthotropic layup ($[0; 90]_{2s}$) and a quasi-isotropic layup ($[0; -45; 90; +45]_s$), in analogy to the experimental tests. In the scope of this chapter, the intermediate process settings (cf. Table 2.1) are adopted. Each of the 8 single plies is modeled by means of separate element layers with 42,672 triangular elements per layer. The tool kinematics is modeled by a displacement boundary condition in real time, to accurately account for the rate-dependent forming behavior.
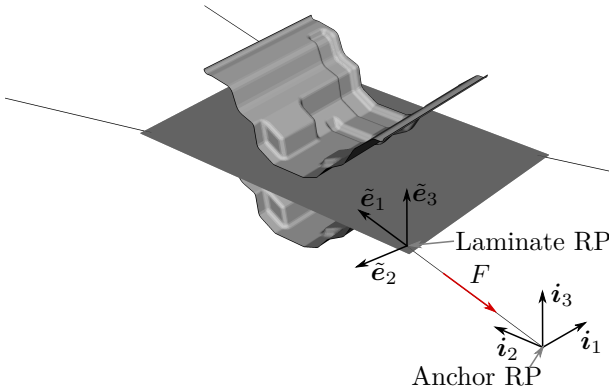
Figure 3.25: Forming simulation setup for the complexly shaped geometry and exemplary illustration of the global system $\boldsymbol{i}_i$ and local gripper reference frame $\tilde{\boldsymbol{e}}_i$ to model the gripping force F and its kinematics.

Regarding laminate gripping, it has to be considered that the pneumatic needle grippers, which are mounted on a spatially moving transport frame, can elongate in axial direction and rotate about the vertical axis at the fixation on the transport frame. Additionally, the transport frame is lowered in vertical direction after positioning over the mold in the horizontal plane and prior to forming. To account for this boundary conditions and kinematics, the gripper modeling approach proposed by Poppe et al. [250], which is based on the application of

in Abaqus called connector elements [242], is used. The approach applied for the complexly shaped geometry is illustrated in Figure 3.25. A laminate reference point (Laminate RP), onto which the nodes of the laminate in the gripped area are kinematically coupled, as well as a reference point representing the fixation of the gripper on the transport frame, the so-called anchor reference point (Anchor RP), are introduced. These two reference points are connected by a hinge element and a translator element, to account for the gripper kinematics. The latter introduces a local gripper reference frame $\tilde{\boldsymbol{e}}_i$, additionally to the spatially fixed frame $\boldsymbol{i}_i$. This enables to assign the experimentally determined gripping force F in the accurate direction throughout forming. Also the elongation of the gripper in axial direction $\tilde{\boldsymbol{e}}_1$ and the rotation about the vertical axis $\tilde{\boldsymbol{e}}_3$ at the laminate gripping point is accounted for. Moreover, the rotation about the vertical axis $\boldsymbol{i}_3$ at the anchor reference point as well as the moving transport frame is introduced by according boundary conditions at the anchor reference point. Besides gripper modeling, also gravity loading is considered as additional boundary condition.

In the following, forming simulation results for the complexly shaped geometry are investigated and compared to experimental forming tests for the intermediate process parameter settings (cf. Table 2.1). It is to be noted that forming simulation is isothermal in the scope of this chapter. Therefore, thermomechanical effects are not captured.

Validation orthotropic layup   Figure 3.26 shows the comparison of forming simulation to the experimental test for the orthotropic layup and the fully formed part, under application of the Voigt-Kelvin approach for bending modeling, by means of the final shape as well as the obtained outer contours. The latter is determined by means of the approach outlined in Section 2.1.1. A high prediction accuracy is observed for the outer contour. This includes the general course of the outer contour as well as the areas of laminate gripping, which reveals that laminate gripping, consisting of load magnitude and kinematics, is well captured. Nonetheless, some slight defects at the transition from the actual part to the outer areas of surplus material are not predicted by simulation. This, however, might also be reducible to

(a) Simulation   (b) Experiment   (c) Contours
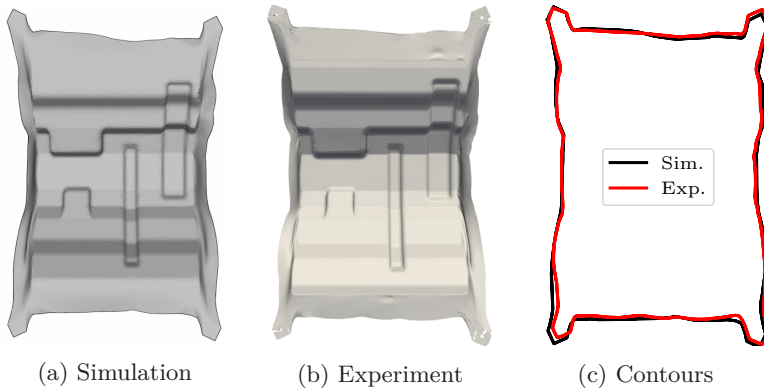
Figure 3.26: Forming simulation result (a), 3D measurement of the experimental test (b) and comparison of the outer contours (c) for the orthotropic layup ($[0; 90]_{2s}$) and fully closed tools.

local disturbances in the material or the process, which cannot be captured by simulation.

Figure 3.27 shows forming results at several remaining tool travels Δz for forming simulation (left) and the related experimental tests (right). The experimental results reveal a mostly good formability of the orthotropic layup, except a material accumulation above the bigger corner bending, which develops to a large fold in the course of forming. Moreover, some localized small wrinkles are observed to the end of forming below and above the corner bendings as well as around the beads. The comparison of forming simulation, under the application of the Voigt-Kelvin approach for bending modeling, to the related experimental tests reveals that the general formability and the outer contour are predicted in a good agreement. The material accumulations above the bigger corner bending becomes slightly apparent, but is predicted less pronounced as observed in the experimental tests. Beyond that, local wrinkling to the end of forming (Stage 3) is predicted too less pronounced as observed in the experimental tests.

Stage 1: $\Delta z = 30\,\text{mm}$

Stage 2: $\Delta z = 17.5\,\text{mm}$

Stage 3: $\Delta z = 5\,\text{mm}$
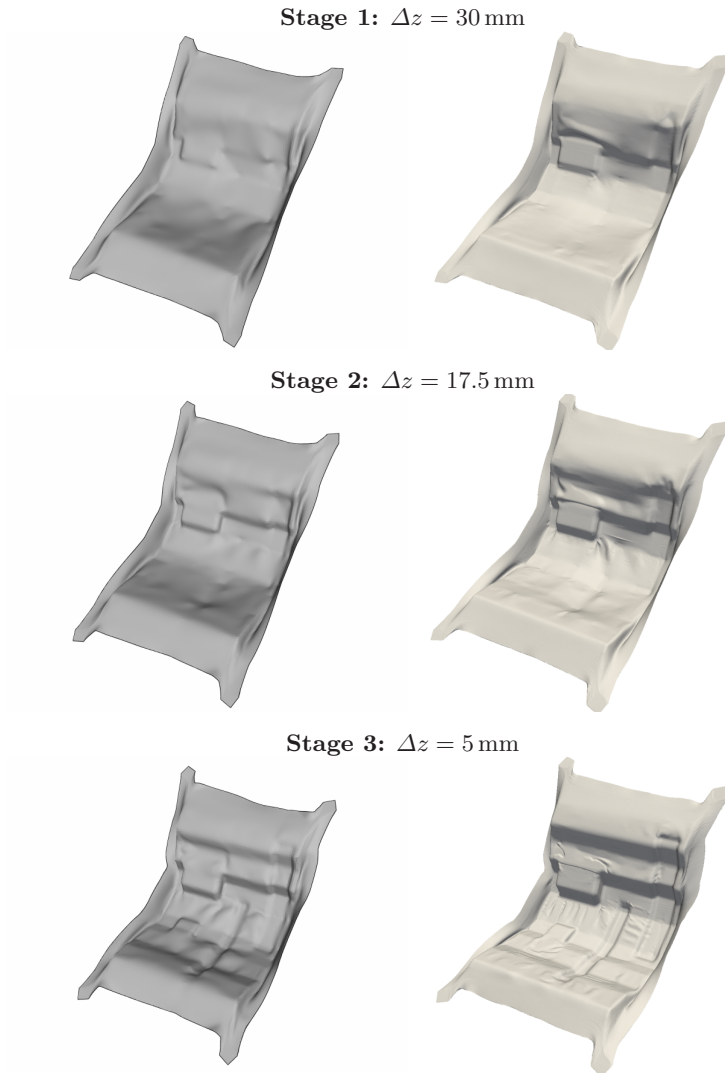
Figure 3.27: Comparison of forming simulation (left) to 3D measurements of experimental tests (right) for the orthotropic layup ($[0; 90]_{2\text{s}}$) at several remaining tool travels Δz.

Validation quasi-isotropic layup   Figure 3.28 shows the comparison of forming simulation to the experimental test for the quasi-isotropic layup and the fully formed part, under application of the Voigt-Kelvin approach for bending modeling, by means of the final shape as well as the obtained outer contours. A general good agreement between forming simulation and experimental test is observed. This is valid for wrinkling at the outer areas as well as for the outer contour. Nonetheless, some deviations are observed for the outer contour at the lower end of the part, which is reducible to slight deviations for wrinkling and the sag of the laminate due to gravity loading. Additionally, the gripping area at the upper right corner rotates slightly in forming simulation, which is not observed in the experimental test.

Figure 3.29 shows the forming results at several remaining tool travels for forming simulation (left) and the experimental tests (right). The experimental results reveal a distinctively limited formability of the quasi-isotropic layup, which is expressed by distinct wrinkling of the laminate. This behavior is reflected by forming simulation, where the general amount, position and direction of wrinkles are well captured. Besides this, also the sag of the laminate due to gravity loading is well predicted, especially for Stage 1 and 3. In Stage 2, the sag is slightly over-predicted, which yields a slightly different unfolding in the up-

| (a) Simulation | (b) Experiment | (c) Contours |
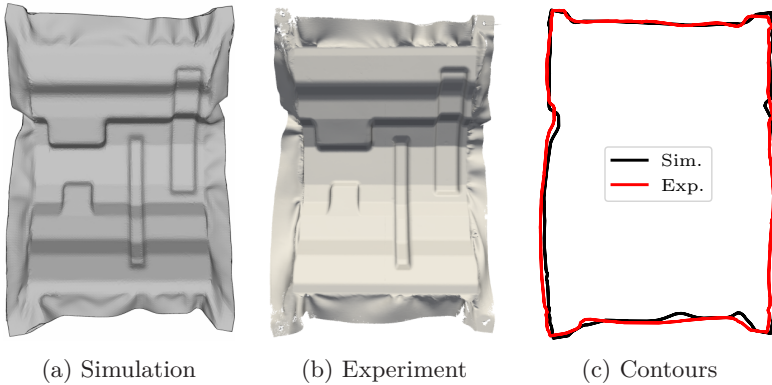
Figure 3.28: Forming simulation result (a), 3D measurement of the experimental test (b) and comparison of the outer contours (c) for the quasi-isotropic layup ($[0; -45; 90; 45]_\mathrm{s}$) and fully closed tools.

Stage 1: $\Delta z = 30\,\text{mm}$
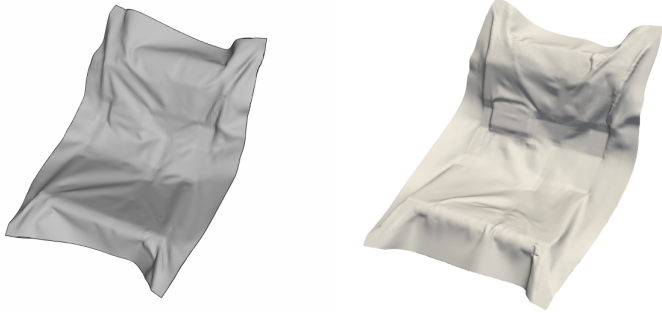
Stage 2: $\Delta z = 17.5\,\text{mm}$
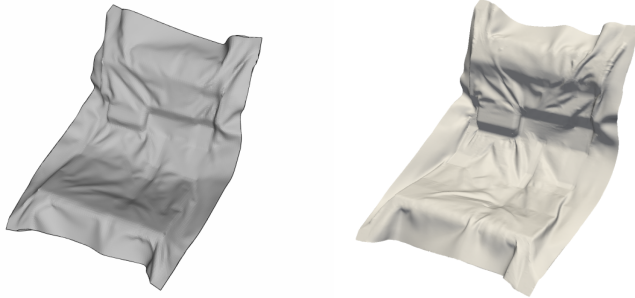
Stage 3: $\Delta z = 5\,\text{mm}$
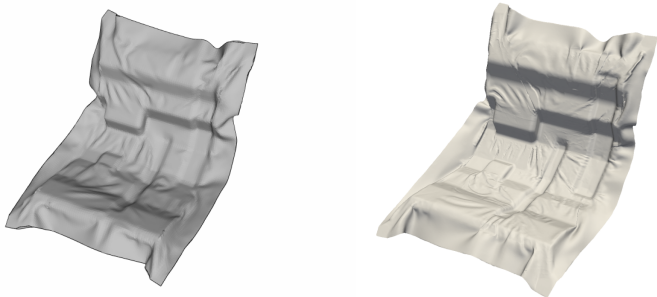
Figure 3.29: Comparison of forming simulation (left) to 3D measurements of experimental tests (right) for the quasi-isotropic layup $([0; -45; 90; 45]_\text{s})$ at several remaining tool travels Δz.

per outer area. Moreover, wrinkling behavior seems to be predicted slightly too less pronounced as observed in the experimental tests. Especially in Stage 3, some small wrinkles are observed in the experimental test e.g. around the beads, which are not clearly reflected by forming simulation.

Variation of bending modeling approaches Finally, the bending modeling approaches are varied for the orthotropic and the quasi-isotropic layup, while membrane and inter-ply modeling remain unchanged, in analogy to the related investigation on the hemisphere test in the previous section. Figure 3.30 shows the comparison of the obtained forming simulation results to the according experimental test for the orthotropic layup and the elemental modified mean curvature $\bar{\kappa}^{\text{el}}$ at a remaining tool travel of 5 mm. This configuration is chosen, to investigate the influence of the different bending modeling approaches on wrinkling behavior.

Almost no difference between the Voigt-Kelvin, the generalized Maxwell and the elastic approach fitted to the "initial stiffness" is observed. In contrast, slightly more pronounced wrinkling the bigger corner bending as well as around the beads is predicted by the elastic approach and the "best-fit" parameterization. More pronounced wrinkling behavior is also observed in experimental tests. Nonetheless, the large fold above the bigger corner bending is not predicted by any of the bending modeling approaches.

Figure 3.31 shows the results under variation of the bending modeling approaches for the quasi-isotropic layup. The pronounced wrinkling behavior observed for the quasi-isotropic layup is predicted by all of the approaches. Again, similar results are obtained for the Voigt-Kelvin, the generalized Maxwell and the Elastic approach fitted to the "initial stiffness". A more pronounced sag of the laminate in the outer areas due to gravity loading is observed for the elastic "best-fit" approach. Moreover and in analogy to the orthotropic layup, more pronounced wrinkling behavior is predicted, where more pronounced wrinkling behavior is also observed in the experimental test.

Experimental

Voigt-Kelvin   **Generalized Maxwell**

Elastic "initial stiffness"   **Elastic "best-fit"**

$\bar{\kappa}^{\mathrm{el}}$ (mm^{-1})

0.0   0.1   0.2
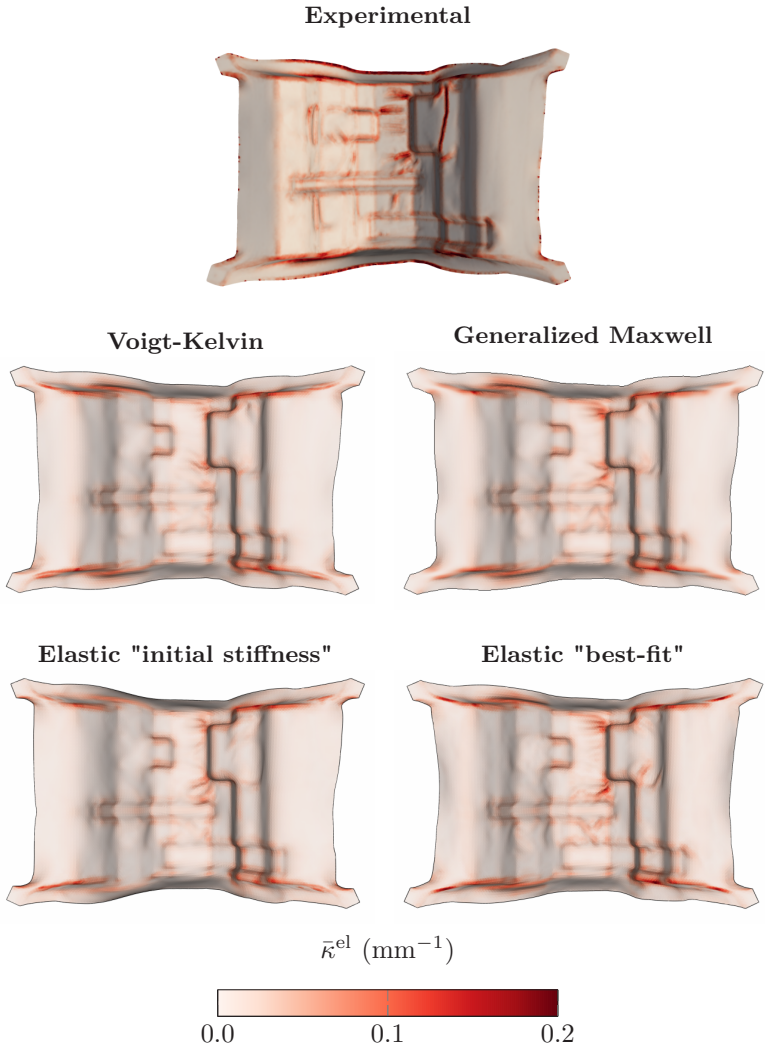
Figure 3.30: Forming simulation results under variation of the bending model-
ing approaches and comparison the the experimental test for the
orthotropic layup ($[0; 90]_{2\mathrm{s}}$) at a remaining tool travel of 5 mm.

Experimental

Voigt-Kelvin   **Generalized Maxwell**

Elastic "initial stiffness"   **Elastic "best-fit"**

$\bar{\kappa}^{\mathrm{el}} \ (\mathrm{mm}^{-1})$

0.0   0.1   0.2
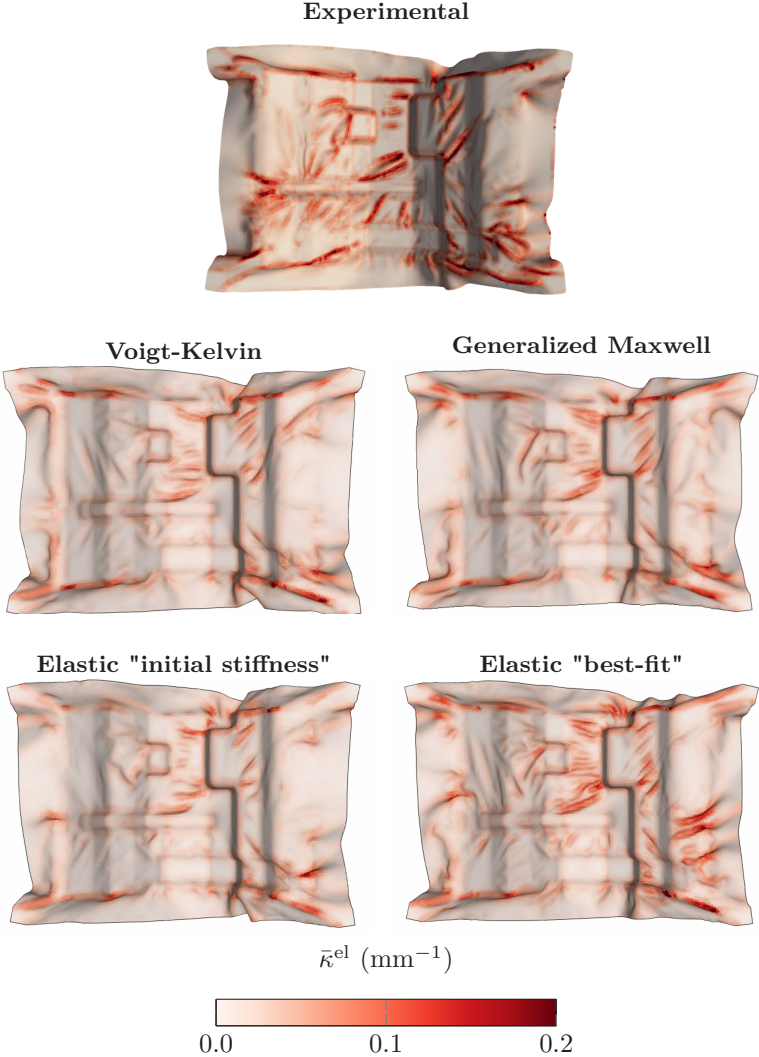
Figure 3.31: Forming simulation results under variation of the bending modeling approaches and comparison the the experimental test for the quasi-isotropic layup ($[0; -45; 90; 45]_{\mathrm{s}}$) at a remaining tool travel of 5 mm.

3.6 Discussion and conclusion

Intra-ply modeling approaches for isothermal thermoforming simulation based on superimposed elements, and using the commercial FE solver Abaqus in combination with several user-subroutines are presented and investigated in the scope of this chapter.

Membrane and bending decoupling Initially, the restrictions of Abaqus following built-in modeling approaches for the decoupling of membrane and bending behavior are outlined. In the context of decoupled bending behavior, it is to be noted that only physical linear bending behavior can be modeled based on Abaqus built-in approaches. Moreover, the rotation of the principal material directions due to large shear deformation cannot be captured accurately. Therefore, either approximate isotropic bending properties or anisotropic bending properties becoming inaccurate under shear deformation can be modeled following Abaqus built-in approaches, and rate-dependency cannot be accounted for.

As remedy, user-defined material modeling (VUMAT) assigned to a membrane element, which is superimposed with a shell element using a user-defined shell section integration (VUGENS), is proposed. This enables to implement accurate material modeling approaches separately for membrane and bending behavior and enables Abaqus to be applied to composite forming simulation in general. Thereby, the proposed framework is not only applicable to thermoforming simulation, but has also been successfully applied in the scope of several studies, including draping simulation of UD-NCF by Schirmaier et al. [24, 73] as well as wet compression molding (WCM) simulation by Poppe et al. [30, 251, 252].

Intra-ply material modeling approaches Based on the proposed framework for intra-ply modeling, a hyperelastic material modeling approach as well as a hypoelastic material modeling approach in combination with a fiber-parallel material frame are presented and investigated. A detailed assessment of the according constitutive equations is provided and both approaches are compared on unit cell level and in virtual bias extension tests. The investigations reveal that the

137

main requirement to accurately capture the rotation of the principal material directions under shear deformation is fulfilled by both approaches. Nonetheless, a major drawback of hypoelastic approaches in combination with a fiber-parallel material frame is revealed, since sufficiently small time increments are necessary to accurately capture the rotation of the principal material directions. This is no issue for explicit time integration, since time increments are intrinsically small. Implicit time integration, however, can go along with large time increments. Based on this, implicit time integration might become favorable for numerical efficiency for inverse material parameter extraction according to characterization tests lasting several seconds or minutes. This applies also for this study. Therefore, the application of hyperelastic material modeling is clearly recommended, since these approaches are accurate for arbitrary time (deformation) step widths. The latter is expected to be also the reason for hyperelastic material modeling in the commercial FE code AniForm [119], which is to the author's knowledge the only available implicit code for composite forming simulation.

Furthermore, finite strain and rate-dependent material modeling approaches for membrane and bending behavior are presented. A nonlinear hyperviscoelastic Voigt-Kelvin approach is presented for membrane modeling, which is similar to that applied by Haanappel et al. [119]. Although a clear recommendation to apply hyperelastic material modeling is given, hypoviscoelastic bending modeling approaches following a nonlinear Voigt-Kelvin and a nonlinear generalized Maxwell approach are presented. The application of a hypoelastic approach for bending modeling is necessary in the scope of the framework presented in this chapter, since the kinematic magnitudes supplied by the user-defined shell section integration (VUGENS) prevent the implementation of hyperelastic approaches. This, however, is no drawback for bending modeling. On the one hand, no rotation of the principal material directions due to shear deformation is observed during bending characterization, which enables large time step widths in inverse parameter identification using implicit time integration. On the other hand, time increments are intrinsically small in thermoforming simulation, where large shear deformation and thus fiber rotation is observed, due to the explicit time integration.

Parameterization The presented hypoviscoelastic bending modeling approaches are successfully parameterized to isothermal bending characterization at $270\,°C$ and several deformation rates. It turns out that only the generalized Maxwell approach in conjunction with a nonlinear viscous behavior is capable to predict the bending characteristic completely. In contrast, the Voigt-Kelvin approach with nonlinear viscous behavior gives only approximate results, but basically captures the observed rate-dependency. On the contrary, the elastic approach is not suitable to describe the complete characteristic observed for the rheometer bending test. The elastic approach may either describe the "initial stiffness", which is caused by the rate-dependent material behavior, or describe the array of different deformation rates via an averaged straight line.

Additionally to the parameterization for different deformation rates, a virtual study on the extrapolation behavior of the hypoviscoelastic bending modeling approaches w.r.t. deformation rate is presented. The generalized Maxwell approach converges in a maximum bending stiffness defined by the elastic elements of the rheological network. On the contrary, the Voigt-Kelvin approach correlates directly the rate of deformation to the bending stiffness, which results in a distinctively higher bending stiffness compared to the generalized Maxwell approach. This behavior could be compensated by adjusting the dependency of the viscosity for high deformation rates of the applied Cross model in terms of η_∞ (cf. Equation 3.41). This, however, would not be subject to an adaption according to material characterization results. Unfortunately, higher deformation rates are not possible in a transient testing procedure using the rheometer bending test. As remedy and for future research, DMA analyses of bending behavior for small deflections could provide a reasonable enhancement of the data basis for parameterization of bending behavior w.r.t. a wide range of deformation rates. Such tests were already considered in experimental investigations by Margossian et al. [75] and Ropers et al. [76].

Regarding membrane behavior, previous studies [57, 119] parameterize shear behavior of thermoplastic UD tapes at process conditions in the small strain regime, where no significant rate-dependency was found and membrane behavior was therefore modeled purely hyperelastic. The parameterization outside the small strain regime pursued in this study, however, reveals a significant rate-dependency, which

is expected to be an important extension of the characterization and parameterization strategy, especially since also for organosheets a distinct rate-dependency of shear behavior is observed in characterization and considered in material modeling outside the small strain regime [57, 119, 134, 156]. Small deviations are observed in parameterization of the nonlinear Voigt-Kelvin approach employed in the scope of this chapter. Therefore, a nonlinear generalized Maxwell approach is presented in the next chapter, to improve the prediction accuracy also for membrane behavior.

Thermoforming simulation   Finally, the presented intra-ply modeling approaches are applied to thermoforming simulation of a hemisphere and a complexly shaped and generic geometry. The hemisphere test is investigated as a purely virtual but directly amenable geometry. On the contrary, the generic geometry is adopted for validation by means of the comparison of the simulation results to experimental tests. For both geometries, an emphasis is laid on the influence of the different bending modeling approaches on wrinkling prediction.
The virtual hemisphere study reveals that modeling of rate-dependent bending behavior is relevant to be considered for thermoforming simulation, since neglecting the rate-dependent material characteristic leads to an increase in the predicted wrinkling behavior. The viscoelastic approaches and the elastic approach fitted to the "initial stiffness" of the rheometer test lead to a similar amount of wrinkles. Nonetheless, slight differences are observed, where slightly less pronounced wrinkling behavior is observed for the nonlinear Voigt-Kelvin approach and slightly more pronounced wrinkling behavior for the generalized Maxwell approach. This behavior can be reduced to the different extrapolation behavior discussed in the context of bending parameterization, since bending rates above the characterized range are observed to a large extend for all layups, whereas curvature remains mostly in the characterized range. This underlines the fact that considering additionally DMA results for bending characterization could be a reasonable enhancement for the bending parameterization strategy. Nonetheless, the onset of wrinkling usually occurs in areas with no or moderate curvatures and curvature rates of the partially formed laminate. Hence, the onset of wrinkling is expected to be

mostly controlled by the "initial bending stiffness" at low curvatures, which is caused by the rate-dependent material characteristic. This behavior is captured by the purely elastic approach fitted to the "initial stiffness", which gives thermoforming results comparable to those obtained by the hypoviscoelastic approaches. Therefore, if only a purely elastic approach is available, a practical solution would be to fit the elastic bending stiffness to the initial stiffness observed in the rheometer bending characterization, rather than using the "best-fit" solution, since the latter yields an overprediction of wrinkling behavior. Besides this, the tendency of a purely elastic approach accompanied with a very low bending stiffness, possibly yielding artificial wrinkling due to bending oscillations, would require special consideration.

In comparison of the simulation results to experimental tests for the complexly shaped geometry, in general a good agreement is observed. This is valid for material accumulations and the outer contour for the orthotropic layup and additionally for the amount, location and direction of wrinkling for the quasi-isotropic layup. In a detailed comparison, however, wrinkling seems to be predicted too less pronounced, especially for the generalized Maxwell, the Voigt-Kelvin and the elastic approach fitted to the "initial stiffnes". In comparison, slightly more pronounced wrinkling behavior is predicted by the elastic "best-fit" approach. However, the too less pronounced wrinkling intensity observed for both layups is expected to have another physical cause than the employed bending modeling approach, since the rate-dependent bending modeling approaches include in contrast to the purely elastic approaches the whole material characteristic observed in material characterization. It is rather more expected that thermomechanical effects due to local cooling of the laminate, which is not captured in the scope of this chapter, is the cause for the deviations between experimental tests and forming simulation observed regarding wrinkling intensity.

4 Hyperviscoelastic intra-ply modelling with a single DKT shell formulation

Abstract

The proposed framework for isothermal forming simulation using the commercial FE solver Abaqus is enhanced by a "Discrete Kirchhoff Triangle" shell formulation, which is implemented as a user-element. This enables to implement hyper(visco)elastic constitutive equations for both, membrane and bending behavior. Based on this, rate-dependent modeling approaches for intra-ply deformation behavior, following either a nonlinear Voigt-Kelvin or a nonlinear generalized Maxwell approach, which is based on a multiplicative decomposition of the deformation gradient, are presented. Parametrization results reveal that only the generalized Maxwell approach is capable to represent the whole material characteristic for all of the considered deformation rates and temperatures. Finally, the presented approaches are applied to thermoforming simulation with a good agreement to experimental tests. The results reveal that a nonlinear Voigt-Kelvin approach is sufficient for membrane modeling. Nonetheless, an influence of the temperature employed for isothermal forming simulation is observed, which emphasizes that further investigations of thermal behavior in a thermomechanical approach are being worthwhile.

Isothermal hyperviscoelastic intra-ply modeling for thermoforming simulation based on a single DKT ("Discrete Kirchhoff Theory") shell formulation is presented in the scope of this chapter, which is enabled by the implementation of a DKT shell element as user-element in the commercial FE solver Abaqus. The according framework is schematically illustrated in Figure 4.1 and reveals an extension of the approach presented in Chapter 3, where hyperviscoelastic and hypoelastic modeling approaches were required to be applied for membrane and bending behavior, respectively. Moreover, a hyperviscoelastic material modeling approach following a nonlinear generalized Maxwell approach is presented as enhancement to the hyperviscoelastic nonlinear Voigt-Kelvin approach outlined in Chapter 3.
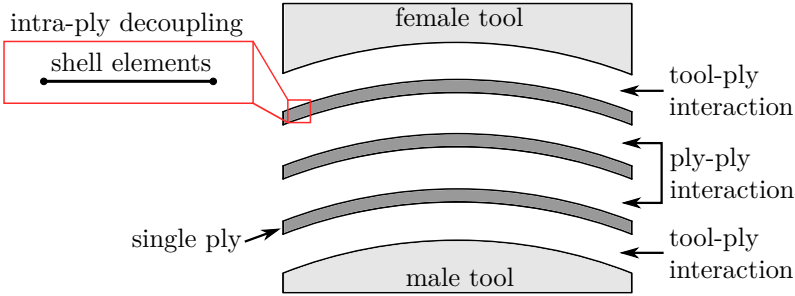
Figure 4.1: Schematic illustration of the framework for macroscopic FE forming simulation with a single DKT shell formulation.

Previous thermoforming simulation approaches model membrane behavior either purely elastic [119] or rate-dependent following a nonlinear elastic approach [134], a nonlinear Voigt-Kelvin approach [119] or a linear generalized Maxwell approach based on Prony series [156]. Besides this, bending behavior is usually assumed to behave purely elastic [119, 152, 156]. The first approach following a nonlinear generalized Maxwell approach for both, membrane and bending behavior, was presented by Dörr et al. [253]. This approach is adopted and related studies are extended in the scope of this chapter.

In the following, the geometric nonlinear DKT shell formulation is presented in Section 4.1. Subsequently, the hyperviscoelastic constitutive equations following a nonlinear Voigt-Kelvin and a nonlinear

generalized Maxwell approach are presented in Section 4.2. Finally, the intra-ply modeling approaches are parametrized for several deformation rates and temperatures in Section 4.3 and applied to thermoforming simulation of a complexly shaped geometry for validation in Section 4.4. Thereby, the influence of the temperature adopted for isothermal thermoforming simulation is investigated.

4.1 DKT shell formulation

A geometric nonlinear, triangular shell formulation based on the DKT ("Discrete Kirchhoff Theory") [254, 255] is applied for intra-ply modeling in the scope of this chapter. The shell formulation is implemented as user-element (VUEL) in the commercial FE solver Abaqus, which is outlined in detail in the following. Throughout this section, Greek subscripts range from 1 to 2 and Latin subscripts from 1 to 3.

4.1.1 Shell kinematics

The position x_i in shell space in the actual (deformed) configuration is in general given with respect to a global (inertial) system $\{i_i\}$ by

$$x_i(\xi_1, \xi_2, \xi_3) = r_i(\xi_1, \xi_2) + \xi_3 d_i(\xi_1, \xi_2), \tag{4.1}$$

where ξ_1 and ξ_2 denote curvilinear coordinates of the mid-face of the shell element, ξ_3 the coordinate in thickness direction, r_i the position on the mid-surface and d_i the unit normal vector (director). The position on the mid-face as well as the unit director are known exactly only at the nodes of the element in terms of the nodal degrees of freedom, as schematically illustrated in Figure 4.2.

Following Abaqus conventions [242], each node n of the triangular element has three translational u_{in} and three rotational degrees of freedom ϕ_{in}. The actual position r_{in} of the mid-face is obtained by the initial position R_{in} of the mid-face and the displacement of the nodes u_{in} by

$$r_{in} = R_{in} + u_{in}. \tag{4.2}$$
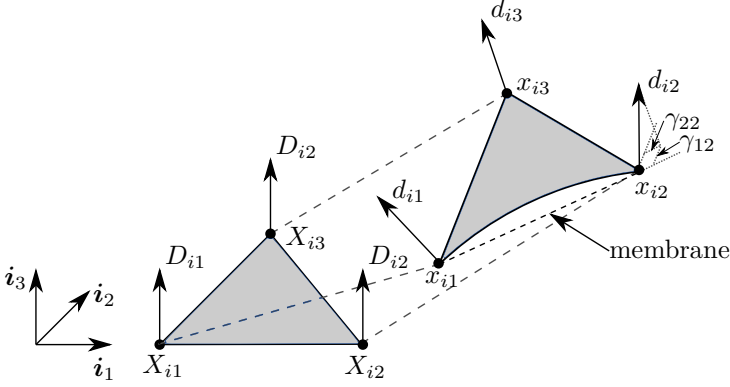
Figure 4.2: Schematic illustration of the DKT shell element in the initial and deformed configuration with the nodal coordinates and unit directors.

On the contrary, the unit director d_{jn} in the actual configuration is obtained at each node n from a rotation of the unit director D_{in} in the initial configuration by

$$d_{in} = \Lambda_{ijn} D_{jn}, \tag{4.3}$$

where Λ_{ijn} are orthogonal tensors at each node n. To describe this nodal orthogonal transformation, Rodrigues formulae [256] is adopted:

$$\Lambda_{ij} = \cos(\sqrt{\phi_k \phi_k})\delta_{ij} + \frac{\sin(\sqrt{\phi_k \phi_k})}{\sqrt{\phi_k \phi_k}}\hat{\phi}_{ij} + \frac{1 - \cos(\sqrt{\phi_k \phi_k})}{\phi_k \phi_k}\phi_i \phi_j, \tag{4.4}$$

where $\hat{\phi}_{ij}$ is the skew-symmetric matrix related to the axial vector ϕ_i:

$$\hat{\boldsymbol{\phi}} \cdot \boldsymbol{v} = \boldsymbol{\phi} \times \boldsymbol{v}. \tag{4.5}$$

4.1.2 Nonlinear strain measure

The constitutive equations applied in the scope of this chapter are evaluated based on the deformation gradient $\boldsymbol{F}$, which is obtained

146

by the differentiation of the actual configuration x_i w.r.t. the initial configuration X_α in the shell plane by

$$F_{i\alpha} = \frac{\partial x_i}{\partial X_\alpha} = x_{i,\alpha} = r_{i,\alpha} + \xi_3 d_{i,\alpha} = F_{i\alpha}^0 + \xi_3 F_{i\alpha}^1. \qquad (4.6)$$

This differentiation results in an additive split of the deformation gradient into a membrane part $F_{i\alpha}^0$ and a bending part $F_{i\alpha}^1$. It is to be noted that the deformation gradient in Equation 4.6 relates the two-dimensional initial configuration to the actual three-dimensional configuration of the shell element. Therefore, the total deformation gradient $F_{i\alpha}$ is projected onto the membrane triangle (cf. Figure 4.2). This results in a two-dimensional deformation gradient $F_{\alpha\beta}$, which enables to evaluate arbitrary constitutive equations.

In the scope of this study, Green-Lagrange strain is adopted as nonlinear strain measure, which can be expressed based on the differentiation of the actual position r_i and actual unit director d_i w.r.t. the initial configuration by

$$\begin{aligned} E_{\alpha\beta} = &\frac{1}{2}(r_{i,\alpha} r_{i,\beta} - \delta_{\alpha\beta}) \\ &+ \frac{1}{2}\xi_3(r_{i,\alpha} d_{i,\beta} + d_{i,\alpha} r_{i,\beta}) \\ &+ \frac{1}{2}\left(\xi_3\right)^2 d_{i,\alpha} d_{i,\beta}. \end{aligned} \qquad (4.7)$$

The above equation reveals that Green-Lagrange strain additively splits into a constant $E_{\alpha\beta}^0$ (membrane strains) and a linear $E_{\alpha\beta}^1$ and quadratic $E_{\alpha\beta}^2$ term (bending strains). Besides this, no local element coordinate system is necessary for the determination of Green-Lagrange strain w.r.t. the element plane as it is required for the determination of the deformation gradient, since rigid body rotation is intrinsically eliminated in the right Cauchy-Green tensor $C_{\alpha\beta}$:

$$E_{\alpha\beta} = \frac{1}{2}\left(F_{\alpha i}^\top F_{i\beta} - \delta_{\alpha\beta}\right) = \frac{1}{2}\left(C_{\alpha\beta} - \delta_{\alpha\beta}\right). \qquad (4.8)$$

147

4.1.3 Finite element discretization

A linear shape function [122] is adopted for the finite element discretization of the membrane triangle, which yields a constant membrane deformation gradient:

$$F^0_{i\alpha} = r_{i,\alpha} = r_{in}B^0_{n\alpha}, \tag{4.9}$$

where $B^0_{n\alpha}$ is the linear membrane gradient operator for a triangle [122] w.r.t. the initial configuration. The bending part of the shell element is discretized using the so-called "Discrete Kirchhoff Theory" (DKT) [254, 255]. For this purpose, the tilt of the unit director $\gamma_{\alpha n}$ against the membrane triangle is introduced ($\gamma_{\alpha n} = F^0_{i\alpha}d_{in}$) as kinematic measure (cf. Figure 4.2). Since the tilt represents a degree of freedom, it is known exactly only at the nodes. Given the constant membrane deformation gradient $F^0_{i\alpha}$, the linear bending strains in Equation 4.7 can be rewritten to

$$\begin{aligned} E^1_{\alpha\beta} &= \frac{1}{2}\xi_3 \left((F^0_{i\alpha}d_i)_{,\beta} + (F^0_{i\beta}d_i)_{,\alpha}\right) \\ &= \frac{1}{2}\xi_3 \left(\gamma_{\alpha,\beta} + \gamma_{\beta,\alpha}\right) \\ &= \frac{1}{2}\xi_3\kappa_{\alpha\beta}, \end{aligned} \tag{4.10}$$

where $\kappa_{\alpha\beta}$ is usually denoted as the physical curvature tensor. As proposed by Wenzel et al. [255], the tilt is interpolated according to the DKT theory [254], resulting in a discretized expression for the linear bending strains

$$E^1_{\alpha\beta} = \frac{1}{2}\xi_3 \left(B^1_{\alpha\beta\varepsilon j} + B^1_{\beta\alpha\varepsilon j}\right) B^0_{k\varepsilon}r_{ik}d_{ij}, \tag{4.11}$$

where the DKT gradient operator $B^1_{\alpha\beta\varepsilon j}$ can be reconstructed from the equations given by Batoz et al. [254]. Based on the discretized gradient of the tilt, the bending deformation gradient is obtained through

$$F^1_{\alpha\beta} = (F^0_{\alpha\delta})^{-\top}\gamma_{\delta,\gamma}, \tag{4.12}$$

where $F_{\alpha\delta}^0$ is the membrane deformation gradient projected onto the element plane. Given the membrane deformation gradient in Equation 4.9 and the bending deformation gradient in Equation 4.12, the total deformation gradient can be determined according to Equation 4.6. Hence, arbitrary hyper(visco)elastic constitutive equations can be implemented within the presented shell formulation.

4.1.4 Membrane and bending decoupling

In the weak form of the equilibrium condition, Green-Lagrange strain $\boldsymbol{E}$ is associated with the second Piola-Kirchhoff (PK2) stress $\boldsymbol{S}$ by

$$\delta\Pi = \int_V S_{\alpha\beta}\,\delta E_{\alpha\beta}\,\mathrm{d}V. \tag{4.13}$$

The virtual internal energy $\delta\Pi$ is decomposed into a membrane and a bending part for decoupling of membrane and bending behavior by

$$\delta\Pi = \int_V \left[S_{\alpha\beta}^{\mathrm{mem}} \left(\frac{\partial E_{\alpha\beta}}{\partial r_{in}} \right) \delta r_{in} + S_{\alpha\beta}^{\mathrm{bend}} \left(\frac{\partial E_{\alpha\beta}}{\partial d_{in}} \right) \delta d_{in} \right] \mathrm{d}V. \tag{4.14}$$

Based on the principle of virtual displacements, the resulting nodal forces f_{lm} and nodal moments m_{lm}^{dir} are obtained by the variation of the virtual internal energy $\delta\Pi$ w.r.t. the virtual nodal displacements δr_{in} and the virtual nodal unit directors δd_{in}, respectively:

$$f_{lm} = \int_V \left[S_{\alpha\beta}^{\mathrm{mem}} B_{m\alpha}^0 B_{j\beta}^0 r_{lj} + \xi_3 S_{\alpha\beta}^{\mathrm{bend}} B_{\alpha\beta\varepsilon j}^1 B_{m\varepsilon}^0 d_{lj} \right] \mathrm{d}V, \tag{4.15}$$

$$m_{lm}^{\mathrm{dir}} = \int_V \left[\xi^3 S_{\alpha\beta}^{\mathrm{bend}} B_{\alpha\beta\varepsilon m}^1 B_{k\varepsilon}^0 r_{lk} \right] \mathrm{d}V. \tag{4.16}$$

Gauss quadrature [228] is applied for the integration of both, the element mid-plane and thickness direction. It has to be noted that due to the quadratic discretization according to the DKT, three integration points in the element plane are necessary for full integration. Nonetheless, the application of a single integration point in the element plane, yielding a reduced integration, is also possible to improve numerical efficiency. A reduced integration, however, reduces the accuracy of the integration.

149

It has to be considered that the nodal moments m_{lm}^{dir} are defined w.r.t. the nodal unit director base. Thus, the nodal moments need to be transformed to the global system for each node by

$$m_{lm}^{\text{glob}} = H_{li} m_{im}^{\text{dir}} \quad \text{with} \quad H_{li} = \frac{\delta d_l}{\delta \phi_i} = -\hat{d}_{lk} T_{ki}, \tag{4.17}$$

where T_{ij} is the transformation between the variation of the rotation in the director base $\delta\theta_i$ and the variation of the rotation vector with respect to the global system $\delta\phi_i$ ($\delta\theta_i = T_{ij}\delta\phi_j$). This transformation is given by [256]

$$T_{ij} = \frac{\sin(\phi)}{\phi} \delta_{ij} + \frac{1-\cos(\phi)}{\phi^2} \hat{\phi}_{ij} + \frac{\phi - \sin\phi}{\phi^3} \phi_i \phi_j \quad \text{with} \quad \phi = \sqrt{\phi_k \phi_k}. \tag{4.18}$$

4.2 Hyperviscoelastic intra-ply modeling

The shell formulation introduced in the previous section enables intra-ply material modeling based on the deformation gradient as kinematic measure for the membrane and the bending part. This was not possible for the superimposed approach introduced in Chapter 3, since the deformation gradient including membrane and bending deformation is not available for the adopted user-defined shell section integration (VUGENS). In the scope of this chapter, hyperviscoelastic material modeling following a nonlinear Voigt-Kelvin and a nonlinear generalized Maxwell approach is investigated. The nonlinear Voigt-Kelvin approach is outlined in the previous chapter and therefore, the reader is referred for details to Section 3.3.1. On the contrary, the generalized Maxwell approach is outlined in the following. This approach is based on a multiplicative decomposition of the deformation gradient and the according constitutive equations are defined for the (general) anisotropic case. The latter enables the application to both, membrane and bending modeling. Material behavior is assumed to be incompressible and membrane behavior is modeled following the "Ideal Fibre-Reinforced Material" (IFRM) [145, 146] (cf. Section 3.3.1), in analogy to the Voigt-Kelvin approach.

4.2.1 Nonlinear generalized Maxwell approach

The generalized Maxwell approach is based on the parallel connection of a hyperelastic element with an arbitrary number of Maxwell elements, which consist of an elastic element connected in series with a nonlinear viscous flow element. The according network is schematically illustrated in Figure 4.3.
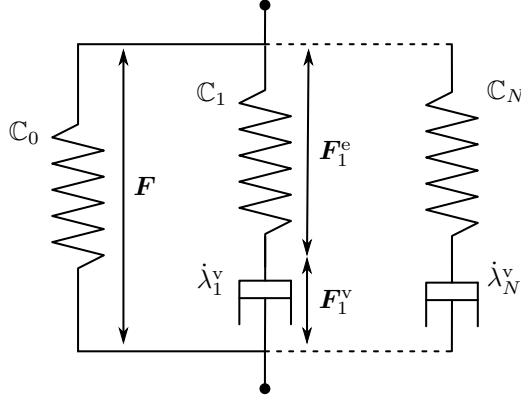
Figure 4.3: Schematic illustration of the nonlinear hyperviscoelastic generalized Maxwell approach based on a multiplicative decomposition of the deformation gradient.

Kinematics For generalized Maxwell approaches, the total deformation is acting on the purely elastic as well as on the Maxwell elements ($\boldsymbol{F} = \boldsymbol{F}_i$). For each Maxwell element i, a multiplicative decomposition of the deformation gradient $\boldsymbol{F}$ into an elastic part $\boldsymbol{F}_i^{\mathrm{e}}$ and a viscous part $\boldsymbol{F}_i^{\mathrm{v}}$ is employed:

$$\boldsymbol{F} = \boldsymbol{F}_i^{\mathrm{e}} \cdot \boldsymbol{F}_i^{\mathrm{v}}. \tag{4.19}$$

This multiplicative decomposition introduces an intermediate (relaxed) configuration $\tilde{\mathscr{B}}_i$ for each Maxwell element, additionally to the well-known initial configuration $\mathscr{B}_0$ and current configuration $\mathscr{B}_1$. An overview of the mappings between these configurations is given in a schematic illustration in Figure 4.4. In the following, the index for numbering the Maxwell elements is omitted for simplicity.

151
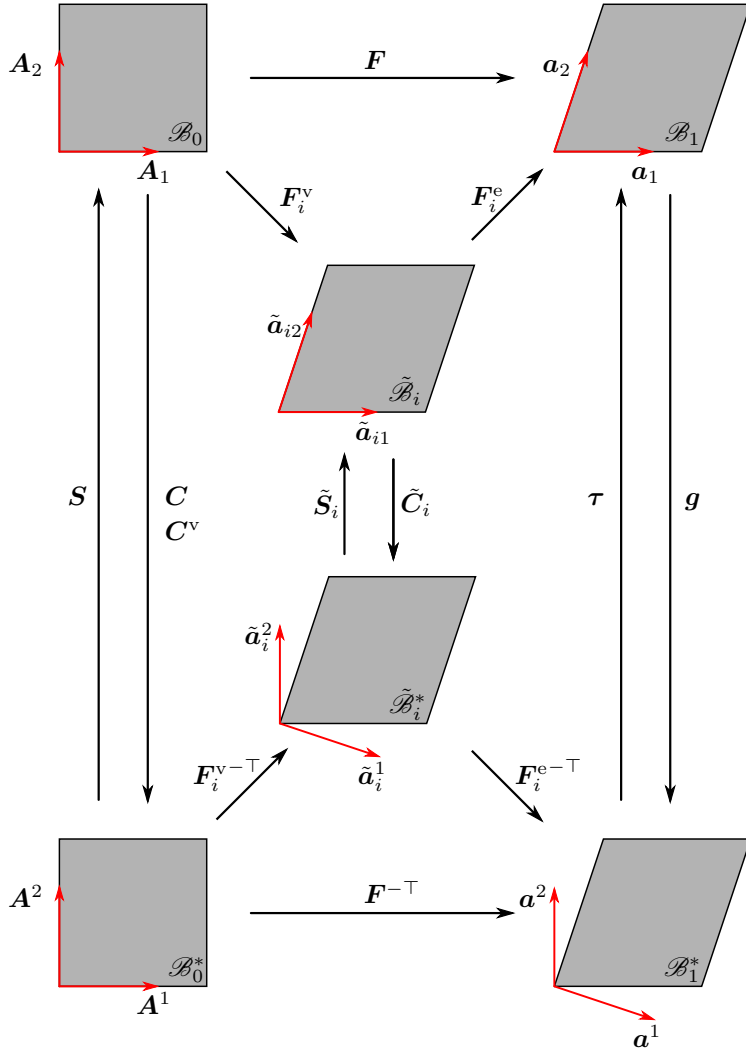
Figure 4.4: Definition of metric and stress tensors as mappings between the co-variant initial configuration $\mathscr{B}_0$, relaxed configuration $\tilde{\mathscr{B}}_i$ and current configuration $\mathscr{B}_1$ and the related contravariant configurations $\mathscr{B}_0^*$, $\tilde{\mathscr{B}}_i^*$ and $\mathscr{B}_1^*$ for the Maxwell elements, respectively.

Under application of the multiplicative decomposition in Equation 4.19, it has to be noted that the principal material orientations $\boldsymbol{A}_i$ rotate and lengthen between the initial, relaxed and current configuration, which can be determined by

$$
\begin{aligned}
\boldsymbol{a}_i &= \boldsymbol{F} \cdot \boldsymbol{A}_i \\
&= \boldsymbol{F}^{\mathrm{e}} \cdot \tilde{\boldsymbol{a}}_i \quad \text{with} \quad \tilde{\boldsymbol{a}}_i = \boldsymbol{F}^{\mathrm{v}} \cdot \boldsymbol{A}_i,
\end{aligned}
\tag{4.20}
$$

where $\boldsymbol{a}_i$ and $\tilde{\boldsymbol{a}}_i$ are the principal material orientations in the relaxed and the current configuration, respectively. Furthermore, the convected current metric $\boldsymbol{C}$ and the convected relaxed metric $\boldsymbol{C}^{\mathrm{v}}$ can be evaluated by

$$
\boldsymbol{C} = \boldsymbol{F}^{\top} \cdot \boldsymbol{g} \cdot \boldsymbol{F} \qquad \text{and} \qquad \boldsymbol{C}^{\mathrm{v}} = \boldsymbol{F}^{\mathrm{v}\top} \cdot \boldsymbol{g}^{\mathrm{v}} \cdot \boldsymbol{F}^{\mathrm{v}},
\tag{4.21}
$$

where $\boldsymbol{g}$ and $\boldsymbol{g}^{\mathrm{v}}$ represent the standard covariant metric tensors. The kinematic magnitudes in Equation 4.21 are usually denoted as the right Cauchy-Green tensors. Since Cartesian coordinates are applied in the scope of this study, the covariant metric tensors reduce to the second order identity tensor ($\boldsymbol{g} = \boldsymbol{g}^{\mathrm{v}} = \boldsymbol{1}$). The elastic Green-Lagrange strain $\tilde{\boldsymbol{E}}^{\mathrm{e}}$ w.r.t. the intermediate configuration

$$
\begin{aligned}
\tilde{\boldsymbol{E}}^{\mathrm{e}} &= f_2 \left(\boldsymbol{F}^{\mathrm{v}-\top} \cdot \boldsymbol{C} \cdot \boldsymbol{F}^{\mathrm{v}-1} \right) \\
&= \frac{1}{2} \left(\boldsymbol{F}^{\mathrm{v}-\top} \cdot \boldsymbol{C} \cdot \boldsymbol{F}^{\mathrm{v}-1} - \boldsymbol{1} \right) \\
&= \frac{1}{2} \left(\boldsymbol{F}^{\mathrm{e}\top} \cdot \boldsymbol{F}^{\mathrm{e}} - \boldsymbol{1} \right),
\end{aligned}
\tag{4.22}
$$

is obtained based on the Seth-Hill family of generalized strain measures [257]. It can be shown by a straightforward transformation that Green-Lagrange strain additively splits into an elastic part and a viscous part in the initial configuration:

$$
\begin{aligned}
\boldsymbol{E}^{\mathrm{e}} &= \boldsymbol{F}^{\mathrm{v}\top} \cdot \tilde{\boldsymbol{E}}^{\mathrm{e}} \cdot \boldsymbol{F}^{\mathrm{v}} \\
&= \frac{1}{2} \left(\boldsymbol{C} - \boldsymbol{C}^{\mathrm{v}} \right) \\
&= \boldsymbol{E} - \boldsymbol{E}^{\mathrm{v}}.
\end{aligned}
\tag{4.23}
$$

A similar relation is obtained for the velocity gradient ($\boldsymbol{L} = \dot{\boldsymbol{F}} \cdot \boldsymbol{F}^{-1}$), which is defined in the current configuration and splits additively into an elastic velocity gradient $\boldsymbol{L}^{\mathrm{e}}$ and a viscous velocity gradient $\boldsymbol{L}^{\mathrm{v}}$:

$$
\begin{aligned}
\boldsymbol{L} &= \left[\frac{\mathrm{d}}{\mathrm{d}t} \left(\boldsymbol{F}^{\mathrm{e}} \cdot \boldsymbol{F}^{\mathrm{v}} \right) \right] \cdot \left(\boldsymbol{F}^{\mathrm{e}} \cdot \boldsymbol{F}^{\mathrm{v}} \right)^{-1} \\
&= \dot{\boldsymbol{F}}^{\mathrm{e}} \cdot \left(\boldsymbol{F}^{\mathrm{e}} \right)^{-1} + \boldsymbol{F}^{\mathrm{e}} \cdot \dot{\boldsymbol{F}}^{\mathrm{v}} \cdot \left(\boldsymbol{F}^{\mathrm{v}} \right)^{-1} \cdot \left(\boldsymbol{F}^{\mathrm{e}} \right)^{-1} \\
&= \boldsymbol{L}^{\mathrm{e}} + \boldsymbol{F}^{\mathrm{e}} \cdot \tilde{\boldsymbol{L}}^{\mathrm{v}} \cdot \left(\boldsymbol{F}^{\mathrm{e}} \right)^{-1} \\
&= \boldsymbol{L}^{\mathrm{e}} + \boldsymbol{L}^{\mathrm{v}} .
\end{aligned}
\tag{4.24}
$$

Hyperviscoelastic constitutive equations The total stress $\boldsymbol{S}$ is determined by the summation of the stress contribution of the purely elastic $\boldsymbol{S}_0$ and each Maxwell element $\boldsymbol{S}_i$ by

$$
\boldsymbol{S} = \boldsymbol{S}_0 + \sum_{i=1}^{N} \boldsymbol{S}_i ,
\tag{4.25}
$$

due to their parallel connection in the rheological network. For the purely hyperelastic element, the stress $\boldsymbol{S}_0$ is determined by means of the total deformation $\boldsymbol{F}$ by

$$
\boldsymbol{S}_0 = \frac{\partial \psi_0}{\partial \boldsymbol{E}} \quad \text{with} \quad \boldsymbol{E} = \frac{1}{2} \left(\boldsymbol{F}^{\top} \cdot \boldsymbol{F} - \boldsymbol{1} \right) ,
\tag{4.26}
$$

where ψ_0 is the strain energy potential of the purely hyperelastic element. The specific energy potential Ψ_i of a Maxwell element i is defined by the sum of an elastic potential Ψ_i^{e} and a dissipation potential D_i:

$$
\Psi_i = \Psi_i^{\mathrm{e}} + D_i .
\tag{4.27}
$$

Based on the additive decomposition of the total Green-Lagrange strain $\boldsymbol{E}$ in an elastic part $\boldsymbol{E}_i^{\mathrm{e}}$ and a viscous part $\boldsymbol{E}_i^{\mathrm{v}}$ (Equation 4.24), the Clausius-Duhem inequality [258]

$$
\boldsymbol{S}_i : \dot{\boldsymbol{E}} - \rho \frac{\mathrm{d}\Psi_i}{\mathrm{d}t} \geq 0
\tag{4.28}
$$

can be reformulated to

$$\left(\boldsymbol{S}_i - \rho \frac{\partial \Psi_i^{\mathrm{e}}}{\partial \boldsymbol{E}_i^{\mathrm{e}}} \right) : \dot{\boldsymbol{E}}_i^{\mathrm{e}} + \boldsymbol{S}_i : \dot{\boldsymbol{E}}_i^{\mathrm{v}} \geq 0. \tag{4.29}$$

Since the Clausius-Duhem inequality holds regardless of any particular $\dot{\boldsymbol{E}}_i^{\mathrm{e}}$, it necessarily follows that [258]

$$\boldsymbol{S}_i = \rho \frac{\partial \Psi_i^{\mathrm{e}}}{\partial \boldsymbol{E}_i^{\mathrm{e}}} = \frac{\partial \psi_i^{\mathrm{e}}}{\partial \boldsymbol{E}_i^{\mathrm{e}}}. \tag{4.30}$$

The remaining quantity for the evaluation of the constitutive equations of the Maxwell elements is the internal variable of viscous deformation $\boldsymbol{F}_i^{\mathrm{v}}$. The according rate of viscous deformation $\boldsymbol{D}_i^{\mathrm{v}}$ is described by means of a constitutively defined equivalent flow rate $\dot{\lambda}_i^{\mathrm{v}}$ and the assumption that viscous deformation evolves in direction of the deviatoric Cauchy stress $\mathrm{dev}\,(\boldsymbol{\sigma}_i)$, in analogy to the approach presented by Bergström [246]:

$$\boldsymbol{D}_i{}^{\mathrm{v}} = \dot{\lambda}_i^{\mathrm{v}} \frac{\mathrm{dev}\,(\boldsymbol{\sigma}_i)}{\|\mathrm{dev}\,(\boldsymbol{\sigma}_i)\|}. \tag{4.31}$$

To make the unloading unique, $\boldsymbol{L}_i^{\mathrm{v}} \equiv \boldsymbol{D}_i^{\mathrm{v}}$ is prescribed [246], which yields an ordinary differential for the evolution of viscous deformation:

$$\dot{\boldsymbol{F}}_i^{\mathrm{v}} = \dot{\lambda}_i^{\mathrm{v}} \boldsymbol{F}_i^{\mathrm{e}-1} \cdot \frac{\mathrm{dev}\,(\boldsymbol{\sigma}_i)}{\|\mathrm{dev}\,(\boldsymbol{\sigma}_i)\|} \cdot \boldsymbol{F}_i^{\mathrm{e}} \cdot \boldsymbol{F}_i^{\mathrm{v}}. \tag{4.32}$$

This ordinary differential equation is integrated incrementally by a discrete time integration scheme. For an FEA with implicit time integration, a fourth-order Runge-Kutta integration procedure [228] has proven to be a good compromise between numerical efficiency and stability. In contrast, an Euler explicit time integration procedure [228] is sufficient in an FEA with explicit time integration, since time steps are intrinsically small.

In the scope of this study, a Saint-Venant Kirchhoff material is applied for each hyperelastic element. The according strain energy potentials are defined by

$$\psi_0 = \frac{1}{2}\boldsymbol{E} : \mathbb{C}_0 : \boldsymbol{E} \quad \text{and} \quad \psi_i^{\text{e}} = \frac{1}{2}\boldsymbol{E}_i^{\text{e}} : \mathbb{C}_i : \boldsymbol{E}_i^{\text{e}}. \tag{4.33}$$

For the viscous elements, a hyperbolic sine law is applied for the definition of the equivalent flow rate [259]:

$$\dot{\lambda}_i^{\text{v}} = A_i \sinh\left(B_i \sqrt{\text{dev}\left(\boldsymbol{\sigma}_i\right) : \text{dev}\left(\boldsymbol{\sigma}_i\right)}\right)^{n_i}, \tag{4.34}$$

where A, B and n are material constants and $\boldsymbol{\sigma}$ is the Cauchy stress within the Maxwell element, which is obtained by

$$\boldsymbol{\sigma}_i = J^{-1}\boldsymbol{F} \cdot \boldsymbol{S}_i \cdot \boldsymbol{F}^\top \quad \text{with} \quad J = \det\left(\boldsymbol{F}\right). \tag{4.35}$$

4.3 Parametrization of intra-ply modeling

The hyperviscoelastic constitutive equations following the nonlinear generalized Maxwell approach (cf. Section 4.2.1) and the nonlinear Voigt-Kelvin approach (cf. Section 3.3.1) are parametrized for both, membrane and bending behavior, in the following. For this purpose, the isothermal characterization results from the torsion bar test (cf. Section 2.3.2) and the rheometer bending test (cf. Section 2.3.3) are adopted. In the scope of this chapter, three different temperatures well above the recrystallization temperature of the thermoplastic (270 °C, 250 °C and 226 °C) and three different deformation rates (0.1 rpm, 1.0 rpm and 10.0 rpm) are considered. The according characterization setups are modeled in an FEA for the inverse identification of the material parameters. For this purpose, similar optimization strategies as outlined in the previous chapter (cf. Section 3.4) are applied. This includes the same target function (cf. Equation 3.55). The obtained material parameters are listed in Appendix A.2.

4.3.1 Membrane behavior

The same approach as outlined in Section 3.4.1 is applied for parametrization of the nonlinear Voigt-Kelvin approach for membrane behavior. This includes an FEA of the torsion bar test and the optimization procedure presented by Nelder and Mead [247] for inverse parameter identification, where the initial values for this gradient-based optimization algorithm are identified manually. The generalized Maxwell approach, however, is not subject to such a manual estimation of reasonable initial values. Therefore, a substitute model (cf. Figure 4.5) is applied to efficiently identify the initial values based on an evolutionary optimization algorithm.

Figure 4.5: Exemplary FEA result of the torsion bar tests and the according substitute model for the longitudinal Green-Lagrange shear strain E_{12} at $30\deg$ deflection.

The deformation gradient history $\boldsymbol{F}\left(t, \boldsymbol{x}^i\right)$ as well as the position $\boldsymbol{x}^i$ of each integration point i is exported for the substitute model from an FEA. Based on this, Cauchy stress $\boldsymbol{\sigma}^i$ is evaluated, which enables to approximate the torsion moment history by means of a discretized version of the formulae proposed by Haanappel et al. [60]:

$$M(t) = \int_{-\frac{y}{2}}^{\frac{y}{2}} \int_{-\frac{y}{2}}^{\frac{y}{2}} [y(t)\sigma_{13}(t) - z(t)\sigma_{12}(t)] \ \mathrm{d}y \, \mathrm{d}z \qquad (4.36)$$

$$\approx \sum_{i=1}^{N^{\mathrm{IP}}} \left[y^i(t)\sigma_{13}^i(t) - z^i(t)\sigma_{12}^i(t) \right] A^i,$$

where y^i and z^i are the coordinates of the integration point i on the cross section and A^i the according related section. This substitute model is applied to an evolutionary optimization algorithm, in order to estimate the initial values for a gradient-based optimization based on a detailed FEA. For this purpose, the open access software toolkit Dakota is used, an implementation of the Sandia National Laboratories [260]. The Dakota toolkit provides diverse operators for genetic algorithms as well as an interface between analysis code and optimization methods. Based on this, the user-material subroutine also applied for the detailed FEA is embedded into the optimization workflow.

Parametrization results Voigt-Kelvin approach A constant elastic stiffness and a nonlinear viscosity following the Cross model is applied for the Voigt-Kelvin (VK) approach. The parametrization results in Figure 4.6 (left) reveal that this approach leads to a constant slope for each deformation rate, induced by the elastic stiffness, and a constant offset between the curves, induced by the nonlinear viscosity model. The Voigt-Kelvin approach is capable to approximately describe the shear characteristic for 270 °C, for which approximately the same slopes are observed for each deformation rate. With decreasing temperature, however, prediction quality deteriorates, since the differing slopes for the different deformation rates become more pronounced. Beyond that, the starting behavior is not captured accurately by the Voigt-Kelvin approach.

Parametrization results generalized Maxwell approach For the generalized Maxwell (GM) approach, a single spring element and two Maxwell elements are used. Each spring element is modeled with a constant stiffness and each dashpot is modeled by means of a hyperbolic sine law (Equation 4.34) as flow rule. The according parametrization results are shown in Figure 4.6 (right). In contrast to the Voigt-Kelvin approach, the starting behavior as well as the varying slopes are well captured by the generalized Maxwell approach. A slight deviation is observed for the low deformation rate ($n = 0.1$ rpm) at 270 °C. This slight deviation might be improved with further parameter optimization, which is not pursued, since the deviation is small.

Figure 4.6: Comparison of characterization results to the parametrization results for membrane behavior obtained from the torsion bar tests for the Voigt-Kelvin (VK, left) and the generalized Maxwell (GM, right) approach at different temperatures.

4.3.2 Bending behavior

For parametrization of the Voigt-Kelvin approach, the parametrization strategy outlined in Section 3.4.2 is applied, including an FEA of the rheometer bending test and the optimization procedure presented by Nelder and Mead [247] for inverse parameter identification, where the initial values for this gradient-based optimization algorithm are identified manually. The generalized Maxwell approach, however, is not subject to a manual estimation of initial values. Therefore, a substitute model (cf. Figure 4.7) is applied to efficiently identify the initial values based on an evolutionary algorithm.
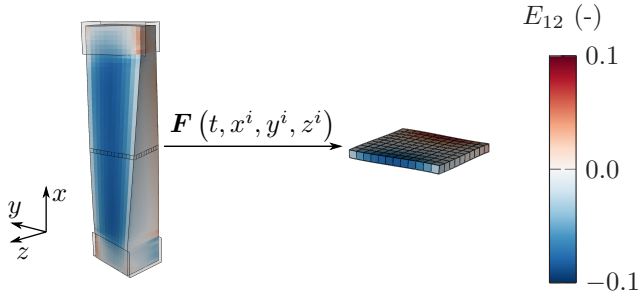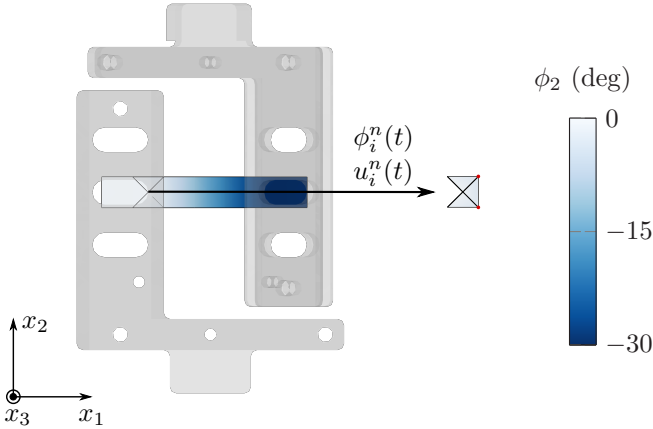

Figure 4.7: Exemplary FEA result of the rheometer bending test and the according substitute model for the nodal rotation ϕ_2 at 30 deg deflection.

This substitute model differs from that applied to the superimposed approach (cf. Section 3.4.2), since only the nodal values and no kinematic magnitudes at the integration point(s) are available as output for the user-element. However, based on the application of the nodal degrees of freedom as input for the substitute model, the user-element code can be directly embedded for inverse parameter estimation using the substitute model. The substitute model applied here is part of an element stripe, which is adopted to reduce the FEA to the minimal

possible number of elements. This reduction is possible, since the specimen is loaded in the rheometer test under uniaxial bending.

For the nodes i attached to the elements of the substitute model, the history of the nodal displacements u_i^n and rotations ϕ_i^n are exported. Based on this, the nodal moments are determined for the nodes highlighted in Figure 4.7. Based on this, the user-element outlined in Section 4.1 is embedded into an evolutionary optimization algorithm, in order to estimate the initial values for a gradient-based optimization using a detailed FEA. For this purpose, the open access software toolkit Dakota is used, an implementation of the Sandia National Laboratories [260]. The Dakota toolkit provides diverse operators for genetic algorithms as well as an interface between analysis code and optimization methods. In the scope of this section, explicit time integration is applied for the detailed FEA, to circumvent an additional implementation of the DKT shell formulation for implicit time integration.

Parametrization results Voigt-Kelvin approach   A constant and orthotropic elastic stiffness and an isotropic and nonlinear viscosity following the Cross model is applied for the Voigt-Kelvin approach. The parametrization results in Figure 4.8 (left) reveal that this approach leads to a constant slope for each deformation rate n and an offset between the different deformation rates, in analogy to the parametrization of membrane behavior in Section 4.3.1. In this manner, the Voigt-Kelvin approach is capable to approximately describe bending behavior for 270 °C. Prediction accuracy, however, deteriorates towards lower temperatures. Especially the high deformation rate ($n = 10.0$ rpm) can only be described approximately, since the varying slope cannot be captured. Besides this, also the starting behavior is not captured appropriately.

Parametrization results generalized Maxwell approach   A single spring element and two Maxwell elements are used for modeling bening behavior by means of the generalized Maxwell approach. Each spring element is modeled by a constant and orthotropic stiffness, whereas a hyperbolic sine law (Equation 4.34) is used as flow rule for the viscous elements. It is observed that the generalized Maxwell
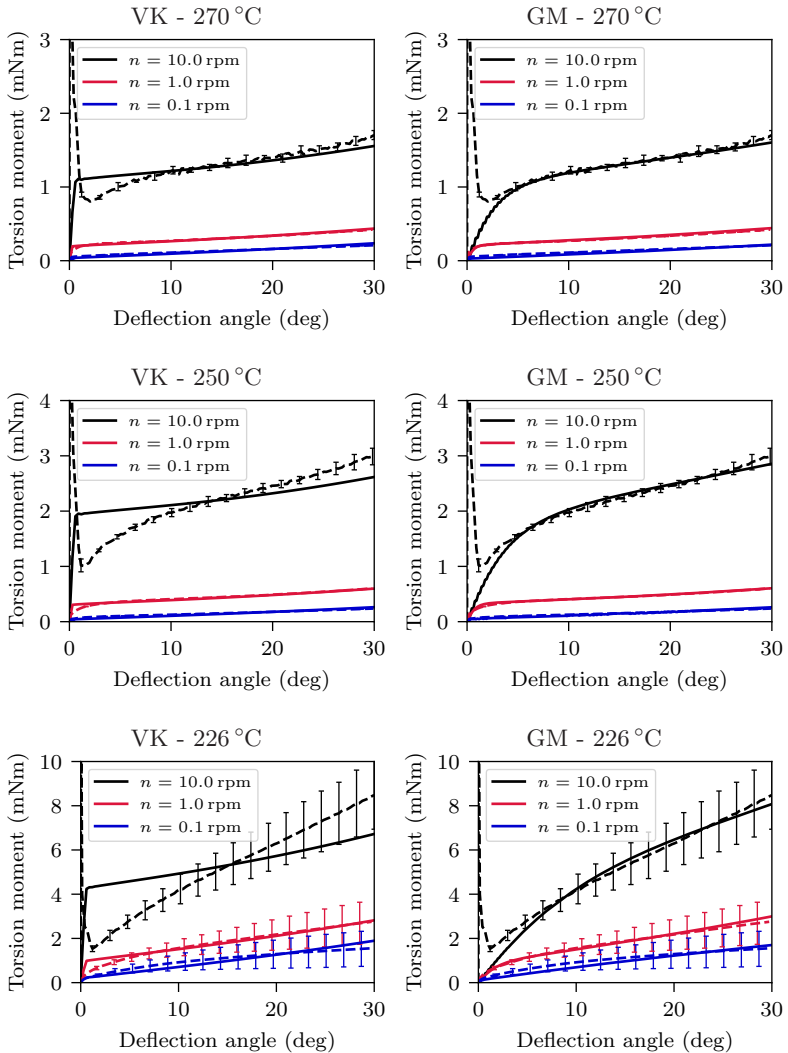
161
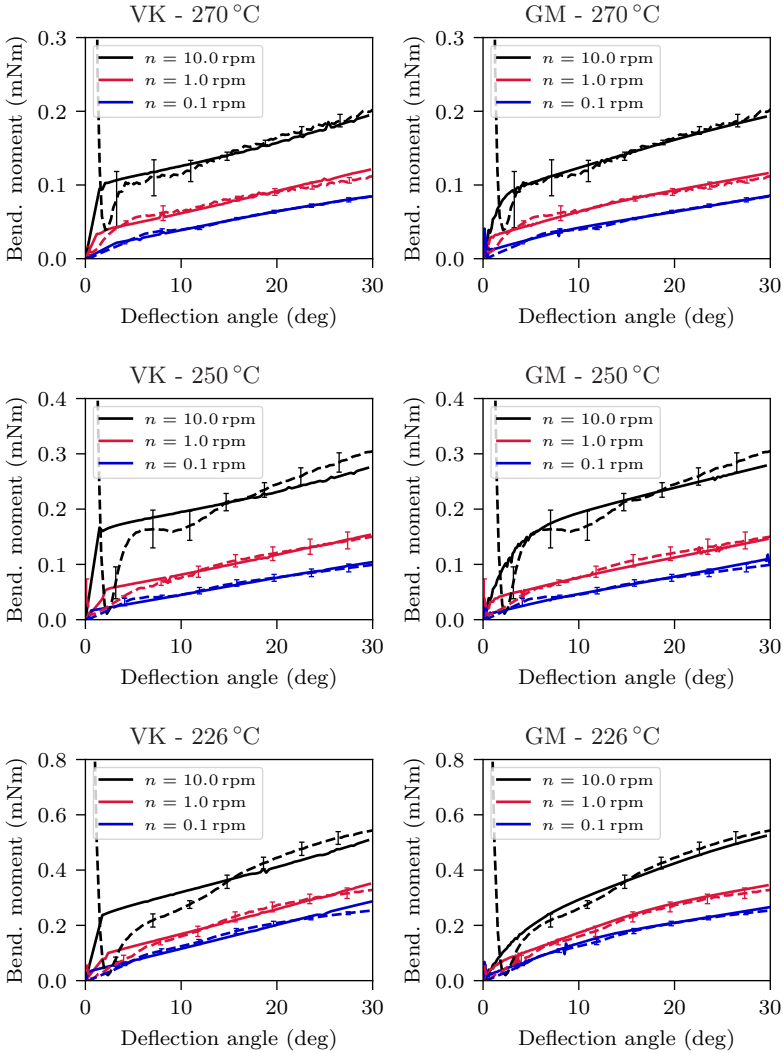
Figure 4.8: Comparison of characterization results to the parametrization results for bending behavior obtained from the rheometer bending tests for the Voigt-Kelvin (VK, left) and the generalized Maxwell (GM, right) approach at different temperatures.

approach is capable to predict the starting behavior of the moment-deflection-curve as well as different and non-constant slopes for the different deformation rates n. This reveals the improved prediction quality of the generalized Maxwell approach against the Voigt-Kelvin approach.

4.4 Validation of isothermal forming simulation

In the following, the above outlined DKT shell formulation and hyper-viscoelastic constitutive equations for intra-ply modeling are applied in combination with the isotropic inter-ply modeling approach presented in Chapter 5 to isothermal forming simulation. In the scope of this chapter, membrane modeling approaches are varied, in order to investigate the necessity to apply a generalized Maxwell approach for membrane modeling, while bending and inter-ply modeling approaches remain unchanged. Thereby, it is to be noted that forming simulation is isothermal in the scope of this chapter, which implies the prediction of formability at a constant temperature. Therefore, also the temperature prescribed for isothermal forming simulation is varied, in order to investigate the influence of the temperature-dependent material behavior on the formability prediction.

The generic geometry and the according process setup presented in Section 2.2.1 is investigated in forming simulation and compared for validation to experimental tests. Two different layups, which namely are an orthotropic layup ($[0; 90]_{2\mathrm{s}}$]) and a quasi-isotropic layup ($[0; -45; 90; +45]_{\mathrm{s}}$), in combination with the intermediate process settings (cf. Table 2.1) are considered. The model setup described in detail in Section 3.5.2 remains unchanged, except the above outlined changes regarding intra-ply modeling, which enable hyperviscoelastic material modeling for both, membrane and bending modeling.

4.4.1 Biaxial layup

Figure 4.9 shows the comparison of forming simulation to the experimental test for the orthotropic layup and the fully formed part, under application of the Voigt-Kelvin approach for membrane modeling and the generalized Maxwell approach for bending modeling. This combination of rheological models is also considered for thermoforming

validation in the previous chapter (cf. Section 3.5.2). The final shape of the simulation result is shown for the high temperature. Moreover, the outer contours obtained for the different temperatures are compared to the experimental test in Figure 4.9(c). The outer contours are determined based on the approach outlined in Section 2.1.1.

(a) Sim. $T = 270\,°\mathrm{C}$ (b) Experiment (c) Contours
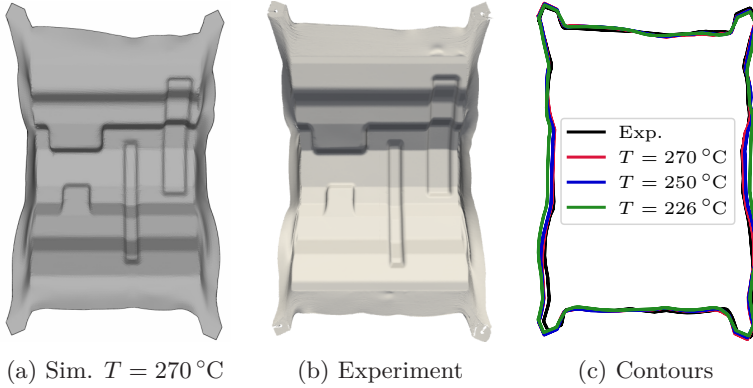
Figure 4.9: Isothermal forming simulation result (a), 3D measurement of the experimental test (b) and comparison of the outer contours (c) for the orthotropic layup ($[0; 90]_{2\mathrm{s}}$) and fully closed tools.

In comparison of the final shapes, a high prediction accuracy is observed, which includes the general course of the outer contour as well as the areas tensioned due to laminate gripping. Nonetheless, some slight defects at the transition from the actual part to the outer areas are not predicted by simulation, in analogy to the results obtained with the superimposed approach in Section 3.5.2. Regarding the outer contours for the different temperatures shown in Figure 4.9(c), similar results and a high prediction accuracy are obtained for the high and the intermediate temperature. On the contrary, the outer contour flares for the low temperature, which reduces the agreement to the experimental result.

Additional results for the same isothermal model setup at the high temperature are shown in Figure 4.10 at several remaining tool travels Δz (left) and compared to experimental tests (right). The comparison of forming simulation to the related experimental tests reveals that the general shape as well as the outer contour are predicted accurately.

Stage 1: $\varDelta z = 30\,\mathrm{mm}$
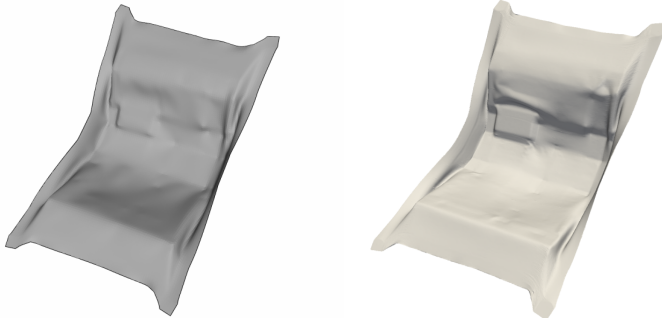
Stage 2: $\varDelta z = 17.5\,\mathrm{mm}$
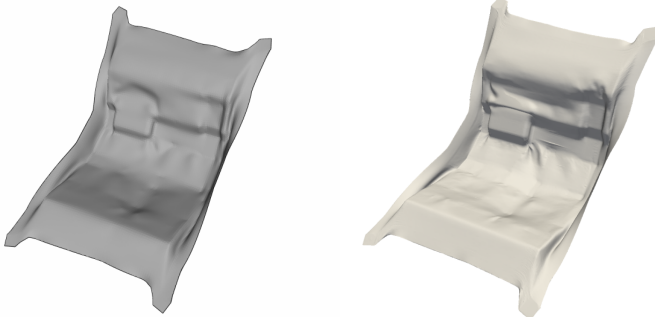
Stage 3: $\varDelta z = 5\,\mathrm{mm}$

Figure 4.10: Comparison of isothermal forming simulation at $270\,^{\circ}\mathrm{C}$ (left) to 3D measurements of experimental tests (right) for the orthotropic layup ($[0; 90]_{2\mathrm{s}}$) at several remaining tool travels $\varDelta z$.
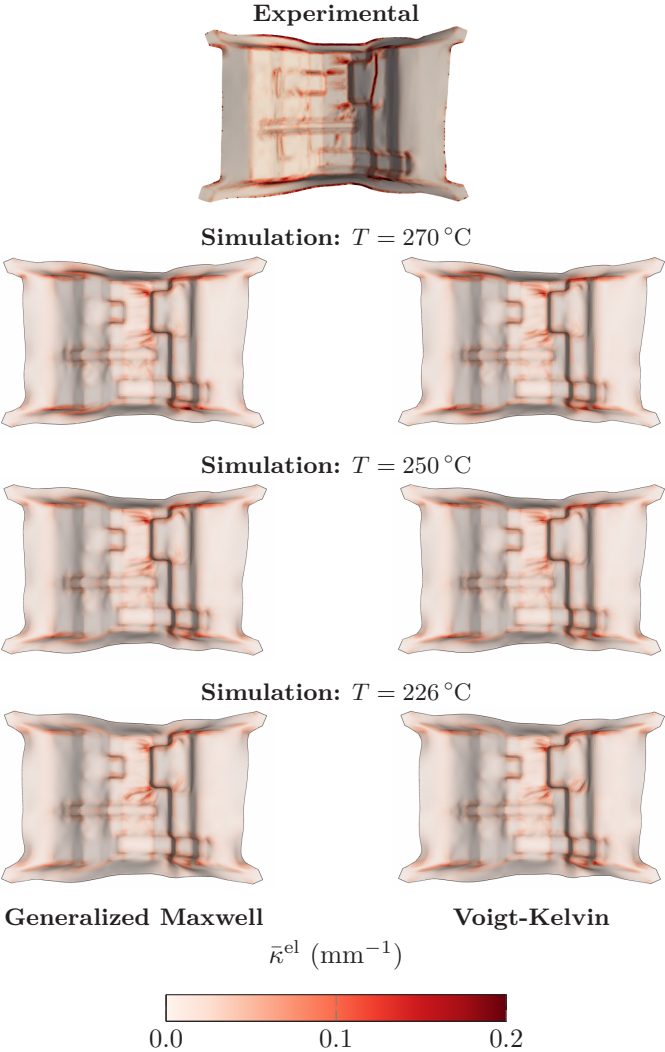
Figure 4.11: Comparison of isothermal forming simulation to an experimental test at a remaining tool travel of 5 mm for the orthotropic layup under variation temperature and membrane modeling, following the generalized Maxwell (left) and Voigt-Kelvin (right) approach.

In analogy to the results obtained with the superimposed approach in Section 3.5.2, however, the material accumulations above the bigger corner bending becomes apparent in Stage 2 and 3, but is predicted less pronounced compared to the experimental tests. Beyond that, local wrinkling to the end of forming (Stage 3) is predicted slightly less pronounced than observed in the experimental test. Thereby, material accumulations become apparent around the beads or above the smaller corner bending, but no wrinkles are predicted.

The aforementioned deviations are observed for all temperatures for both variants regarding material modeling, which is shown for Stage 3 at remaining tool travel of 5 mm based on the elemental modified mean curvature $\bar{\kappa}^{\mathrm{el}}$ in Figure 4.11. In comparison of the results of the generalized Maxwell approach to the results of the Voigt-Kelvin approach for membrane modeling, almost no difference is visible for all of the considered temperatures. Regarding the influence of the considered temperatures, only small differences in wrinkling behavior around the bigger corner bending and regarding the material draw-in between the gripping points are observed.

To investigate shear behavior w.r.t. to temperature in more detail, Figure 4.12 shows the evolution of the observed in-plane Green-Lagrange shear strain E_{12} and deformation rate $\dot{\gamma}$ by means of the median, lower (25 %) and upper (75 %) quantile for the different temperatures and under application of the Voigt-Kelvin approach for membrane modeling. Moreover, also the corresponding maximum values observed during membrane parametrization are shown.

Regarding the shear strain E_{12} (cf. Figure 4.12(a)), mostly no influence due to the varying temperature is observed. For fully closed tools, slightly higher shear strains are observed for a higher temperature. Thereby, 50 % of the observed shear strains exceed the parametrized range for fully closed tools. In contrast, a distinct influence of the varying temperature on the shear-rate $\dot{\gamma}$ is observed (cf. Figure 4.12(b)). For high remaining tool travels Δz, a lower scattering is observed for the lower temperatures, which becomes aligned between the different temperatures to the end of forming. This is accompanied with a monotonous increase of shear-rate. Thereby, shear-rates exceed the parametrized range only right before full tool closure.

(a) (b)

Figure 4.12: Evolution of the median, lower (25 %) and upper (75 %) quantile for the in-plane shear strain E_{12} (a) and the shear rate-rate $\dot{\gamma}$ (b) observed during forming for the orthotropic layup with the Voigt-Kelvin approach, as well as the related maximum values, $E_{12}^{\max}$ and $\dot{\gamma}^{\max}$, observed in membrane characterization.

4.4.2 Quasi-isotropic layup

Figure 4.13 shows the comparison of forming simulation to the experimental test for the quasi-isotropic layup and the fully formed part, under application of the Voigt-Kelvin approach for membrane and the generalized Maxwell approach for bending modeling. This combination of rheological models is also considered for thermoforming validation in the previous chapter (cf. Section 3.5.2). The final shape of the simulation result is shown for the high temperature. Moreover, the outer contours obtained for the different temperatures are compared to the experimental test in Figure 4.13(c). The outer contours are determined based on the approach outlined in Section 2.1.1.

In comparison of the final shape, a general agreement between forming simulation and experimental test is observed. This is valid for the general course of the outer contour as well as for unfolding of the outer areas. However, the too pronounced wrinkle predicted at the top of the part by forming simulation induces a rotation of the gripping are at the upper right vertice, which in turn induces a deviation in this area. Nonetheless, a generally good agreement of the outer contours is observed for the high and the intermediate temperature (cf. Figure 4.13(c)). On the contrary, the outer contour flares in horizontal direc-

(a) Sim. $T = 270\,^\circ$C (b) Experiment (c) Contours
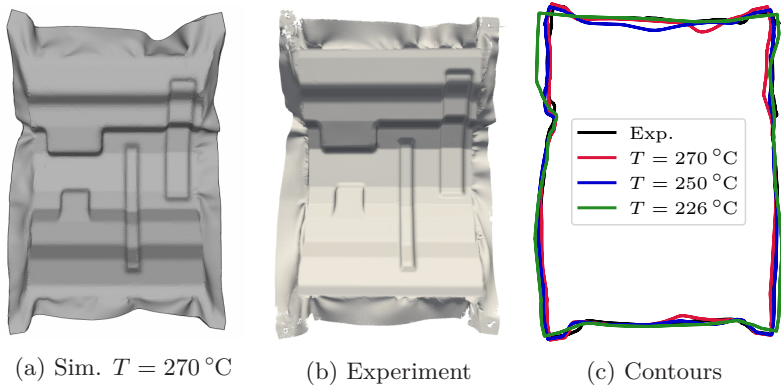
Figure 4.13: Isothermal forming simulation result (a), 3D measurement of the experimental test (b) and comparison of the outer contours (c) for the quasi-isotropic layup ($[0; -45; 90; 45]_\mathrm{s}$) and fully closed tools.

tion and the upper and lower side straighten for the low temperature, which reduces the agreement to the experimental test.

Additional results for the same isothermal model setup at the high temperature are shown in Figure 4.14 at several remaining tool travels Δz (left) and compared to experimental tests (right). The distinctively limited formability of the quasi-isotropic layup is well reflected by forming simulation, where the general amount, position and direction of wrinkles are well captured. This observation is in analogy to the results obtained with the superimposed approach in Section 3.5.2. Besides this, also the sag of the laminate due to gravity loading is generally well predicted, with a slight over-prediction especially for Stage 2. Although the general amount and direction of wrinkling behavior is well predicted, wrinkling behavior seems to be predicted slightly too less pronounced as observed in the experimental tests. This includes the area above the bigger corner bending in Stage 2 as well as some small wrinkles around the beads in Stage 3.

The aforementioned observations are valid for almost all variants regarding the varied modeling approaches and temperatures, as shown for the elemental modified mean curvature and a remaining tool travel of 5 mm in Figure 4.15. In comparison of the results of the generalized Maxwell approach to the results of the Voigt-Kelvin approach

169

Stage 1: $\Delta z = 30\,\mathrm{mm}$

Stage 2: $\Delta z = 17.5\,\mathrm{mm}$
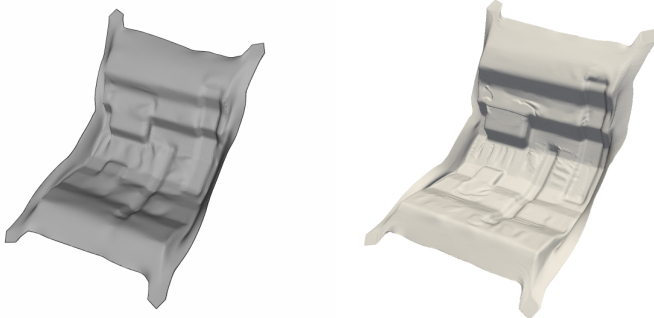

Stage 3: $\Delta z = 5\,\mathrm{mm}$
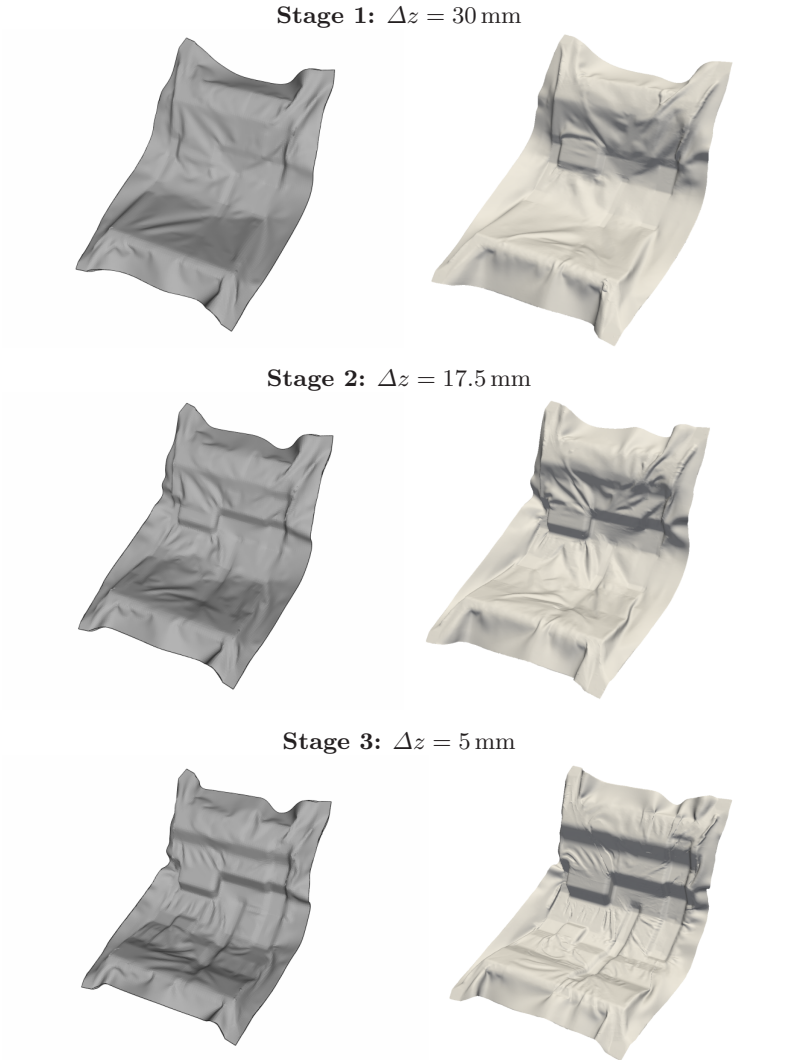
Figure 4.14: Comparison of isothermal forming simulation at 270 °C (left) to 3D measurements of experimental tests (right) for the quasi-isotropic layup ($[0; -45; 90; 45]_{\mathrm{s}}$) at several remaining tool travels Δz.

Experimental

Simulation: $T = 270\,^{\circ}\text{C}$

Simulation: $T = 250\,^{\circ}\text{C}$

Simulation: $T = 226\,^{\circ}\text{C}$

Generalized Maxwell **Voigt-Kelvin**

$\bar{\kappa}^{\text{el}}\ (\text{mm}^{-1})$

0.0 0.1 0.2
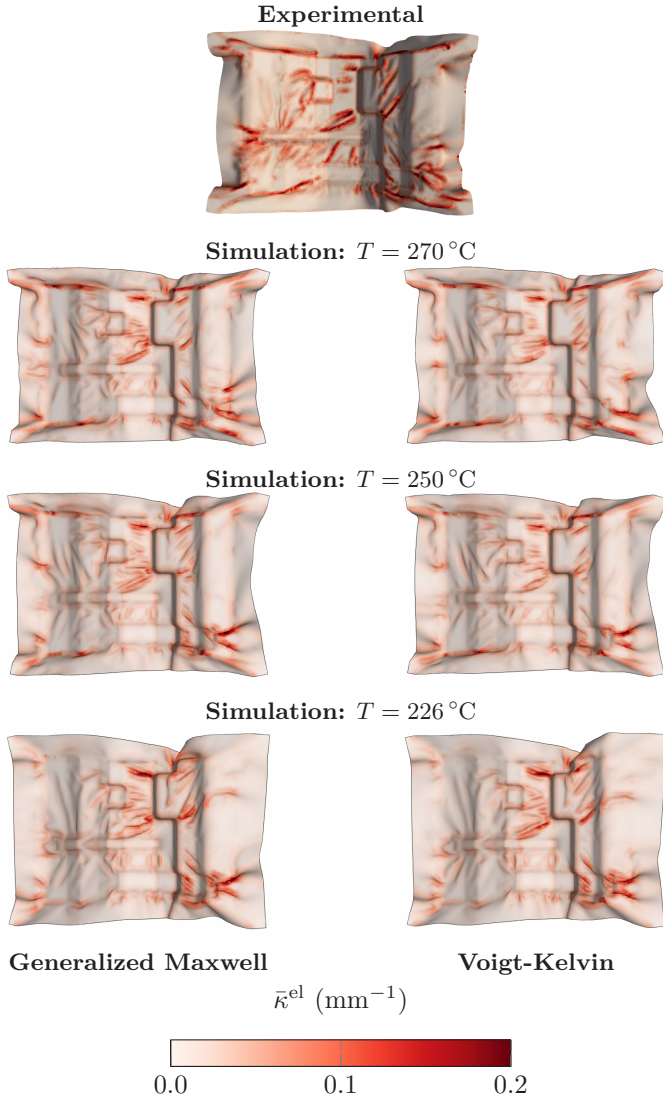
Figure 4.15: Comparison of isothermal forming simulation to an experimental test at a remaining tool travel of 5 mm for the quasi-isotropic layup under variation temperature and membrane modeling, following the generalized Maxwell (left) and Voigt-Kelvin (right) approach.

171

for membrane modeling, almost no difference is visible for all of the considered temperatures. Regarding the varied temperatures, the results at 226 °C show a better agreement to the experimental test for wrinkling behavior in the inner areas. Nonetheless, the agreement of the outer areas and contour is better for 270 °C and 250 °C, since only for these temperature unfolding of the outer areas is well captured. In contrast, the outer areas straighten for 226 °C.

To investigate the influence of the varying temperature on shear behavior, Figure 4.16 shows the evolution of the observed in-plane Green-Lagrange shear strain E_{12} and deformation rate $\dot{\gamma}$ by means of the median, lower (25 %) and upper (75 %) quantile for the different temperatures and under application of the Voigt-Kelvin approach for membrane modeling. Moreover, also the corresponding maximum values observed in membrane parametrization are shown.
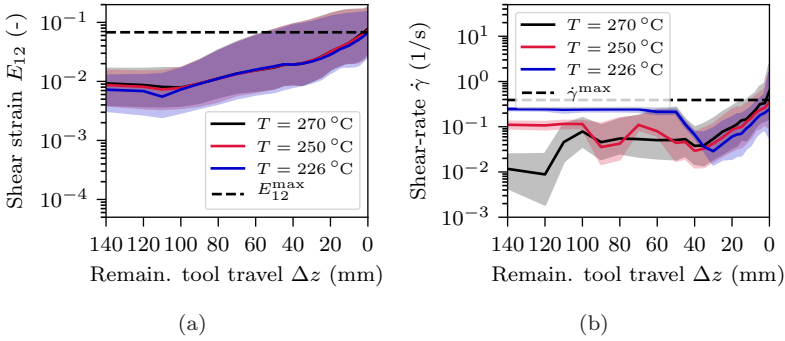

(a) (b)
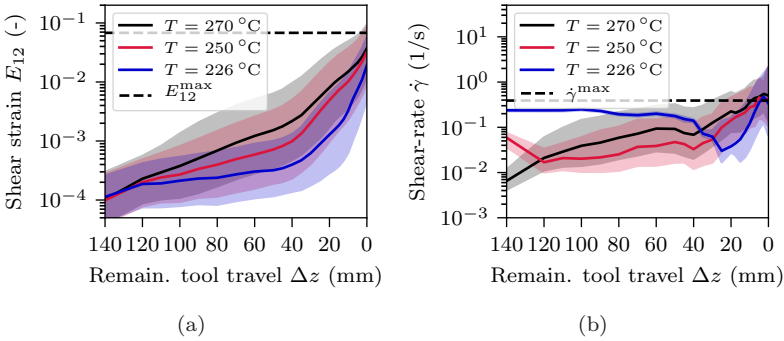
Figure 4.16: Evolution of the median, lower (25 %) and upper (75 %) quantile for the in-plane shear strain E_{12} (a) and the shear rate-rate $\dot{\gamma}$ (b) observed during forming for the quasi-isotropic layup with the Voigt-Kelvin approach, as well as the related maximum values, $E_{12}^{\max}$ and $\dot{\gamma}^{\max}$, observed in membrane characterization.

Regarding shear strain E_{12} (cf. Figure 4.16(a)), a distinct influence of temperature is observed, where a higher temperature induces higher shearing. In comparison of the final values for the median, comparable results are observed for 270 °C and 250 °C. Thereby, almost 75 % of the observed shear strains are below the maximum parametrized value $E_{12}^{\max}$. Regarding shear-rate $\dot{\gamma}$ (cf. Figure 4.16(b)), a similar behavior

as for the orthotropic layup is observed, where the lower temperatures diminish the scattering of shear rate. This is aligned for the different temperatures to the end of forming, accompanied with a monotonous increase of shear-rate. Thereby, about 50 % of the observed shear-rates to the end of forming are below the maximum value $\dot{\gamma}^{\mathrm{max}}$ observed in parametrization.

4.5 Discussion and conclusion

Nonlinear hyperviscoelastic modeling approaches for rate-dependent intra-ply deformation behavior in combination with a DKT ("Discrete Kirchhoff Theory") shell formulation implemented as user-element in the commercial FE solver Abaqus are presented and investigated in the scope of this chapter.

Shell formulation Initially, the DKT shell formulation is outlined. The deformation gradient for the membrane and the bending part is derived for this shell formulation. Based on this, arbitrary hyper(visco)elastic constitutive equations can be implemented into the shell formulation, since any further kinematic magnitude can be derived from the deformation gradient. This reveals the main enhancement compared to the approach presented in the previous chapter, where the deformation gradient was not available for the bending part. Based on the total (membrane and bending) deformation gradient, the same constitutive equations with different parameter sets are applied for membrane and bending modeling, yielding a physical decoupling of membrane and bending behavior.

Intra-ply material modeling approaches A nonlinear generalized Maxwell approach for rate-dependent modeling of membrane and bending behavior based on a multiplicative decomposition of the deformation gradient is presented. The application to both, membrane and bending behavior, is enabled by the definition of the constitutive equations for the (general) anisotropic case at finite strains. In the scope of this study, a St. Venant-Kirchhoff model is applied for the hyperelastic elements and a hyperbolic sine law for the viscous flow elements. However, any hyperelastic constitutive equation can

be adopted and besides this, a large variety of different flow rules exists in literature for this type of rheological framework [246, 259], which gives this framework many opportunities to be applied to other materials and material classes in composite forming simulation.

The approach outlined in the scope of this chapter is the first of this type in the context of viscoelasticity in composite forming simulation. In the context of dissipative modeling of shear behavior of woven engineering textiles, a similar approach also based on a multiplicative decomposition of the deformation gradient is presented by Denis et al. [157]. In this study, however, rate-dependency is not addressed. Nonetheless, including dissipative effects for capturing non-monotonous loading is expected to be a reasonable further development for composite forming simulation. An approach for intra-ply modeling for composite forming considering both, rate-dependency and dissipation, is not available yet. Nonetheless, the enhancement of the presented generalized Maxwell approach to a viscoplastic approach would be straightforward by adapting the constitutively defined flow rules. This would then require further characterization tests including e.g. hysteresis analyses, as proposed by Ropers et al. [241] for bending characterization of organosheets using the rheometer bending test proposed by Sachs et al. [83]. Nonetheless, the presented rheological framework could serve as a basis for future investigations in the context of viscoplasticity.

Intra-ply parametrization The hyperviscoelastic nonlinear generalized Maxwell approach as well as the hyperviscoelastic nonlinear Voigt-Kelvin approach outlined in the previous chapter are successfully parametrized to isothermal characterization results for membrane and bending behavior at several temperatures and deformation rates. It turns out that only the generalized Maxwell approach is capable to represent the whole material characteristic for both, membrane and bending behavior, whereas the Voigt-Kelvin approach is capable to describe material behavior only approximately. This applies especially for lower temperatures and high deformation rates. However, parametrization is straightforward for the Voigt-Kelvin approach, since the elastic stiffness and the viscosity can be directly related to the slope and offset of the moment-deflection-curves, re-

spectively. In contrast, parametrization of the generalized Maxwell approach is more challenging. The outlined substitute models, however, serve as remedy, since a large number of iterations can be conducted in short time. This is necessary for global optimization for the inverse identification of material parameters, which could not be handled by a detailed FEA analysis of the according characterization test setups.

Forming simulation Finally, the presented approach for intra-ply material modeling is applied to thermoforming simulation of a complexly shaped geometry for two different layups. Thereby, membrane modeling approaches are varied, following either the nonlinear generalized Maxwell approach or the nonlinear Voigt-Kelvin approach. In contrast, the nonlinear generalized Maxwell approach is kept for bending modeling, since bending modeling is analyzed in detail in the previous chapter. Beyond that, the temperature prescribed for the isothermal forming simulations is varied for temperatures well above the melting temperature of the thermoplastic. A good agreement between forming simulation and experimental tests is observed, where the outer contour and general shape are well captured for both layups. Wrinkling behavior, however, is predicted too less pronounced for the orthotropic layup, since only material accumulations are predicted by simulation where a large fold is observed in experimental tests. In contrast, the amount and direction of wrinkles is well reflected for the quasi-isotropic.

In comparison of the varied nonlinear Voigt-Kelvin and nonlinear generalized Maxwell approach for membrane modeling, a negligible difference is observed for all of the temperatures. Therefore, it can be concluded that a nonlinear Voigt-Kelvin approach is sufficient to capture the rate-dependent membrane deformation behavior in thermoforming simulation for the material investigated in the scope of this study. Nonetheless, the rheological framework of the proposed nonlinear generalized Maxwell approach might become useful for the enhancement to viscoplastic intra-ply modeling, as outlined above.

In comparison of the forming simulation under variation of temperature, a slight influence is observed for the orthotropic layup. On the contrary, a more pronounced influence is observed for the quasi-

isotropic layup, where an influence on the outer contour as well as on wrinkling behavior is observed. Increasing wrinkling behavior for lower temperatures was also observed in isothermal thermoforming simulation well above the melting temperature of the according thermoplastic by Guzman-Maldonado et al. [261]. Nonetheless, the according results seem more sensitive compared to the results of this study. However, bending stiffness was assumed constant in their study, which explains the higher sensitivity of wrinkling behavior compared to the results of this study. In a more detailed comparison of the thermoforming results to the experimental test for the quasi-isotropic layup at 226 °C, a better agreement to the experimental is observed for the inner areas, especially around the bigger corner bending and the beads. In contrast, the agreement of the outer areas and contour is better for the intermediate, which seems contradictory in a first glance. However, it is expected that the cause of this observation is pronounced local cooling of the inner areas, which is to be expected due to local tool-ply contact (gap conductance). In contrast, the outer areas are exposed solely to the cooler environment (convection), where a less pronounced cooling is expected. Hence, the according results are an indicator that local temperature influences the formability prediction, which makes the development and investigation of a thermomechanical approach for thermoforming simulation desirable. The development and investigation of a coupled thermomechanical approach is pursued in Chapter 6.

Moreover, the evolution of the in-plane shear strain and shear-rate throughout forming is evaluated. It is observed that both exceed the maximum value observed in parametrization, which indicates an extrapolation membrane modeling. However, exceeding shear-rates are limited to low remaining tool travels, where wrinkles are well developed. Therefore, the characterized range of deformation rates is expected to be sufficient for the considered forming velocity. In contrast, the maximum shear strains observed during forming exceed the maximum value observed in parametrization for the orthotropic layup already for large remaining tool travels. Hence, characterization results at higher shear strains are desirable. The characterization tests employed for this study apply moderate deflection angles. The suitability of the torsion bar test for larger deflection angles is to be investigated. Thereby, special attention should be paid for in-plane fiber bending in

material modeling, which is not captured by first order modeling approaches usually applied for composite forming. This applies also for this study. Nonetheless, current research focuses on higher order approaches in the context of generalized continua for composite forming simulation [74, 160, 161, 163, 164]. Such approaches would enable to account for fiber bending in three-dimensional modeling approaches and would also enable to account for the fiber bending most likely observed in the torsion bar test for large deflection angles.

5 Isotropic and anisotropic inter-ply slip modeling

Abstract

Inter-ply slip modeling approaches using the commercial FE solver Abaqus, in combination with user-defined contact constitutive equations, are presented. These user-defined contact constitutive equations are necessary, since Abaqus built-in modeling techniques enable either tacking in normal direction or friction in tangential, but not both simultaneously. First, an isotropic approach accounting for the rate-, pressure-, and temperature-dependent frictional behavior is presented, which is well-established in thermoforming simulation. Subsequently, an advanced approach accounting additionally for the relative orientation between the slipping plies is proposed. Parametrization results reveal that the employed linear model is sufficient for the investigated material. In application of the anisotropic inter-ply slip modeling approach to forming simulation, negligible differences are observed compared to an isotropic approach, which is expected to be reducible to the comparably high inter-ply rigidity, yielding small slip distances throughout forming. This insight might change for other composite forming processes with more pronounced inter-ply slip.

In the scope of this study, continuous thermoforming simulation is investigated. Therefore, each ply of the stacked laminate is modeled by separate element layers. The resulting interfaces split into tool-ply and ply-ply interfaces and the deformation mechanisms to be considered at these interfaces can be categorized into tool-ply slip, ply-ply slip and tacking at the ply-ply interfaces (cf. Figure 5.1).
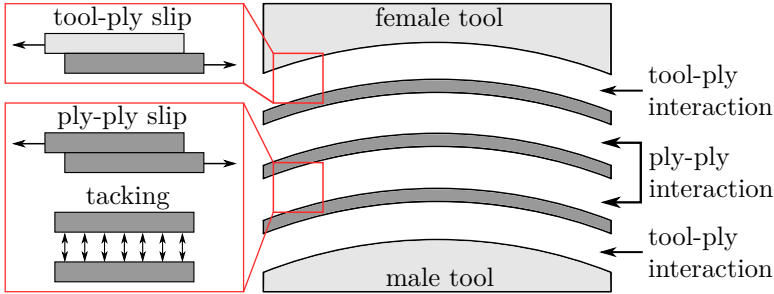
Figure 5.1: Schematic illustration of inter-ply mechanisms in continuous FE forming simulation.

Experimental studies in literature [52, 96, 97, 98, 99, 100, 101], as well as the experimental investigations in this study (cf. Section 2.3.4) reveal that inter-ply slip of thermoplastic prepregs is depending on slip velocity, transversal pressure and temperature at process conditions. The consideration of these dependencies in continuous thermoforming simulation is well established [57, 119, 218, 219]. Besides this, also an influence of relative orientation between the slipping plies on inter-ply slip is observed in experimental studies in literature [96, 97], as well as in the experimental investigations of this study (cf. Section 2.3.4). This mechanism was first incorporated and investigated in continuous thermoforming simulation by Dörr et al. [236], based on an approach implemented in the commercial FE solver Abaqus in combination with several user-subroutines.

In the following, initially an isotropic approach for inter-ply slip modeling is outlined (Section 5.1). This includes the discussion of the restrictions of the built-in methods of the commercial FE solver Abaqus for inter-ply modeling and the resulting necessity to use the contact user-interface (VUINTERACTION). Subsequently, an anisotropic ap-

proach for inter-ply slip modeling is presented (Section 5.2). This approach is based on the aforementioned approach [236], which is revisited and improved in a joint work with Christian Poppe (KIT-FAST) for numerical efficiency, based on the advanced modeling techniques for information exchange between Abaqus user-subroutines by means of global arrays worked out by Poppe et al. [251]. Finally, both approaches are parametrized (Section 5.3) and applied to isothermal thermoforming simulation (Section 5.4), in order to investigate the necessity to account for anisotropic inter-ply slip in thermoforming simulation.

5.1 Isotropic inter-ply slip modeling

The in Abaqus called "General Contact" [242] algorithm is applied for inter-ply modeling in the scope of this study. This contact algorithm is based on slave nodes and proximal master surface points, which are called proximity points. Based on this, a local and orthonormal coordinate system e_i is introduced at each proximity point, which describes the normal distance ξ_3 and the tangential slip $\boldsymbol{\xi}_t$ of the two interacting surfaces, as schematically illustrated in Figure 5.2. Thereby, no proximity points exist for slave nodes that are separated from the master surfaces, which is defined by the so-called tracking thickness.
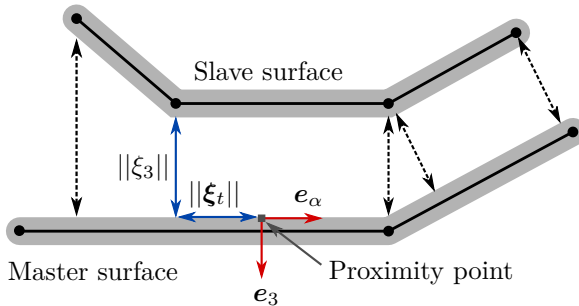
Figure 5.2: Schematic illustration of the general contact algorithm based on the identification of the interaction between the master surface and slave nodes by means of proximity points on the master surface.

Based on the normal distance ξ_3 and the tangential slip $\boldsymbol{\xi}_t$, the contact tractions $\boldsymbol{Z}$ are determined, which are naturally split into normal traction $\boldsymbol{N}$ and tangential traction $\boldsymbol{T}$ ($\boldsymbol{Z} = \boldsymbol{N} + \boldsymbol{T}$). Based on these contact tractions, non-penetration, tacking, as well as sticking and sliding can be modeled.

Under application of Abaqus built-in methods, tacking can be accounted for by cohesive zones. As soon as cohesive zones are used in Abaqus, however, slipping (friction) is modeled solely if the cohesive zone is fully damaged, which is described by a single damage variable for both, normal and tangential direction. Thus, either tacking in normal direction or slipping (friction) in tangential direction can be modeled by means of Abaqus built-in methods. As remedy, the contact user-interface (VUINTERACTION) is applied for modeling ply-ply interaction. Based on this, normal and tangential behavior can be described separately. The according constitutive equations for isotropic inter-slip modeling are outlined in the following.

Normal traction The non-penetration condition in normal direction is regularized by means of Penalty method [262] and the introduction of a Penalty stiffness ϵ_N, if the interface is in a pressure state. In contrast, the stiffness ϵ_T is introduced if the contact is in a tension state, to account for the tacking between the plies, as long as a maximum admissible distance $\xi_3^{\max}$ in normal direction is not exceeded. This results in the contact constitutive equation for the normal traction ($\boldsymbol{N} = N\boldsymbol{e}_3$) defined by

$$N = \begin{cases} \epsilon_N \xi_3 & , \xi_3 > 0 & \text{(penetration)} \\ \epsilon_T \xi_3 & , \xi_3^{\max} < \xi_3 \leq 0 & \text{(tacking)} \\ 0 & , \xi_3 < \xi_3^{\max} & \text{(separation)} \end{cases} , \qquad (5.1)$$

where ξ_3 is the distance ($\xi_3 \leq 0$) or the penetration ($\xi_3 > 0$) of the interacting surfaces in normal direction.

Tangential direction   Frictional behavior is modeled in tangential direction. A yield function defining the transition from sticking to slipping is given for this purpose for the general anisotropic case by [262]

$$\Phi := \sqrt{f^{ij}T_iT_j} - 1 \quad \text{with} \quad f^{ij} = \frac{G^{ij}}{\left(\tau^{\text{crit}}_{ij}\right)^2}, \tag{5.2}$$

where G^{ij} are contravariant metric coefficients, T_α the tangential traction components and τ^{crit}_{ij} an anisotropic yield stress. This relation can be reduced for the isotropic case to [262]

$$\Phi := \frac{\sqrt{G^{ij}T_iT_j}}{\tau^{\text{crit}}} - 1, \tag{5.3}$$

where τ^{crit} is the isotropic yield stress, which is also referred to as critical tangential traction. This yield function defines, whether the interacting surfaces stick ($\Phi \leq 0$) or slip ($\Phi > 0$). In the scope of this study, the stick-slip-condition is regularized by Penalty method for the numerical implementation, resulting in the constitutive equation for the tangential traction given by

$$\boldsymbol{T} = \begin{cases} \epsilon_t\boldsymbol{\xi}_t & ,\Phi \leq 0 \quad \text{(sticking)} \\ \tau^{\text{crit}}\dfrac{\dot{\boldsymbol{\xi}}_t}{||\dot{\boldsymbol{\xi}}_t||} & ,\Phi > 0 \quad \text{(sliding)} \end{cases}, \tag{5.4}$$

where $\boldsymbol{\xi}_T$ is the displacement in tangential direction ($\boldsymbol{\xi}_t = \xi_\alpha\boldsymbol{e}_\alpha$) and ϵ_t the Penalty stiffness in tangential direction. The yield stress τ^{crit} is modeled by means of a Coulomb frictional law superimposed with a slip-rate-dependent and a constant offset term, including a dependency on ξ_3, the distance respectively penetration in normal direction:

$$\tau^{\text{crit}} = \begin{cases} \mu N + \eta||\dot{\boldsymbol{\xi}}_t|| + \tau_0 & ,\xi_3 > 0 & \text{(penetration)} \\ \eta||\dot{\boldsymbol{\xi}}_t|| + \tau_0 & ,\xi_3^{\text{max}} < \xi_3 \leq 0 & \text{(tacking)} \\ 0 & ,\xi_3 < \xi_3^{\text{max}} & \text{(separation)} \end{cases}, \tag{5.5}$$

where μ, η and τ_0 are material parameters. Thereby, it is to be noted that the material parameter μ is in general different from the CoF adopted for the experimental investigations in Section 2.3.4. Based on these constitutive equations for the normal traction $\boldsymbol{N}$ and the

tangential traction $\boldsymbol{T}$, tacking and inter-ply slip, including the dependency of inter-ply slip on transversal pressure and slip rate, are captured for the application to isothermal thermoforming simulation. This isothermal inter-ply slip approach is straightforward to be extended to a temperature-dependent approach by defining the material parameters as a function of temperature, due to the linear nature of the constitutive equations.

5.2 Anisotropic inter-ply slip modeling

Experimental studies reveal that inter-ply slip depends on the relative fiber orientation between the slipping plies. To account for this material characteristic, the principal material orientations $\boldsymbol{a}_{ij}$ of the slipping ply j are the essential internal variables for the formulation of a suitable inter-ply slip constitutive equation. Based on this, also the relative angle φ_i^{rel} between the principal material orientation i of the slipping plies (cf. Figure 5.3) can be defined as internal variable.
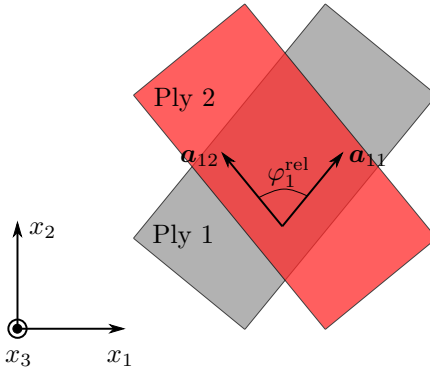
Figure 5.3: Schematic illustration of the relative orientation φ_1^{rel} as the the angle between the first principal material orientation of the slipping plies.

Internal variables   Unfortunately, neither the principal material orientation nor the elemental deformation gradient is supplied as input value by the employed contact user-interface (VUINTERACTION).

This impedes the direct determination of the principal material orientations $\boldsymbol{a}_{ij}$ or the relative orientation φ^{rel} between the slipping plies. As remedy, the principal material orientations $\boldsymbol{a}_{ij}$ are determined in an additional user-interfaces and transfered to the contact user-interface by so-called global arrays [242]. First, the local deformation gradient $\boldsymbol{F}$ is determined in a global and spatially fixed system $\{\boldsymbol{i}_i\}$ for each ply through

$$\boldsymbol{F} = \boldsymbol{R}^{\mathrm{GN}} \cdot \boldsymbol{U}^{\mathrm{GN}}, \tag{5.6}$$

by means of an elemental user-defined field (VUSDFLD). Here, $\boldsymbol{R}^{\mathrm{GN}}$ is the orthogonal rotation tensor describing the rotation of Green-Naghdi's frame w.r.t. to $\{\boldsymbol{i}_i\}$ and $\boldsymbol{U}^{\mathrm{GN}}$ is the right stretch tensor in Green-Naghdi's frame. The rotation tensor $\boldsymbol{R}^{\mathrm{GN}}$ is supplied by the elemental user-defined field (VUSDFLD). In contrast, the right stretch tensor $\boldsymbol{U}^{\mathrm{GN}}$ is made available in the user-defined field through user-defined state variables (SDV) defined in the user-interface for material modeling (VUMAT). Based on this, the principal material orientations in the global system $\{\boldsymbol{i}_i\}$ are obtained for each ply as elemental value through

$$\boldsymbol{a}_i^{\mathrm{el}} = \frac{\boldsymbol{F} \cdot \boldsymbol{A}_i^{\mathrm{el}}}{||\boldsymbol{F} \cdot \boldsymbol{A}_i^{\mathrm{el}}||}, \tag{5.7}$$

where $\boldsymbol{A}_i^{\mathrm{el}}$ are the principal material orientations in the initial configuration. Since the employed contact user-interface (VUINTERACTION) uses nodal information only, the elemental principal material orientation $\boldsymbol{a}_i^{\mathrm{el}}$ is additionally interpolated to a nodal principal material orientation $\boldsymbol{a}_i^{\mathrm{node}}$ in a user-defined nodal field (VUFIELD). This magnitude is transferred to the contact user-interface to determine the relative orientation φ_i^{rel} between the slipping plies by:

$$\varphi_i^{\mathrm{rel}} = \arccos\left(\frac{|\boldsymbol{b}_i^{\mathrm{m}} \cdot \boldsymbol{b}_i^{\mathrm{s}}|}{||\boldsymbol{b}_i^{\mathrm{m}}|| \, ||\boldsymbol{b}_i^{\mathrm{s}}||}\right) \quad \text{with} \quad \boldsymbol{b}_i^{\mathrm{m}} = \boldsymbol{a}_i^{\mathrm{surf}} - \left(\frac{\boldsymbol{a}_i^{\mathrm{surf}} \cdot \boldsymbol{e}_3}{||\boldsymbol{e}_3||^2}\right)\boldsymbol{e}_3$$

$$\text{and} \quad \boldsymbol{b}_i^{\mathrm{s}} = \boldsymbol{a}_i^{\mathrm{node}} - \left(\frac{\boldsymbol{a}_i^{\mathrm{node}} \cdot \boldsymbol{e}_3}{||\boldsymbol{e}_3||^2}\right)\boldsymbol{e}_3, \tag{5.8}$$

where $\boldsymbol{e}_3$ is the normal direction of the contact master surface (cf. Figure 5.2) and $\boldsymbol{b}_i^{\mathrm{m}}$ and $\boldsymbol{b}_i^{\mathrm{s}}$ are the principal material orientations of the master surface and slave node projected onto the master surface, respectively. Thereby, the master surface principal material orientations $\boldsymbol{a}^{\mathrm{surf}}$ are obtained by an interpolation from the nodes of the master surface. Based on this, the essential internal status variable φ_i^{rel} ranging between $0\,\mathrm{deg}$ and $90\,\mathrm{deg}$ is obtained, which enables the consideration of the relative fiber orientation between the slipping plies in the contact constitutive equations.

Constitutive modeling For inter-ply slip modeling, two principles for anisotropy have to be distinguished. On the one hand, the yield function Φ can be anisotropic (cf. Equation 5.2), which implies that slip conditions in the different principal material directions differ. Besides this, the yield function itself can also depend on the relative orientation between the two slipping plies.

In the scope of this study, it is assumed that the yield function Φ is isotropic (cf. Equation 5.3), but depending on the relative fiber orientation between the first principal material directions of the interacting plies. This assumption is necessary, since only the sliding along fiber direction can be characterized with the testing setup applied in Section 2.3.4. Nonetheless, the consideration of the related dependency on the orientation of the slipping plies remains. Therefore, inter-ply slip modeling is referred to as anisotropic, although an isotropic but nonlinear yield function is applied.

For constitutive modeling, only the first principal material orientation is considered ($\varphi^{\mathrm{rel}} = \varphi_1^{\mathrm{rel}}$), due to the unidirectional fiber-reinforcement investigated in the scope of this study. Henceforth, anisotropy is considered by means of the definition of the yield stress τ^{crit} depending on the relative fiber orientation φ^{rel}:

$$
\tau^{\mathrm{crit}} = \left\{ \begin{array}{ll}
\mu(\varphi^{\mathrm{rel}})N + \eta(\varphi^{\mathrm{rel}})\|\dot{\boldsymbol{\xi}}_{\mathrm{t}}\| + \tau_0(\varphi^{\mathrm{rel}}) & ,\xi_3 > 0 \\
\eta(\varphi^{\mathrm{rel}})\|\dot{\boldsymbol{\xi}}_{\mathrm{t}}\| + \tau_0(\varphi^{\mathrm{rel}}) & ,\xi_3^{\mathrm{max}} < \xi_3 \leq 0 \\
0 & ,\xi_3 < \xi_3^{\mathrm{max}}
\end{array} \right. .
$$

$$(5.9)$$

5.3 Parametrization of inter-ply slip modeling

The characterization results outlined in Section 2.3.4 are adopted for parametrization of inter-ply slip. Inter-ply slip is parametrized in the stationary regime for tool-ply and ply-ply slip, under variation of transversal pressure ($p^\perp = N$), slip velocity ($v^{\text{slip}} = ||\dot{\xi}_{\text{t}}||$) and temperature T. Henceforth, the peak observed in inter-ply slip characterization (cf. Section 2.3.4) is not considered for parametrization. The frictional models in Equation 5.5 and 5.9 are considered for the isotropic and anisotropic case, respectively. The according parameters are identified inversely by an evolutionary algorithm with the normalized summed squared error as target function:

$$SSEN = \frac{1}{N} \sum_{i=1}^{N} \left(\frac{(\tau_i^{\text{crit}} - \tau_i)^2}{(\tau_i)^2} \right), \qquad (5.10)$$

where τ_i^{crit} and τ_i are the predicted and the experimentally determined yield stresses, also referred to as friction stresses. For optimization, the open access software toolkit Dakota [260] is applied.

5.3.1 Isotropic inter-ply slip

For parametrization of the isotropic approach, the pull-out characterization results for tool-ply and ply-ply slip presented in the master's thesis of Michael Lang [233] are adopted, since only in this study transversal pressure $p^\perp$, slip rate v^{slip} and temperature T are varied with no relative orientation between the slipping plies following a full-factorial test plan. The according levels are listed in Table 5.1. Five replicates are conducted for the center level, whereas only a single replicate is conducted for all other levels.

Inter-ply slip is parametrized for the stationary regime from 20 mm to 40 mm slip distance and one parameter set following Equation 5.5 is determined for each temperature. Since the adopted characterization results are determined by pull-out tests, the current transversal pressure $p_1^\perp$ is determined by

$$p_1^\perp(u^{\text{slip}}) = p_0^\perp A_0^{\text{fric}} \left(\frac{l_0^{\text{fric}}}{l_0^{\text{fric}} - u^{\text{slip}}} \right), \qquad (5.11)$$

Factors	Unit	Levels
Transversal pressure $p^\perp$	(MPa)	$\{0.0165 \; ; 0.0353 \; ; 0.0579\}$
Slip rate v^{slip}	(mm/s)	$\{0.83 \; ; 2.5 \; ; 8.33\}$
Temperature T	(°C)	$\{210 \; ; 240 \; ; 260\}$

Table 5.1: Factors and according levels for isotropic inter-slip characterization for the tool-ply and the ply-ply interfaces.

where u^{slip} is the slip distance, $p_0^\perp$ the initial transversal pressure and l_0^{fric} the initial length of the friction surface in slip direction. The current transversal pressure $p_1^\perp$ is considered for parametrization.

Ply-ply slip A comparison of the parametrization results for the isotropic ply-ply slip to the experimental tests is shown in Figure 5.4 w.r.t. the mean friction stresses observed in the stationary regime. The experimental results reveal a dependency on all of the varied parameters, where an increase in friction stress is observed for increasing slip velocity v^{slip}, increasing transversal pressure $p^\perp$ and decreasing temperature T.

In comparison of the sensitivity of the varied parameters, slip rate shows the most significant influence. These sensitivities are observed for all levels, excluding one outlier at 210 °C, 0.0165 MPa and 8.33 mm/s, which does not follow the systematic pressure-, rate- and temperature-dependency. Since only one replicate is available for this level, this replicate is not considered for parameter identification.

In comparison of the mean friction stress in the stationary regime predicted by Equation 5.5 to the experimental tests, in general, minor deviations are observed. The dependency of friction stress on slip rate and pressure is well captured for each of the considered temperatures. The observed deviation between prediction and experimental tests could be further minimized by higher order approaches, such as a Cross approach for the rate-dependent term η. However, since the deviations between experimental tests and the friction model are comparably low, the linear friction model is kept for simplicity.
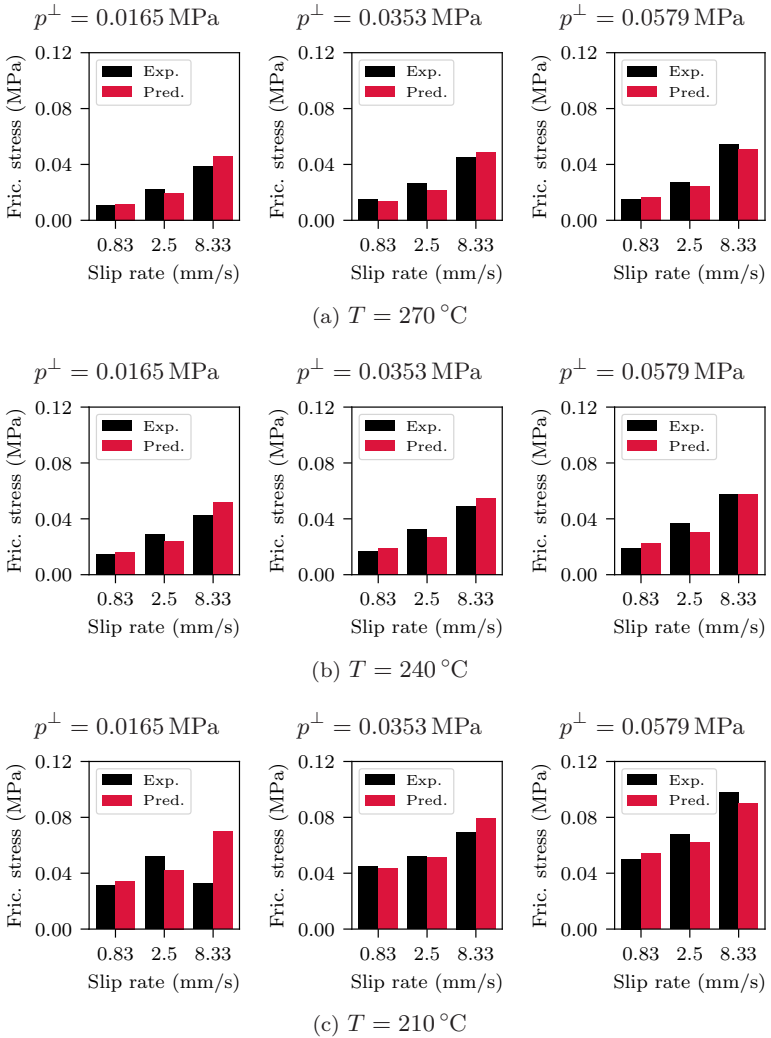
Figure 5.4: Parametrization results for ply-ply slip in the stationary regime at several temperatures T, transversal pressures $p^\perp$ and slip rates v^{slip} shown w.r.t. the mean friction stress observed in the stationary regime.

$p^\perp = 0.0165\,\mathrm{MPa}$ $p^\perp = 0.0353\,\mathrm{MPa}$ $p^\perp = 0.0579\,\mathrm{MPa}$

(a) $T = 270\,^\circ\mathrm{C}$

$p^\perp = 0.0165\,\mathrm{MPa}$ $p^\perp = 0.0353\,\mathrm{MPa}$ $p^\perp = 0.0579\,\mathrm{MPa}$

(b) $T = 240\,^\circ\mathrm{C}$

$p^\perp = 0.0165\,\mathrm{MPa}$ $p^\perp = 0.0353\,\mathrm{MPa}$ $p^\perp = 0.0579\,\mathrm{MPa}$

(c) $T = 210\,^\circ\mathrm{C}$
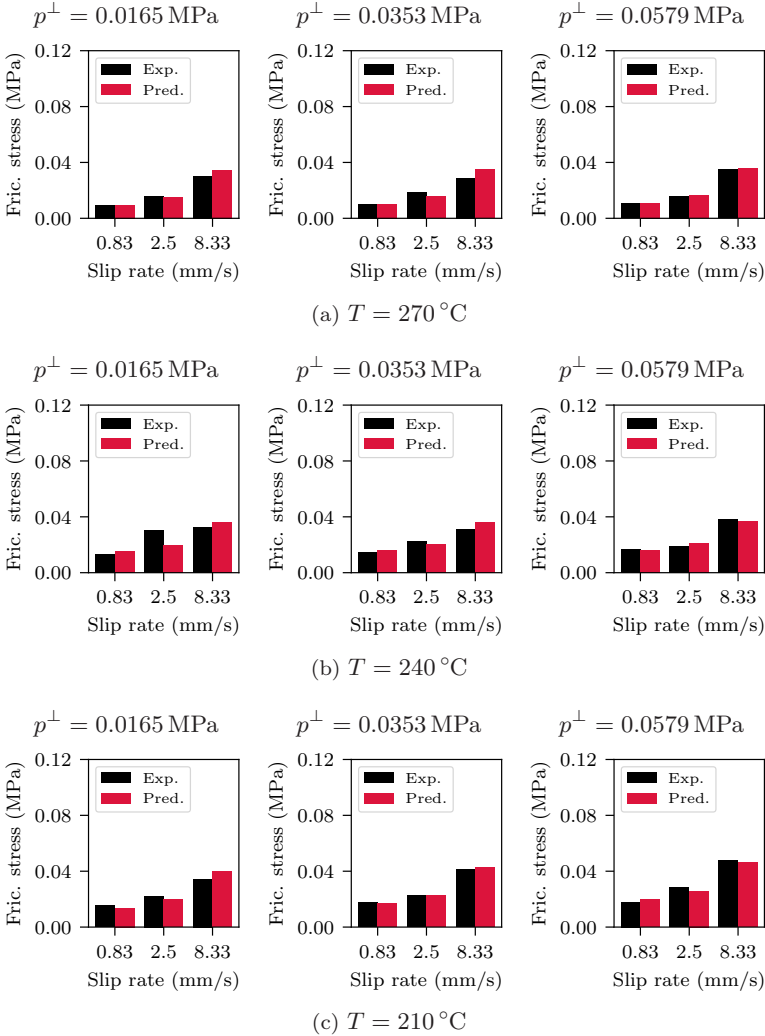
Figure 5.5: Parametrization results for tool-ply slip in the stationary regime at several temperatures T, transversal pressures $p^\perp$ and slip rates v^{slip} shown w.r.t. the mean friction stress observed in the stationary regime.

Tool-ply slip   Also the tool-ply characterization results are adopted for parametrization of Equation 5.5 separately for each temperature for consistency. Thereby, it is to be noted that in thermoforming simulation the coefficient of friction (CoF) is assigned discretely in dependence of slip rate, transversal pressure and temperature, since the Abaqus built-in contact modeling approach is adopted for the tool-ply interfaces. Based on this, the Abaqus built-in interpolation is adopted to capture the varying coefficient of friction.

A comparison of the parametrization results for the isotropic tool-ply slip to the experimental tests is shown in Figure 5.5 w.r.t. the mean friction stress observed in the stationary regime. Compared to the ply-ply characterization results, lower friction stresses are observed. Nonetheless, the dependencies on slip-rate v^{slip}, transversal pressure $p^\perp$ and temperature T are maintained. In contrast, temperature T shows a lower influence on friction stress for the tool-ply interface compared to the ply-ply interface.

In analogy to the ply-ply parametrization, minor deviations between the prediction and the experimental tests are observed. The dependency of friction stress on slip rate and pressure is well captured for each of the considered temperatures. Therefore, this linear model would also be applicable to inter-ply slip modeling of the tool-ply interfaces.

5.3.2 Anisotropic inter-ply slip

The pull-through characterization results for ply-ply slip presented in the bachelor's thesis of Florian Schulz [234] are adopted for parametrization of the anisotropic inter-ply slip modeling approach, since only in this study transversal pressure $p^\perp$, slip rate v^{slip} and relative orientation φ^{rel} are varied following a full-factorial test plan. The according levels at a constant temperature of 240 °C are listed in Section 2.3.4.2 and Table 2.2. Five replicates are conducted for each level.

Anisotropic ply-ply slip is parametrized for the stationary regime from 40 mm to 60 mm slip distance. For each of the two considered relative orientations φ^{rel}, one parameter set following Equation 5.9 is determined. The parametrization results are shown in Figure 5.6 w.r.t. to the mean friction stress observed in the stationary regime.

191

(a) $\varphi^{\mathrm{rel}} = 0\,\mathrm{deg}$

(b) $\varphi^{\mathrm{rel}} = 90\,\mathrm{deg}$
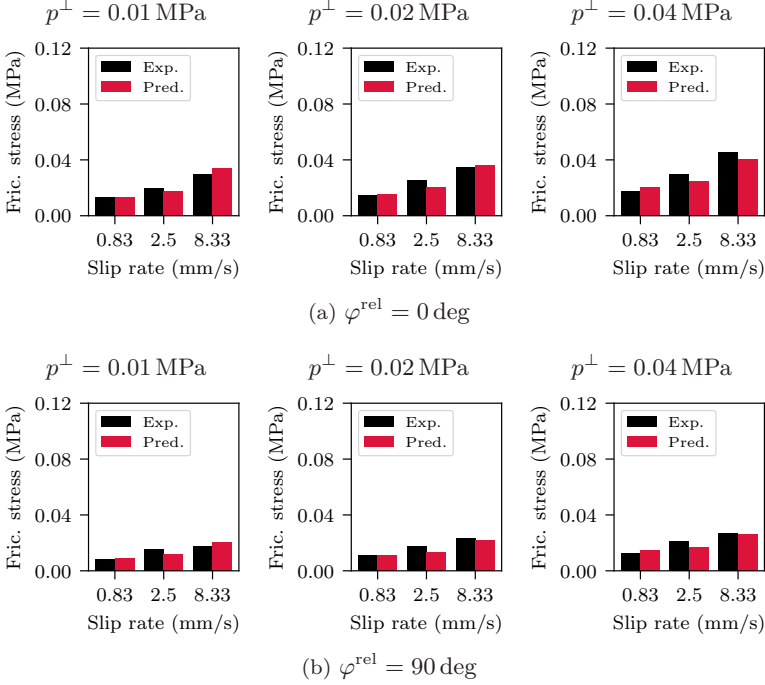
Figure 5.6: Parametrization results for ply-ply slip in the stationary regime at several transversal pressures $p^{\perp}$ and slip rates v^{slip} at 240 °C and under variation of relative orientation φ^{rel} shown w.r.t. the mean friction stress observed in the stationary regime.

The experimental results reveal a dependency on all of the varied parameters. In analogy to the isotropic ply-ply slip, an increase in friction stress is observed for increasing transversal pressure $p^{\perp}$ and slip rate v^{slip}. Besides this, a systematic decrease of friction stress of approximately 40 % is observed for the relative orientation φ^{rel} of 90 deg compared to the results with 0 deg relative orientation. In comparison of the results with 0 deg to the isotropic ply-ply slip results (cf. Figure 5.4), lower friction stresses are observed, where it is to be noted that not all of the factor levels are directly comparable w.r.t. the transversal pressure. A possible cause for this deviation

could be the different characterization setup w.r.t. pull-out and pull-through testing. In comparison of the mean friction stress observed in the stationary regime predicted by Equation 5.9 to the experimental results, again, minor deviations are observed. The dependency of friction stress on slip rate v^{slip} and transversal pressure $p^{\perp}$ is well captured for both relative orientations φ^{rel}. Hence, the linear constitutive equations are kept for simplicity also for the anisotropic inter-ply slip modeling at the ply-ply interfaces rather than adopting a higher order approach, in analogy to the parametrization of the isotropic inter-ply slip in Section 5.3.1.

5.4 Analyzing anisotropic inter-ply slip in forming simulation

The anisotropic modeling approach presented in Section 5.2 is applied to isothermal thermoforming simulation in the scope of this section, in order to investigate the necessity to account for anisotropic inter-ply slip in thermoforming simulation. Thereby, three different scenarios are considered. First, inter-ply slip is modeled under consideration of the relative orientation between the slipping ($\varphi^{\mathrm{rel}} = \mathrm{var.}$), where a linear relation between the parameter sets at 0 deg and 90 deg relative orientation is assumed. Second, a relative orientation of 0 deg is prescribed and kept constant for inter-ply slip modeling throughout forming ($\varphi^{\mathrm{rel}} = 0\,\mathrm{deg}$). Third, a relative orientation of 90 deg is prescribed and also kept constant ($\varphi^{\mathrm{rel}} = 90\,\mathrm{deg}$). For all scenarios, the parametrization presented in Section 5.3.2 is adopted.

The generic geometry and the according process setup presented in Section 2.2.1 is investigated in thermoforming simulation. Two different layups, which namely are an orthotropic layup ($[0; 90]_{2\mathrm{s}}$) and a quasi-isotropic layup ($[0; -45; 90; +45]_{\mathrm{s}}$), in combination with the intermediate process settings (cf. Table 2.1), are considered. The model setup described in detail in Section 3.5.2 remains unchanged, except for the above outlined changes regarding inter-ply material modeling.

Results orthotropic layup Figure 5.7 shows the results for the orthotropic layup for several remaining tool travels Δz, under application of the anisotropic inter-ply slip modeling approach. The results show a moderate and localized change of the relative orientation φ^{rel}. The change in relative orientation is observed in the sheared areas in elongation of the gripped areas in Stage 1 and Stage 2 and additionally around the beads in Stage 2 and 3. This localized change in relative orientation yields up to approximately 75 deg. Regarding the slip distance $||\boldsymbol{\xi}_\alpha||$, highly localized slipping is observed, which is restricted to the gripping area in Stage 1 and 2. In Stage 3, minimal and localized slipping is additionally observed around the bigger corner bending. This reveals that the change in relative orientation is mainly induced by shear deformation.

In comparison of the relative orientation φ^{rel} and slip distance $||\boldsymbol{\xi}_\alpha||$ for the fully formed part in Figure 5.8, qualitatively the same results are observed for all three inter-ply modeling approaches. In a detailed comparison of the slip distance on the bigger corner bending and around the beads, slightly larger slip distances are observed for the anisotropic and the isotropic approach with the parameter set for 90 deg relative orientation. This reveals that the decreased frictional properties for relative orientations different from 0 deg influence locally, but slightly the slip distance. Besides this, no influence of the different inter-ply modeling approaches is observed.

The evolution of the median, lower (25 %) and upper quantile (75 %) of the relative orientation φ^{rel} of the top ply-ply interface and the slip distance $||\boldsymbol{\xi}_\alpha||$ of all ply-ply interfaces shown in Figure 5.9 reveal that the overall influence of anisotropic inter-ply is negligible for the orthotropic layup. Moreover, it is emphasized that slip distances are in general small, since more than 75 % of the observed slip distances are distinctively smaller than 1 mm. Nonetheless, at least 25 % of the relative orientations observed in the top interface undergo a change of approximately 20 deg.

Stage 1: $\Delta z = 30\,\mathrm{mm}$

Stage 2: $\Delta z = 17.5\,\mathrm{mm}$

Stage 3: $\Delta z = 5\,\mathrm{mm}$

$E_{12}\ (-)$ $\varphi^{\mathrm{rel}}\ (\mathrm{deg})$ $||\boldsymbol{\xi}_\alpha||\ (\mathrm{mm})$

$-0.6 \quad 0.0 \quad 0.6$ $0.0 \quad 45.0 \quad 90.0$ $0.0 \quad 3.0 \quad 6.0$
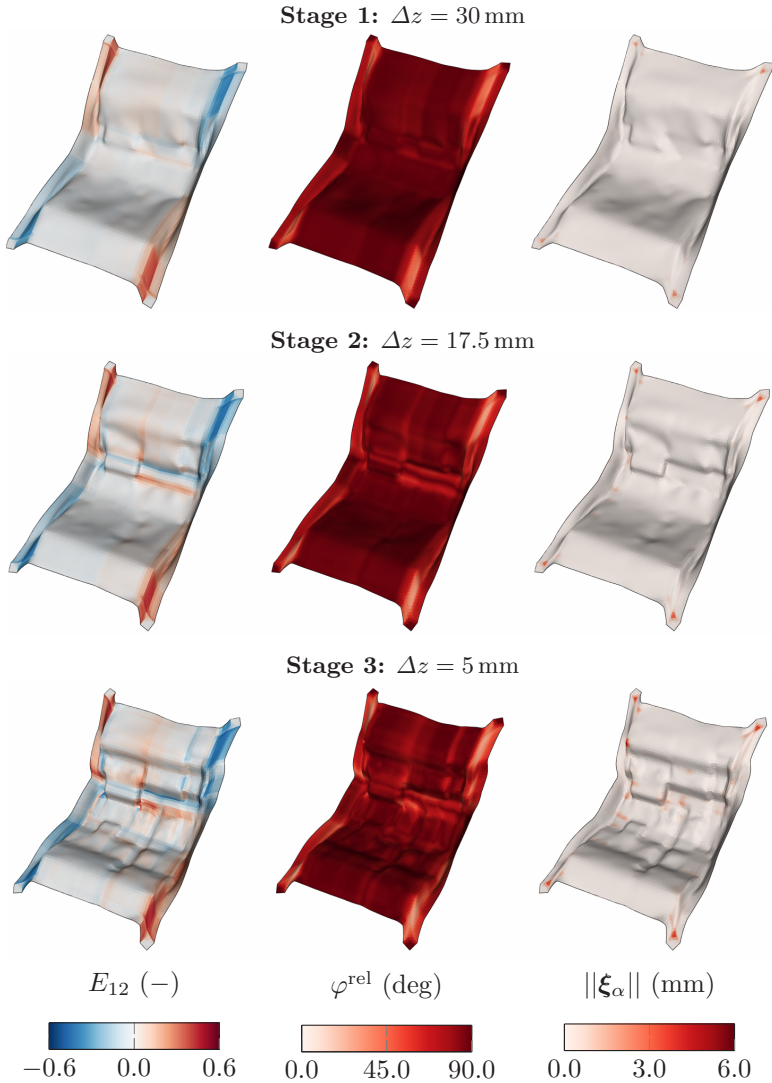
Figure 5.7: Intra-ply shear strain E_{12} for the top ply and relative orientation φ^{rel} and slip distance $||\boldsymbol{\xi}_\alpha||$ for the top ply-ply interface for the orthotropic layup at several remaining tool travels Δz under application of the anisotropic inter-ply slip modeling approach.

195

Anisotropic inter-ply slip: $\varphi_1^{\mathrm{rel}} = \mathrm{var.}$

Isotropic inter-ply slip: $\varphi_1^{\mathrm{rel}} = 0\,\mathrm{deg}$

Isotropic inter-ply slip: $\varphi_1^{\mathrm{rel}} = 90\,\mathrm{deg}$

| φ^{rel} (deg) | $||\boldsymbol{\xi}_\alpha||$ (mm) |

| 0.0 45.0 90.0 | 0.0 3.0 6.0 |
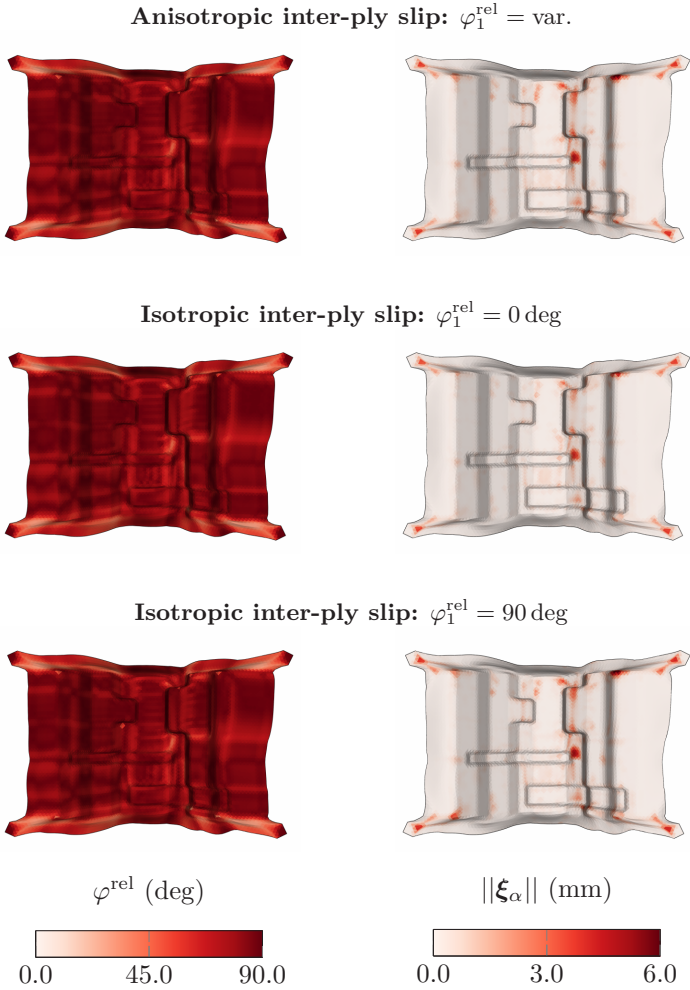
Figure 5.8: Comparison of relative orientation φ^{rel} (left) and slip distance $||\boldsymbol{\xi}_\alpha||$ (right) for the top ply-ply interface for the orthotropic layup and fully formed part under variation of the inter-ply slip modeling approach.
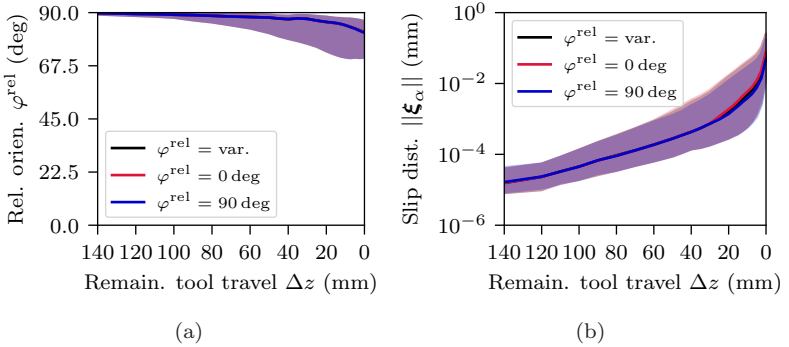
Figure 5.9: Evolution of the median, lower (25 %) and upper (75 %) quantile for the relative orientation φ^{rel} for the top ply-ply interface (a) and the slip distance $||\boldsymbol{\xi}_\alpha||$ for all ply-ply interfaces (b) during forming for the orthotropic layup under variation of the inter-ply slip modeling approach.

Results quasi-isotropic layup Figure 5.10 shows the results for the quasi-isotropic layup at several remaining tool travels Δz and under application of the anisotropic inter-ply slip modeling approach. The results reveal a localized change of the relative orientation φ^{rel}, which is induced by localized shearing. The localized change in relative orientation yields up to approximately 25 deg, which is distinctively lower than the maximum change observed for the orthotropic layup (cf. Figure 5.7).

Besides this, localized slipping is observed, which is restricted in Stage 1 to the areas in elongation of the grippers, where the laminate is being pulled over the comparably sharp part flanges. More pronounced slipping is additionally observed in Stage 2 and 3 around the bigger corner bending and beads.

In comparison of the relative orientation φ^{rel} and slip distance $||\boldsymbol{\xi}_\alpha||$ for the fully formed part in Figure 5.11, qualitatively the same results are observed for all three inter-ply modeling approaches. In a detailed comparison of the slip distance on the bigger corner bending and around the beads, slightly larger slip distances are observed for the anisotropic and the isotropic approach with the parameter set for 90 deg relative orientation. Besides this, no influence of the dif-

197

Stage 1: $\Delta z = 30\,\mathrm{mm}$

Stage 2: $\Delta z = 17.5\,\mathrm{mm}$

Stage 3: $\Delta z = 5\,\mathrm{mm}$

$E_{12}\ (-)$	$\varphi^{\mathrm{rel}}\ (\mathrm{deg})$	$||\boldsymbol{\xi}_\alpha||\ (\mathrm{mm})$
-0.6 0.0 0.6	0.0 45.0 90.0	0.0 3.5 7.0
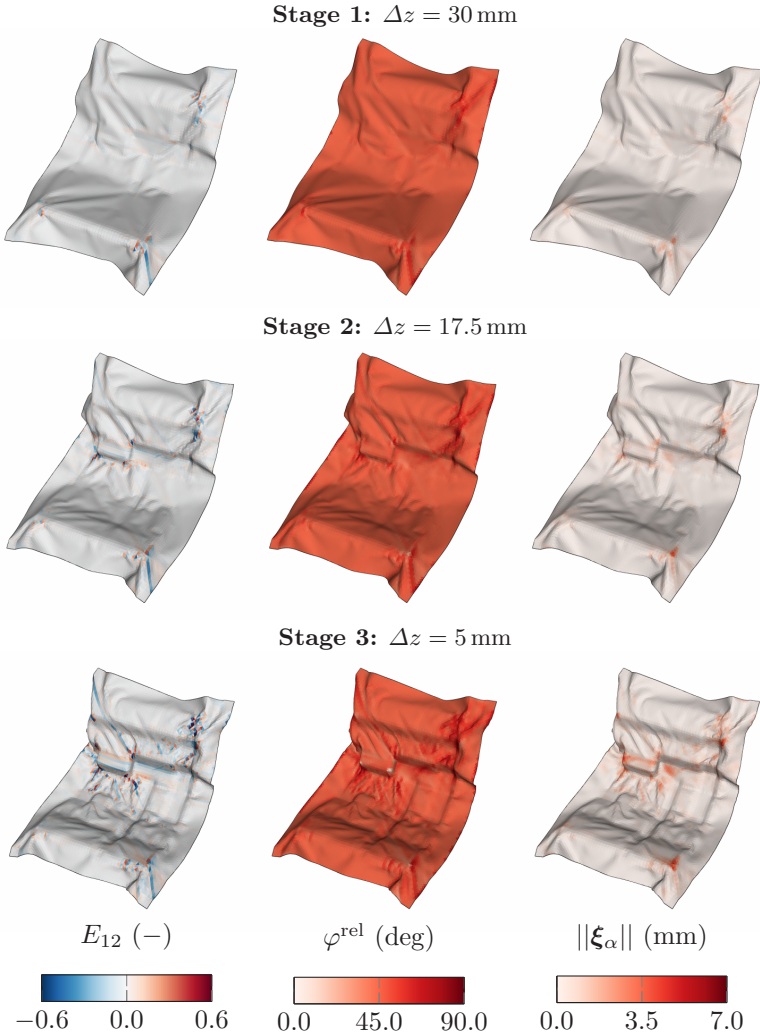
Figure 5.10: Intra-ply shear strain E_{12} for the top ply and relative orientation φ^{rel} and slip distance $||\boldsymbol{\xi}_\alpha||$ for the top ply-ply interface for the quasi-isotropic layup at several remaining tool travels Δz under application of the anisotropic inter-ply slip modeling approach.

Anisotropic inter-ply slip: $\varphi_1^{\mathrm{rel}} = \mathrm{var.}$
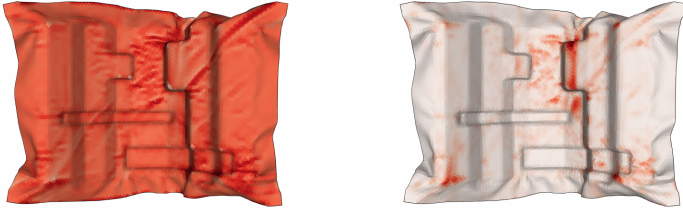
Isotropic inter-ply slip: $\varphi_1^{\mathrm{rel}} = 0\,\mathrm{deg}$

Isotropic inter-ply slip: $\varphi_1^{\mathrm{rel}} = 90\,\mathrm{deg}$

φ^{rel} (deg)

$||\boldsymbol{\xi}_\alpha||$ (mm)

| 0.0 | 45.0 | 90.0 |

| 0.0 | 3.5 | 7.0 |
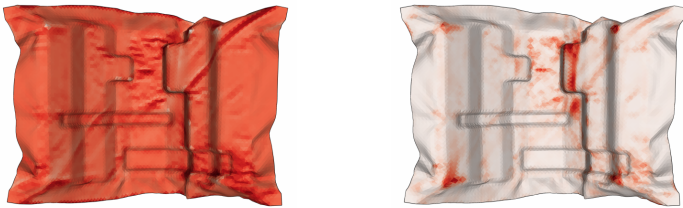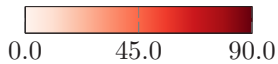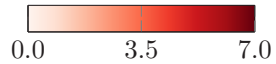
Figure 5.11: Comparison of relative orientation φ^{rel} (left) and slip distance $||\boldsymbol{\xi}_\alpha||$ (right) for the top ply-ply interface for the quasi-isotropic layup and fully formed part under variation of the inter-ply slip modeling approach.

199

ferent inter-ply modeling approaches is observed. Nonetheless, the observed slip distances are more pronounced and larger compared to the orthotropic layup (cf. Figure 5.8).

The evolution of the median, lower (25 %) and upper quantile (75 %) of the relative orientation φ^{rel} of the top ply-ply interface and the slip distance $||\boldsymbol{\xi}_\alpha||$ of all ply-ply interfaces shown in Figure 5.12 reveal that the overall influence of anisotropic inter-ply slip is negligible for the quasi-isotropic layup. Throughout forming, differences in the order of 10 μm are observed for the slip distance. An even smaller influence is observed for the relative orientation. Besides this, it is emphasized again that slip distances are in general small, since more than 75 % of the observed slip distances are equal or smaller than 1 mm. Nonetheless, higher slip distances are observed compared to the orthotropic layup (cf. Figure 5.9(b)). In contrast, the change in relative orientation is distinctively smaller for the quasi-isotropic layup.

(a)   (b)
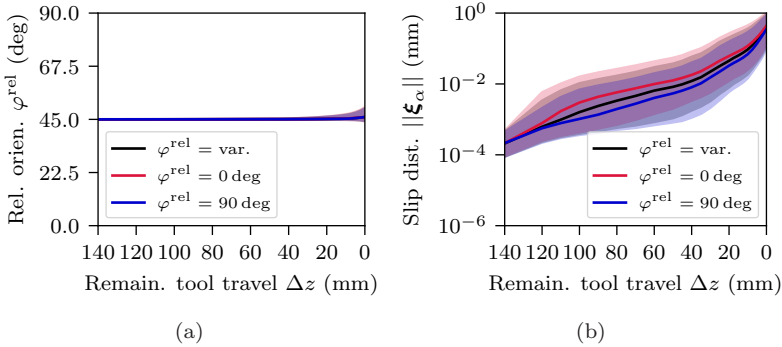
Figure 5.12: Evolution of the median, lower (25 %) and upper (75 %) quantile for the relative orientation φ^{rel} (a) and the slip distance $||\boldsymbol{\xi}_\alpha||$ (b) observed during forming for the quasi-isotropic layup under variation of the inter-ply slip modeling approach.

5.5 Discussion and conclusion

In the scope of this chapter, approaches for inter-ply slip modeling in thermoforming simulation using the commercial FE solver Abaqus are presented. For this purpose, the contact user-interface (VUINTER-ACTION) is applied, since Abaqus is only capable to model either tacking in normal direction or slipping (friction) in tangential direction.

Inter-ply slip modeling approaches Initially, an isotropic inter-ply slip modeling approach accounting for pressure- and rate-dependency is outlined. Accounting for these material characteristics is well-established in thermoforming simulation [119, 217, 218, 219] and the only further development presented here is the implementation in the commercial FE solver Abaqus. Subsequently, an advanced approach considering additionally the relative orientation between the slipping plies is presented. This dependency is not considered in composite forming simulation in general so far. Unfortunately, Abaqus does not supply the principal material orientations nor the relative orientation between slipping plies as essential status variables within the adopted contact user-interface. Hence, several additional subroutines and so-called global arrays are applied to determine and transfer the relevant information, in order to obtain the principal material orientations within the contact user-interface.

Based on the internal variable for the relative orientation between the slipping plies, a constitutive modeling approach for unidirectional reinforcements is presented, which defines an isotropic but nonlinear yield function. Based on this, the dependency of frictional behavior on the relative orientation between the slipping plies is captured. Due to the isotropic yield function, however, slipping along fiber direction behaves equally to slipping perpendicular to fiber direction. Unfortunately, no characterization data is available so far for this mechanism. Therefore, only the dependency of inter-ply slip on the relative orientation between the slipping plies is considered.

The presented approach is basically applicable to any material class with unidirectional fiber architecture at the slipping interface, such as for thermoplastic UD tape laminates or NCF. The application of the presented approach to woven fiber-reinforcements would require fur-

ther investigations, since the relative orientation between two different principal material orientations accompanied with intra-ply shearing need to be considered in the related constitutive equations.

Inter-ply slip parametrization   The presented inter-ply slip modeling approaches are successfully parametrized using a linear model, which has proven to sufficiently capture the pressure- and rate-dependency at constant temperature for the material investigated in the scope of this study. A nonlinear approach, such as a viscosity depending on slip rate, could further enhance the agreement to characterization results. However, since deviations are small, the linear model is kept throughout this study, since the impact on formability prediction is expected to be of minor relevance. Moreover, the enhancement to a temperature-dependent approach is straightforward for this approach by defining the parameters as a function of temperature, which makes the linear approach preferable.

It is to be noted that only two different relative orientations are investigated experimentally for parametrization of the inter-ply slip modeling approach, where the characterizations at 0 deg and 90 deg relative orientation are expected to define the upper and lower bound, respectively. Based on this, a linear relation between these two relative orientations is assumed for thermoforming simulation. This relation, however, is most likely nonlinear. Therefore, further relative orientations are reasonable to be investigated, to enable further insights regarding the evolution of the frictional resistance w.r.t. relative orientation.

Forming simulation   Finally, the parametrized inter-ply slip modeling approaches are applied to thermoforming simulation of a complexly shaped geometry for an orthotropic and a quasi-isotropic layup. Thereby, the inter-ply slip modeling approaches are varied, considering either the changing relative orientation or prescribing a relative orientation of 0 deg or 90 deg throughout forming for inter-ply slip modeling. Based on this, the influence of the different modeling approaches on formability prediction is investigated.

A significant change in relative orientation is observed locally for both layups. The according areas correlate directly to intra-ply shearing.

In contrast, slip distances are small for both layups. Nonetheless, the change in relative orientation is more pronounced for the orthotropic layup, since smooth and pronounced shear zones develop in the course of forming. On the contrary, local shear bands due to wrinkling are observed for the quasi-isotropic layup. Nonetheless, the locally changing relative orientation correlates also here. Nevertheless, the changing relative orientation is distinctively lower compared to the orthotropic layup. This is attributable to the comparably high shear stiffness of the quasi-isotropic layup, due to the four fiber families. For that reason, also higher slip distances and wrinkling are observed for the quasi-isotropic layup. In contrast, smaller slip distances only to the end of forming are observed highly localized for the orthotropic layup, which emphasizes that an orthotropic layup mostly deforms based on "pure shear" deformation.

In comparison of the inter-ply slip modeling approaches, the lowest slip distance is observed for the isotropic approach in combination with the parameter set for 0 deg relative orientation, which is reducible to the higher friction stresses observed in the related characterizations. The resulting difference in forming simulation, however, is small. A similar behavior is also observed by Haanappel [57] in a virtual forming study, for which material properties are systematically varied by factor 10. In this case, a minor influence of inter-ply slip compared to shear and bending behavior is observed. In the present case, inter-ply slip parameters deviate with relative orientation of the slipping plies only by a factor from approximately 1.25 to 1.85. Based on this, the observed minor sensitivity is reasonable. Regarding the slip distances observed for anisotropic approach and the isotropic approach in combination with the parameter set for 90 deg relative orientation, comparable results are observed. This leads to the conclusion, that it is not strictly necessary to consider the changing relative orientation for modeling inter-ply slip. Although there is an influence of relative orientation on inter-ply slip in thermoforming simulation, the obtained differences are indeed small.

These insights, however, might change for other material systems, especially for material systems with a lower frictional resistance, such as engineering textiles. This induces a more pronounced inter-ply slip, which then in turn might be more distinctively affected by anisotropic inter-ply slip behavior. Beyond that, the additional consideration

of the direction of slip in inter-ply slip modeling could influence the observed overall low sensitivity of a variation inter-ply slip resistance on formability, which might be investigated in future studies.

6 Coupled thermomechanical modeling of thermoforming processes

Abstract

The proposed framework for thermoforming simulation using the commercial FE solver Abaqus is enhanced to a coupled thermomechanical approach. For this purpose, the isothermal DKT shell formulation in combination with the nonlinear generalized Maxwell approach outlined in Chapter 4 is enhanced by a temperature degree of freedom. The related thermal modeling takes into account radiation, convection and heat conduction as well as the prediction of crystallization. Mechanical behavior is coupled to thermal behavior w.r.t. temperature and relative crystallinity. Based on this, the transition from the molten to the solid material state is predicted, which is not considered so far in thermoforming simulation. An improved agreement to experimental thermoforming results is observed for the thermomechanical approach, where also the local temperature evolution is accurately predicted. Crystallization during forming is observed for a disadvantageous choice of process parameters. Moreover, only the thermomechanical approach reflects the influence of varying process parameters. Hence, the consideration of thermal effects is favorable for the virtual process design.

The thermoforming process was assumed to be isothermal for simulation in the preceding chapters. Based on this, a good agreement to experimental forming tests is observed. Nonetheless, the experimental process analyses and material characterizations reveal both, an influence of process parameters on cooling behavior and temperature-dependent forming behavior (cf. Chapter 2). The consideration of thermal behavior in a thermomechanical analysis would enable besides improved material modeling also to consider the influence of additional process parameters. Thermomechanical forming simulation, however, is investigated only sparsely so far. Machado et al. [135] presented a coupled thermomechanical approach, in which shear behavior of the considered semi-crystalline organosheet (PP-GF) is modeled temperature-dependent. Beyond that, Guzman-Maldonado et al. [156] presented a thermomechanical approach based on alternating thermal and mechanical analyses for a semi-crystalline organosheet (PA66-GF). Both studies [135, 156] are restricted to temperatures well above the onset of crystallization of the semi-crystalline thermoplastics. The onset of crystallization, however, induces a significant increase of mechanical properties (cf. Section 2.3.2.2) and it is not known yet, if crystallization already during forming can be excluded in general for thermoforming simulation.

The first approach accounting for crystallization in thermoforming simulation was presented by Dörr et al. [49]. In the scope of this chapter, this coupled thermomechanical approach is adopted and related studies are extended.

The coupled thermomechanical approach is implemented in the commercial FE solver Abaqus in combination with several user-subroutines. It is based on the isothermal approach presented in Chapter 4, which includes a nonlinear DKT ("Discrete Kirchhoff Theory") shell-formulation, implemented as user-element (VUEL), and hyperviscoelastic constitutive equations for intra-ply modeling. Besides this, the contact constitutive equations implemented within a user-contact (VUINTERACTION) outlined in Chapter 5 are adopted. The according isothermal approach is extended in the scope of this chapter to a coupled thermomechanical approach by an additional temperature degree of freedom (DOF). This includes the prediction of crystallization kinetics, which enables to predict temperature- and recrystallization-dependent forming behavior, in addition to the already captured rate-

dependent forming behavior. Based on this, also the influence of tool and initial laminate temperature are considered, which is not possible by a purely isothermal approach.

In the following, thermal modeling including crystallization kinetics modeling is outlined in Section 6.1 and parametrized in Section 6.2. Subsequently, the coupling between thermal and mechanical modeling is outlined in Section 6.3 and the parametrization of temperature- and crystallization-dependent forming behavior is presented in Section 6.4. Finally, the coupled thermomechanical approach is applied to thermoforming simulation for validation in Section 6.5.

6.1 Thermal modeling

The governing equation for thermal modeling is the heat balance equation in combination with the generalized Fourier's law for heat conductivity, which is given in the strong form by [263]

$$\rho c_p \dot{T} = \boldsymbol{\nabla} \cdot (\boldsymbol{\lambda} \cdot \boldsymbol{\nabla} T) + r. \tag{6.1}$$

Here, T is the temperature, ρ the material density, c_p the heat capacity, $\boldsymbol{\lambda}$ the heat conductivity tensor and r a heat flux source term. The weak form of the heat balance equation is obtained by multiplying Equation 6.1 with a test function δT, integrating over the domain Ω and applying chain rule and divergence theorem, which yields:

$$\underbrace{\int_\Omega \rho c_p \dot{T} \delta T \, \mathrm{d}V}_{\delta W^{\mathrm{cap}}} = \underbrace{-\int_\Omega (\boldsymbol{\lambda} \cdot \boldsymbol{\nabla} T) \cdot (\boldsymbol{\nabla} \delta T) \, \mathrm{d}V}_{\delta W^{\mathrm{cond}}} \underbrace{-\int_{\Gamma_\Omega} s \delta T \, \mathrm{d}A}_{\delta W^{\mathrm{surf}}} + \underbrace{\int_\Omega r \delta T \, \mathrm{d}V}_{\delta W^{\mathrm{source}}},$$

$$\tag{6.2}$$

where s is a surface flux on the boundary Γ_Ω. This balance equation is adopted in this study for thermal modeling in thermoforming simulation. Thereby, the conductivity term W^{cond} is applied to account for intra-ply conductivity. In contrast, the surface flux s splits into three different terms, to account for inter-ply conductivity, convection and radiation $\left(s = s^{\mathrm{cond}} + s^{\mathrm{conv}} + s^{\mathrm{rad}}\right)$ and the source term is applied to account for the latent heat due to recrystallization. The according modeling approaches for these different parts of the heat balance equation are outlined in the following. Thereby, it is to be

207

noted that only heat loss due to radiation and no radiative heat transfer is accounted for.

6.1.1 Heat capacity

Heat capacity is modeled by the capacity term δW^{cap} and the according nodal fluxes can be determined by

$$f_i^{\mathrm{cap}} = \frac{\partial W^{\mathrm{cap}}}{\partial T_i} \approx M_{ij}\dot{T}_j \quad \text{with} \quad M_{ij} = \int_\Omega \rho c_p N_i N_j \, \mathrm{d}\Omega \approx \frac{1}{9}V^1\rho c_p, \tag{6.3}$$

where V^1 is the current element volume, N_i the linear triangular, shape function [122] and M_{ij} the element mass matrix. Since no coupling between the nodal degrees of freedom can be assigned in mass matrices M_{ij} in an explicit Abaqus user-element [242], row summation [122] is applied for the diagonalization of the mass matrix, which yields

$$M_{ij}^* = \frac{1}{3}V^1\rho c_p \delta_{ij}. \tag{6.4}$$

It is well known that heat capacity of thermoplastics varies w.r.t. temperature [231]. Therefore, heat capacity is defined linearly in sections:

$$c_p = c_p^0 + \begin{cases} c_p^1 + d_{c_p^1}(T - T^1) & , T < T^1 \\ c_p^1 + \dfrac{c_p^2 - c_p^1}{T^2 - T^1}(T - T^1) & , T^1 \le T \le T^2 \\ c_p^2 + d_{c_p^2}(T - T^2) & , T > T^2 \end{cases}, \tag{6.5}$$

where c_p^i, T^α and $d_{c_p^\alpha}$ are material parameters. This enables a straightforward parametrization and reduces computational cost against the interpolation of a point cloud describing the temperature-dependent heat capacity.

6.1.2 Crystallization kinetics

Thermoforming processes often comprise semi-crystalline thermoplastics due to their improved mechanical performance against amorphous thermoplastics. Depending on the thermal history and crystallization conditions, semi-crystalline thermoplastics form crystals besides

a significant amorphous phase while cooling from the molten material state. Based on this, the procedure of crystallization reveals the most important phase change in thermoforming of semi-crystalline thermo-plastics, since it defines the transition from the molten to the solid material state. Various approaches for crystallization kinetics modeling exist in literature, where comprehensive reviews are presented among others by Piorkowska and Rutledge [231] or Di Lorenzo and Silvestre [264]. In general, the crystallinity fraction $\alpha(t)$ at the time t is predicted. The general approach for the prediction of the conversion of an amorphous phase into growing crystalline domains was introduced by Avrami [265], which is based on the concept of so-called "extended volume". The "extended volume" is equal to the total volume of all domains growing from all nucleation attempts that occurred up to time t. The impingement of growing domains is not considered. All domains are taken into account, including the "phantom" domains expanding from nucleation attempts in already crystallized areas. Based on this, the well-known Avrami equation is derived [265]:

$$\alpha(t) = 1 - \exp\left(-\tilde{\alpha}(t)\right). \tag{6.6}$$

Here, $\tilde{\alpha}$ is the "extended" transformed volume fraction. In isothermal conditions, Equation 6.6 can be expressed by [231]

$$\alpha(t) = 1 - \exp\left(-kt^n\right), \tag{6.7}$$

where k is the crystallization rate constant, which is a function of temperature, and n is the Avrami index, which contains information on nucleation and growth geometry. The Avrami rate constant k can alternatively be described by the crystallization half-time $t_{0.5}$ ($k = \ln(2)/t_{0.5}$). To inter- and extrapolate the temperature-dependency of the crystallization half-time $t_{0.5}$, often the theory of Hoffmann and Lauritzen [266, 267] given by

$$\left(\frac{1}{t_{0.5}}\right) = \left(\frac{1}{t_{0.5}}\right)_0 \exp\left[-\frac{U^*}{R(T - T_\infty)}\right] \exp\left[-\frac{C_3}{T \Delta T f}\right], \tag{6.8}$$

is adopted. An alternative and empirical approach for the description of the crystallization half-time was presented by Ziabicki [268] by

$$\left(\frac{1}{t_{0.5}}\right) = \left(\frac{1}{t_{0.5}}\right)_{\max} \exp\left(-4\ln(2)\frac{(T - T_{\max})^2}{D^2}\right).$$

(6.9)

Based on this, isothermal crystallization processes can be described. However, thermoforming is a non-isothermal process and therefore an enhanced approach is required to predict crystallization in thermoforming processes.

To enable the application of the above outlined theories to non-isothermal crystallization, Nakamura et al. [269] presented an approach very popular in polymer processing based on the extension of Equation 6.7 by

$$\alpha(t) = 1 - \exp\left[-\left(\int_0^t K(T(\tilde{t}))\,\mathrm{d}\tilde{t}\right)^n\right] \quad \text{with} \quad K(T) = k(T)^{\frac{1}{n}},$$

(6.10)

where $T(\tilde{t})$ is the time-dependent temperature. An alternative approach for non-isothermal crystallization under constant cooling rates is proposed by Ozawa [270] by

$$\alpha(t) = 1 - \exp\left(-\frac{\chi(T)}{|\dot{T}^n|}\right),$$

(6.11)

which is generalized by Billon et al. [271] to non-constant cooling rates by

$$\alpha(t) = 1 - \exp\left[-\left(-\frac{\mathrm{d}\chi^{\frac{1}{n}}(T)}{\mathrm{d}T}\right)^n\right].$$

(6.12)

In comparison of Ozawa-Billon's approach (Equation 6.12) to Nakamura's approach (Equation 6.10), it can be seen that both approaches are formally the same:

$$\frac{\mathrm{d}\chi^{\frac{1}{n}}(T)}{\mathrm{d}T} = -k^{\frac{1}{n}}(T) = -K(T). \tag{6.13}$$

Therefore and due to the fact that Nakamura's model is widely spread in polymer processing, Nakamura's model is applied within this study. The differential form of Nakamura's model proposed by Patel et al. [272] is adopted for the implementation, which is given by

$$\dot{\alpha}(t) = nK(T)(1 - \alpha(t))\ln\left[-\left(1 - \alpha(t)\right)\right]^{\frac{n-1}{n}}. \tag{6.14}$$

Our previous study [232] has shown that Hoffmann Lauritzen theory (cf. Equation 6.8) fails to describe crystallization rate over wide range of cooling rates and that in contrast, Ziabicki's approach (cf. Equation 6.9) is suitable to be applied to a wide range of cooling rates. Therefore, Ziabicki's approach is applied in the scope of this study, which can be expressed in terms of the crystallization rate constant $K(T)$ by [268]

$$K(T) = K_{\max}\exp\left(\frac{-4\ln(2)\left(T - T_{\max}\right)^2}{D^2}\right), \tag{6.15}$$

where $K_{\max}$, $T_{\max}$ and D are material parameters depending on cooling rate $\dot{T}$. Crystallization kinetics is implemented as nodal user-field (VUFIELD), which is reasonable, since temperature is a nodal degree of freedom. Equation 6.14 is integrated in time by means of an Euler explicit integration scheme [228] and the parameters in Equation 6.15 are interpolated linearly between the different cooling rates.

6.1.3 Latent heat

Crystallization is an exothermal phase change and thus releases the so-called crystallization heat. This is accounted for by coupling crys-

tallization kinetics to the heat balance equation (cf. Equation 6.2) by means of the source term by

$$f_i^{\text{source}} = \frac{\partial W^{\text{source}}}{\partial T_i} \approx \rho V^1 \Delta h^{\text{cryst}} N_i N_j \dot{\alpha}_j, \qquad (6.16)$$

where V^1 is the element volume in the current configuration, $\dot{\alpha}_j$ the rate of crystallinity at the nodes of the triangular element and Δh^{cryst} the specific crystallization enthalpy.

6.1.4 Intra-ply heat conductivity

Intra-ply heat conductivity is implemented on element level within the DKT user-element and takes into account anisotropy by means of an orthotropic heat conductivity tensor $\boldsymbol{\lambda}$. The according constitutive equation is evaluated w.r.t. the initial configuration by

$$f_i^{\text{cond}} = \frac{\partial W^{\text{cond}}}{\partial T_i} \approx t^0 A^0 \left(B_{i\alpha}^0 \lambda_{\alpha\beta}^0 B_{\beta j}^{0 \top} \right) T_j, \qquad (6.17)$$

where f_i^{cond} is the nodal conductivity flux and t^0 the element thickness, A^0 the element area, $\lambda_{\alpha\beta}^0$ the orthotropic heat conductivity tensor and $B_{\alpha i}^0$ the linear triangular gradient operator [228] w.r.t. the initial configuration, respectively. However, heat conductivity is usually evaluated in the current configuration and the according orthotropic heat conductivity tensor can be defined for arbitrarily oriented principal material directions by

$$\boldsymbol{\lambda}^1 = \frac{\lambda_{11}}{G_{11}} \boldsymbol{g}_1 \otimes \boldsymbol{g}_1 + \frac{\lambda_{22}}{G_{22}} \boldsymbol{g}_2 \otimes \boldsymbol{g}_2, \qquad (6.18)$$

where λ_{11} and λ_{22} are the heat conductivities in the principal material directions and G_{ij} are the covariant metric coefficients, which are adopted to normalize the principal material directions $\boldsymbol{g}_\alpha$ in the

current configuration. The heat conductivity can be expressed w.r.t. the initial configuration by

$$\boldsymbol{\lambda}^0 = J\boldsymbol{F}^{-1} \cdot \boldsymbol{\lambda}^1 \cdot \boldsymbol{F}^{-\top} \tag{6.19}$$
$$= J\left(\frac{\lambda_{11}}{G_{11}}\boldsymbol{G}_1 \otimes \boldsymbol{G}_1 + \frac{\lambda_{22}}{G_{22}}\boldsymbol{G}_2 \otimes \boldsymbol{G}_2\right),$$

based on the well-knwon pull-back operation, where $\boldsymbol{G}_\alpha$ are the principal material directions in the initial configuration and J the Jacobian. Based on this, the rotation of the principal material orientations due to shear deformation is intrinsically captured. Nonetheless, it is to be noted that only geometric nonlinearities are captured. Physical nonlinearities due to e.g. an increasing fiber volume content would require further considerations regarding the parametrization. Anyhow, since heat conductivity is evaluated in the initial configuration, no local element coordinate system is necessary, since the elements are aligned to the 1-2-plane in the initial configuration, which alleviates the implementation.

6.1.5 Inter-ply heat conductivity

In the scope of this study, thermoforming simulation is based on a layer-by-layer analysis. Consequently, the according single plies of the stacked laminate are connected via contact constitutive equations. Based on this, inter-ply heat conductivity needs to be considered in the contact constitutive equations and is therefore part of the heat balance equation in terms of a surface flux s (cf. Equation 6.2). Inter-ply heat conductivity is derived by reducing Fourier's law into one dimension:

$$f_i^{\text{contact}} = \frac{\partial W^{\text{contact}}}{\partial T_i} \approx A^{\text{contact}} s^{\text{cond}} N_i^1 \tag{6.20}$$
$$\text{with} \quad s^{\text{cond}} \approx -\frac{\lambda_{33}}{||\boldsymbol{x}_2 - \boldsymbol{x}_1||}\left(T_2 - T_1\right),$$

where f_i^{contact} is the nodal inter-ply heat conductivity flux, N_i^1 a one-dimensional shape function, $\boldsymbol{x}_\alpha$ and T_α the position and temperature of the two interacting surfaces, respectively, A^{contact} the area of the contact point and λ_{33} the heat conductivity in thickness direc-

tion. Based on this, heat conductivity λ_{33} can be directly assigned as material property to model thermal conductivity of the laminate in thickness direction. On the contrary, thermal conductivity at the tool-ply interfaces is modeled by means of the Abaqus built-in contact algorithm by [242]

$$s^{\text{cond}} \approx -k^{\text{gap}}\left(T_2 - T_1\right),\tag{6.21}$$

where k^{gap} is the so-called thermal gap conductance of the interface.

6.1.6 Convection and radiation

The hot laminate is exposed to a cooler environment during forming. Therefore, heat loss due to convection and radiation is modeled by means of a surface flux for the outer plies, which is incorporated on element level into the DKT user-element by

$$f_i^{\text{surf}} = \frac{\partial W^{\text{surf}}}{\partial T_i} \approx N_i A^1 \left(s^{\text{conv}} + s^{\text{rad}}\right)\tag{6.22}$$

where N_i is the linear triangular shape function [228], A^1 the current element area and s^{conv} and s^{rad} the surface fluxes due to convection and radiation. The surface flux due to convection is modeled by

$$s^{\text{conv}} \approx h(N_i T_i - T_\infty),\tag{6.23}$$

where h is convection coefficient and T_∞ the sink temperature. The surface flux due to radiation is modeled by

$$s^{\text{rad}} \approx \epsilon\sigma\left[\left(N_i T_i - T_0\right)^4 - \left(T_\infty - T_0\right)^4\right],\tag{6.24}$$

where ϵ is the emissivity coefficient, σ the Stefan-Boltzmann constant, T_0 the absolute zero temperature and T_∞ the sink temperature.

6.2 Thermal parametrization

In the following, thermal behavior is parametrized for the material investigated in the scope of this study (cf. Section 1.5). The determined parameters are listed in the Appendix A.4.

214

6.2.1 Heat capacity

For characterization of heat capacity, standard differential scanning calorimetry (S-DSC) measurements were conducted at the Institute of Physics at the University of Rostock for the material investigated in this study, under the commissioning of Dipl.-Ing. Daniel Kugele [232]. In the scope of this study, the experimental results for cooling at $10\,°C/min$ are adopted for parametrization of the temperature-dependent heat capacity c_p following Equation 6.5.

The experimental result as well as the parametrization result are shown in Figure 6.1. The experimental result reveals the characteristic decrease of heat capacity with decreasing temperature as well as the characteristic peak due to the exothermic heat flow during recrystallization. The crystallization peak is not considered for parametrization of heat capacity, since the exothermic heat flow due to recrystallization is captured by crystallization kinetics modeling and the associated latent heat (cf. Section 6.1.3). Therefore, a linear baseline eliminating this peak is adopted for parametrization of heat capacity. For temperatures outside the characterized range, heat capacity is extrapolated linearly.
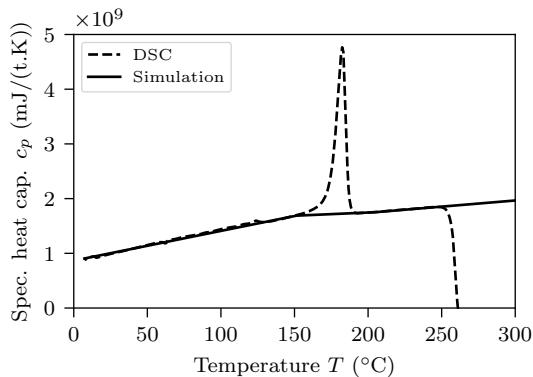
Figure 6.1: Parametrization result for the heat capacity c_p based on a Standard-DSC measurement at $10\,°C/min$ cooling rate.

6.2.2 Crystallization kinetics

Differential scanning calorimetry (DSC) measurements are usually employed to parametrize crystallization kinetics. In the scope of this study, the standard differential scanning calorimetry (S-DSC) and flash differential scanning calorimetry (F-DSC) measurements outlined in Section 2.3.1 are adopted. Thereby, it is to be noted that the relative and not the absolute degree of crystallinity is evaluated. This is necessary, since the mass of the F-DSC specimens is unknown and therefore, the measured absolute crystallization enthalpy cannot be related to the specific crystallization enthalpy $\Delta h^{\mathrm{cryst}}$. It is to be noted that considering the relative crystallinity is sufficient in the scope of this study, since the main objective of crystallization kinetics modeling in the scope of this chapter is to identify the phase transition from the molten to the solid material state, which is not influenced by considering the relative instead of the absolute crystallinity. Besides this, no isothermal crystallization characterization results for the investigated material were available, which prevents the experimental determination of the Avrami index n. Therefore, an Avrami index of $n = 2$ is chosen, based on the observations by Patel et al. [272] on neat PA6 and the experimental tests of Feng et al. [273], which show that the carbon fiber-reinforcement acts as a nucleation agent w.r.t. to the crystallization half-time $t_{0.5}$, but with a moderate influence on the Avrami index n.

Based on the evolution of the relative crystallinity determined from S- and F-DSC measurements, the parameters of the crystallization kinetics modeling approach $K_{\max}$, $T_{\max}$ and D are extracted for each cooling rate, following Ziabicki's approach (cf. Equation 6.15) in combination with Nakaumra's approach (cf. Equation 6.10) and the optimization algorithm presented by Nelder and Mead [247]. This gradient-based algorithm is sufficient, since only a single solution exists for this optimization problem. The according parametrization results are shown in Figure 6.2.

A high overall agreement between prediction and experimental results is observed, which reveals the suitability of the crystallization kinetics modeling approach to be applied to a wide range of cooling rates.
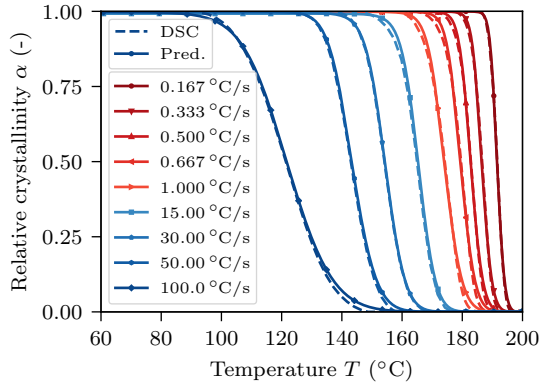
Figure 6.2: Comparison of crystallization kinetics modeling to experimental results from S-DSC measurements (red) and F-DSC measurements (blue) for the relative crystallinity α.

6.2.3 Latent heat

The exothermal heat during recrystallization is quantified by the specific crystallization enthalpy $\Delta h^{\mathrm{cryst}}$, which is determined in the scope of this study from S-DSC results at $10\,^\circ\mathrm{C/min}$ cooling rate. For this purpose, the absolute crystallization enthalpy $\Delta H^{\mathrm{cryst}}$ (cf. Equation 2.5) is adopted to determine the specific crystallization enthalpy by

$$\Delta h^{\mathrm{cryst}} = \frac{\Delta H^{\mathrm{cryst}}}{m^{\mathrm{spec}}}, \qquad (6.25)$$

where m^{spec} is the specimen mass. The according results are shown in Figure 6.3, where a low deviation between the in total five replicates is observed.

The determined specific crystallization enthalpy $\Delta h^{\mathrm{cryst}}$ is adopted for latent heat modeling in thermoforming simulation independent from cooling rate, since no significant change was observed for the S-DSC measurement. Further, the determination of the specific crystallization enthalpy is not possible for F-DSC measurements, as outlined above. This might yield an overestimation of the latent heat for higher cooling rates, since the degree of crystallinity will diminish for higher

cooling rates. Nevertheless, the cooling experiments in the Section 6.2.5 will reveal if this assumption is reasonable.
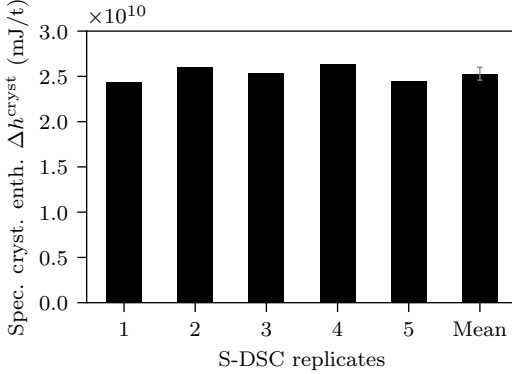
Figure 6.3: Specific crystallization enthalpy $\Delta h^{\mathrm{cryst}}$ determined from S-DSC measurements at $10\,^{\circ}\mathrm{C/min}$ cooling rate.

6.2.4 Heat conductivity

Heat conductivity needs to be characterized for both, the solid and the molten material state. For characterization of heat conductivity in the molten material state, unfortunately, suitable characterization setups are rare. Since no literature data is available for the composite material investigated in the scope of this study, the anisotropic heat conductivity is approximated by suitable rule of mixtures and literature data for the material constituents. On micro-level, the unidirectional tapes can be seen locally as a series of cylindrical inclusions (fibers) embedded in an isotropic medium (matrix). For the approximation of the in-plane heat conductivity λ_{11} of the composite in longitudinal direction, the Voigt model is applied:

$$\lambda_{11} = \lambda_{\mathrm{f}}^{\|}\nu_{\mathrm{f}} + \lambda_{\mathrm{m}}(1 - \nu_{\mathrm{f}}),\qquad(6.26)$$

where ν_{f} is the fiber volume fraction, $\lambda_{\mathrm{f}}^{\|}$ the longitudinal heat conductivity of the fibers and λ^{m} the heat conductivity of the neat matrix. In contrast, the rule of mixture proposed by Hasselman et al. [274],

under the assumption of a perfect contact between fiber and matrix, is applied for the in-plane transversal conductivity λ_{22} of the composite, in analogy to Guzman-Maldonado et al. [156], by

$$\lambda_{22} = \lambda_{\mathrm{m}} \frac{\left(\frac{\lambda_{\mathrm{f}}^{\perp}}{\lambda_{\mathrm{m}}} - 1\right) \nu_{\mathrm{f}} + \left(1 + \frac{\lambda_{\mathrm{f}}^{\perp}}{\lambda_{\mathrm{m}}}\right)}{\left(1 - \frac{\lambda_{\mathrm{f}}^{\perp}}{\lambda_{\mathrm{m}}}\right) \nu_{\mathrm{f}} + \left(1 + \frac{\lambda_{\mathrm{f}}^{\perp}}{\lambda_{\mathrm{m}}}\right)}, \tag{6.27}$$

where $\lambda_{\mathrm{f}}^{\perp}$ is the transversal heat conductivity of the fibers. Since no characterization data is available also for the conductivity in thickness direction, transversal isotropy is assumed for the conductivity ($\lambda_{22} = \lambda_{33}$), which is reasonable for a homogeneous distribution of fibers in both, in-plane and out-of-plane transversal direction.

In the scope of this study, the literature data for a T-300 type carbon fiber presented by Villière et al. [275] is adopted for the carbon fibers. For the neat PA6 in the molten material state, the experimental data presented by Keating and Mc Laren [276] is adopted, which is in good agreement with further literature data. For the neat PA6 in the solid material state, the value given by Yang [277] is adopted.

6.2.5 Convection and tool-ply gap conductance

The cooling experiments presented by Kugele et al. [278, 279] are adopted for parametrization of convection, radiation and tool-ply gap conductance. These experiments use among others laminates of the material investigated in the scope of this study with a [0;90] stacking sequence, a side length of 150 mm and a thickness of 1 mm. Thermocouples of type K are incorporated into the laminate prior to pre-consolidation with a variothermal mold, in order to quantify cooling behavior. Three different boundary conditions are considered for parametrization: natural convection, forced convection and two-sided tool-laminate contact.

For natural convection, the laminates are heated well above the melting temperature of the thermoplastic in a convection oven and cooled in a quiescent environment [278]. In contrast, a Göttinger-type wind-tunnel with open test section is adopted for forced convection, where the laminates are first heated beyond the melting temperature of the thermoplastic in the vicinity of the test section in a convection oven

and then instantly moved to the free stream of the wind tunnel with
3 m/s and 5 m/s air speed [278]. The test setup considered for these
studies is shown in Figure 6.4(a).

(a)   (b)
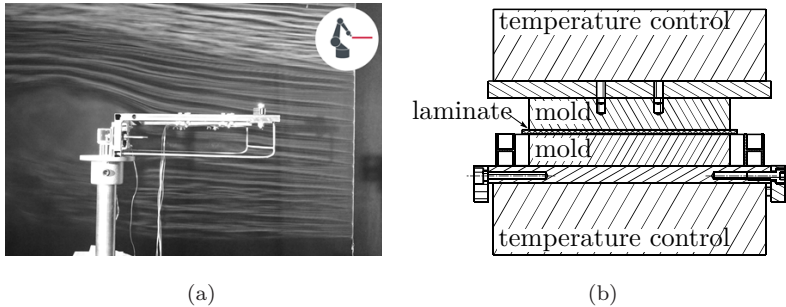
Figure 6.4: Experimental setups for characterization of cooling behavior: Cool-
ing experiments in a wind tunnel [278] (a) and within a plane mold
[279] (b).

For the tool-laminate contact, a plane mold mounted on a press is
adopted. The according experimental setup is shown in Figure 6.4(b).
First, the laminate is heated within a suitable clamping frame in a con-
vection oven beyond the melting temperature of the thermoplastic in
the vicinity of the press. Subsequently, the clamping frame is instantly
transfered to the mold and placed on springs. This enables wellnigh
simultaneous contact while closing the upper and lower mold, which
are heated to 80 °C, and applying a part pressure of 0.06 bar.
For inverse identification of the parameters for convection, radia-
tion and gap conductance, the experimental setups are modeled by
a layer-by-layer FEA based on the approach presented in Section 6.1.
Thereby, temperature-dependent heat-capacity, intra- and inter-ply
heat conductivity as well as crystallization kinetics and the related
latent heat are considered, based on the parametrization outlined in
Section 6.2.1 to 6.2.4.
The experimental and numerical results for the core temperature evo-
lution are shown in Figure 6.5(a). Regarding the experimental results,
a distinct influence of the different boundary conditions on cooling
behavior is observed, where obviously the intimate tool-ply contact
induces the highest cooling rate. Nonetheless, a distinct influence of

forced convection against natural convection on cooling behavior is observed. Besides this, a distinct retardation of cooling due to the exothermal heat during crystallization as well as a low standard deviation is observed for natural and forced convection. In contrast, standard deviation and cooling rate are high for the tool-ply contact, which smears and reduces the cooling retardation due to crystallization, respectively. Based on this, the experimental determination of the onset of crystallization is prevented.

In comparison of the numerical to the experimental results, a good agreement for all boundary conditions is observed for the evolution of core temperature (cf. Figure 6.5(a)). Beyond that, the onset of recrystallization as well as the retardation of cooling due recrystallization is well captured, especially for forced convection. For a more detailed insight into the prediction of recrystallization, cooling rate is determined for natural and forced convection in Figure 6.5(b). Recrystallization is clearly represented by a peak in cooling rate for all of the results. Regarding the simulation results, the position of the onset, maximum and end of this peak w.r.t. temperature (time) is determined by crystallization kinetics modeling, whereas the area under the peak is determined by the latent heat. A good agreement for the onset of crystallization is observed for forced convection. However, crystallization ends slightly too early in simulation, due to the symmetry of the
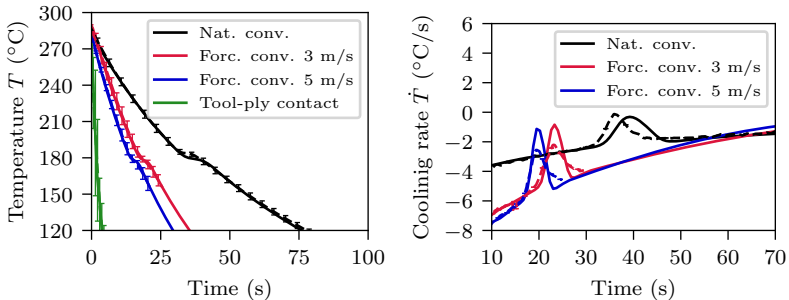
Figure 6.5: Comparison of experimental results from laminate cooling tests for PA6-CF [278, 279] to simulation results of the parametrized thermal model including the prediction of crystallization and related heat: Core temperatures T (a) and cooling rates $\dot{T}$ (b).

221

crystallization rate constant in simulation and the non-symmetry of the peak observed in the cooling experiments. Nonetheless, the area under the peak is in a good agreement. Regarding natural convection, a slight delay of the onset of recrystallization is observed. Here, the peak height and area under the peak are comparable.

The results reveal that the assumption about a constant crystallization enthalpy $\Delta h^{\mathrm{cryst}}$ (cf. Section 6.2.3) is reasonable, since the crystallization peak is not overestimated tremendously. Thereby, it is to be noted that cooling rates observed in the cooling experiments are about 25 times higher compared to the cooling rate from which the crystallization enthalpy was determined in DSC measurements. Besides this, it is to be noted that cooling rates observed for free and forced convection are between the ranges characterized by S- and F-DSC measurements (cf. Figure 6.1). Nonetheless, the onset of crystallization is well described, which emphasizes in summary the suitability and validity of the applied crystallization kinetics modeling approach and according parametrization strategy, including the interpolation between S- an F-DSC measurements.

6.3 Thermomechanical coupling

The thermomechanical approach for thermoforming simulation presented in this chapter includes besides modeling of thermal behavior also temperature- and crystallization-dependent modeling of mechanical behavior. Thermal modeling is outlined in detail in Section 6.1. In the following, mechanical modeling and according coupling to thermal modeling is outlined.

6.3.1 Thermomechanical intra-ply modeling

The isothermal approach based on the "Discrete Kirchhoff Theory" (DKT) shell formulation presented in Chapter 4 is adopted for modeling of intra-ply deformation behavior. The triangular DKT shell element has three translational r_{in} and three rotational ϕ_{in} mechanical degrees of freedom (DoFs) at each node n, where the rotational DoFs are applied to describe the rotation of a unit director base d_{in}. The virtual internal energy of the mechanical part is decomposed into

a membrane and a bending part, resulting in modeling of intra-ply mechanisms in a physically decoupled fashion by

$$\delta W^{\mathrm{in}} = \int_V \left[S_{\alpha\beta}^{\mathrm{mem}} \left(\frac{\partial E_{\alpha\beta}}{\partial r_{in}} \right) \delta r_{in} + S_{\alpha\beta}^{\mathrm{bend}} \left(\frac{\partial E_{\alpha\beta}}{\partial d_{in}} \right) \delta d_{in} \right] \mathrm{d}V, \quad (6.28)$$

where $E_{\alpha\beta}$ is the Green-Lagrange strain and $S_{\alpha\beta}^{\mathrm{mem}}$ and $S_{\alpha\beta}^{\mathrm{bend}}$ are the second Piola-Kirchhoff (PK2) stress tensors for membrane and bending behavior, respectively. This decoupling is a basic requirement on composite forming simulation, as already outlined in the previous chapters.

It is to be noted that neither thermal expansion nor shrinkage due to recrystallization is considered in the scope of this study, since these mechanisms are expected to not significantly influence formability prediction, because related deformations act on a lower scale compared to the deformations during forming. Therefore, the virtual internal energy in Equation 6.28 does not include an additional term due to a changing temperature T since

$$\frac{\partial E_{\alpha\beta}}{\partial T} = 0. \qquad (6.29)$$

Nonetheless, for the coupling of thermal behavior to mechanical behavior, the PK2 stresses are defined as a function of temperature. Both, the PK2 stress for membrane and for bending behavior, are evaluated for the molten and the solid material state. The resulting PK2 stress tensors $\boldsymbol{S}^{\mathrm{m}}$ and $\boldsymbol{S}^{\mathrm{s}}$ are superimposed based on the relative crystallinity α by

$$\boldsymbol{S} = (1-\alpha)\boldsymbol{S}^{\mathrm{m}} + \alpha\boldsymbol{S}^{\mathrm{s}}. \qquad (6.30)$$

This guarantees a smooth transition of intra-ply deformation behavior from the molten to the solid material state. The related constitutive equations are outlined in the following.

Molten material state   A hyperviscoelastic approach following a nonlinear generalized Maxwell approach is applied for mechanical intra-ply modeling in the molten material state, to account for rate-dependent forming behavior. The according constitutive equations are outlined for the isothermal case in detail in Section 4.2.1. Therefore, only

the main equations and enhancements for the non-isothermal case are outlined in the following.

Membrane behavior is modeled based on the "Ideal Fibre-Reinforced Material" (IFRM) presented by Spencer [145, 146] with a linear-elastic, uniaxial fiber model for the regularization of the fiber inextensibility constraint and a superimposed isotropic hyperviscoelastic generalized Maxwell approach. On the contrary, an anisotropic generalized Maxwell approach is applied for bending behavior. The same constitutive equations are applied for membrane and bending behavior, since these are implemented for the (general) anisotropic case. The generalized Maxwell approach is based on the parallel connection of one hyperelastic element with an arbitrary number of Maxwell elements, where each Maxwell element consist of an elastic element connected in series with a nonlinear viscous flow element. Hence, the total stress results from the summation of the stresses of each Maxwell element ($i = 1...N$) plus the purely hyperelastic element ($i = 0$) by

$$\boldsymbol{S} = \boldsymbol{S}_0 + \sum_{i=1}^{N} \boldsymbol{S}_i. \tag{6.31}$$

The purely hyperelastic element is evaluated by means of the total deformation. In contrast, a multiplicative decomposition of the deformation gradient $\boldsymbol{F}$ into an elastic part $\boldsymbol{F}^{\mathrm{e}}$ and a viscous part $\boldsymbol{F}^{\mathrm{v}}$ is applied for the Maxwell elements by

$$\boldsymbol{F} = \boldsymbol{F}^{\mathrm{e}} \cdot \boldsymbol{F}^{\mathrm{v}}. \tag{6.32}$$

Based on this, total Green-Lagrange strain $\boldsymbol{E}$ additively splits into a an elastic part $\boldsymbol{E}^{\mathrm{e}}$ and a viscous part $\boldsymbol{E}^{\mathrm{v}}$ by

$$\boldsymbol{E} = \boldsymbol{E}^{\mathrm{e}} + \boldsymbol{E}^{\mathrm{v}}. \tag{6.33}$$

In this study, each hyperelastic element is modeled by means of a so-called St. Venant-Kirchhoff material [122] by

$$\boldsymbol{S}_0 = \mathbb{C}_0 : \boldsymbol{E} \quad \text{and} \quad \boldsymbol{S}_i = \mathbb{C}_i : \boldsymbol{E}_i^{\mathrm{e}}. \tag{6.34}$$

The according elastic stiffnesses $\mathbb{C}_i$ are interpolated w.r.t. temperature T by

$$\mathbb{C}_i(T) = \mathbb{C}_i\left(T^1\right) + \frac{T - T^1}{T^2 - T^1}\left[\mathbb{C}_i\left(T^2\right) - \mathbb{C}_i\left(T^1\right)\right], \qquad (6.35)$$

where T^1 and T^2 are the temperatures considered for characterization of mechanical behavior below and above the actual temperature T, respectively. In case of a temperature T outside the characterized range, the parametrization of the closest temperature is kept constant and no extrapolation is made. In analogy, the constitutively defined equivalent flow rates $\dot{\lambda}_i^\mathrm{v}$, which define the evolution of viscous deformation $\boldsymbol{F}^\mathrm{v}$ (cf. Equation 4.32), are interpolated w.r.t. temperature T by

$$\dot{\lambda}_i^\mathrm{v}(T) = \dot{\lambda}_i^\mathrm{v}\left(T^1\right) + \frac{T - T^1}{T^2 - T^1}\left[\dot{\lambda}_i^\mathrm{v}\left(T^2\right) - \dot{\lambda}_i^\mathrm{v}\left(T^1\right)\right]. \qquad (6.36)$$

This is necessary, since a direct interpolation of the material parameters is hindered by the strongly nonlinear nature of the constitutively defined equivalent flow rate (cf. Equation 4.34).

Solid material state Intra-ply deformation is assumed to behave purely elastic in the solid material state, since rate-dependency is expected to be negligible in this material state compared to the molten material state. Besides this, it is assumed that the solidified material state is stress-free at the onset of recrystallization. Therefore, the total deformation gradient $\boldsymbol{F}$ is multiplicatively decomposed into a solid part $\boldsymbol{F}^\mathrm{s}$ and a molten part $\boldsymbol{F}^\mathrm{m}$ by

$$\boldsymbol{F} = \boldsymbol{F}^\mathrm{s} \cdot \boldsymbol{F}^\mathrm{m} \quad \text{with} \quad \boldsymbol{F}^\mathrm{m} = \boldsymbol{F}(\min\{t : \alpha > 0\}). \qquad (6.37)$$

Thus, the molten part of the deformation $\boldsymbol{F}^\mathrm{m}$ is defined by the deformation state at the onset of recrystallization ($\alpha > 0$), which can be regarded as the introduction of a new reference configuration for the solid material state. The according multiplicative split of the deformation gradient $\boldsymbol{F}$ follows the same approach as applied for the molten material state and the mappings of related kinematic and stress mag-

nitudes between the different configuration illustrated in Figure 4.4 apply also here ($\boldsymbol{F}^{\mathrm{m}} \hat{=} \boldsymbol{F}^{\mathrm{v}}$ and $\boldsymbol{F}^{\mathrm{s}} \hat{=} \boldsymbol{F}^{\mathrm{e}}$).

The multiplicative decomposition in Equation 6.37 yields an additive split of the Green-Lagrange strain in the initial configuration ($\boldsymbol{E} = \boldsymbol{E}^{\mathrm{m}} + \boldsymbol{E}^{\mathrm{s}}$). Based on this, material behavior is modeled in the solid material state by means of a hyperelastic St. Venant-Kirchhoff material [122] by

$$\boldsymbol{S}^{\mathrm{s}} = \mathbb{C}^{\mathrm{s}} : \boldsymbol{E}^{\mathrm{s}} \quad \text{with} \quad \boldsymbol{E}^{\mathrm{s}} = \frac{1}{2}\left(\boldsymbol{F}^{\top} \cdot \boldsymbol{F} - \boldsymbol{F}^{\mathrm{m}\top} \cdot \boldsymbol{F}^{\mathrm{m}}\right), \qquad (6.38)$$

where $\mathbb{C}^{\mathrm{s}}$ is the fourth order elasticity tensor in the solid material state, which is applied to account for orthotropic material behavior.

6.3.2 Thermomechanical inter-ply modeling

For modeling of mechanical inter-ply behavior, the isothermal approach outlined in Section 5.1 is adopted for the molten material state. Also here, temperature-dependency is introduced, which is straightforward due to the linear nature of the related constitutive equations. Therefore, the inter-ply material parameters are interpolated linearly w.r.t. temperature. Based on this, pressure-, temperature- and rate-dependent inter-ply slip is accounted for in the molten material state. On the contrary, purely elastic tacking is assumed for the solid material state. This results in the constitutive equations for inter-ply slip given by

$$\tau_\alpha^{\mathrm{m}} = \left(\mu(T)\,p + \eta(T)\,||\dot{\xi}_\alpha||\right)\frac{\dot{\xi}_\alpha}{||\dot{\xi}_\alpha||} + \tau_0(T) \quad \text{and} \quad \tau_\alpha^{\mathrm{s}} = \epsilon^{\mathrm{s}}\xi_\alpha. \quad (6.39)$$

Here, ξ_α is the tangential displacement, τ_α the tangential stress and ϵ^{s} the tangential solid stiffness, where Penalty method is adopted to regularize τ_α^{m}. The transition from the molten to the solid material state is modeled in analogy to intra-ply behavior based on the relative crystallinity α by

$$\tau_\alpha = (1 - \alpha)\tau_\alpha^{\mathrm{m}} + \alpha\tau_\alpha^{\mathrm{s}}. \qquad (6.40)$$

6.4 Thermomechanical parametrization

The parametrization of thermomechanical intra- and inter-ply deformation behavior splits into the parametrization in the molten and the solid material state, since constitutive equations are evaluated for these material states separately (cf. Equation 6.30 and 6.40). For intra-ply modeling in the molten material state, the parametrization of the nonlinear generalized Maxwell approach presented in Section 4.3 is applied. For inter-ply slip, the parametrization of tool-ply and ply-ply slip without relative orientation presented in Section 5.3.1 is applied. Henceforth, temperature-dependency is considered for material modeling in the molten material state for all deformation mechanisms.

For parametrization of material modeling in the solid material state, standard tensile testing for different layups can be conducted to identify the required orthotropic elastic properties. Unfortunately, such tests were not available for the investigated material. Therefore, the virtual characterization results based on unit cell modeling on microscopic scale presented by Roesner et al. [280] are adopted. These characterization results include all engineering constants necessary for modeling orthotropic elastic behavior.

6.5 Validation of thermomechanical forming simulation

The above outlined coupled thermomechanical approach is finally applied to thermoforming simulation and the results are compared for validation to experimental thermoforming tests and temperature measurements. For this purpose, the complexly shaped geometry and the according process setup presented in Section 2.2.1 is investigated. Accordingly, two different layups are considered, which namely are an orthotropic layup ($[0; 90]_{2s}$]) and a quasi-isotropic layup ($[0; -45; 90; +45]_s$). Moreover, different process parameter settings are investigated, since the thermomechanical approach is capable to take into account the influence of all varied parameters. The varied parameters namely are tool temperature, forming velocity and gripping force (cf. Table 2.1).

The simulation model setup is described in detail in Section 3.5.2 and remains unchanged, except the additional boundary and initial conditions for thermal modeling. Thereby, the tools are modeled with a constant temperature, since the heating of the tools during forming is expected to be negligible, due to their enormous thermal mass against the heat capacity of the formed laminate. In contrast, the laminate is modeled with a homogeneous initial temperature of 280 °C, which is the expected average temperature of the laminate at the beginning of the forming stage. In analogy to the previous thermoforming simulations, tool kinematics is modeled in real time, to accurately account for rate-dependency and in the scope of this chapter additionally for cooling behavior.

In the following, initially the results for the intermediate process settings ($T^{\mathrm{tool}} = 110\,^\circ\mathrm{C}$, $\bar{v}^{\mathrm{tool}} = 15\,\mathrm{mm/s}$, $F^{\mathrm{grip}} = 24.73\,\mathrm{N}$) are compared to experimental results for both layups (Section 6.5.1). Subsequently, process parameters are varied for the intermediate gripper force, in order to investigate the capability of the thermomechanical approach to predict the influence of the varying process parameters on cooling behavior and formability (Section 6.5.2). In each section, an emphasis is laid on the comparison of the thermomechanical to the related isothermal approach from Chapter 4, in order to investigate the necessity of a thermomechanical approach for thermoforming simulation.

6.5.1 Intermediate process settings

Orthotropic layup Figure 6.6 shows the comparison of thermoforming simulation results, under application of the isothermal approach and the thermomechanical approach, to the according experimental thermoforming test for the orthotropic layup and fully formed part for the intermediate process settings (cf. Table 2.1).

In comparison of the final shapes, a high prediction accuracy is observed for both simulation approaches. Mostly no difference is observed in a qualitative comparison of the simulation results, except w.r.t. the material draw-in at the top and bottom of the part, which differs to a small degree. In comparison of the obtained outer contours in Figure 6.6(d), an overall high agreement with a small difference between the thermomechanical and the isothermal approach is observed.

(a) Isothermal
$T = 270\,^{\circ}\mathrm{C}$

(b) Thermome-
chanical

(c) Experimental
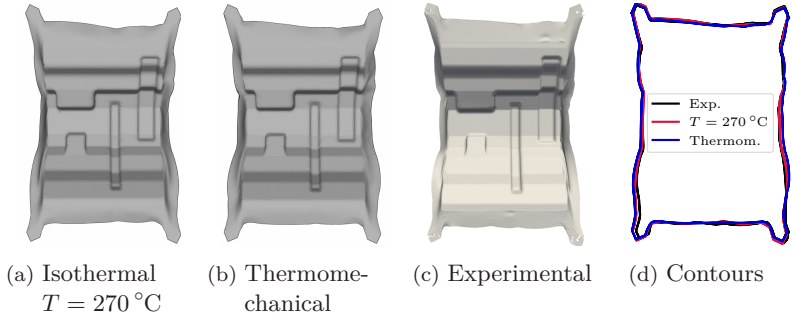
(d) Contours

Figure 6.6: Forming simulation results (a, b), 3D measurement of the exper-
imental test (c) and comparison of the outer contours (d) for the
orthotropic layup ($[0; 90]_{2s}$) and fully closed tools.

The thermomechanical contour slightly flares in horizontal direction,
which yields a better and a slightly lower agreement to the experimen-
tal test, depending on the position compared. Just minor deviations
remain for both approaches, in particular for the lower left gripping
area.

Additional results at several remaining tool travels Δz are shown in
Figure 6.7. The comparison of both forming simulation approaches to
the related experimental test reveals a good agreement of the obtained
overall shapes and outer contour. In a more detailed comparison,
however, it is observed that some local defects are predicted only
by the thermomechanical approach. This applies especially for the
large fold and wrinkles above the bigger corner bending, which is
predicted clearly by the thermomechanical approach in Stage 2 and
3. In Stage 1, however, the evolving fold is not observed for both
approaches. Besides this, local wrinkling around the beads, between
the corner bendings as well as between the bigger corner bending
and the bead is predicted more pronounced by the thermomechanical
approach. This more pronounced wrinkling behavior is in agreement
with the experimental tests.

The difference between the isothermal and the thermomechanical ap-
proach can be reduced to local cooling and crystallization of the lam-
inate, which is shown for several remaining tool travels in Figure 6.8.
The results are shown for the lowest ply, for which the most distinct

Stage 1: $\Delta z = 30\,\mathrm{mm}$

Stage 2: $\Delta z = 17.5\,\mathrm{mm}$

Stage 3: $\Delta z = 5\,\mathrm{mm}$

| **Isothermal** | **Thermomechanical** | **Experimental** |
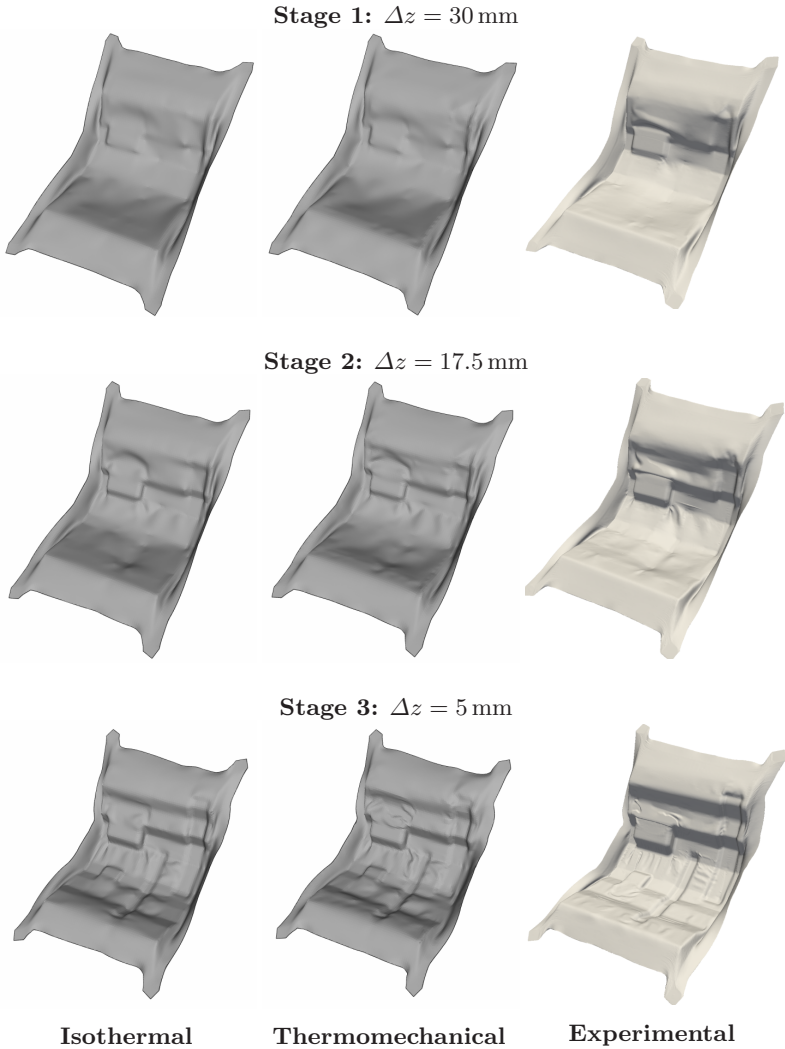
Figure 6.7: Comparison of thermoforming simulation, under application of the isothermal ($T = 270\,°\mathrm{C}$) and the thermomechanical approach, to 3D measurements of experimental tests for the orthotropic layup ($[0; 90]_{2\mathrm{s}}$) at several remaining tool travels Δz.

Stage 1: $\Delta z = 30\,\mathrm{mm}$

Stage 2: $\Delta z = 17.5\,\mathrm{mm}$

Stage 3: $\Delta z = 5\,\mathrm{mm}$

Stage 4: $\Delta z = 0\,\mathrm{mm}$

T (°C)　　　　$\dot{T}$ (°C/s)　　　　α (−)

140.0　210.0　280.0　　−100.0　0.0　100.0　　0.0　　0.5　　1.0
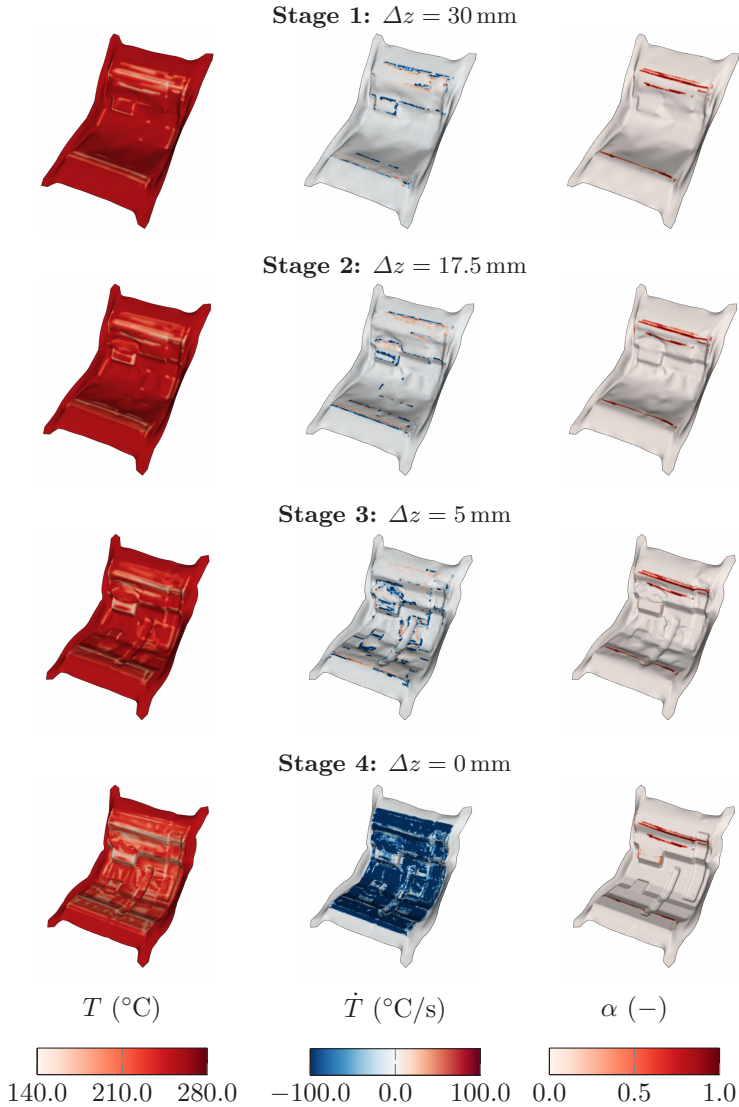
Figure 6.8: Temperature T, rate of temperature $\dot{T}$, and relative crystallinity α for the orthotropic layup ($[0; 90]_{2\mathrm{s}}$) at several remaining tool travels Δz, obtained from the thermomechanical approach for the lowest ply.

cooling is observed. Thereby, low temperature changes are observed at the free surfaces, due to moderate cooling rates under free convection and radiation. On the contrary, tool-ply contact (gap conductance) induces locally a significant cooling of the laminate. This is mostly limited to the part flanges in the early stages and additionally to the area around the bigger corner bending in the later stages. In these areas, also local crystallization is observed. Besides this, local wrinkling is directly reflected in the temperature distribution, due to the local tool-ply contact, which induces locally high cooling rates. Moreover, also slight local heating is observed throughout forming, which can be induced either by the latent heat due to crystallization or due to high through the thickness temperature gradients in combination with a hotter core and a loss of tool-ply contact, inducing a rapid change in heat loss for the outer plies. In contrast, cooling rates are mostly evenly distributed and yield up to $250\,°C/s$ for fully closed tools.

To validate the prediction of thermal behavior, the simulation results are compared to local temperature measurements, which are conducted by means of local thermocouples (type K). Details on the according experimental tests can be found in Section 2.2.3. Two different positions (TC-1 and TC-2) are considered in the experimental tests. Moreover, an additional position (TC-2$-\Delta y$), which is located in approximately $5\,mm$ distance in negative y-direction to TC-2, is considered in thermoforming simulation (cf. Figure 6.9).
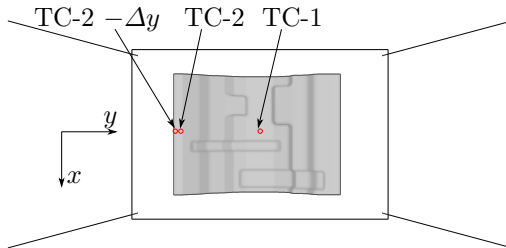
Figure 6.9: CAD model of the investigated generic geometry, as well as a schematic illustration of the gripper arrangement, initial blank and thermocouple (TC) positions considered for validation.
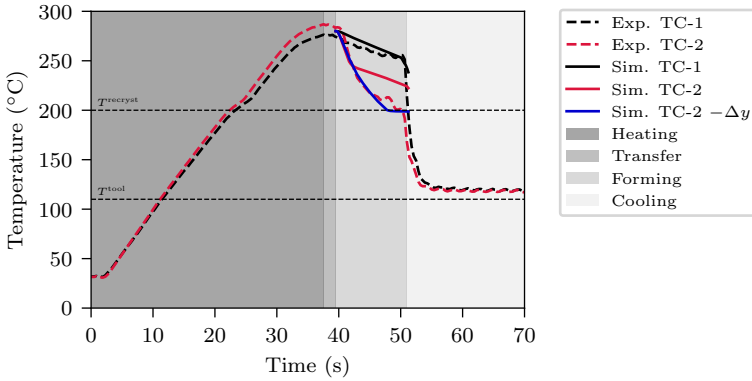
Figure 6.10: Comparison of local temperature measurements to the according temperature evolutions predicted by thermomechanical thermoforming simulation for the orthotropic layup ($[0; 90]_{2s}$).

A comparison of the experimental and simulation results is shown in Figure 6.10. The results reveal that the initial homogeneous laminate temperature is well chosen. Besides this, the moderate cooling at TC-1 throughout forming is well captured by simulation. This is followed by a distinct increase of cooling rate when the tools are mostly closed. The pronounced cooling at TC-2 due to the local tool-ply contact is well captured for the first few seconds during forming, until the tool-ply contact situation changes in simulation. This results in the same cooling rate as observed at TC-1, since cooling due to free convection and radiation is observed. Since TC-2 is located at the part flanges, where high local temperature gradients are observed (cf. Figure 6.8), the position TC-2$-\Delta y$ is additionally evaluated, since uncertainties in positioning of the laminate itself or of the thermocouple within the laminate cannot be excluded. The position of this additional evaluation point is shown in Figure 6.9. A high agreement of the temperature evolution predicted by simulation with the experimental test is observed.

Based on the good agreement for the core temperature observed above, the cross-sectional temperature is evaluated throughout forming in equidistant time steps at TC-1 and TC-2 (cf. Figure 6.11). Moderate cooling with a symmetric temperature profile is observed for TC-1,
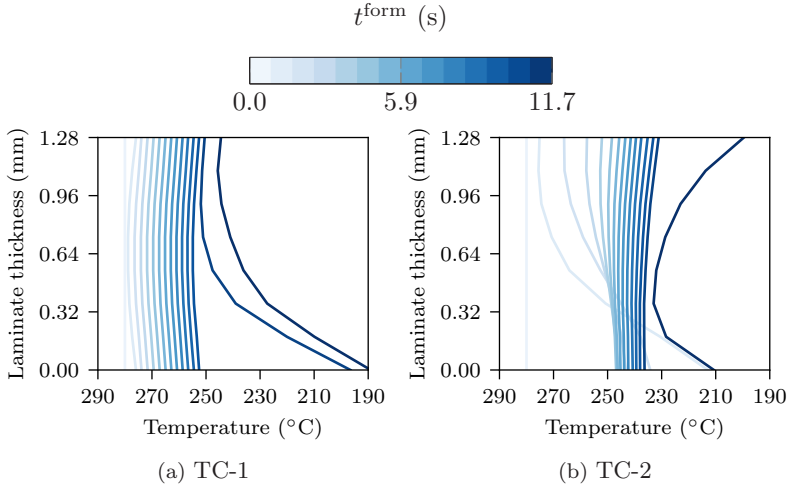
Figure 6.11: Evolution of cross-sectional temperature in equidistant time steps throughout the forming cycle time t^{form} at the thermocouples TC-1 and TC-2, determined by thermoforming simulation.

until a high temperature gradient is induced by tool-ply contact on the bottom-side of the laminate. In contrast, a high temperature gradient is observed at TC-2 already at the beginning of the forming process. This results from positioning of the laminate on the tool flanges. Throughout forming, tool-ply contact is lost, which yields a heating of the lower plies by the hotter inner plies, while the laminate further cools moderately due to convection and radiation. Finally, a high temperature gradient is observed, which is induced by both-sided tool-ply contact. For both positions, temperature gradients over the thickness of the laminate up to $50\,^{\circ}\mathrm{C}$ are observed.

Quasi-isotropic layup   Figure 6.12 shows the comparison of thermoforming simulation results, under application of the isothermal approach and the thermomechanical approach, to the according experimental test for the quasi-isotropic layup and fully formed part for the intermediate process settings (cf. Table 2.1).

(a) Isothermal
$T = 270\,°\text{C}$

(b) Thermome-
chanical

(c) Experimental
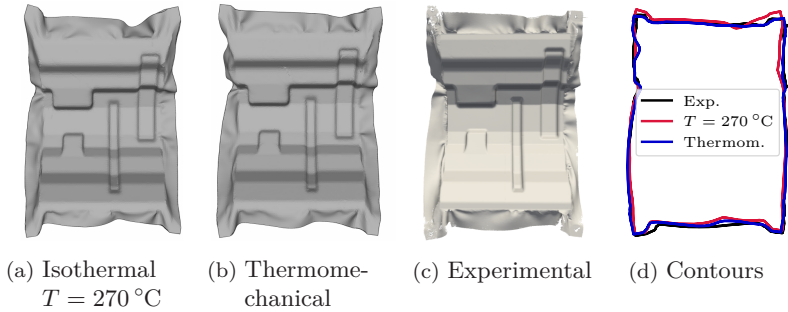
(d) Contours

Figure 6.12: Forming simulation results in (a) and (b), 3D measurement of the experimental test (c) and comparison of the outer contours (d) for the quasi-isotropic layup ($[0; -45; 90; 45]_\text{s}$) and fully closed tools.

In comparison of the final shapes, an increased prediction accuracy is observed for the thermomechanical approach. This applies especially for the unfolding of the outer areas, which is observed distinctively more pronounced for the quasi-isotropic layup compared to the orthotropic layup (cf. Figure 6.6). The course of the outer contours in Figure 6.12(d) also reveals a better agreement of the thermomechanical approach. Nonetheless, slight deviations are observed also for the thermomechanical approach, in particular at the upper left edge, where a dip of the laminate is predicted.

Additional results at several remaining tool travels Δz are compared to experimental tests in Figure 6.13. Throughout forming, distinctive wrinkling behavior is observed in the experimental tests, which is clearly captured by both simulation approaches. In a detailed comparison, however, an increased wrinkling behavior is predicted by the thermomechanical approach. Here, a high level of agreement to the experimental test is observed in comparison of the location, amount and direction of wrinkles. This is also valid for the sag and unfolding of the outer areas, which is in better agreement for the thermomechanical approach. In contrast, wrinkling behavior is predicted too little pronounced for the isothermal approach. Moreover, also deviations in the outer areas regarding unfolding and the sag of the laminate are observed. This difference, obviously, is reducible to local cooling of the laminate.

Stage 1: $\Delta z = 30\,\text{mm}$

Stage 2: $\Delta z = 17.5\,\text{mm}$

Stage 3: $\Delta z = 5\,\text{mm}$

Isothermal   **Thermomechanical**   **Experimental**
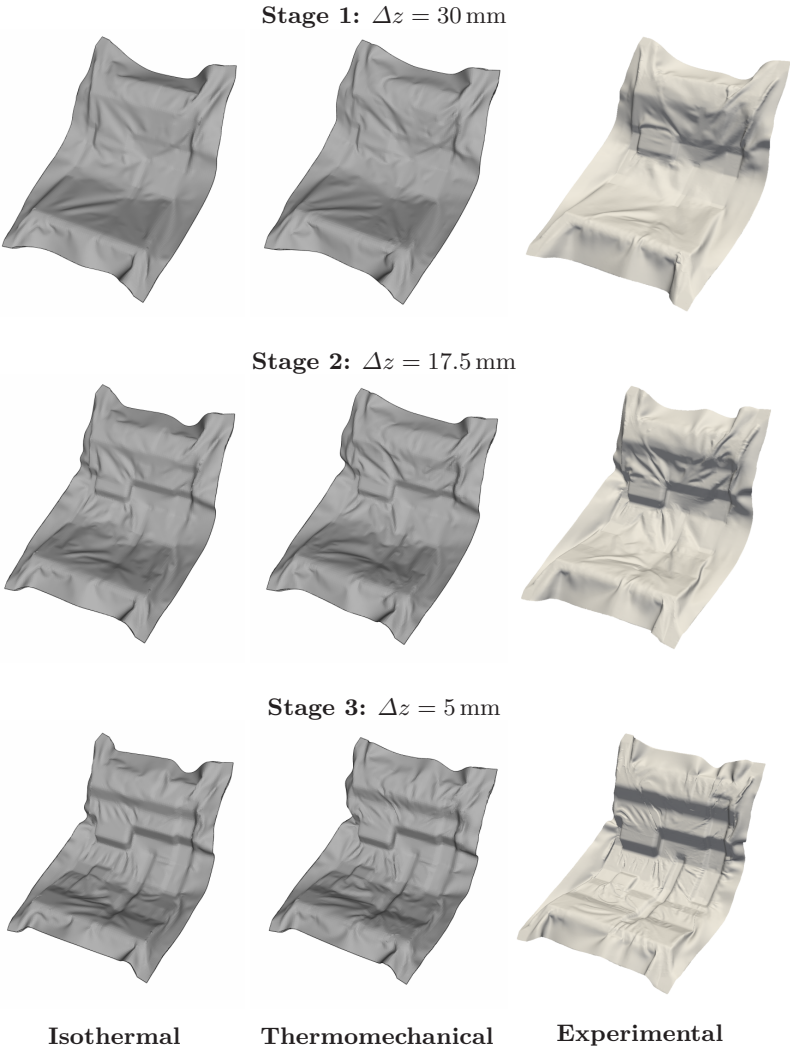
Figure 6.13: Comparison of thermoforming simulation, under application of the isothermal ($T = 270\,°\text{C}$) and the thermomechanical approach, to 3D measurements of experimental tests for the quasi-isotropic layup ($[0; -45; 90; 45]_\text{s}$) at several remaining tool travels Δz.

Stage 1: $\Delta z = 30\,\mathrm{mm}$

Stage 2: $\Delta z = 17.5\,\mathrm{mm}$

Stage 3: $\Delta z = 5\,\mathrm{mm}$

Stage 4: $\Delta z = 0\,\mathrm{mm}$

$T\ (^\circ\mathrm{C})$ $\qquad\qquad$ $\dot{T}\ (^\circ\mathrm{C/s})$ $\qquad\qquad$ $\alpha\ (-)$

140.0 210.0 280.0 $\qquad$ -100.0 0.0 100.0 $\qquad$ 0.0 0.5 1.0
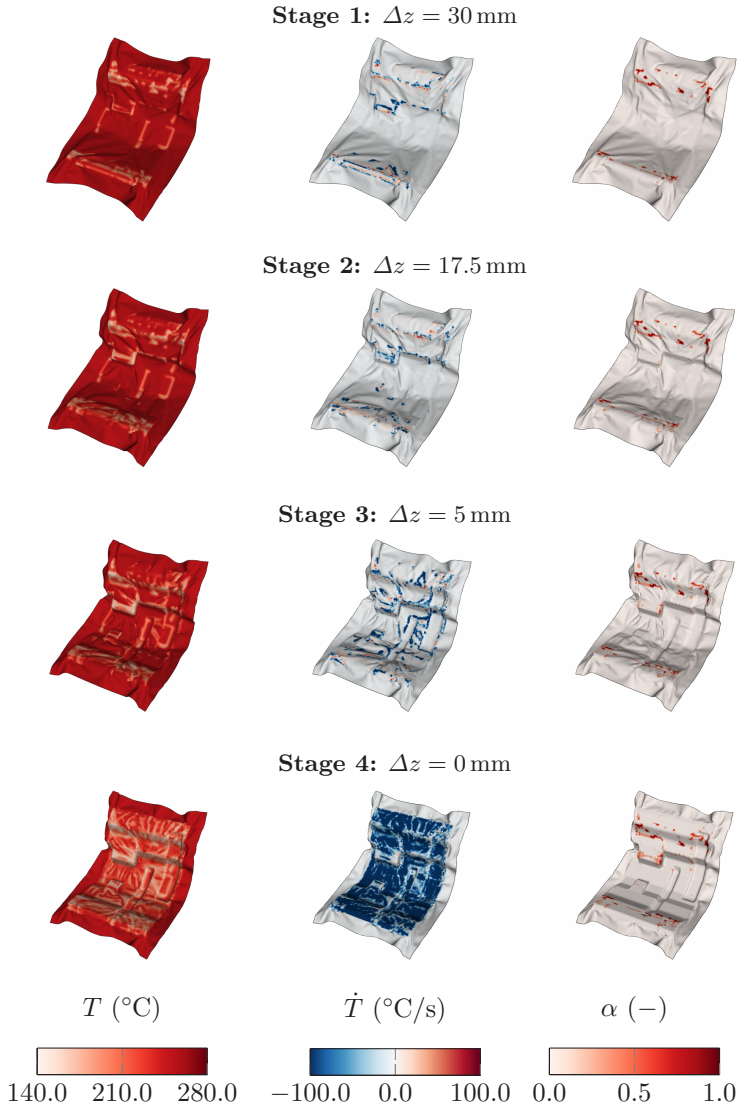
Figure 6.14: Temperature T, rate of temperature $\dot{T}$, and relative crystallinity α for the quasi-isotropic $([0; -45; 90; 45]_\mathrm{s})$ layup at several remaining tool travels Δz, obtained from the thermomechanical approach for the lowest ply.

237

Figure 6.14 shows the evolution of temperature T, rate of temperature $\dot{T}$ and relative crystallinity α for several stages Δz during forming and the lowest ply, since the most pronounced cooling is observed for this ply. Pronounced local cooling is observed around the bigger corner bending and the flanges of the part, which explains the more pronounced wrinkling for the thermomechanical approach in these areas. Nonetheless, areas with pronounced cooling are more localized compared to the orthotropic layup (cf. Figure 6.8), which can be reduced to distinctively pronounced wrinkling behavior, reducing the areas of tool-ply contact and thus also heat loss. Besides this, high cooling rates are observed locally in Stage 1 to 3 and evenly distributed in Stage 4 due to local tool-ply contact areas. In these areas, cooling rates yield up to 270 °C/s. Besides this, also local heating and localized crystallization is observed, in analogy to the orthotropic layup.

6.5.2 Variation of process parameters

In the scope of this section, the process parameters tool temperature T^{tool} and forming velocity $\bar{v}^{\text{tool}}$ are varied for both layups, following the factor levels of the experimental forming study listed in Table 2.1. The gripping force is kept on the intermediate level, to delimit the investigations to the seminal factors in the context of thermomechanics. Based on this, the adopted central composite design (CCD) provides factor levels with a variation of either forming velocity or tool temperature, which supports an unambiguous evaluation of the influence of the varied factors. Initially, the influence of the process parameters on laminate temperature and crystallization evolution is investigated (Section 6.5.2.1). Subsequently, wrinkling behavior is analyzed and the results of the thermomechanical approach are compared to the results of the related isothermal approach (Section 6.5.2.2 and 6.5.2.3).

6.5.2.1 Temperature and crystallization

Orthotropic layup Figure 6.15 shows the comparison of the temperature evolution measured in the experimental tests to the related simulation results. Details on the experimental measurements are outlined in Section 2.2.3. Two different positions are considered for temperature measurements, TC-1 and TC-2 (cf. Figure 6.9). Again,
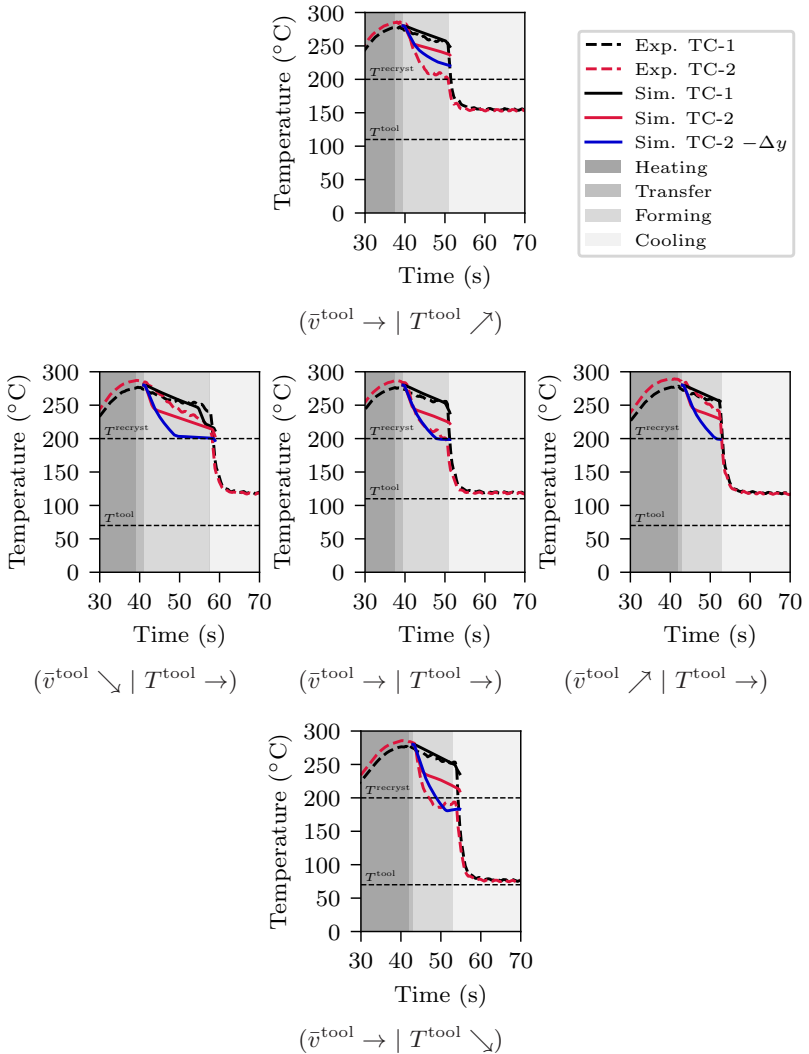
Figure 6.15: Temperature measurement and comparison to thermoforming simulation results for the orthotropic layup ($[0; 90]_{2s}$) under variation of tool temperature T^{tool} and mean forming velocity $\bar{v}^{\mathrm{tool}}$ for the intermediate gripper force F^{grip}; recrystallization temperature T^{cryst} characterized at a constant cooling rate of $10\,^{\circ}\mathrm{C/min}$.

239

also the additional position TC-2$-\Delta y$ is evaluated, since high in-plane temperature gradients are observed at TC-2.

The simulation results reveal a systematic influence of the varied process parameters on temperature evolution, where a lower tool temperature T^{tool} and a lower mean forming velocity $\bar{v}^{\text{tool}}$ induce lower temperatures in the laminate. The lowest temperatures are observed for the design point with low tool temperature ($\bar{v}^{\text{tool}} \rightarrow | T^{\text{tool}} \searrow$). The qualitative evolution of temperature is maintained for each design point, where the most pronounced cooling is observed at TC-2$-\Delta y$. Under variation of forming velocity, however, the tool-ply contact situation seems to change, since otherwise distinctively lower temperatures would to be expected especially for the low forming velocity ($\bar{v}^{\text{tool}} \searrow | T^{\text{tool}} \rightarrow$). In comparison of the simulation results to the according experimental tests, an overall good agreement is observed for TC-1. In contrast, the degree of agreement varies for TC-2. A good agreement is observed for the design points ($\bar{v}^{\text{tool}} \rightarrow | T^{\text{tool}} \rightarrow$) and ($\bar{v}^{\text{tool}} \rightarrow | T^{\text{tool}} \searrow$). On the contrary, deviations are observed for the remaining design points. Thereby, it is to be noted that a small delay in time yields large deviations between the temperature evolutions. Besides this, a high sensitivity to the evaluated position due to high in-plane temperature gradients exists in the area of TC-2. Therefore, a comprehensive validation of TC-2 is hindered.

Figure 6.16 shows the temperature T at the moment of full tool closure for the lowest ply. It is clearly observed that a lower forming velocity $\bar{v}^{\text{tool}}$ and a lower tool temperature T^{tool} induce lower temperatures. The lowest temperatures are observed for the design point with low forming velocity ($\bar{v}^{\text{tool}} \searrow | T^{\text{tool}} \rightarrow$), where temperatures close to the tool temperature of $110\,°\text{C}$ are observed. Based on this, forming velocity seems to have a larger impact on the temperature distribution than tool temperature in a qualitative comparison of the influence of the varied factors.

Figure 6.17 shows the related relative crystallinity α. Severe recrystallized areas are observed for the low forming velocity ($\bar{v}^{\text{tool}} \searrow | T^{\text{tool}} \rightarrow$), which is distinctively reduced by increasing forming velocity $\bar{v}^{\text{tool}}$ and tool temperature T^{tool}. The least recrystallized areas are observed for the high tool temperature ($\bar{v}^{\text{tool}} \rightarrow | T^{\text{tool}} \nearrow$). However, forming velocity shows the more significant influence on recrystallized areas, in line with the observed temperature distribution.

$(\bar{v}^{\text{tool}} \to \mid T^{\text{tool}} \nearrow)$

$(\bar{v}^{\text{tool}} \searrow \mid T^{\text{tool}} \to)$ $\qquad$ $(\bar{v}^{\text{tool}} \to \mid T^{\text{tool}} \to)$ $\qquad$ $(\bar{v}^{\text{tool}} \nearrow \mid T^{\text{tool}} \to)$

$(\bar{v}^{\text{tool}} \to \mid T^{\text{tool}} \searrow)$

T $(°\text{C})$

70 $\quad$ 110 $\quad$ 150 175 $\qquad\qquad$ 280
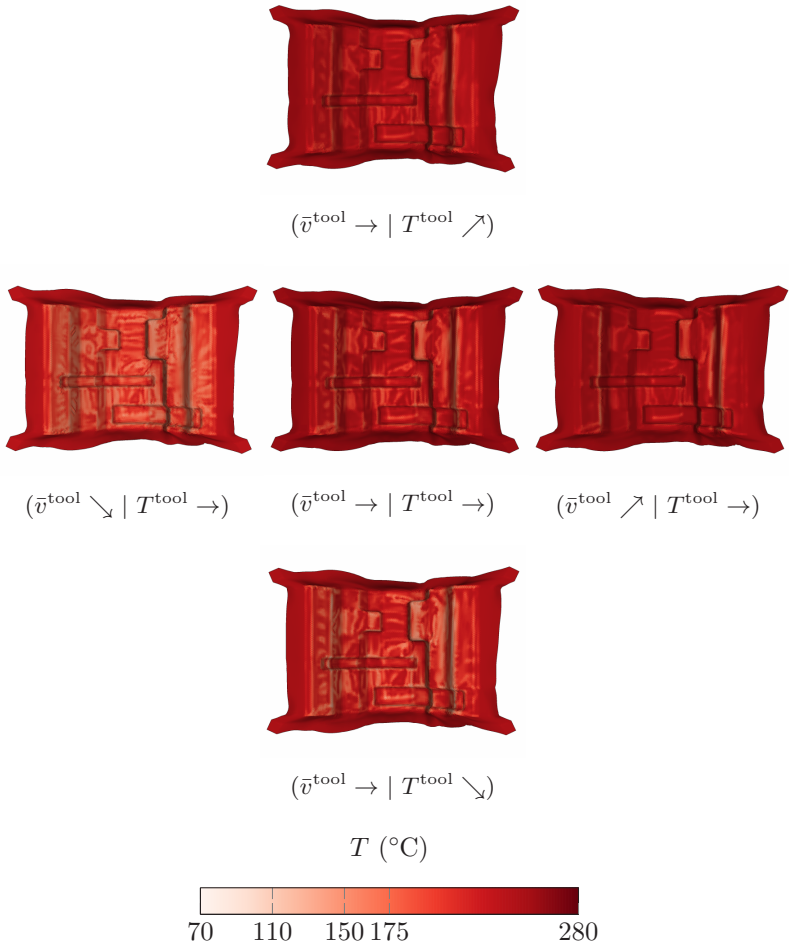
Figure 6.16: Results for the temperature T of the lowest ply at the moment of full tool closure under variation of tool temperature T^{tool} and forming velocity $\bar{v}^{\text{tool}}$ for the intermediate gripping force F^{grip} and the orthotropic layup $([0; 90]_{2\text{s}})$.

$$(\bar{v}^{\text{tool}} \rightarrow \mid T^{\text{tool}} \nearrow)$$

$$(\bar{v}^{\text{tool}} \searrow \mid T^{\text{tool}} \rightarrow) \qquad (\bar{v}^{\text{tool}} \rightarrow \mid T^{\text{tool}} \rightarrow) \qquad (\bar{v}^{\text{tool}} \nearrow \mid T^{\text{tool}} \rightarrow)$$

$$(\bar{v}^{\text{tool}} \rightarrow \mid T^{\text{tool}} \nearrow)$$

$$\alpha \ (\text{-})$$

Figure 6.17: Results for the relative crystallinity α of the lowest ply at the moment of full tool closure under variation of tool temperature T^{tool} and forming velocity $\bar{v}^{\text{tool}}$ for the intermediate gripping force F^{grip} and the orthotropic layup $([0; 90]_{2\text{s}})$.

$(\bar{v}^{\mathrm{tool}} \rightarrow \mid T^{\mathrm{tool}} \nearrow)$

$(\bar{v}^{\mathrm{tool}} \searrow \mid T^{\mathrm{tool}} \rightarrow)$ $(\bar{v}^{\mathrm{tool}} \rightarrow \mid T^{\mathrm{tool}} \rightarrow)$ $(\bar{v}^{\mathrm{tool}} \nearrow \mid T^{\mathrm{tool}} \rightarrow)$

$(\bar{v}^{\mathrm{tool}} \rightarrow \mid T^{\mathrm{tool}} \searrow)$

$T\ (^{\circ}\mathrm{C})$

70   110   150 175   280

Figure 6.18: Results for the temperature T of the lowest ply at the moment of full tool closure under variation of tool temperature T^{tool} and forming velocity $\bar{v}^{\mathrm{tool}}$ for the intermediate gripping force F^{grip} and the quasi-isotropic layup ($[0; -45; 90; 45]_{\mathrm{s}}$).

243

$(\bar{v}^{\mathrm{tool}} \rightarrow \mid T^{\mathrm{tool}} \nearrow)$

$(\bar{v}^{\mathrm{tool}} \searrow \mid T^{\mathrm{tool}} \rightarrow)$ $\qquad$ $(\bar{v}^{\mathrm{tool}} \rightarrow \mid T^{\mathrm{tool}} \rightarrow)$ $\qquad$ $(\bar{v}^{\mathrm{tool}} \nearrow \mid T^{\mathrm{tool}} \rightarrow)$

$(\bar{v}^{\mathrm{tool}} \rightarrow \mid T^{\mathrm{tool}} \searrow)$

α (-)

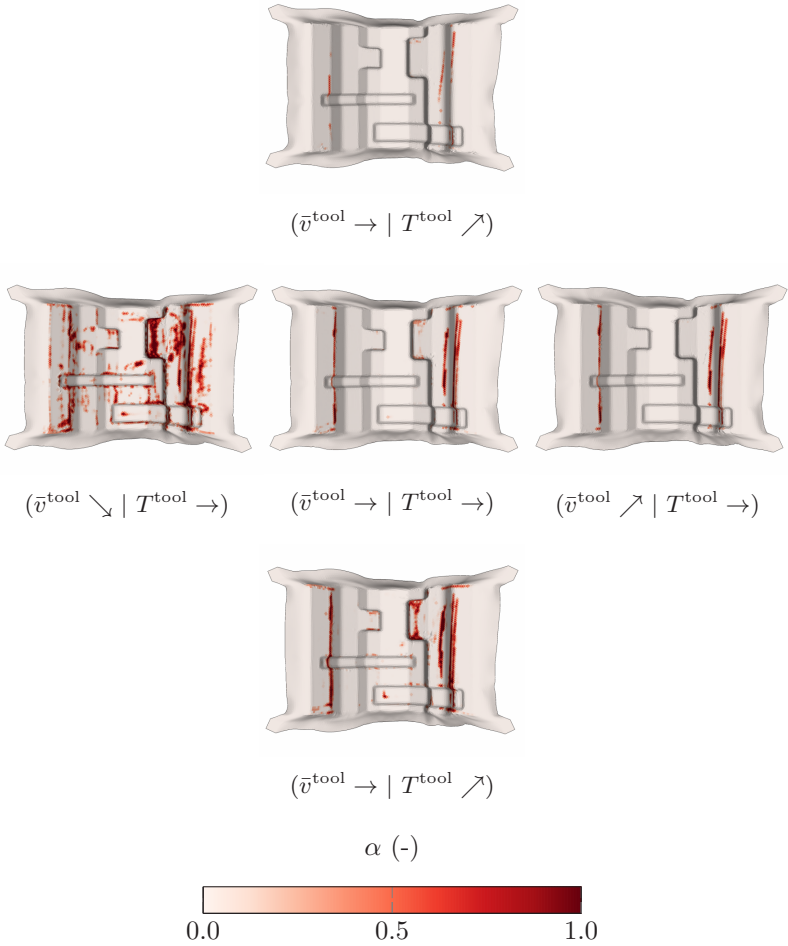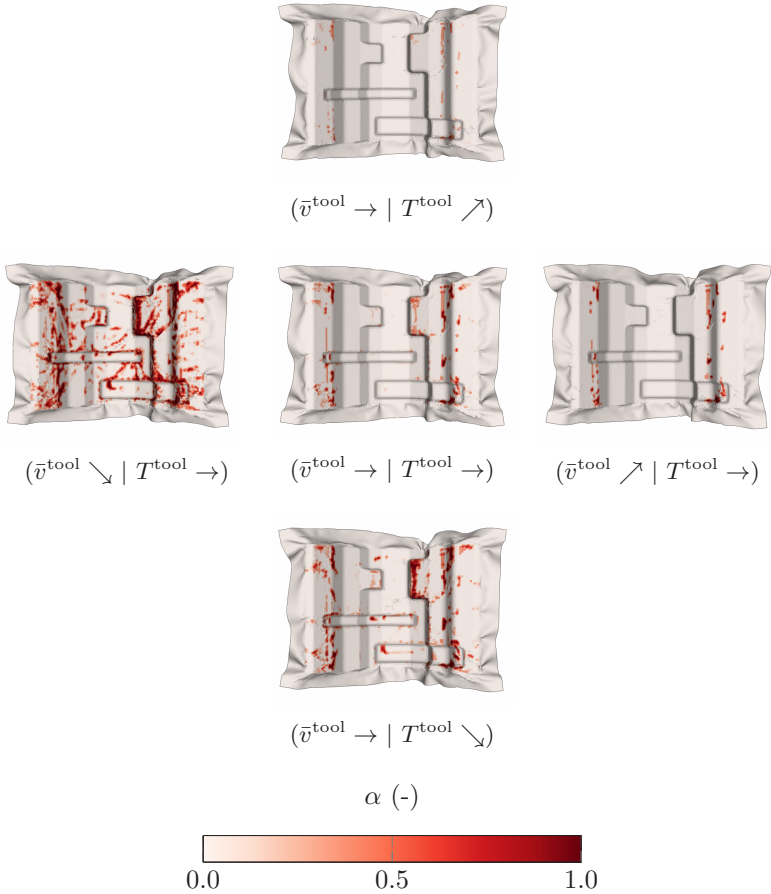0.0 $\qquad$ 0.5 $\qquad$ 1.0

Figure 6.19: Results for the relative crystallinity α of the lowest ply at the moment of full tool closure under variation of tool temperature T^{tool} and forming velocity $\bar{v}^{\mathrm{tool}}$ for the intermediate gripping force F^{grip} and the quasi-isotropic layup ($[0; -45; 90; 45]_{\mathrm{s}}$).

Quasi-isotropic layup Figure 6.18 and 6.19 show the simulation results for the quasi-isotropic layup for the temperature T and the relative crystallinity α, respectively. The same dependencies as for the orthotropic layup are observed for the quasi-isotropic, where the most distinct cooling and recrystallization is observed for the design point with low forming velocity ($\bar{v}^{\text{tool}} \searrow \mid T^{\text{tool}} \rightarrow$). Here, temperatures close to the tool temperature of $110\,^{\circ}\text{C}$ are observed. Thereby, the variation of forming velocity seems again to have a larger impact on temperature distribution. The least recrystallized areas are observed for the design point with high tool temperature ($\bar{v}^{\text{tool}} \rightarrow \mid T^{\text{tool}} \nearrow$).

6.5.2.2 Qualitative analysis of wrinkling behavior

Orthotropic layup Figure 6.20 shows the elemental modified mean curvature $\bar{\kappa}^{\text{el}}$ according to Equation 2.2 (cf. Section 2.1.2) for the orthotropic layup and a remaining tool travel of $5\,\text{mm}$, to investigate the influence of the varied factors on wrinkling behavior. A clear influence of the varied factors on wrinkling behavior is observed, where a lower forming velocity $\bar{v}^{\text{tool}}$ and a lower tool temperature T^{tool} yield an increase in wrinkling behavior. This is clearly visible by an increase of the large fold above the bigger corner bending, as well as by an increase of wrinkling between the corner bendings and the beads, in agreement with the experimental tests (cf. Figure 2.9). Based on this, the most pronounced wrinkling behavior is observed for the design points ($\bar{v}^{\text{tool}} \searrow \mid T^{\text{tool}} \rightarrow$) and ($\bar{v}^{\text{tool}} \rightarrow \mid T^{\text{tool}} \searrow$). In contrast, the least wrinkling tendency is observed for the design point with high tool temperature ($\bar{v}^{\text{tool}} \rightarrow \mid T^{\text{tool}} \nearrow$), which is mainly reflected by the reduction of the large fold above the bigger corner bending.

To investigate the influence of the thermomechanical approach against the related isothermal approach, the initial laminate temperature of $280\,^{\circ}\text{C}$ is assigned constant by a boundary condition, which yields a purely isothermal approach. Consequently, the influence of a varying tool temperature cannot be captured. Therefore, only the forming velocity is varied. The according results are shown in Figure 6.21. The isothermal results reveal mostly no influence of forming velocity on wrinkling behavior. In a qualitative comparison, the only visible difference is the small additional wrinkle above the bigger corner bending evolving with an increase of forming velocity.

245

$(\bar{v}^{\text{tool}} \rightarrow | \ T^{\text{tool}} \nearrow)$

$(\bar{v}^{\text{tool}} \searrow | \ T^{\text{tool}} \rightarrow)$ $(\bar{v}^{\text{tool}} \rightarrow | \ T^{\text{tool}} \rightarrow)$ $(\bar{v}^{\text{tool}} \nearrow | \ T^{\text{tool}} \rightarrow)$

$(\bar{v}^{\text{tool}} \rightarrow | \ T^{\text{tool}} \searrow)$

$\bar{\kappa}^{\text{el}} \ (\text{mm}^{-1})$

0.000   0.075   0.150

Figure 6.20: Results for the elemental modified mean curvature $\bar{\kappa}^{\text{el}}$ for the or-thotropic layup and a remaining tool travel of 5 mm under variation of tool temperature T^{tool} and forming velocity $\bar{v}^{\text{tool}}$ for the intermediate gripping force F^{grip} and application of the thermomechanical approach.

$(\bar{v}^{\text{tool}} \searrow \,|\, - \,)$ $(\bar{v}^{\text{tool}} \rightarrow \,|\, - \,)$ $(\bar{v}^{\text{tool}} \nearrow \,|\, - \,)$

$$\bar{\kappa}^{\text{el}} \; (\text{mm}^{-1})$$
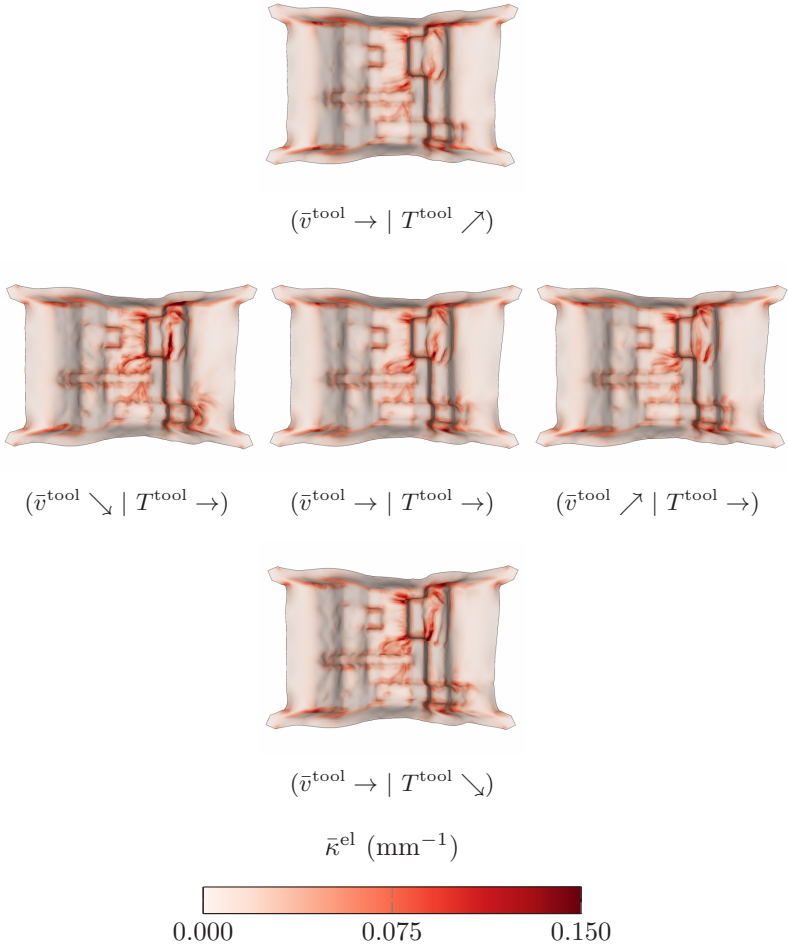
0.000   0.075   0.150

Figure 6.21: Results for the elemental modified mean curvature $\bar{\kappa}^{\text{el}}$ for the orthotropic layup and a remaining tool travel of 5 mm under variation of forming velocity $\bar{v}^{\text{tool}}$ for the intermediate gripping force F^{grip} and application of the isothermal approach.

In comparison of the isothermal results to the related thermomechanical results, large deviations are observed, since less pronounced wrinkling behavior is predicted for all design points. This observation is already made in the detailed analysis of the intermediate factor level in Section 6.5.1. Furthermore, the increase of wrinkling behavior towards lower forming velocities and tool temperatures observed for the thermomechanical approach, which is in agreement with the experimental tests (cf. Figure 2.9), is obviously not captured by the isothermal approach.

Quasi-isotropic layup The elemental modified mean curvature $\bar{\kappa}^{\text{el}}$ (cf. Section 2.1.2) is evaluated also for the quasi-isotropic layup at a remaining tool travel of 5 mm, to investigate the influence of the varied process parameters on wrinkling prediction. The according results are shown in Figure 6.22.

Severe wrinkling behavior is predicted for all factor levels, where differences between the different factor levels are observed. This is visible in particular above the bigger corner bending. These differences, however, are not as obvious as observed for the orthotropic layup (cf.

247

$(\bar{v}^{\text{tool}} \rightarrow | \ T^{\text{tool}} \nearrow)$

$(\bar{v}^{\text{tool}} \searrow | \ T^{\text{tool}} \rightarrow)$ $\qquad$ $(\bar{v}^{\text{tool}} \rightarrow | \ T^{\text{tool}} \rightarrow)$ $\qquad$ $(\bar{v}^{\text{tool}} \nearrow | \ T^{\text{tool}} \rightarrow)$

$(\bar{v}^{\text{tool}} \rightarrow | \ T^{\text{tool}} \searrow)$

$\bar{\kappa}^{\text{el}} \ (\text{mm}^{-1})$

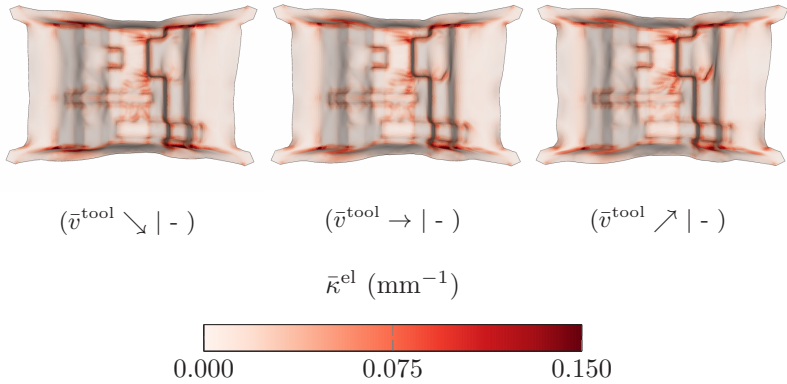0.000 $\qquad$ 0.075 $\qquad$ 0.150

Figure 6.22: Results for the elemental modified mean curvature $\bar{\kappa}^{\text{el}}$ for the quasi-isotropic layup and a remaining tool travel of $5\,\text{mm}$ under variation of tool temperature T^{tool} and forming velocity $\bar{v}^{\text{tool}}$ for the intermediate gripping force F^{grip} and application of the thermomechanical approach.

$(\bar{v}^{\text{tool}} \searrow | -)$ $\qquad$ $(\bar{v}^{\text{tool}} \rightarrow | -)$ $\qquad$ $(\bar{v}^{\text{tool}} \nearrow | -)$

$$\bar{\kappa}^{\text{el}} \ (\text{mm}^{-1})$$
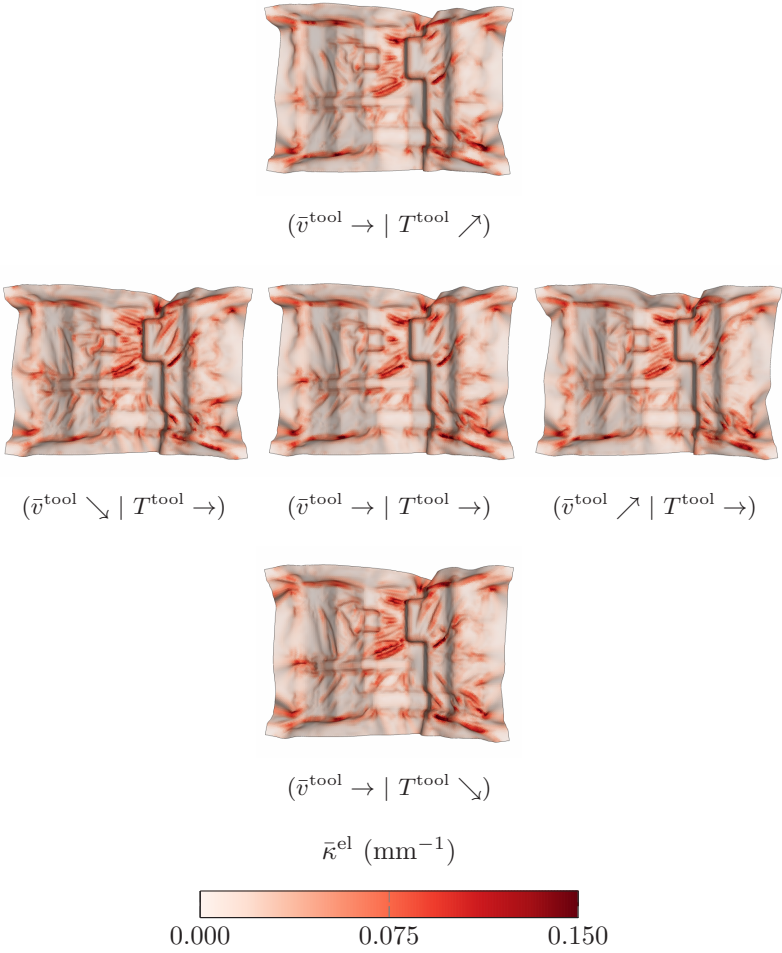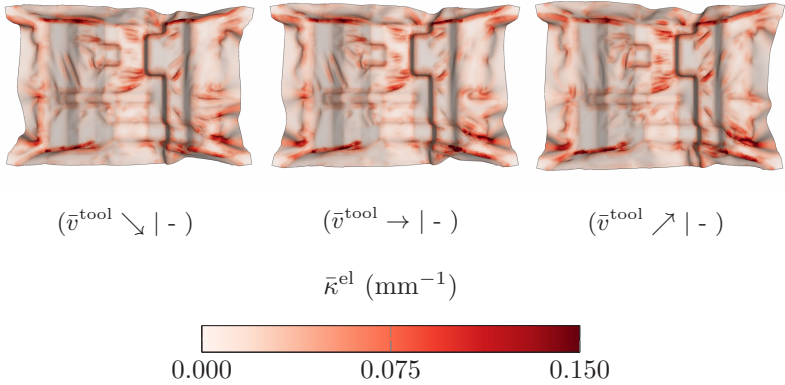
0.000 $\qquad$ 0.075 $\qquad$ 0.150

Figure 6.23: Results for the elemental modified mean curvature $\bar{\kappa}^{\text{el}}$ for the quasi-isotropic layup and a remaining tool travel of 5 mm under variation of forming velocity $\bar{v}^{\text{tool}}$ for the intermediate gripping force F^{grip} and application of the isothermal approach.

Figure 6.20). Nonetheless, a decrease of wrinkling tendency towards a higher forming velocity $\bar{v}^{\text{tool}}$ and higher tool temperature T^{tool} is observed, which is in agreement with the experimental tests (cf. Figure 2.12). Thereby, the least wrinkling is observed for the design point with high tool temperature $(\bar{v}^{\text{tool}} \rightarrow | T^{\text{tool}} \nearrow)$.

To investigate the influence of the thermomechanical approach against the related isothermal approach, the initial laminate temperature of 280 °C is assigned constant by a boundary condition, which yields a purely isothermal approach. Only forming velocity is varied, since the isothermal approach is not capable to account for the changing tool temperature. The according results are shown in Figure 6.23. In analogy to the orthotropic layup (cf. Figure 6.21), mostly no influence of the varied tool velocity on wrinkling behavior is observed for the isothermal approach.

In comparison of the isothermal results to the related thermomechanical results, large deviations are observed, since in analogy to the orthotropic layup less pronounced wrinkling behavior is predicted for all design points. This observation is already made in the detailed analysis of the intermediate factor level in Section 6.5.1. Besides this, the

249

slight increase of wrinkling behavior towards lower forming velocities and tool temperatures observed for the thermomechanical approach, which is in agreement with the experimental tests (cf. Figure 2.12), is obviously not captured by the isothermal approach.

6.5.2.3 Quantitative analysis of wrinkling behavior

To enable a quantitative investigation of the predicted influence of the varied process parameters on wrinkling behavior, response surface methodology is applied to the obtained simulation results, following the thermomechanical and the isothermal approach, as well as to the surface measurements of the experimental forming tests. For this purpose, a similar approach as in Section 2.2.2.2 is pursued, with the only difference that only the intermediate gripping force is considered for parametrization of the model function. Also here, the arithmetic mean of the elemental modified mean curvature weighted by the element area $\langle \bar{\kappa}^{\mathrm{el}} \rangle$ (cf. Section 2.1.2) is adopted as scalar measure for wrinkling intensity. Here, the first-order model given by

$$\langle \bar{\kappa}^{\mathrm{el}} \rangle \approx \alpha_0 + \alpha_{\mathrm{v}} x_{\mathrm{v}}^* + \alpha_{\mathrm{T}} x_{\mathrm{T}}^* + \epsilon, \tag{6.41}$$

is chosen, where α_0 is a constant offset, α_{v} and α_{T} the regression coefficients for forming velocity and tool temperature, x_{v}^* and x_{T}^* the related normalized factors, respectively, and ϵ an error, which is allowed but minimized by the method of least squares [229]. For the experimental tests, all of the three available replicates are considered for regression.

The regression results are shown in Figure 6.24. In these plots, the equidistant contour intervals reflect constant levels of curvature. Thus, the narrower the contour intervals, the higher the sensitivity of the varied process parameters on wrinkling behavior. On the contrary, the inclination of the contour intervals reflects the balance of the sensitivity between the varied factors.

The contour plots reveal in general higher curvature values for the experimental tests compared to the simulation results. Besides this, a clear sensitivity to forming velocity and tool temperature is determined for both layups. This sensitivity is clearly reflected by the thermomechanical approach for both layups. Thereby, the inclination
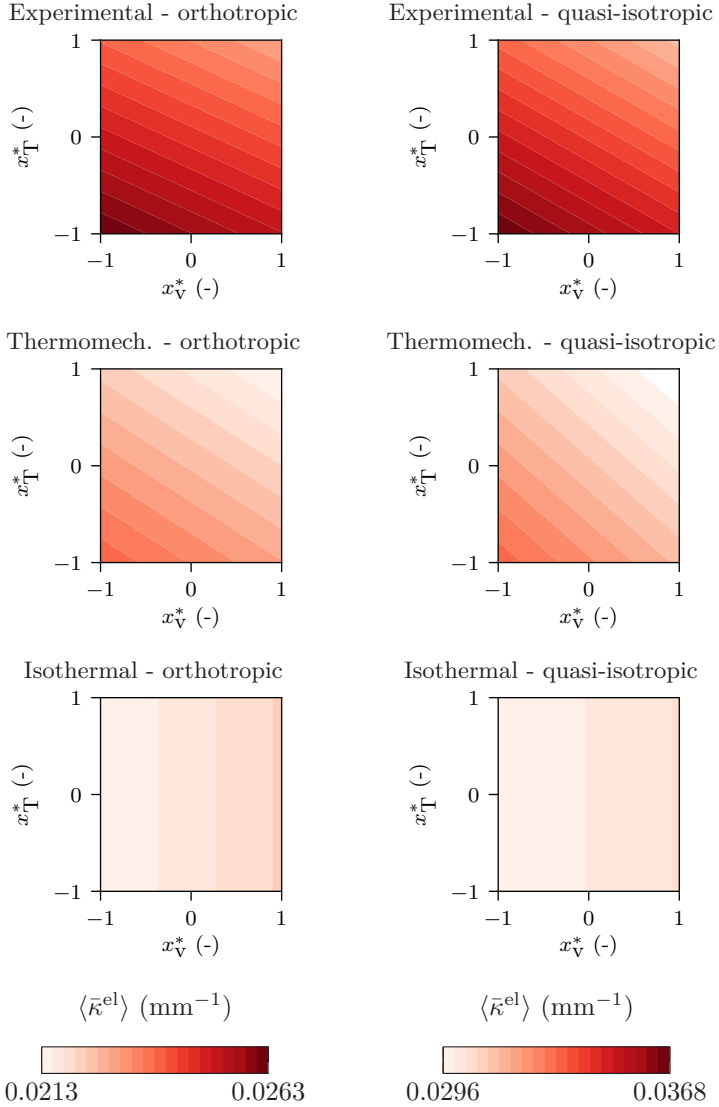
Figure 6.24: Contour plots for the first-order response surfaces for the orthotropic (left) and the quasi-isotropic (right) layup for the experimental tests and thermoforming simulation.

of the contour intervals of the experimental tests and the thermo-
mechanical approach are basically comparable. However, a higher
sensitivity to forming velocity, respectively a lower sensitivity to tool
temperature, is observed for the thermomechanical forming simula-
tion results. Moreover, a lower overall sensitivity, which is reflected
by the broader contour intervals, is observed. Nonetheless, the slightly
higher sensitivity to tool temperature, respectively the slightly lower
sensitivity to forming velocity, observed for the experimental tests for
the orthotropic layup is captured by the thermomechanical approach.
Regarding the isothermal simulation results, obviously no sensitivity
w.r.t. to tool temperature exists. Beyond that, a negligible sensitivity
is observed for the isothermal approach for both layups w.r.t. forming
velocity, which is reflected by broad contour intervals. Thereby, it is to
be noted that the remaining sensitivity behaves vice versa compared
to the experimental tests and the thermomechanical approach.

6.6 Discussion and conclusion

A coupled thermomechanical approach for thermoforming simulation
considering crystallization kinetics as well as temperature- and rate-
dependent forming behavior, which is implemented in the commercial
FE solver Abaqus in combination with several user-subroutines, is
presented.

Material modeling The proposed thermomechanical framework for
thermoforming simulation is based on the isothermal DKT shell for-
mulation in combination with the nonlinear generalized Maxwell ap-
proach outlined in Chapter 4, which is enhanced in the scope of this
chapter by a temperature degree of freedom. The related thermal
modeling takes into account radiation, convection and heat conduc-
tion as well as the prediction of crystallization kinetics. Mechanical
behavior is coupled to thermal behavior w.r.t. temperature and rela-
tive crystallinity. Based on this, the transition from the molten to the
solid material state is predicted and considered in forming behavior.
This is the first approach of this type, since the phase transition is
usually not considered in thermoforming simulation.

At the onset of crystallization, the material is assumed to be stress-free by means of the introduction of an additional reference configuration for the solidified material state. Moreover, the material is assumed to behave purely elastic in this material state. These assumptions are expected to be reasonable for the prediction of wrinkling behavior, which is pursued in the scope of this study, since material modeling in the solid material state serves rather for the introduction of a forming limit than predicting the accurate stress and strain distribution.

This changes, if thermoforming simulation is adopted for the prediction of part distortion or residual stresses, which would basically be possible, if thermal expansion and shrinkage due to crytallization are additionally considered in material modeling. In this context, also the internal energy stored in the fibers might influence the obtained result, which could be directly considered by adapting material modeling w.r.t. the transition from the molten to the solid material state. Nonetheless, the prediction of through the thickness stresses might become necessary for an accurate prediction of part distortion and residual stresses. For this purpose, three-dimensional shell elements, which are currently entering composite forming simulation [17, 281], could serve as remedy.

Besides this, a further deformation of the solidified areas is most likely to be accompanied with nonlinear material behavior. Therefore, accounting for plasticity and damage in material modeling in the solidified material is expected to be worth to be investigated in future activities. Modeling of these mechanisms would also enable to further investigate the part quality obtained after forming. Additionally, the obtained additional information could be passed on to subsequent simulation steps in the context of a continuous CAE chain [6, 282], to enhance the prediction accuracy of subsequent simulation steps, such as structural analyses.

Parametrization A parametrization strategy for the coupled thermo-mechanical approach is proposed, which includes thermal parametrization as well as mechanical parametrization separately for the molten and the solid material state. Thermal parametrization uses DSC measurements for heat capacity and latent heat, literature data and

rule of mixtures for heat conductivity and cooling experiments for convection, radiation and tool-ply gap conductance.

The cooling experiments serve on the one hand for parametrization of the aforementioned material-dependent boundary conditions, convection and tool-ply gap conductance. On the other hand, the cooling experiments are adopted for validation of crystallization kinetics modeling. Based on this, the strategy of combining S- and F-DSC measurements has proven to be suitable to characterize and parametrize crystallization kinetics over a wide range of cooling rates, since a good agreement is observed for the crystallization peak determined from the temperature rate of the cooling experiments. Thereby, it is to be noted that according cooling rates lie in between the cooling rates considered in S- and F-DSC measurements. Henceforth, the missing overlay of cooling rates in S- and F-DSC measurements is expected to be no drawback for the presented parametrization strategy. Also crystallization enthalpy, which was determined at $0.16\,°C/s$, yields a good approximation of the cooling retardation at cooling rates around $4\,°C/s$. Moreover, even higher cooling rates observed for tool-ply conductance did not yield unreasonable results. Therefore, the missing specimen mass and resulting hindered determination of specific crystallization enthalpy for F-DSC measurements at higher cooling rates is deemed to be acceptable in the context of thermoforming simulation.

Thermoforming simulation The application of the coupled thermomechanical approach and related parametrization to the complexly shaped and generic geometry reveals an improved agreement to the according experimental forming tests compared to the isothermal approach. It is observed for the orthotropic layup that some forming defects are not captured by the isothermal approach, which in contrast are clearly captured by the thermomechanical approach. Moreover, the distinct wrinkling behavior observed in experimental tests for the quasi-isotropic layup is better reflected by the thermomechanical approach compared to isothermal approach, for which wrinkling behavior is predicted too little pronounced. This observation is reducible to local cooling of the laminate, which obviously is not captured by the isothermal approach, but which is indeed observed locally at the tool-ply contact areas.

Besides forming behavior, also thermal behavior is compared to experimental tests by means of local temperature measurements. Thereby, it is to be noted that high temperature gradients impede the validation process, since a strong sensitivity to local deviations exists. Besides this, high temperature rates induce also a high sensitivity to small deviations w.r.t. time. This is shown in the scope of this study by means of the variation of the positions evaluated for the comparison of the local temperature measurements. However, validation of local temperature evolution based on measurements at a single point is not sufficiently comprehensive. Therefore, the application of fiber optical sensors rather than thermocouples could serve as remedy, since these enable to measure along a line rather than at a discrete point.

Besides pronounced local cooling, also local recrystallization is observed already during forming. For this particular geometry and process strategy, recrystallized areas result mainly from the initial positioning of the laminate onto the lower (female) tool. Possibly, this localized recrystallization could be prevented by an adapted process strategy. Nonetheless, the simulation results reveal that recrystallization already during forming cannot be excluded in general, which is expected to be an important finding for the application of thermoforming simulation to virtual process design.

Finally, the process parameters tool temperature and forming velocity are varied in thermoforming simulation, under application of the thermomechanical and related isothermal approach. A distinct influence of the varied parameters on local crystallization is observed. Both, a low forming velocity and a low tool temperature induce severe crystallization already during forming for both layups. In comparison, a higher sensitivity is observed for forming velocity. Besides this, a clear influence of process parameters on forming behavior is predicted by the thermomechanical approach. It is shown qualitatively and quantitatively that a higher tool temperature and a higher forming velocity yields a lower wrinkling tendency, which is in agreement with the experimental tests. Nonetheless, some deviations regarding the influence of the varied parameters are observed. First, higher curvature values are observed for the experimental test. Since wrinkling behavior is in a good agreement in a qualitative comparison, this deviation is expected to result mainly from the differing discretization, since three times larger elements are adopted for thermoforming sim-

ulation compared to the triangularized surface measurement results. Second, a slightly differing sensitivity to the varied process parameters observed, where the thermomechanical thermoforming simulation shows a slightly too little pronounced sensitivity to tool temperature. Thereby, it is to be noted that comparably small differences in the experimental tests are discussed. Nonetheless, two major issues are expected to possibly induce the deviation.

On the one hand, the high uncertainty in parametrization of the tool-ply gap conductance, due to the high standard deviations observed in the related experimental characterization tests, could be one possible origin, although the analysis of local temperature evolution has shown valid results. Tool-ply gap conductance is the main driver for heat loss of the laminate and therefore a high sensitivity of the overall cooling and forming behavior to this parameter exists. Henceforth, future research should focus on an improved determination of tool-ply gap conductance, including the dependency of the tool-ply gap conductance on normal traction. In combination with a three-dimensional shell element, which enhances modeling capabilities among others w.r.t. to an accurate prediction of contact normal traction, the prediction of the heat loss due to tool-ply gap conductance could be improved.

On the other hand, prediction of thermal behavior could be influenced by the limited tool-ply interaction tracking thickness, which is set in the scope of this study to 0.1 mm according to the default values of Abaqus [242]. Accompanied with the limited spatial discretization, heat loss due to local tool-ply contact might be captured not accurately enough, especially for the quasi-isotropic layup, which is accompanied with distinct wrinkling behavior. Since the possibility for a global mesh refinement is limited due to numerical efficiency, adaptive meshing techniques could be worthwhile to be investigated in this context.

Furthermore, the thermomechanical results are compared to the results of the related isothermal approach, which is capable to consider only the changing forming velocity by means of rate-dependent material modeling. Mostly no influence of a changing forming velocity onto wrinkling prediction is observed for the isothermal approach. This is in contrast to the investigations by Guzman-Maldonado et al. [261], where a distinct influence of forming velocity on wrinkling prediction is observed. In this study, however, bending stiffness is purely

elastic and thus does not increase with an increasing forming velocity. On the contrary, the approach presented in this study considers rate-dependency for both, membrane and bending modeling. Accompanied with the fact that the remaining sensitivity to forming velocity shows the opposite behavior for the isothermal approach compared to the experimental tests and the thermomechanical forming simulation, the changing thermal behavior is expected to be the main driver for the influence of forming velocity on wrinkling behavior, since forming velocity also influences cooling behavior by means of the time of local tool-ply contact.

Based on the above outlined insights, the presented approach is considered as a next step for thermoforming simulation, taking into account the relevant process parameters as well as the relevant material characteristics, including the consideration of the phase transition from the molten to the solid material state. Based on this, prediction accuracy of thermoforming simulation has proven to be improved. Therefore, the proposed modeling techniques are expected to be a useful further development in direction of a holistic approach for the virtual process design of thermoforming processes.

7 Conclusions and recommendations

The forming behavior of UD fiber-reinforced thermoplastic tape laminates in thermoforming processes was investigated and modeling approaches for thermoforming simulation were developed. The results of this research contribute to the enhancement of the predictive capabilities of thermoforming simulation. The major conclusions and recommendations from these achievements are summarized in this chapter.

Conclusions

- Experimental investigations verified a distinct rate- and temperature-dependent material behavior at process conditions, as well as an influence of the process parameters forming velocity, tool temperature and gripping force on formability and local cooling.

- Viscoelastic material modeling approaches are capable to describe the rate-dependent intra-ply deformation behavior in the molten material state. Only a nonlinear generalized Maxwell approach is capable to predict the whole material characteristic. In contrast, a nonlinear Voigt-Kelvin approach yields only approximate results, especially for lower temperatures and higher deformation rates.

- The consideration of rate-dependent bending behavior influences wrinkling prediction, where more pronounced wrinkling behavior is observed if this material characteristic is not considered. This observation emphasizes the necessity to use a transient testing procedures for bending characterization and the application of rate-dependent bending modeling approaches.

- A nonlinear Voigt-Kelvin approach is sufficient for modeling rate-dependent membrane behavior in thermoforming simula-

tion, since negligible differences between the nonlinear generalized Maxwell and the nonlinear Voigt-Kelvin approach are observed for isothermal thermoforming simulation.

- A linear friction model is sufficient to capture the pressure- and rate-dependency for a given temperature and relative orientation between the slipping plies. The consideration of anisotropic inter-ply slip in thermoforming prediction does not significantly influence the formability prediction.

- Membrane tensioning can be predicted accurately under the consideration of gripper force and gripper kinematics.

- Coupled thermomechanical thermoforming simulation improves the prediction accuracy for wrinkling behavior and is capable to take into account the influence of a varying tool temperature and forming velocity.

- Crystallization during forming cannot be excluded in general in thermoforming processes and should therefore be considered in thermomechanical modeling approaches.

- Isothermal thermoforming simulation predicts the general shape and formability in a good agreement to experimental tests, but with a risk to a nonconservative result. Wrinkling behavior was appropriately reflected for a quasi-isotropic layup. On the contrary, some defects were only predictable by the thermomechanical approach for an orthotropic layup.

Recommendations

- Deformation rates outside the range characterized by the rheometer bending test are observed during forming. The additional consideration of DMA bending characterization results for bending parameterization could prevent the extrapolation of bending behavior for high deformation rates.

- Shear strains outside the range characterized by the torsion bar test are observed during forming. Higher deflection angles could possibly cover the necessary range. In this context, the influence of fiber bending should be investigated by means of e.g. generalized continua modeling approaches, since fiber bending is not captured by first order material modeling approaches.

- The nonlinear generalized Maxwell approach is straightforward to be enhanced to a viscoplastic approach. Based on this, the influence of non-monotonous loading in thermoforming simulation could be investigated.

- The application of three-dimensional shell approaches would enable an accurate prediction of the contact normal traction. This could improve the prediction accuracy of the heat loss due to tool-ply gap conductance, in combination with an appropriate characterization strategy.

- The further deformation of solidified areas in thermoforming simulation is most likely accompanied with nonlinear material behavior. Therefore, plasticity and damage could be considered, to enable an accurate prediction of stress and strain in these areas.

- The consideration of thermal expansion and shrinkage due to crystallization would enable to predict residual stresses and part distortion, which should be investigated in combination with three-dimensional shell approaches, since through the thickness stresses are likely to influence part distortion.

A Appendix

A.1 Material parameters superimposed approach

Constitutive eq.	Ref.	Parameter	Input data
Voigt-Kelvin			
Elastic fiber		E_{f} (MPa)	1000.0
Cross model		η_0 (MPa $\cdot$ s)	0.082
		η_∞ (MPa $\cdot$ s)	0.008
		m (s$^{1-\mathrm{n}}$)	15.418
		n (-)	0.523
SVK		E (MPa)	0.012
		ν (-)	0.0

Table A.1: Material parameters for membrane modeling for the superimposed modeling approach.

Constitutive eq.	Parameter(s)	Input data
Voigt-Kelvin		
Hypoelastic	E_1 (MPa)	309.997
	$E_2 = G_{12}$ (MPa)	3.1
	ν_{12} (MPa)	0.0
Cross model	η_0 (MPa $\cdot$ s)	4989.407
	η_∞ (MPa $\cdot$ s)	282.500
	m (s^{1-n})	34071943.279
	n (-)	-0.880
Generalized Maxwell		
Hypoelastic	E_1 (MPa)	2351.848
	$E_2 = G_{12}$ (MPa)	23.519
	ν_{12} (MPa)	0.0
Maxwell element 1	λ_1 (-)	0.070
	A_1 (MPa $\cdot$ s)	227901.565
	B_1 (MPa^{-1})	9.638
	n_1 (-)	-4.137
Maxwell element 2	λ_2 (-)	0.865
	A_2 (MPa $\cdot$ s)	20.157
	B_2 (MPa^{-1})	0.110
	n_2 (-)	-0.911
Elastic (best-fit)		
Hypoelastic	E_1 (MPa)	525.801
	$E_2 = G_{12}$ (MPa)	5.258
	ν_{12} (-)	0.0
Elastic (initial)		
Hypoelastic	E_1 (MPa)	4000.0
	$E_2 = G_{12}$ (MPa)	40.0
	ν_{12} (-)	0.0

Table A.2: Material parameters for bending modeling for the superimposed modeling approach.

A.2 Material parameters DKT approach

Constitutive eq.	Parameter	Input data		
		270 °C	250 °C	226 °C
Voigt-Kelvin				
Cross model	η_0 (MPa·s)	2785.30	2544.20	6076.98
	η_∞ (MPa·s)	54.481	85.473	128.951
	m (s^{1-n})	4914.65	1716.52	4352.61
	n (-)	0.126	0.200	0.130
SVK	E_1 (MPa)	285.601	345.503	997.613
	E_2 (MPa)	0.286	0.346	0.998
	G_{12} (MPa)	0.286	0.346	0.998
	ν_{12} (-)	0.0	0.0	0.0
Gener. Maxwell				
SVK	E_1 (MPa·s)	6518.60	6465.76	6403.00
	E_2 (MPa·s)	65.186	64.658	64.030
	G_{12} (MPa·s)	65.186	64.658	64.030
	ν (-)	0.0	0.0	0.0
Maxwell 1	λ_1 (−)	0.035	0.026	0.149
	A_1 (s^{-1})	46.819	0.018	102.719
	B_1 (MPa^{-1})	0.400	3.179	0.122
	n_1 (-)	4.715	4.758	6.085
Maxwell 2	λ_2 (−)	0.934	0.926	0.764
	A_2 (s^{-1})	0.434	0.053	3.447
	B_2 (MPa^{-1})	0.149	0.159	0.017
	n_2 (-)	2.007	1.563	1.799

Table A.3: Material parameters for bending modeling for the DKT modeling approach.

Constitutive eq.	Parameter(s)	Input data		
		$270\,°C$	$250\,°C$	$226\,°C$
Voigt-Kelvin				
Elastic fiber	E_f (MPa)	1000.0	1000.0	1000.0
Cross model	η_0 (MPa $\cdot$ s)	0.082	0.095	1.384
	η_∞ (MPa $\cdot$ s)	0.008	0.006	0.004
	m (s^{1-n})	15.418	4.722	42.562
	n (-)	0.523	0.607	0.606
SVK	E (MPa)	0.0117	0.0130	0.1064
	ν (-)	0.0	0.0	0.0
Gener. Maxwell				
Elastic fiber	E_f (MPa)	1000.0	1000.0	1000.0
SVK	E (MPa $\cdot$ s)	0.407	0.546	0.653
	ν (-)	0.0	0.0	0.0
Maxwell 1	λ_1 (MPa)	0.826	0.703	0.897
	A_1 (s^{-1})	1.750	2.192	1.473
	B_1 (MPa^{-1})	60.988	33.473	5.638
	n_1 (-)	1.587	1.537	1.229
Maxwell 2	λ_2 (MPa)	0.160	0.286	0.090
	A_2 (s^{-1})	275.179	51.110	101.044
	B_2 (MPa^{-1})	0.116	0.147	0.113
	n_2 (-)	0.08	0.846	1.552

Table A.4: Material parameters for membrane modeling for the DKT modeling approach.

A.3 Material parameters inter-ply modeling

Constitutive eq.	Parameter(s)	Input data		
		270 °C	240 °C	210 °C
Ply-ply				
Penalty model	ϵ_n (MPa/mm)	10.0	10.0	10.0
Friction model	μ (-)	0.0962	0.1223	0.3812
	τ_0 (MPa)	0.0059	0.0100	0.0226
	η_0 (MPa s/mm)	0.0046	0.0047	0.0048
Tool-ply				
Penalty model	ϵ_n (MPa/mm)	10.0	10.0	10.0
Friction model	μ (-)	0.0266	0.0152	0.1218
	τ_0 (MPa)	0.0061	0.0129	0.0083
	η_0 (MPa s/mm)	0.0033	0.0027	0.0035

Table A.6: Material parameters for interface modeling extracted from characterization with no relative orientation.

Constitutive eq.	Parameter(s)	Input data	
Ply-ply		$\varphi^{\mathrm{rel}} = 0\,\mathrm{deg}$	$\varphi^{\mathrm{rel}} = 90\,\mathrm{deg}$
Penalty model	ϵ_n (MPa/mm)	10.0	10.0
Friction model	μ (-)	0.2282	0.1818
	τ_0 (MPa)	0.0087	0.0061
	η_0 (MPa s/mm)	0.0028	0.0015

Table A.8: Material parameters for ply-ply interface modeling extracted from characterization under variation of relative orientation at 240 °C.

A.4 Material parameters thermomechanical approach

Constitutive eq.	Parameter(s)	Input data		
Heat capacity				
	T^1 (°C)			150.0
	T^2 (°C)			200.0
	c_p^0 (mJ/(t K))			2000000000.0
	c_p^1 (mJ/(t K))			-312970107.5
	c_p^2 (mJ/(t K))			-259290729.7
	$d_{c_p^1}$ (mJ/(t K^2))			5475233.0
	$d_{c_p^2}$ (mJ/(t K^2))			2252198.2
Surf. heat transfer		0 m/s	3 m/s	5 m/s
Convection	h (mW/(mm^2 K))	0.008	0.0325	0.04
Radiation	ϵ (-)	0.95	0.95	0.95
Heat conductivity		Solid	220 °C	240 °C
PA6-CF (long.)	λ_{11} (mW/(mm K))	4.531	4.434	4.455
PA6-CF (transv.)	λ_{22} (mW/(mm K))	0.828	0.541	0.608
Tool-ply conduct.	g (mW/K)			1.05
Cryst. enthalpy	h^{cryst} (mJ/t)			25293638909.0

Table A.10: Material parameters for thermal modeling.

Cooling rate	Parameters		
$\dot{T}$ (°C/s)	K_{max} (1/s)	D (°C)	T_{max} (°C)
0.167	0.046	9.3325	189.620
0.333	0.068	12.165	183.984
0.500	0.085	14.473	179.883
0.667	0.095	16.989	176.096
1.000	0.116	20.776	170.013
15.00	1.632	18.909	162.850
30.00	2.896	22.682	150.752
50.00	4.294	29.960	136.738
100.0	4.441	54.410	111.096

Table A.12: Material parameters for crystallization kinetics modeling.

Constitutive eq.	Parameter(s)	Input data
SVK		
	E_1 (MPa)	121513.21
	E_2 (MPa)	6067.40
	ν_{12} (-)	0.24
	G_{12} (MPa))	2210.30

Table A.14: Material parameters for mechanical modeling in the solid material state.

B Bibliography

[1] F. Henning and E. Moeller, editors. *Handbuch Leichtbau: Methoden, Werkstoffe, Fertigung.* Hanser Verlag, München, 2011.

[2] F. Henning, L. Kärger, D. Dörr, F. J. Schirmaier, J. Seuffert, and A. Bernath. Fast processing and continuous simulation of automotive structural composite components. *Composites Science and Technology*, (171):261–279, 2019.

[3] E. R. Fuchs, F. R. Field, R. Roth, and R. E. Kirchain. Strategic materials selection in the automobile body: Economic opportunities for polymer composite design. *Composites Science and Technology*, 68(9):1989–2002, 2008.

[4] P. Beardmore and C. F. Johnson. The potential for composites in structural automotive applications. *Composites Science and Technology*, 26(4):251–281, 1986.

[5] M. F. Ashby. *Materials selection in mechanical design.* Elsevier/Butterworth-Heinemann, Amsterdam, 4. ed. edition, 2011.

[6] L. Kärger, A. Bernath, F. Fritz, S. Galkin, D. Magagnato, A. Oeckerath, A. Schön, and F. Henning. Development and validation of a CAE chain for unidirectional fibre reinforced composite components. *Composite Structures*, 132:350–358, 2015.

[7] K. Friedrich and A. A. Almajid. Manufacturing Aspects of Advanced Polymer Composites for Automotive Applications. *Applied Composite Materials*, 20(2):107–128, 2013.

[8] P. K. Mallick, editor. *Materials, design and manufacturing for lightweight vehicles.* Woodhead Publishing in materials. CRC Press, Boca Raton, 2010.

[9] P. Ermanni, C. Di Fratta, and F. Trochu. Molding: Liquid Composite Molding (LCM). *Encyclopedia of Composites*, 2011.

271

[10] P. Rosenberg, R. Chaudhari, M. Karcher, F. Henning, and P. El-sner. Investigating cavity pressure behavior in high-pressure RTM process variants. In *PROCEEDINGS OF PPS-29: The 29th International Conference of the Polymer Processing Society - Conference Papers*, AIP Conference Proceedings, pages 463–466. American Institute of Physics, 2014.

[11] F. J. Schirmaier, K. A. Weidenmann, L. Kärger, and F. Henning. Characterisation of the draping behaviour of unidirectional non-crimp fabrics (UD-NCF). *Composites Part A: Applied Science and Manufacturing*, 80:28–38, 2016.

[12] P. Boisse, editor. *Advances in composites manufacturing and process design*, volume number 56 of *Woodhead publishing series in composites science and engineering*. Woodhead Publishing, Cambridge, UK, 2015.

[13] A. Long, editor. *Composites Forming Technologies*. Woodhead Publishing Limited, Cambridge, England, 2007.

[14] M. H. Kashani, A. Rashidi, B. J. Crawford, and A. S. Milani. Analysis of a two-way tension-shear coupling in woven fabrics under combined loading tests: Global to local transformation of non-orthogonal normalized forces and displacements. *Composites Part A: Applied Science and Manufacturing*, 88:272–285, 2016.

[15] F. Nosrat-Nezami, T. Gereke, C. Eberdt, and C. Cherif. Characterisation of the shear–tension coupling of carbon-fibre fabric under controlled membrane tensions for precise simulative predictions of industrial preforming processes. *Composites Part A: Applied Science and Manufacturing*, 67:131–139, 2014.

[16] M. Komeili and A. S. Milani. On effect of shear-tension coupling in forming simulation of woven fabric reinforcements. *Composites Part B: Engineering*, 99:17–29, 2016.

[17] P. Boisse, J. Colmars, N. Hamila, N. Naouar, and Q. Steer. Bending and wrinkling of composite fiber preforms and prepregs. A review and new developments in the draping simulations. *Composites Part B: Engineering*, (141):234–249, 2018.

[18] S. Allaoui, G. Hivet, D. Soulat, A. Wendling, P. Ouagne, and S. Chatel. Experimental preforming of highly double curved shapes with a case corner using an interlock reinforcement. *International Journal of Material Forming*, 7(2):155–165, 2014.

[19] F. Nosrat Nezami, T. Gereke, and C. Cherif. Analyses of interaction mechanisms during forming of multilayer carbon woven fabrics for composite applications. *Composites Part A: Applied Science and Manufacturing*, 84:406–416, 2016.

[20] F. Nosrat Nezami, T. Gereke, and C. Cherif. Active forming manipulation of composite reinforcements for the suppression of forming defects. *Composites Part A: Applied Science and Manufacturing*, 99:94–101, 2017.

[21] A. R. Labanieh, C. Garnier, P. Ouagne, O. Dalverny, and D. Soulat. Intra-ply yarn sliding defect in hemisphere preforming of a woven preform. *Composites Part A: Applied Science and Manufacturing*, 107:432–446, 2018.

[22] E. Capelle, P. Ouagne, D. Soulat, and D. Duriatti. Complex shape forming of flax woven fabrics: Design of specific blankholder shapes to prevent defects. *Composites Part B: Engineering*, 62:29–36, 2014.

[23] C. Tephany, J. Gillibert, P. Ouagne, G. Hivet, S. Allaoui, and D. Soulat. Development of an experimental bench to reproduce the tow buckling defect appearing during the complex shape forming of structural flax based woven composite reinforcements. *Composites Part A: Applied Science and Manufacturing*, 81:22–33, 2016.

[24] F. Schirmaier. *Experimentelle Untersuchung und Simulation des Umformverhaltens nähgewirkter unidirektionaler Kohlenstofffasergelege.* Doctoral thesis (in German), Karlsruhe Institute of Technology, Karlsruhe, Germany, 2017.

[25] T. Fürst. *Experimentelle Charakterisierung von Designvarianten überlappend gefügter Kohlenstofffaserverbundstrukturen im Kontext der Entwicklung neuartiger Drapiertechnologien.* Doctoral thesis (in German), Karlsruhe Institute of Technology, Karlsruhe, Germany, 2017.

[26] G. Reinhart and G. Straßer. Flexible gripping technology for the automated handling of limp technical textiles in composites industry. *Production Engineering*, 5(3):301–306, 2011.

[27] M. Hübner, O. Diestel, C. Sennewald, T. Gereke, and C. Cherif. Simulation of the Drapability of Textile Semi-Finished Products with Gradient-Drapability Characteristics. *FIBRES & TEXTILES in Eastern Europe*, 20(5(94)):88–93, 2012.

[28] H. Krieger, T. Gries, and S. E. Stapleton. Design of Tailored Non-Crimp Fabrics Based on Stitching Geometry. *Applied Composite Materials*, 25(1):113–127, 2018.

[29] S. Chen, A. Endruweit, L. T. Harper, and N. A. Warrior. Interply stitching optimisation of highly drapeable multi-ply preforms. *Composites Part A: Applied Science and Manufacturing*, 71:144–156, 2015.

[30] C. Poppe, D. Dörr, F. Henning, and L. Kärger. Experimental and numerical investigation of the shear behaviour of inltrated woven fabrics. *Composites Part A: Applied Science and Manufacturing*, (114):327–337.

[31] J. Bergmann, H. Dörmann, and R. Lange. Interpreting process data of wet pressing process. Part 1: Theoretical approach. *Journal of Composite Materials*, 50(17):2399–2407, 2015.

[32] J. Bergmann, H. Dörmann, and R. Lange. Interpreting process data of wet pressing process. Part 2: Verification with real values. *Journal of Composite Materials*, 50(17):2409–2419, 2015.

[33] P. Bockelmann. *Process Control in Compression Molding of Composites.* PhD thesis, Technical University of Munich, Munich, Germany, 2017.

[34] J. Hüttl, F. Albrecht, C. Poppe, F. Lorenz, B. Thoma, L. Kärger, P. Middendorf, and F. Henning. Investigations on friction behaviour and forming simulation of plain woven fabrics for wet compression moulding. *SAMPE Europe, Stuttgart, Germany*, 2017.

[35] BASF SE. Automotive Summit 2014, Green Mobility Changing the World. *Bitec Bangna, Bangkok, Thailand*, 19.-20.06.2014.

[36] Z. Qureshi, T. Swait, R. Scaife, and H. M. El-Dessouky. In situ consolidation of thermoplastic prepreg tape using automated tape placement technology: Potential and possibilities. *Composites Part B: Engineering*, 66:255–267, 2014.

[37] J. Verrey, M. D. Wakeman, V. Michaud, and J.-A. Månson. Manufacturing cost comparison of thermoplastic and thermoset RTM for an automotive floor pan. *Composites Part A: Applied Science and Manufacturing*, 37(1):9–22, 2006.

[38] S. Baumgärtner, C. Lohr, and F. Henning. Development of a novel consolidation process for continuous-fiber-reinforced thermoplastics. *Proceedings ECCM17, München, Germany*, 2016.

[39] T. K. Slange, L. Warnet, W. J. B. Grouve, and R. Akkerman. Influence of preconsolidation on consolidation quality after stamp forming of C/PEEK composites. *AIP Conference Proceedings 1769*, page 170022, 2016.

[40] A. Schug, D. Rinker, R. Hinterhoelzl, and K. Drechsler. Evaluating the potential of forming spot-welded layups out of fibre reinforced thermoplastic tape without previous consolidation. *International Journal of Material Forming*, 43(22):41, 2018.

[41] S. Baumgärtner, J. John, F. Henning, T. Huber, and B. Hangs. Effizienz zum maßgeschneiderten Organoblech. *Kunststoffe*, (10/2016):180–184, 2016.

[42] C. M. O'Brádaigh, R. B. Pipes, and P. J. Mallon. Issues in diaphragm forming of continuous fiber reinforced thermoplastic composites. *Polymer Composites*, 12(4):246–256, 1991.

[43] J. Krebs, K. Friedrich, and D. Bhattacharyya. A direct comparison of matched-die versus diaphragm forming. *Composites Part A: Applied Science and Manufacturing*, 29(1-2):183–188, 1998.

[44] T. K. Slange, L. L. Warnet, W. Grouve, and R. Akkerman. Deconsolidation of C/PEEK blanks: On the role of prepreg, blank manufacturing method and conditioning. *Composites Part A: Applied Science and Manufacturing*, 2018.

[45] H. Bersee and L. Robroek. The role of the thermoplastic matrix in forming processes of composite materials. *Composites Manufacturing*, 2(3-4):217–222, 1991.

[46] J. Chen, J. A. Sherwood, P. Buso, S. Chow, and D. Lussier. Stamping of continuous fiber thermoplastic composites. *Polymer Composites*, 21(4):539–547, 2000.

[47] G. Sala, L. Di Landro, and D. Cassago. A numerical and experimental approach to optimise sheet stamping technologies: Polymers thermoforming. *Materials & Design*, 23(1):21–39, 2002.

[48] S. Wijskamp. *Shape distortions in composites forming*. PhD thesis, University of Twente, Enschede, The Netherlands, 2005.

[49] D. Dörr, T. Joppich, and Henning, F., Kärger, L. A coupled thermomechanical approach for finite element forming simulation of continuously fiber-reinforced semi-crystalline thermoplastics. *Composites Part A: Applied Science and Manufacturing*, (125):105508, 2019.

[50] K. Vanclooster. *Forming of multilayerd fabric reinforced thermoplastic composites*. PhD thesis, KU Leuven, Leuven, Belgien, 2009.

[51] P. Harrison, R. Gomes, and N. Curado-Correia. Press forming a 0/90 cross-ply advanced thermoplastic composite using the double-dome benchmark geometry. *Composites Part A: Applied Science and Manufacturing*, 54:56–69, 2013.

[52] U. Sachs. *Friction and bending in thermoplastic composites forming processes*. PhD thesis, Universiteit Twente, Twente, Enschede, The Netheralands, 2014.

[53] A. Benkaddour, G. Lebrun, and L. Laberge-Lebel. Thermostamping of [0/90] n carbon/peek laminates: Influence of support configuration and demolding temperature on part consolidation. *Polymer Composites*, 22:42, 2017.

[54] A. Schug, J. Winkelbauer, R. Hinterhölzl, and K. Drechsler. Thermoforming of glass fibre reinforced polypropylene: A study on the influence of different process parameters. *AIP Conference Proceedings 1896*, page 030010, 2017.

[55] M. Hou. Stamp forming of continuous glass fibre reinforced polypropylene. *Composites Part A: Applied Science and Manufacturing*, 28(8):695–702, 1997.

[56] F. N. Cogswell. The experience of thermoplastic structural composites during processing. *Composites Manufacturing*, 2(3-4):208–216, 1991.

[57] S. Haanappel. *Forming of UD fibre reinforced thermoplastics: A critical evaluation of intra-ply shear*. PhD thesis, Universiteit Twente, Enschede, the Netherlands, 2013.

[58] Y. M. Tarnopol'skii and T. Y. Kintsis. Methods for testing composites in shear (review). *Mechanics of Composite Materials*, 17(3):364–376, 1981.

[59] S. Lee and M. Munro. Evaluation of in-plane shear test methods for advanced composite materials by the decision analysis technique. *Composites*, 17(1):13–22, 1986.

[60] S. P. Haanappel and R. Akkerman. Shear characterisation of uni-directional fibre reinforced thermoplastic melts by means of torsion. *Composites Part A: Applied Science and Manufacturing*, 56:8–26, 2014.

[61] G. Lebrun, M. N. Bureau, and J. Denault. Evaluation of bias-extension and picture-frame test methods for the measurement of intraply shear properties of PP/glass commingled fabrics. *Selected Papers from the Symposium on Design and Manufacturing of Composites*, 61(4):341–352, 2003.

[62] P. Harrison, M. J. Clifford, and A. C. Long. Shear characterisation of viscous woven textile composites: a comparison between picture frame and bias extension experiments. *Composites Science and Technology*, 64(10–11):1453–1465, 2004.

[63] J. Cao, R. Akkerman, P. Boisse, J. Chen, H. S. Cheng, E. F. de Graaf, J. L. Gorczyca, P. Harrison, G. Hivet, J. Launay, W. Lee, L. Liu, S. V. Lomov, A. Long, E. de Luycker, F. Morestin, J. Padvoiskis, X. Q. Peng, J. Sherwood, T. Stoilova, X. M. Tao, I. Verpoest, A. Willems, J. Wiggers, T. X. Yu, and B. Zhu. Characterization of mechanical behavior of woven fabrics: Experimental methods and benchmark results. *Composites Part A: Applied Science and Manufacturing*, 39(6):1037–1053, 2008.

[64] B. Zhu, T. YU, and X. TAO. An experimental study of in-plane large shear deformation of woven fabric composite. *Composites Science and Technology*, 67(2):252–261, 2007.

[65] S. Bel, P. Boisse, and F. Dumont. Analyses of the Deformation Mechanisms of Non-Crimp Fabric Composite Reinforcements during Preforming. *Applied Composite Materials*, 19(3):513–528, 2012.

[66] S. V. Lomov, M. Barburski, T. Stoilova, I. Verpoest, R. Akkerman, R. Loendersloot, and R. Thije. Carbon composites based on multiaxial multiply stitched preforms. Part 3: Biaxial tension, picture frame and compression tests of the preforms. *Composites Part A: Applied Science and Manufacturing*, 36(9):1188–1206, 2005.

[67] P. Harrison. Normalisation of biaxial bias extension test results considering shear tension coupling. *Composites Part A: Applied Science and Manufacturing*, 43(9):1546–1554, 2012.

[68] P. Harrison, F. Abdiwi, Z. Guo, P. Potluri, and W. R. Yu. Characterising the shear–tension coupling and wrinkling behaviour of woven engineering fabrics. *Composites Part A: Applied Science and Manufacturing*, 43(6):903–914, 2012.

[69] Y. R. Larberg, M. Åkermo, and M. Norrby. On the in-plane deformability of cross-plied unidirectional prepreg. *Journal of Composite Materials*, 46(8):929–939, 2011.

[70] K. Potter. Bias extension measurements on cross-plied unidirectional prepreg. *Composites Part A: Applied Science and Manufacturing*, 33(1):63–73, 2002.

[71] D. Lussier and J. Chen. Material Characterization of Woven Fabrics for Thermoforming of Composites. *Journal of Thermoplastic Composite Materials*, 15(6):497–509, 2002.

[72] G. B. McGuinness and C. M. ÓBrádaigh. Characterisation of thermoplastic composite melts in rhombus-shear: The picture-frame experiment. *Composites Part A: Applied Science and Manufacturing*, 29(1-2):115–132, 1998.

[73] F. J. Schirmaier, D. Dörr, F. Henning, and L. Kärger. A macroscopic approach to simulate the forming behaviour of stitched

unidirectional non-crimp fabrics (UD-NCF). *Composites Part A: Applied Science and Manufacturing*, (102):322–335, 2017.

[74] P. Boisse, R. Bai, J. Colmars, N. Hamila, B. Liang, and A. Madeo. The Need to Use Generalized Continuum Mechanics to Model 3D Textile Composite Forming. *Applied Composite Materials*, 47(11):7, 2018.

[75] A. Margossian, S. Bel, and R. Hinterhoelzl. Bending characterisation of a molten unidirectional carbon fibre reinforced thermoplastic composite using a Dynamic Mechanical Analysis system. *Composites Part A: Applied Science and Manufacturing*, 77:154–163, 2015.

[76] S. Ropers, M. Kardos, and T. A. Osswald. A thermo-viscoelastic approach for the characterization and modeling of the bending behavior of thermoplastic composites. *Composites Part A: Applied Science and Manufacturing*, 90:22–32, 2016.

[77] F. T. Peirce, F. Inst. P. The handle of cloth as measurable quantity. *Journal of the Textile Institute Transactions*, (21:9):377–416, 1930.

[78] E. de Bilbao, D. Soulat, G. Hivet, and A. Gasser. Experimental Study of Bending Behaviour of Reinforcements. *Experimental Mechanics*, 50(3):333–351, 2010.

[79] B. Liang, N. Hamila, M. Peillon, and P. Boisse. Analysis of thermoplastic prepreg bending stiffness during manufacturing and of its influence on wrinkling simulations. *Composites Part A: Applied Science and Manufacturing*, 67:111–122, 2014.

[80] B. Liang, P. Chaudet, and P. Boisse. Curvature determination in the bending test of continuous fibre reinforcements. *Strain*, 53(1):e12213, 2017.

[81] S. Kawabata. The Standardization and Analysis of Hand Evaluation (2nd Ed). *The Textile Machinery Society Japan*, 1980.

[82] N. Lammens, M. Kersemans, G. Luyckx, W. van Paepegem, and J. Degrieck. Improved accuracy in the determination of flexural rigidity of textile fabrics by the Peirce cantilever test (ASTM D1388). *Textile Research Journal*, 84(12):1307–1314, 2014.

[83] U. Sachs and R. Akkerman. Viscoelastic bending model for continuous fiber-reinforced thermoplastic composites in melt. *Composites Part A: Applied Science and Manufacturing*, (100):333–341.

[84] L. M. Dangora, C. J. Mitchell, and J. A. Sherwood. Predictive model for the detection of out-of-plane defects formed during textile-composite manufacture. *Composites Part A: Applied Science and Manufacturing*, 78:102–112, 2015.

[85] L. M. Dangora, C. Mitchell, K. D. White, J. A. Sherwood, and J. C. Parker. Characterization of temperature-dependent tensile and flexural rigidities of a cross-ply thermoplastic lamina with implementation into a forming model. *International Journal of Material Forming*, 11(1):43–52, 2018.

[86] H. Alshahrani and M. Hojjati. A new test method for the characterization of the bending behavior of textile prepregs. *Composites Part A: Applied Science and Manufacturing*, 97:128–140, 2017.

[87] H. Alshahrani and M. Hojjati. Bending behavior of multilayered textile composite prepregs: Experiment and finite element modeling. *Materials & Design*, 124:211–224, 2017.

[88] K. Buet-Gautier and P. Boisse. Experimental analysis and modeling of biaxial mechanical behavior of woven composite reinforcements. *Experimental Mechanics*, 41(3):260–269, 2001.

[89] O. Erol, B. Powers, and M. Keefe. Development of a nonorthogonal macroscale material model for advanced woven fabrics based on mesoscale structure. *Composites Part B: Engineering*, 110:497–510, 2017.

[90] P. Boisse, A. Gasser, and G. Hivet. Analyses of fabric tensile behaviour: determination of the biaxial tension-strain surfaces and their use in forming simulations. *Composites Part A: Applied Science and Manufacturing*, 32(10):1395–1414, 2001.

[91] P. Boisse. Meso-macro approach for composites forming simulation. *Journal of Materials Science*, 41(20):6591–6598, 2006.

[92] A. Margossian, S. Bel, and R. Hinterhoelzl. On the characterisation of transverse tensile properties of molten unidirectional

thermoplastic composite tapes for thermoforming simulations. *Composites Part A: Applied Science and Manufacturing*, 88:48–58, 2016.

[93] U. Sachs, R. Akkerman, K. Fetfatsidis, E. Vidal-Sallé, J. Schumacher, G. Ziegmann, S. Allaoui, G. Hivet, B. Maron, K. Vanclooster, and S. V. Lomov. Characterization of the dynamic friction of woven fabrics: Experimental methods and benchmark results. *Composites Part A: Applied Science and Manufacturing*, 67:289–298, 2014.

[94] S. Allaoui, G. Hivet, A. Wendling, P. Ouagne, and D. Soulat. Influence of the dry woven fabrics meso-structure on fabric/fabric contact behavior. *Journal of Composite Materials*, 46(6):627–639, 2012.

[95] B. Cornelissen, U. Sachs, B. Rietman, and R. Akkerman. Dry friction characterisation of carbon fibre tow and satin weave fabric for composite applications. *Composites Part A: Applied Science and Manufacturing*, 56:127–135, 2014.

[96] S. R. Morris and C. T. Sun. An investigation of interply slip behaviour in AS4/PEEK at forming temperatures. *Composites Manufacturing*, (5 (4)):217–224, 1994.

[97] A. M. Murtagh, J. J. Lennon, and P. J. Mallon. Surface friction effects related to pressforming of continuous fibre thermoplastic composites. *Composites Manufacturing*, 6(3-4):169–175, 1995.

[98] K. A. Fetfatsidis, D. Jauffrès, J. A. Sherwood, and J. Chen. Characterization of the tool/fabric and fabric/fabric friction for woven-fabric composites during the thermostamping process. *International Journal of Material Forming*, 6(2):209–221, 2013.

[99] J. L. Gorczyca-Cole, J. A. Sherwood, and J. Chen. A friction model for thermostamping commingled glass–polypropylene woven fabrics. *Composites Part A: Applied Science and Manufacturing*, 38(2):393–406, 2007.

[100] R. H. W. ten Thije, R. Akkerman, L. van der Meer, and M. P. Ubbink. Tool-ply friction in thermoplastic composite forming. *International Journal of Material Forming*, 1(1):953–956, 2008.

[101] K. Vanclooster, S. V. Lomov, and I. Verpoest. Investigation of interply shear in composite forming. *International Journal of Material Forming*, 1(1):957–960, 2008.

[102] W. Zhang, X. Ma, J. Lu, Z. Zhang, Q. Jane Wang, X. Su, D. Zeng, M. Mirdamadi, and J. Cao. Experimental Characterization and Numerical Modeling of the Interaction Between Carbon Fiber Composite Prepregs During a Preforming Process. *Journal of Manufacturing Science and Engineering*, 140(8):081003, 2018.

[103] S. Erland, T. J. Dodwell, and R. Butler. Characterisation of inter-ply shear in uncured carbon fibre prepreg. *Composites Part A: Applied Science and Manufacturing*, 77:210–218, 2015.

[104] M. Åkermo, Y. R. Larberg, J. Sjölander, and P. Hallander. Influence of Interply Friction On The Forming Of Stacked UD Prepreg. *Proceedings of the 19th International Conference On Composite Materials*, pages 919–28., 2013.

[105] Y. R. Larberg and M. Åkermo. On the interply friction of different generations of carbon/epoxy prepreg systems. *Composites Part A: Applied Science and Manufacturing*, 42(9):1067–1074, 2011.

[106] T.-C. Lim and S. Ramakrishna. Modelling of composite sheet forming: a review. *Composites Part A: Applied Science and Manufacturing*, 33(4):515–537, 2002.

[107] C. Mack and H. M. Taylor. 39—The Fitting of Woven Cloth to Surfaces. *Journal of the Textile Institute Transactions*, 47(9):T477–T488, 1956.

[108] F. L. Heisey and K. D. Haller. Fitting Woven Fabric to Surfaces in Three Dimensions. *Journal of the Textile Institute*, 79(2):250–263, 1988.

[109] F. van der Weeën. Algorithms for draping fabrics on doubly-curved surfaces. *International Journal for Numerical Methods in Engineering*, 31(7):1415–1426, 1991.

[110] B. P. van West and S. C. Luby. Fabric draping simulation in composites manufacturing part I: Description and applications. *Journal of Advanced Materials*, (3):29–35, 1997.

[111] B. P. van West and S. C. Luby. Fabric draping simulation in composites manufacturing part II: Analytical methods. *Journal of Advanced Materials*, (3):36–41, 1997.

[112] S. G. Hancock and K. D. Potter. Inverse drape modelling—an investigation of the set of shapes that can be formed from continuous aligned woven fibre reinforcements. *Composites Part A: Applied Science and Manufacturing*, 36(7):947–953, 2005.

[113] S. G. Hancock and K. D. Potter. The use of kinematic drape modelling to inform the hand lay-up of complex composite components using woven reinforcements. *Composites Part A: Applied Science and Manufacturing*, 37(3):413–422, 2006.

[114] K. Vanclooster, S. V. Lomov, and I. Verpoest. Experimental validation of forming simulations of fabric reinforced polymers using an unsymmetrical mould configuration. *Composites Part A: Applied Science and Manufacturing*, 40(4):530–539, 2009.

[115] P. Bussetta and N. Correia. Numerical forming of continuous fibre reinforced composite material: A review. *Composites Part A: Applied Science and Manufacturing*, 113:12–31, 2018.

[116] E. Syerko, S. Comas-Cardona, and C. Binetruy. Models for shear properties/behavior of dry fibrous materials at various scales: A review. *International Journal of Material Forming*, 8(1):1–23, 2015.

[117] P. Boisse, Y. Aimène, A. Dogui, S. Dridi, S. Gatouillat, N. Hamila, M. Aurangzeb Khan, T. Mabrouki, F. Morestin, and E. Vidal-Sallé. Hypoelastic, hyperelastic, discrete and semi-discrete approaches for textile composite reinforcement forming. *International Journal of Material Forming*, 3(2):1229–1240, 2009.

[118] S. Allaoui, P. Boisse, S. Chatel, N. Hamila, G. Hivet, D. Soulat, and E. Vidal-Salle. Experimental and numerical analyses of textile reinforcement forming of a tetrahedral shape. *Composites Part A: Applied Science and Manufacturing*, 42(6):612–622, 2011.

[119] S. P. Haanappel, R. ten Thije, U. Sachs, B. Rietman, and R. Akkerman. Formability analyses of uni-directional and textile

reinforced thermoplastics. *Composites Part A: Applied Science and Manufacturing*, 56:80–92, 2014.

[120] P. Boisse, N. Hamila, E. Vidal-Sallé, and F. Dumont. Simulation of wrinkling during textile composite reinforcement forming. Influence of tensile, in-plane shear and bending stiffnesses. *Composites Science and Technology*, 71(5):683–692, 2011.

[121] D. Soulat, A. Cheruet, and P. Boisse. Simulation of continuous fibre reinforced thermoplastic forming using a shell finite element with transverse stress. *Computers & Structures*, 84(13-14):888–903, 2006.

[122] T. Belytschko. *Nonlinear finite elements for continua and structures.* Wiley, Chichester, 2. ed., 1. publ edition, 2014.

[123] X. Yu, B. Cartwright, D. McGuckin, L. Ye, and Y.-W. Mai. Intra-ply shear locking in finite element analyses of woven fabric forming processes. *Composites Part A: Applied Science and Manufacturing*, 37(5):790–803, 2006.

[124] N. Hamila and P. Boisse. Locking in simulation of composite reinforcement deformations. Analysis and treatment. *Composites Part A: Applied Science and Manufacturing*, 53:109–117, 2013.

[125] R. ten Thije and R. Akkerman. Solutions to intra-ply shear locking in finite element analyses of fibre reinforced materials. *Composites Part A: Applied Science and Manufacturing*, 39(7):1167–1176, 2008.

[126] T. J. R. Hughes and Winget J. Finite rotation effects in numerical integration of rate constitutive equations arising in large-deformation analysis. *Numerical Methods in Engineering*, (15, 12):1862–1867, 1980.

[127] X. Q. Peng and J. Cao. A continuum mechanics-based non-orthogonal constitutive model for woven composite fabrics. *Composites Part A: Applied Science and Manufacturing*, 36(6):859–874, 2005.

[128] X. Peng and F. Ding. Validation of a non-orthogonal constitutive model for woven composite fabrics via hemispherical stamping simulation. *Composites Part A: Applied Science and Manufacturing*, 42(4):400–407, 2011.

[129] X. Peng and Z. U. Rehman. Textile composite double dome stamping simulation using a non-orthogonal constitutive model. *Composites Science and Technology*, 71(8):1075–1081, 2011.

[130] P. Badel, E. Vidal-Sallé, and P. Boisse. Large deformation analysis of fibrous materials using rate constitutive equations. *Computers & Structures*, 86(11–12):1164–1175, 2008.

[131] P. Badel, S. Gauthier, E. Vidal-Sallé, and P. Boisse. Rate constitutive equations for computational analyses of textile composite reinforcement mechanical behaviour during forming. *Composites Part A: Applied Science and Manufacturing*, 40(8):997–1007, 2009.

[132] M. A. Khan, T. Mabrouki, E. Vidal-Sallé, and P. Boisse. Numerical and experimental analyses of woven composite reinforcement forming using a hypoelastic behaviour. Application to the double dome benchmark. *Journal of Materials Processing Technology*, 210(2):378–388, 2010.

[133] M. A. Khan, N. Reynolds, G. Williams, and K. N. Kendall. Processing of thermoset prepregs for high-volume applications and their numerical analysis using superimposed finite elements. *Composite Structures*, 131:917–926, 2015.

[134] M. Machado, M. Fischlschweiger, and Z. Major. A rate-dependent non-orthogonal constitutive model for describing shear behaviour of woven reinforced thermoplastic composites. *Composites Part A: Applied Science and Manufacturing*, 80:194–203, 2016.

[135] M. Machado, L. Murenu, M. Fischlschweiger, and Z. Major. Analysis of the thermomechanical shear behaviour of woven-reinforced thermoplastic-matrix composites during forming. *Composites Part A: Applied Science and Manufacturing*, 86:39–48, 2016.

[136] W. R. Yu, F. Pourboghrat, K. Chung, M. Zampaloni, and T. J. Kang. Non-orthogonal constitutive equation for woven fabric reinforced thermoplastic composites. *Composites Part A: Applied Science and Manufacturing*, 33(8):1095–1105, 2002.

285

[137] W. R. Yu, M. Zampaloni, F. Pourboghrat, K. Chung, and T. J. Kang. Analysis of flexible bending behavior of woven preform using non-orthogonal constitutive equation. *Composites Part A: Applied Science and Manufacturing*, 36(6):839–850, 2005.

[138] H. Lin, J. Wang, A. C. Long, M. J. Clifford, and P. Harrison. Predictive modelling for optimization of textile composite forming. *Composites Science and Technology*, 67(15–16):3242–3252, 2007.

[139] P. Xue, X. Peng, and J. Cao. A non-orthogonal constitutive model for characterizing woven composites. *Composites Part A: Applied Science and Manufacturing*, 34(2):183–193, 2003.

[140] J. Cao, P. Xue, X. Peng, and N. Krishnan. An approach in modeling the temperature effect in thermo-stamping of woven composites. *Composite Structures*, 61(4):413–420, 2003.

[141] W. Lee and J. Cao. Numerical simulations on double-dome forming of woven composites using the coupled non-orthogonal constitutive model. *International Journal of Material Forming*, 2(S1):145–148, 2009.

[142] W. Lee, M.-K. Um, J.-H. Byun, P. Boisse, and J. Cao. Numerical study on thermo-stamping of woven fabric composites based on double-dome stretch forming. *International Journal of Material Forming*, 3(S2):1217–1227, 2010.

[143] G. A. Holzapfel. *Nonlinear Solid Mechanics: A Continuum Approach for Engineering.* John Wiley & Sons Lt., West Sussex, England, 2000.

[144] R. ten Thije, R. Akkerman, and J. Huétink. Large deformation simulation of anisotropic material using an updated Lagrangian finite element method. *Computer Methods In Applied Mechanics And Engineering*, 196(33-34):3141–3150, 2007.

[145] A. J. M. Spencer. *Continuum Theory of the Mechanics of Fibre-Reinforced Composites.* Springer Vienna, Vienna, 1984.

[146] A. Spencer. Theory of fabric-reinforced viscous fluids. *Composites Part A: Applied Science and Manufacturing*, 31(12):1311–1321, 2000.

286

[147] C. W. Macosko. *Rheology: Principles, measurements, and applications.* Advances in interfacial engineering series. Wiley-VCH, New York NY u.a., 1994.

[148] Y. Aimène, E. Vidal-Sallé, B. Hagège, F. Sidoroff, and P. Boisse. A Hyperelastic Approach for Composite Reinforcement Large Deformation Analysis. *Journal of Composite Materials*, 44(1):5–26, 2010.

[149] X. Q. Peng, Z. Y. Guo, Zia-Ur-Rehman, and P. Harrison. A Simple Anisotropic Fiber Reinforced Hyperelastic Constitutive Model for Woven Composite Fabrics. *International Journal of Material Forming*, 3(S1):723–726, 2010.

[150] X. Peng, Z. Guo, T. Du, and W.-R. Yu. A simple anisotropic hyperelastic constitutive model for textile fabrics with application to forming simulation. *Composites Part B: Engineering*, 52:275–281, 2013.

[151] H. Yin, X. Peng, T. Du, and Z. Guo. Draping of plain woven carbon fabrics over a double-curvature mold. *Composites Science and Technology*, 92:64–69, 2014.

[152] Y. Gong, X. Peng, Y. Yao, and Z. Guo. An anisotropic hyperelastic constitutive model for thermoplastic woven composite prepregs. *Composites Science and Technology*, 128:17–24, 2016.

[153] Y. Gong, D. Yan, Y. Yao, R. Wei, H. Hu, P. Xu, and X. Peng. An Anisotropic Hyperelastic Constitutive Model with Tension–Shear Coupling for Woven Composite Reinforcements. *International Journal of Applied Mechanics*, 09(06):1750083, 2017.

[154] A. Charmetant, J. G. Orliac, E. Vidal-Sallé, and P. Boisse. Hyperelastic model for large deformation analyses of 3D interlock composite preforms. *Composites Science and Technology*, 72(12):1352–1360, 2012.

[155] S. Mathieu, N. Hamila, F. Dupé, C. Descamps, and P. Boisse. Stability of 3D Textile Composite Reinforcement Simulations: Solutions to Spurious Transverse Modes. *Applied Composite Materials*, 23(4):739–760, 2016.

[156] E. Guzman-Maldonado, N. Hamila, N. Naouar, G. Moulin, and P. Boisse. Simulation of thermoplastic prepreg thermoforming

based on a visco-hyperelastic model and a thermal homogenization. *Materials & Design*, 93:431–442, 2016.

[157] Y. Denis, E. Guzman-Maldonado, N. Hamila, J. Colmars, and F. Morestin. A dissipative constitutive model for woven composite fabric under large strain. *Composites Part A: Applied Science and Manufacturing*, 105:165–179, 2018.

[158] E. H. Lee. Elastic-Plastic Deformation at Finite Strains. *Journal of Applied Mechanics*, 36(1):1, 1969.

[159] A. Madeo, G. Barbagallo, M. V. D'Agostino, and P. Boisse. Continuum and discrete models for unbalanced woven fabrics. *International Journal of Solids and Structures*, 94-95:263–284, 2016.

[160] M. V. d'Agostino, I. Giorgio, L. Greco, A. Madeo, and P. Boisse. Continuum and discrete models for structures including (quasi-) inextensible elasticae with a view to the design and modeling of composite reinforcements. *International Journal of Solids and Structures*, 59:1–17, 2015.

[161] G. Barbagallo, A. Madeo, I. Azehaf, I. Giorgio, F. Morestin, and P. Boisse. Bias extension test on an unbalanced woven composite reinforcement: Experiments and modeling via a second-gradient continuum approach. *Journal of Composite Materials*, 51(2):153–170, 2016.

[162] M. Ferretti, A. Madeo, F. dell'Isola, and P. Boisse. Modeling the onset of shear boundary layers in fibrous composite reinforcements by second-gradient theory. *Zeitschrift für angewandte Mathematik und Physik*, 65(3):587–612, 2014.

[163] A. Madeo, M. Ferretti, F. dell'Isola, and P. Boisse. Thick fibrous composite reinforcements behave as special second-gradient materials: Three-point bending of 3D interlocks. *Zeitschrift für angewandte Mathematik und Physik*, 66(4):2041–2060, 2015.

[164] M. Cuomo, F. dell'Isola, L. Greco, and N. L. Rizzi. First versus second gradient energies for planar sheets with two families of inextensible fibres: Investigation on deformation boundary layers, discontinuities and geometrical instabilities. *Composites Part B: Engineering*, 115:423–448, 2017.

[165] U. Andreaus, F. dell'Isola, I. Giorgio, L. Placidi, T. Lekszycki, and N. L. Rizzi. Numerical simulations of classical problems in two-dimensional (non) linear second gradient elasticity. *International Journal of Engineering Science*, 108:34–50, 2016.

[166] I. Giorgio. Numerical identification procedure between a micro-Cauchy model and a macro-second gradient model for planar pantographic structures. *Zeitschrift für angewandte Mathematik und Physik*, 67(4):2855, 2016.

[167] G. Barbagallo, A. Madeo, F. Morestin, and P. Boisse. Modelling the deep drawing of a 3D woven fabric with a second gradient model. *Mathematics and Mechanics of Solids*, 22(11):2165–2179, 2016.

[168] P. P. Valentini, M. Falcone, E. Marotta, E. Pennestrì, and P. Salvini. Theoretical and experimental characterization of a FEM element assembly for the simulation of very compliant knitted mesh. *International Journal for Numerical Methods in Engineering*, 107(5):419–429, 2016.

[169] S. B. Sharma and M. Sutcliffe. A simplified finite element model for draping of woven material. *Composites Part A: Applied Science and Manufacturing*, 35(6):637–643, 2004.

[170] A. A. Skordos, C. Monroy Aceves, and M. Sutcliffe. A simplified rate dependent model of forming and wrinkling of pre-impregnated woven composites. *Composites Part A: Applied Science and Manufacturing*, 38(5):1318–1330, 2007.

[171] A. A. Skordos and M. Sutcliffe. Stochastic simulation of woven composites forming. *Composites Science and Technology*, 68(1):283–296, 2008.

[172] K. Y. Sze and X. H. Liu. A new skeletal model for fabric drapes. *International Journal of Mechanics and Materials in Design*, 2(3-4):225–243, 2005.

[173] B. Ben Boubaker, B. Haussy, and J.-F. Ganghoffer. Discrete models of fabric accounting for yarn interactions. *Revue Européenne des Éléments*, 14(6-7):653–675, 2005.

[174] B. Ben Boubaker, B. Haussy, and J. F. Ganghoffer. Discrete models of woven structures. Macroscopic approach. *Composites Part B: Engineering*, 38(4):498–505, 2007.

[175] F. dell Isola, A. Della Corte, I. Giorgio, and D. Scerrato. Pantographic 2D sheets: Discussion of some numerical investigations and potential applications. *International Journal of Non-Linear Mechanics*, 80:200–208, 2016.

[176] E. Turco, K. Barcz, M. Pawlikowski, and N. L. Rizzi. Nonstandard coupled extensional and bending bias tests for planar pantographic lattices. Part I: Numerical simulations. *Zeitschrift für angewandte Mathematik und Physik*, 67(5):3473, 2016.

[177] E. Turco, K. Barcz, and N. L. Rizzi. Non-standard coupled extensional and bending bias tests for planar pantographic lattices. Part II: Comparison with experimental evidence. *Zeitschrift für angewandte Mathematik und Physik*, 67(5):3473, 2016.

[178] E. Turco, F. dell'Isola, A. Cazzani, and N. L. Rizzi. Hencky-type discrete model for pantographic structures: Numerical comparison with second gradient continuum models. *Zeitschrift für angewandte Mathematik und Physik*, 67(4):060804, 2016.

[179] A. Cherouat and J. L. Billoët. Mechanical and numerical modelling of composite manufacturing processes deep-drawing and laying-up of thin pre-impregnated woven fabrics. *Journal of Materials Processing Technology*, 118(1-3):460–471, 2001.

[180] A. Cherouat, H. Borouchaki, and J.-L. Billoët. Geometrical and mechanical draping of composite fabric. *Revue Européenne des Éléments Finis*, 14(6-7):693–707, 2005.

[181] L. Giraud-Moreau, A. Cherouat, and H. Borouchaki. Adaptive Remeshing of Composite Fabrics During the Forming Process. *International Journal of Material Forming*, 3(S1):659–662, 2010.

[182] A. Cherouat, H. Borouchaki, and L. Giraud-Moreau. Mechanical and geometrical approaches applied to composite fabric forming. *International Journal of Material Forming*, 3(S2):1189–1204, 2010.

[183] A. Cherouat, L. Moreau, R. Ayad, and T. Ben Zineb. Remeshing procedure for discrete membrane finite element: Application to woven composite forming. *European Journal of Computational Mechanics*, 21(1-2):4–21, 2012.

[184] A. Cherouat and H. Bourouchaki. Numerical Tools for Composite Woven Fabric Preforming. *Advances in Materials Science and Engineering*, 2013(1):1–18, 2013.

[185] X. Li, J. Sherwood, L. Liu, and J. Chen. A material model for woven commingled glass-polypropylene composite fabrics using a hybrid finite element approach. *International Journal of Materials and Product Technology*, 21(1/2/3):59, 2004.

[186] J. L. Gorczyca, J. A. Sherwood, and J. Chen. A friction model for use with a commingled fiberglass-polypropylene plain-weave fabric and the metal tool during thermostamping. *Revue Européenne des Éléments Finis*, 14(6-7):729–751, 2005.

[187] L. M. Dangora, C. J. Mitchell, J. Sherwood, and J. C. Parker. Deep-Drawing Forming Trials on a Cross-Ply Thermoplastic Lamina for Helmet Preform Manufacture. *Journal of Manufacturing Science and Engineering*, 139(3):031009, 2017.

[188] P. Harrison, W.-R. Yu, and A. C. Long. Rate dependent modelling of the forming behaviour of viscous textile composites. *Composites Part A: Applied Science and Manufacturing*, 42(11):1719–1726, 2011.

[189] F. Abdiwi, P. Harrison, I. Koyama, W. R. Yu, A. C. Long, N. Corriea, and Z. Guo. Characterising and modelling variability of tow orientation in engineering fabrics and textile composites. *Composites Science and Technology*, 72(9):1034–1041, 2012.

[190] P. Harrison, M. J. Clifford, A. C. Long, and C. D. Rudd. Constitutive modelling of impregnated continuous fibre reinforced composites Micromechanical approach. *Plastics, Rubber and Composites*, 31(2):76–86, 2013.

[191] P. Harrison. Modelling the forming mechanics of engineering fabrics using a mutually constrained pantographic beam and membrane mesh. *Composites Part A: Applied Science and Manufacturing*, 81:145–157, 2016.

[192] R. Tavana, S. S. Najar, M. T. Abadi, and M. Sedighi. Meso/macro-scale finite element model for forming process of woven fabric reinforcements. *Journal of Composite Materials*, 47(17):2075–2085, 2012.

[193] A. Iwata, T. Inoue, N. Naouar, P. Boisse, and S. V. Lomov. Meso-macro simulation of the woven fabric local deformation in draping. In *AIP Conference Proceedings 1960*, volume 020012 (2018).

[194] A. Iwata, T. Inoue, N. Naouar, P. Boisse, and S. V. Lomov. Coupled meso-macro simulation of woven fabric local deformation during draping. *Composites Part A: Applied Science and Manufacturing*, 118:267–280, 2019.

[195] D. Wang, N. Naouar, E. Vidal-Salle, and P. Boisse. Longitudinal compression and Poisson ratio of fiber yarns in meso-scale finite element modeling of composite reinforcements. *Composites Part B: Engineering*, 141:9–19, 2018.

[196] P. Boisse, A. Gasser, B. Hagege, and J.-L. Billoet. Analysis of the mechanical behavior of woven fibrous material using virtual tests at the unit cell level. *Journal of Materials Science*, 40(22):5955–5962, 2005.

[197] P. Badel, E. Vidal-Sallé, and P. Boisse. Computational determination of in-plane shear mechanical behaviour of textile composite reinforcements. *Computational Materials Science*, 40(4):439–448, 2007.

[198] X. Q. Peng and J. Cao. A dual homogenization and finite element approach for material characterization of textile composites. *Composites Part B: Engineering*, (33):45–56, 2002.

[199] H. Lin, A. C. Long, M. Sherburn, and M. J. Clifford. Modelling of mechanical behaviour for woven fabrics under combined loading. *International Journal of Material Forming*, 1(1):899–902, 2008.

[200] A. Charmetant, E. Vidal-Sallé, and P. Boisse. Hyperelastic modelling for mesoscopic analyses of composite reinforcements. *Composites Science and Technology*, 71(14):1623–1631, 2011.

[201] P. Boisse, H. Hamila, P. Wang, S. Gatouillat, S. Bel, and A. Charmetant. Composite reinforcement forming simulation: continous and mesoscopic approaches. *Proceedings of the 18th International Conference on Composite Materials (ICCM18)*, 2011.

[202] A. K. Pickett, G. Creech, and P. de Luca. Simplified and advanced simulation methods for prediction of fabric draping. *Revue Européenne des Éléments Finis*, 14(6-7):677–691, 2005.

[203] G. Creech and A. Pickett. Meso-modelling of Non-Crimp Fabric composites for coupled drape and failure analysis. *Journal of Materials Science*, 41(20):6725–6736, 2006.

[204] J. Sirtautas, A. K. Pickett, and P. Lépicier. A mesoscopic model for coupled drape-infusion simulation of biaxial Non-Crimp Fabric. *Composites Part B: Engineering*, 47:48–57, 2013.

[205] A. Margossian, S. Bel, J. M. Balvers, D. Leutz, R. Freitas, and R. Hinterhoelzl. Finite element forming simulation of locally stitched non-crimp fabrics. *Composites Part A: Applied Science and Manufacturing*, 61:152–162, 2014.

[206] P. Böhler, F. Härtel, and P. Middendorf. Identification of Forming Limits for Unidirectional Carbon Textiles in Reality and Mesoscopic Simulation. *Key Engineering Materials*, 554-557:423–432, 2013.

[207] T. Senner, S. Kreissl, M. Merklein, J. Meinhardt, and A. Lipp. A modular modeling approach for describing the in-plane forming behavior of unidirectional non-crimp-fabrics. *Production Engineering*, 8(5):635–643, 2014.

[208] N. Hamila and P. Boisse. Simulations of textile composite reinforcement draping using a new semi-discrete three node finite element. *Composites Part B: Engineering*, 39(6):999–1010, 2008.

[209] P. Boisse, M. Borr, K. Buet, and A. Cherouat. Finite element simulations of textile composite forming including the biaxial fabric behaviour. *Composites Part B: Engineering*, 28(4):453–464, 1997.

[210] P. Boisse, B. Zouari, and A. Gasser. A mesoscopic approach for the simulation of woven fibre composite forming. *Composites Science and Technology*, 65(3-4):429–436, 2005.

[211] B. Zouari, J.-L. Daniel, and P. Boisse. A woven reinforcement forming simulation method. Influence of the shear stiffness. *Computers & Structures*, 84(5-6):351–363, 2006.

293

[212] N. Hamila, P. Boisse, F. Sabourin, and M. Brunet. A semi-discrete shell finite element for textile composite reinforcement forming simulation. *International Journal for Numerical Methods in Engineering*, 79(12):1443–1466, 2009.

[213] P. Wang, X. Legrand, P. Boisse, N. Hamila, and D. Soulat. Experimental and numerical analyses of manufacturing process of a composite square box part: Comparison between textile reinforcement forming and surface 3D weaving. *Composites Part B: Engineering*, 78:26–34, 2015.

[214] P. Wang, N. Hamila, and P. Boisse. Thermoforming simulation of multilayer composites with continuous fibres and thermoplastic matrix. *Composites Part B: Engineering*, 52:127–136, 2013.

[215] S. Bel, N. Hamila, P. Boisse, and F. Dumont. Finite element model for NCF composite reinforcement preforming: Importance of inter-ply sliding. *Composites Part A: Applied Science and Manufacturing*, 43(12):2269–2277, 2012.

[216] D. Dörr, F. J. Schirmaier, F. Henning, and L. Kärger. A viscoelastic approach for modeling bending behavior in finite element forming simulation of continuously fiber reinforced composites. *Composites Part A: Applied Science and Manufacturing*, 94:113–123, 2017.

[217] R. H. W. ten Thije and R. Akkerman. Finite Element Simulations of Laminated Composites Forming Processes. *International Journal of Material Forming*, 3(S1):715–718, 2010.

[218] J. L. Gorczyca, J. A. Sherwood, L. Liu, and J. Chen. Modeling of Friction and Shear in Thermostamping of Composites - Part I. *Journal of Composite Materials*, 38(21):1911–1929, 2016.

[219] E.A.D. Lamers. *Shape distortions in fabric reinforced composite products due to processing induced fibre reorientation.* PhD thesis, University of Twente, the Netherlands, 2004.

[220] T. G. Donderwinkel, B. Rietman, S. P. Haanappel, and R. Akkerman. Stamp forming optimization for formability and crystallinity. *AIP Conference Proceedings 1769*, page 170029, 2016.

[221] S. Ropers. *Bending Behavior of Thermoplastic Composite Sheets: Viscoelasticity and Temperature Dependency in the Draping Process*, volume 99 of *AutoUni - Schriftenreihe*. Springer Fachmedien Wiesbaden, Wiesbaden and s.l., 2017.

[222] B. D. Corner, P. Li, and M. Tocheri, editors. *Electronic Imaging 2006*, SPIE Proceedings. SPIE, 2006.

[223] C.-s. Dong and G.-z. Wang. Curvatures estimation on triangular mesh. *Journal of Zhejiang University-SCIENCE A*, 6(S1):128–136, 2005.

[224] H. Edelsbrunner, D. Kirkpatrick, and R. Seidel. On the shape of a set of points in the plane. *IEEE Transactions on Information Theory*, 29(4):551–559, 1983.

[225] J. Sun, M. Yao, B. Xu, and P. Bel. Fabric wrinkle characterization and classification using modified wavelet coefficients and support-vector-machine classifiers. *Textile Research Journal*, 81(9):902–913, 2010.

[226] C. Liu and Y. Fu. Novel measurement for multidirectional fabric wrinkling using wavelet analysis. *Fibers and Polymers*, 15(6):1337–1342, 2014.

[227] J. Hu, B. Xin, and H. Yan. Measuring and Modeling 3D Wrinkles in Fabrics. *Textile Research Journal*, 72(10):863–869, 2016.

[228] O. C. Zienkiewicz, D. Fox, and R. L. Taylor. *The finite element method for solid and structural mechanics.* Butterworth-Heinemann, Oxford, seventh edition edition, 2014.

[229] R. H. Myers, C. Anderson-Cook, and D. C. Montgomery. *Response surface methodology: Process and product optimization using designed experiments.* Wiley series in probability and statistics. John Wiley & Sons, Hoboken, New Jersey, fourth edition edition, 2016.

[230] T. Joppich. *Beitrag zum Umformverhalten von PA6/CF Gelegelaminaten im nicht-isothermen Stempelumformprozess.* Doctoral thesis (in German), Karlsruhe Institute of Technology, Karlsruhe, Germany, 2019.

[231] E. Piorkowska and G. C. Rutledge. *Handbook Of Polymer Crystallization.* John Wiley & Sons, Inc, Hoboken, New Jersey, 2013.

[232] D. Kugele, D. Dörr, F. Wittemann, B. Hangs, J. Rausch, L. Kärger, and F. Henning. Modeling of the Non-Isothermal Crystallization Kinetics of Polyamide 6 Composites During Thermoforming. *AIP Conference Proceedings 1869*, page 030005, 2017.

[233] M. Lang. *Charakterisierung der Reibeigenschaften von PA6- und PPS-UD-Tape.* Master's thesis, Karlsruhe Institute of Technology (KIT), Institute of Applied Materials, Karlsruhe, Germany, July 2015.

[234] F. Schulz. *Analysis of the friction behavior of UD-tapes considering relative layer orientations (in German).* Bachelor's thesis, Karlsruhe Institute of Technology (KIT), Institute of Vehicle System Technology, Karlsruhe, Germany, December 2015.

[235] M. Gully. *Characterization of the material features of the carbon fibre reinforced UD-Laminate (in German).* Master's thesis, Karlsruhe Institute of Technology (KIT), Institute of Vehicle System Technology, Karlsruhe, Germany, March 2017.

[236] D. Dörr, M. Faisst, T. Joppich, C. Poppe, F. Henning, and L. Kärger. Modelling Approach for Anisotropic Inter-Ply Slippage in Finite Element Forming Simulation of Thermoplastic UD-Tapes. In *AIP Conference Proceedings 1960*, page 020005.

[237] I. M. Hutchings and P. Shipway. *Tribology: Friction and wear of engineering materials.* Butterworth-Heinemann an imprint of Elsevier, Oxford, 2017.

[238] P. d. Luca, P. Lefébure, and A. K. Pickett. Numerical and Experimental Investigation of Some Press Forming Parameters of Two Fibre Reinforced Thermoplastics: APC2-AS4 and PEI-CETEX. *Composites Part A: Applied Science and Manufacturing*, (29(1-2)):101–110, 1998.

[239] S. Isogawa, H. Aoki, and M. Tejima. Isothermal Forming of CFRTP Sheet by Penetration of Hemispherical Punch. *Procedia Engineering*, 81:1620–1626, 2014.

[240] K. Vanclooster, S. van Goidsenhoven, S. V. Lomov, and I. Verpoest. Optimizing the deepdrawing of multilayered woven fabric composites. *International Journal of Material Forming*, 2(1):153, 2009.

[241] S. Ropers, U. Sachs, M. Kardos, and T. A. Osswald. A thermo-viscoelastic approach for the characterization and modeling of the bending behavior of thermoplastic composites – Part II. *Composites Part A: Applied Science and Manufacturing*, 96:67–76, 2017.

[242] SIMULIA. Abaqus 6.14 documentation, available online April 4 2019, http://ivt-abaqusdoc.ivt.ntnu.no:2080/v6.14/.

[243] SIMULIA. *Documentation: VUGENS - User subroutine to define the mechanical behavior of a shell section. (supplied by Dassault)*. 2015.

[244] W.-F. Chen and A. F. Saleeb. *Constitutive Equations for Engineering Materials: Elasticity and Modeling*. Elsevier Science, Burlington, 1994.

[245] W. Sun, E. L. Chaikof, and M. E. Levenston. Numerical approximation of tangent moduli for finite element implementations of nonlinear hyperelastic material models. *Journal of biomechanical engineering*, 130(6):061003, 2008.

[246] J. Bergstrom. *Mechanics of solid polymers: Theory and computational modeling*. William Andrew is an imprint of Elsevier, Amsterdam, first edition edition, 2015.

[247] J. A. Nelder and R. Mead. A Simplex Method for Function Minimization. *The Computer Journal*, 7(4):308–313, 1965.

[248] C. D. Han. *Rheology and processing of polymeric materials: Volume 1: Polymer rheology*. Oxford University Press, Oxford and New York, 2007.

[249] N. Hansen and A. Ostermeier. Completely derandomized self-adaptation in evolution strategies. *Evolutionary computation*, 9(2):159–195, 2001.

[250] C. Poppe, T. Joppich, D. Dörr, L. Kärger, and F. Henning. Modeling and validation of gripper induced membrane forces in finite element forming simulation of continuously reinforced composites. *AIP Conference Proceedings 1896*, page 030002, 2017.

[251] C. Poppe, D. Dörr, F. Henning, and Kärger. A 2D modeling approach for fluid propagation during FE-forming simulation of continuously reinforced composites in wet compression moulding. *AIP Conference Proceedings 1960*, page 020022, 2018.

[252] C. Poppe, T. Rosenkranz, D. Dörr, and L. Kärger. Comparative experimental and numerical analysis of bending behaviour of dry and low viscous infiltrated woven fabrics. *Composites Part A: Applied Science and Manufacturing*, 124:105466, 2019.

[253] D. Dörr, F. Henning, and L. Kärger. Nonlinear hyperviscoelastic modelling of intra-ply deformation behaviour in Finite element forming simulation of continuously fibre-reinforced thermoplastics. *Composites Part A: Applied Science and Manufacturing*, (109):585–596, 2018.

[254] J.-L. Batoz, K.-J. Bathe, and L.-W. Ho. A study of three–node triangular plate bending elements. *International Journal for Numerical Methods in Engineering*, 15(12):1771–1812, 1980.

[255] T. Wenzel and H. Schoop. A non–linear triangular curved shell element. *International Journal for Numerical Methods in Biomedical Engineering*, 20(4):251–264, 2004.

[256] A. Ibrahimbegović, F. Frey, and I. Kožar. Computational aspects of vector-like parametrization of three-dimensional finite rotations. *International Journal for Numerical Methods in Engineering*, 38(21):3653–3673, 1995.

[257] C. Miehe, N. Apel, and M. Lambrecht. Anisotropic additive plasticity in the logarithmic strain space: modular kinematic formulation and implementation based on incremental minimization principles for standard materials. *Computer Methods In Applied Mechanics And Engineering*, 191(47–48):5383–5425, 2002.

[258] J. Lemaitre, J.-L. Chaboche, and B. Shrivastava. *Mechanics of solid materials*. Cambridge Univ. Press, Cambridge, 1. paperback ed., reprinted. edition, 1998.

[259] J. Hurtado, I. Lapczyk, and S. Govindarajan. Parallel rheological framework to model non-linear viscoelasticity, permanent set and Mullins effect in elastomers. In N. Gil-Negrete and

A. Alonso, editors, *Constitutive models for rubber VIII*, pages 95–100. CRC Press/Balkema, Boca Raton, Fla., 2013.

[260] B. M. Adams, L. E. Bauman, W. J. Bohnhoff, K. R. Dalbey, M. S. Ebeida, J. P. Eddy, M. S. Eldred, P. D. Hough, and et al. Dakota, A Multilevel Parallel Object-Oriented Framework for Design Optimization, Parameter Estimation, Uncertainty Quantification, and Sensitivity Analysis: Version 6.0 User's Manual. July 2014. Updated November 2015 (Version 6.3), available online: March 13 2017, https://dakota.sandia.gov/content/citing-dakota.

[261] E. Guzman-Maldonado, N. Hamila, P. Boisse, and J. Bikard. Thermomechanical analysis, modelling and simulation of the forming of pre-impregnated thermoplastics composites. *Composites Part A: Applied Science and Manufacturing*, 78:211–222, 2015.

[262] A. Konyukhov and K. Schweizerhof. *Computational Contact Mechanics*, volume 67. Springer Berlin Heidelberg, Berlin, Heidelberg, 2013.

[263] H. D. Baehr and K. Stephan. *Heat and Mass Transfer*. Springer-Verlag Berlin Heidelberg, Berlin, Heidelberg, 3., rev. ed. edition, 2011.

[264] M. L. Di Lorenzo and C. Silvestre. Non-isothermal crystallization of polymers. *Progress in Polymer Science*, 24(6):917–950, 1999.

[265] M. Avrami. Kinetics of Phase Change. I General Theory. *Journal of Chemical Physics*, 7:1103–1112, 1939.

[266] J. D. Hoffman and J. J. Weeks. Rate of Spherulitic Crystallization with Chain Folds in Polychlorotrifluoroethylene. *The Journal of Chemical Physics*, 37(8):1723–1741, 1962.

[267] J. D. Hoffman, G. T. Davis, and J. I. Lauritzen. Treatise on solid state chemistry. *Plenum Press, New York*, (3):497, 1976.

[268] A. Ziabicki. *Fundamentals of Fibre Formation: The Science of Fibre Spinning and Drawing*. John Wiley & Sons, Ltd, London, 1976.

[269] K. Nakamura, T. Watanabe, K. Katayama, and T. Amano. Some aspects of nonisothermal crystallization of polymers. I. Relationship between crystallization temperature, crystallinity, and cooling conditions. *Journal of Applied Polymer Science*, 16(5):1077–1091, 1972.

[270] T. Ozawa. Kinetics of non-isothermal crystallization. *Polymer*, 12(3):150–158, 1971.

[271] N. Billon, P. Barq, and J. M. Haudin. Modelling of the Cooling of Semi-crystalline Polymers during their Processing. *International Polymer Processing*, 6(4):348–355, 1991.

[272] R. M. Patel and J. E. Spruiell. Crystallization kinetics during polymer processing-Analysis of available approaches for process modeling. *Polymer Engineering & Science*, (10):730–738, 1991.

[273] N. Feng, X. Wang, and D. Wu. Surface modification of recycled carbon fiber and its reinforcement effect on nylon 6 composites: Mechanical properties, morphology and crystallization behaviors. *Current Applied Physics*, 13(9):2038–2050, 2013.

[274] D.P.H. Hasselman, K.Y. Donaldson, and J.R. Thomas, and Jr. Effective Thermal Conductivity of Uniaxial Composite with Cylindrically Orthotropic Carbon Fibers and Interfacial Thermal Barrier. *J. Compos. Mater.*, (27 (6)):637–644, 1993.

[275] M. Villière, D. Lecointe, V. Sobotka, N. Boyard, and D. Delaunay. Experimental determination and modeling of thermal conductivity tensor of carbon/epoxy composite. *Composites Part A: Applied Science and Manufacturing*, 46:60–68, 2013.

[276] M. Y. Keating and C. S. Mclaren. Thermal conductivity of polymer melts. *Thermochimica Acta*, 166:69–76, 1990.

[277] J. E. Mark, editor. *Physical properties of polymers handbook*. Springer Science+Business Media LLC, New York, NY, 2. ed. edition, 2007.

[278] D. Kugele, J. Rausch, J. Kriegeseis, K. Gündisch, L. Kärger, and F. Henning. On the Thermal Behavior of Thermoplastic Laminates During Transfer - A Novel Wind-Tunnel Approach. *Proceedings ECCM17, München, Germany*, 2016.

[279] D. Kugele, J. Rausch, P. Müller, L. Kärger, and F. Henning. Temperature Distribution in Thickness Direction of Thermoplastic Laminates During Thermoforming. *Proceedings International Conference of Automotive Composites (IJAUTOC 2016), Lisbon, Portugal*, 2016.

[280] A. M. Roesner, L. Kärger, and F. Henning. Virtual characterization and macroscopic material modeling of a carbon fiber-reinforced PA6 UD composite. *Journal of Composite Materials*, 51(21):3075–3086, 2016.

[281] H. Xiong, E. Guzman Maldonado, N. Hamila, and P. Boisse. A prismatic solid-shell finite element based on a DKT approach with efficient calculation of through the thickness deformation. *Finite Elements in Analysis and Design*, 151:18–33, 2018.

[282] L. Kärger, S. Galkin, C. Zimmerling, D. Dörr, J. Linden, A. Oeckerath, and K. Wolf. Forming optimisation embedded in a CAE chain to assess and enhance the structural performance of composite components. *Composite Structures*, 192:143–152, 2018.

C Publication list

Journal publications

- D. Dörr, T. Joppich, D. Kugele, F. Henning, L. Kärger: A coupled thermomechanical approach for finite element forming simulation of continuously fiber-reinforced semi-crystalline thermoplastics, Composites: Part A 125: 105508, 2019.

- D. Dörr, F. Henning, L. Kärger: Nonlinear hyperviscoelastic modelling of intra-ply deformation behaviour in finite element forming simulation of continuously fibre-reinforced thermoplastics, Composites: Part A 109: 585-596, 2018.

- D. Dörr, F. J. Schirmaier, F. Henning, L. Kärger: A viscoelastic approach for modeling bending behavior in Finite Element forming simulation of continuously fiber reinforced composites, Composites: Part A 94: 113-123, 2017.

- D. Dörr, L. Lipowsky, F. Schirmaier, L. Kärger, F. Henning: An iterative approach for the determination of tailored blanks for waste-free composite forming by means of FE forming simulation. Int. J. Automotive Composites 3(2-4): 323-338, 2017.

Conference contributions

With conference proceedings

- D. Dörr, D. Kugele, T. Joppich, F. Henning, L. Kärger: On the Relevance of Thermomechanics and Crystallization Kinetics for FE Thermoforming Simulation of Semi-Crystalline Thermoplastic Tapes, AIP Conference Proceedings 2113: 020011, ESAFORM 2019, Vittoria-Gasteiz, 2019.

- D. Dörr, L. Schöttl, P. Pinter, F. Henning, L. Kärger: Layer-by-layer analysis of fiber orientation of formed continuously fiber-reinforced polymers based on computer tomographic (CT) scans, EUROMECH Colloquium 602, Lyon, 13.-15.03.2019.

- D. Dörr, M. Faisst, T. Joppich, C. Poppe, F. Henning, L. Kärger: Modelling Approach for Anisotropic Inter-Ply Slippage in Finite Element Forming Simulation of Thermoplastic UD-Tapes, AIP Conference Proceedings 1960: 020005, ESAFORM 2018, Palermo, 2018.

- D. Dörr, W. Brymerski, S. Ropers, D. Leutz, T. Joppich, L. Kärger, F. Henning: A Benchmark Study of Finite Element Codes for Forming Simulation of Thermoplastic UD-Tapes, 1st CIRP Conference on Composite Materials Parts Manufacturing (CIRP CCMPM 2017), Karlsruhe, 2017.

- D. Dörr, F.J. Schirmaier, F. Henning, L. Kärger: On The Relevance of Modeling Viscoelastic Bending Behavior in Finite Element Forming Simulation of Continuously Fiber Reinforced Composites, AIP Conference Proceedings 1896: 030003, ESAFORM 2017, Dublin, 2017.

- D. Dörr, T. Joppich, F. Schirmaier, T. Mosthaf, L. Kärger, F. Henning: Sensitivity of material properties on wrinkling behavior and fiber reorientation of thermoplastic UD-Tape laminates during forming analyzed by Finite Element forming simulation. ECCM17 - 17th European Conference on Composite Materials, Munich, 2016.

- D. Dörr, T. Joppich, F. Schirmaier, T. Mosthaf, L. Kärger, F. Henning: A method for validation of Finite Element forming simulation on basis of a pointwise comparison of distance and curvature. AIP Conference Proceedings 1769: 170011, ESAFORM 2016, Nantes, 2016.

- D. Dörr, L. Lipowsky, F. Schirmaier, L. Kärger, F. Henning: Iterative determination of the tailoring of blanks for a waste-free composite forming by means of finite element forming simulation. Proceedings. ICAutoC2016 - International Conference on Automotive Composites, Lisbon, 2016.

Without conference proceedings

- D. Dörr, C. Poppe, C. Zimmerling, C. Krauß, B. Schäfer, F. Henning, L. Kärger: Advanced Macroscopic Modelling Approaches for FE Composite Forming Simulation Using Abaqus, SIMULIA Regional User Meeting, Hanau, 05.-06.12.2018.

- D. Dörr, B. Fengler, M. Hohberg, L. Kärger, F. Henning: Integrated process simulation as enabler for efficient and robust design of composites and hybrids, Fraunhofer Technology Seminar, Seoul (Korea), 08.11.2018.

- D. Dörr, T. Joppich, D. Kugele, F. Henning, L. Kärger: Thermomechanical analysis of thermoforming processes with continuously fibre-reinforced semi-crystalline thermoplastics. MSE - Materials Science and Engineering Congress 2018, Darmstadt, 26.-28.09.2018.

- D. Dörr, F. Schirmaier, T. Joppich, T. Fürst, L. Kärger, F. Henning: Methoden zur Umformsimulation von Endlosfaserverbunden mit ABAQUS. SIMULIA Konferenz, Aachen, 2015.

Co-authored journal publications

- L. Schöttl, D. Dörr, K. A. Weidenmann, L. Kärger, P. Pinter, P. Elsner: A novel approach for segmenting and mapping of local fiber orientation of continuous fiber-reinforced composite laminates based on volumetric images, NDT & E International, 2019 (submitted).

- C. Poppe, D. Dörr, F. Henning, L. Kärger: Comparative experimental and numerical analysis of bending behaviour of dry and infiltrated woven fabrics, Composites: Part A 124: 105466, 2019.

- C. Zimmerling, D. Dörr, F. Henning, L. Kärger: A Machine Learning Assisted Approach for Textile Formability Assessment and Design Improvement of Composite Components, Composites: Part A 124: 105459, 2019.

- F. Henning, L. Kärger, D. Dörr, F.J. Schirmaier, J. Seuffert, A. Bernath: Fast processing and continuous simulation of automotive structural composite components, Composites Science and Technology 171: 261-279, 2019.

- L. Kärger, S. Galkin, C. Zimmerling, D. Dörr, J. Linden, A. Oeckerath, K. Wolf: Forming optimisation embedded in a CAE chain to assess and enhance the structural performance of composite components. Composite Structures 192: 143-152, 2018.

- C. Poppe, D. Dörr, F. Henning, L. Kärger: Experimental and numerical investigation of the shear behaviour of infiltrated woven fabrics, Composite Part A 14: 327-337, 2018.

- F.J. Schirmaier, D. Dörr, F. Henning, L. Kärger: A macroscopic approach to simulate the forming behaviour of stitched unidirectional non-crimp fabrics. Composites Part A 102: 322-335, 2017.

Co-authored conference contributions

With conference proceedings

- H. O. Werner, D. Dörr, F. Henning, L. Kärger: Numerical Modeling of a Hybrid Forming Process for Three-Dimensionally Curved Fiber-Metal Laminates, AIP Conference Proceedings 2113: 020019, ESAFORM 2019, Vittoria-Gasteiz, 2019.

- C. Poppe, D. Dörr, F. Kraus, L. Kärger: Experimental and Numerical Investigation of the Contact Behavior during FE Forming Simulation of Continuously Reinforced Composites in Wet Compression Molding, AIP Conference Proceedings 2113: 020002, ESAFORM 2019, Vittoria-Gasteiz, 2019.

- C. Poppe, D. Dörr, L. Kärger: Systematic Approach for the development of an FE-based process simulation framework for wet compression moulding of continuously reinforced compsoites, EUROMECH Colloquium 602, Lyon, 13.-15-03.2019.

- L. Kärger, D. Dörr, J. Seuffert, A. Bernath, C. Krauß, F. Henning: Continuous process simulation of automotive structural

composite components, EUROMECH Colloquium 602, Lyon, 13.-15.03.2019.

- C. Zimmerling, D. Dörr, F. Henning, L. Kärger: A Meta-Model Based Approach for Rapid Formability Estimation of Continuous Fibre Reinforced Components, AIP Conference Proceedings 1960: 020042, ESAFORM 2018, Palermo, 2018.

- C. Poppe, D. Dörr, F. Henning, L. Kärger: A 2D modeling approach for fluid propagation during FE-forming simulation of continuously reinforced composites in wet compression moulding, AIP Conference Proceedings 1960: 020022, ESAFORM 2018, Palermo, 2018.

- C. Poppe, D. Dörr, T. Joppich, L. Kärger, F. Henning: Modeling and Validation of Gripper Induced Membrane Forces in Finite Element Forming Simulation of Continuously Reinforced Composites, AIP Conference Proceedings 1896: 030002, ESAFORM 2017, Dublin, 2017.

- D. Kugele, D. Dörr, F. Wittemann, B. Hangs, J. Rausch, L. Kärger, F. Henning: Modelling of the Non-Isothermal Crystallization Kinetics of Polyamide 6 Composites During Thermoforming, AIP Conference Proceedings 1896: 030005, ESAFORM 2017, Dublin, 2017.

- L. Kärger, S. Galkin, C. Zimmerling, D. Dörr, F.J. Schirmaier, A. Oeckerath, K. Wolf, J. Linden: Continuous CAE chain for composite design, established on an HPC system and accessible via web-based user-interfaces. Proceedings NAFEMS World Congress, Stockholm, 2017.

Without conference proceedings

- M. Hohberg, B. Fengler, O. Saburow, N. Meyer, F. Wittemann, D. Dörr, L. Kärger, F. Henning: Durchgehende CAE-Kette durch die Verknüpfung des Design, der Prozess- und der Struktursimulation zur ganzheitlichen Bewertung von langfaserverstärkten Duromeren und Thermoplasten, DVM WS: Qualifizierung von Kunststoffstrukturbauteilen mittels integrativer Simulation, 20.-21.03.2018, Pfinztal, Germany.

- F. Wittemann, M. Hohberg, B. Fengler, O. Saburow, N. Meyer, D. Dörr, L. Kärger, F. Henning: Simulation of Discontinuous Fiber Reinforced Composites along the CAE-Chain. Mahle R&D Networking, Stuttgart, 2018.

- T. Link, S. Baumgärtner, D. Dörr, M. Hohberg, F. Henning: Systemleichtbau mit thermoplastischen Hochleistungsfaserverbunden in Hybridbauweise - neue Konzepte für die Fahrzeugkarosserie, Symposium Composites 2018, Augsburg, 19.-20.09.2018.

- L. Kärger, D. Dörr, C. Poppe, J. Seuffert, A. Bernath, S. Galkin, C. Zimmerling, F. Henning: Continuous Process Simulation for Continuous Fiber Reinforced Composites, International VDI Conference, Amsterdam, 2018.

- L. Schöttl, D. Dörr, P. Pinter, T. Joppich, F. Henning, L. Kärger: An approach for the layer-by-layer analysis of fiber orientation of continuously fiber-reinforced polymers based on orientation analyses of computer-tomographic (CT) scans. MSE - Materials Science and Engineering Congress 2018, Darmstadt, 26.-28.09.2018.

- M. Hohberg, B. Fengler, O. Saburow, N. Meyer, F. Wittemann, D. Dörr, L. Kärger, F. Henning: Simulation of Discontinuous Fiber Reinforced Polymers along the CAE-Chain, Materials Science and Engineering Congress 2018 (MSE), 26.-28.09.2018, Darmstadt, Germany.

- T. Joppich, D. Dörr: Vom Tape zur maßgeschneiderten Leichtbaulösung - Neueste Entwicklungen bei Prozess und Simulation, LBZ Workshop "Vom Tape zur maßgeschneiderten Leichtbaulösung", Pfinztal (Germany), 2017.

- L. Kärger, A. Bernath, D. Dörr, S. Galkin, D. Magagnato, F. Schirmaier, F. Henning: Simulation methods for process design of structural composite components. asc(s simpulseday green-CAE, Weissach, 2016.

- L. Kärger, D. Dörr, S. Galkin, F. Schirmaier, F. Henning: Forming simulation for process design of curved CFRP structures. 19. Airbus Workshop "Tooling for CFRP Production & Assembly", Augsburg, 2016.